H_2GO Final Report

Design Report for the H_2ERMES Reusable Launch Vehicle for Hydrogen Refueling

Group 07

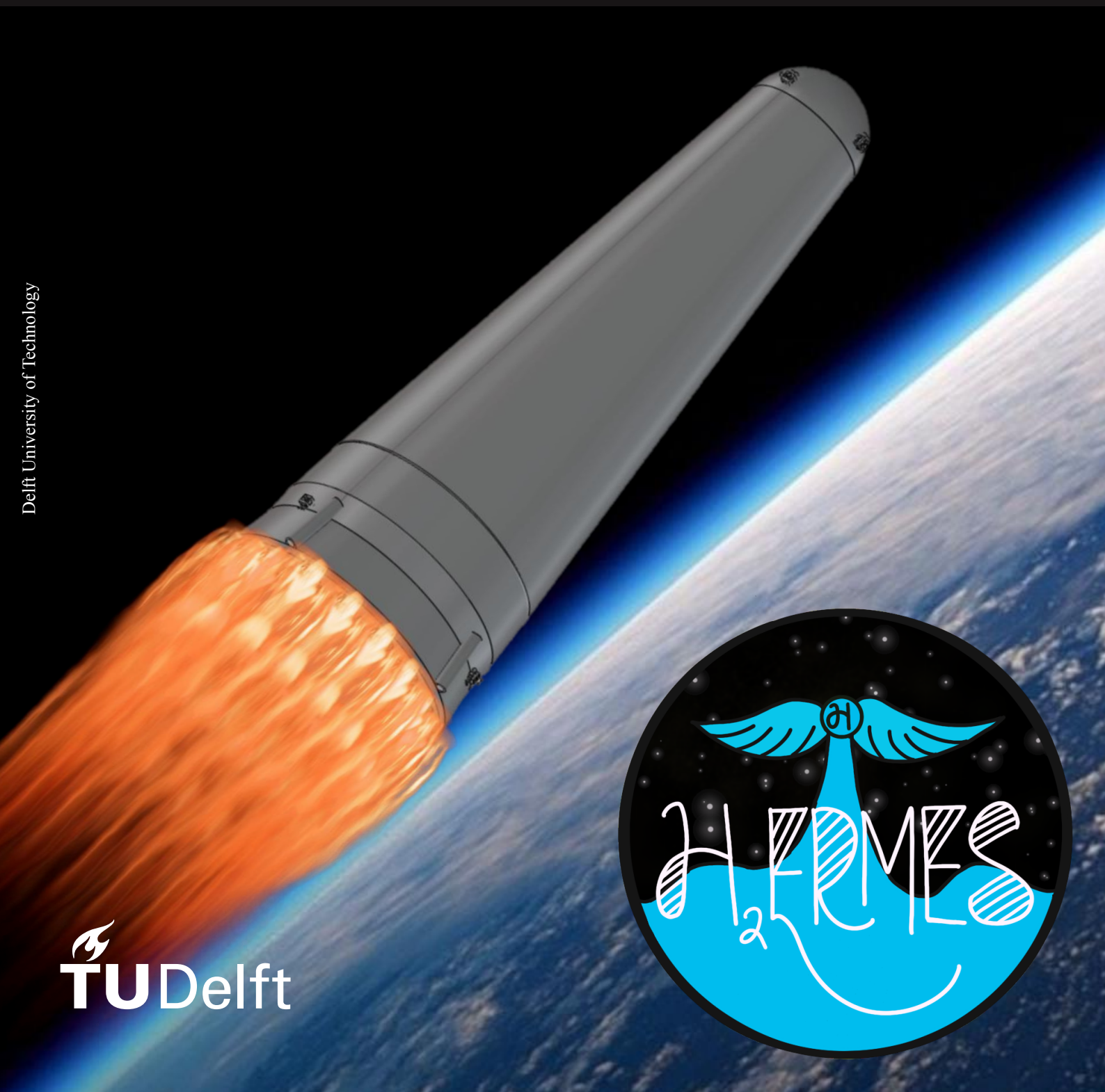

Delft University of Technology

TU Delft

This page is intentionally left blank

H_2GO Final Report

Design Report for the H_2ERMES Reusable Launch Vehicle for Hydrogen Refueling

by

Group 07

Diogo Filipe Cravo da Costa	5686962
Lucía García Gutiérrez	5710308
Thomas van Haarst	5418674
Gergely Homoki	5748771
Matyas Karasek	5701716
Soham Katewale	5725577
Jiří Kovář	5063132
Ashwanth Krishnamoorthi	5718996
Andreea Lupei	4798902
Dhruv Maggon	5685400
Angélique Orban	5779545

Project Duration:	April-June, 2025
Faculty:	Faculty of Aerospace Engineering, Delft
Tutor:	B. V. S. Jyoti
Coaches:	N. Dangi and L. Afilal
Version:	2.0

TU Delft

Contents

Nomenclature

Abbreviations

GH_2	Gaseous hydrogen
LH_2	Liquid hydrogen
AC	Alternating Current
AOCS	Attitude & Orbital Control System
AODCS	Attitude & Orbital Determination and Control System
AODS	Attitude & Orbital Determination System
BLEVE	Boiling Liquid Expanding Vapor Explosion
CERs	Cost Estimation Relationships
CFD	Computational Fluid Dynamics
COTS	Commercial Off-the-Shelf Product
CRM	Continuous Risk Management
CRM	Critical Raw Materials
CSG	Guiana Space Center
DC	Direct Current
DOC	Direct Operational Cost
ECU	Engine Control Unit
ENG	Engineering
ESA	European Space Agency
FBS	Functional Breakdown Structure
FEM	Finite Element Method
FFD	Functional Flow Diagram
FOD	Foreign Object Debris
FTCS	Forward Time-Centered Scheme
HTP	High Test Peroxide
IDEMAT	Industrial Design & Engineering MATerials database
IDSS	International Docking System Standard
IOC	Direct Operational Cost
ISO	International Organization for Standardization
Kbps	Kilobits per second
LCA	Life Cycle Assessment
LCI	Life Cycle Inventory
LEO	Low Earth Orbit
LpA	Launches per Annum
M/PA	Management and Production Assurance
MAIT	Manufacturing, Assembly, Integration, Testing
MMOI	Mass Moment of Inertia $[\text{kgm}^2]$
NASA	National Aeronautics and Space Administration
NPSH	Net Positive Suction Head $[\text{m}]$
O/F	Oxidizer to Fuel Ratio
P&ID	Piping and Instrumentation Diagram
PO	Project Office
QA	Quality Assurance
QC	Quality Control
RCS	Reaction Control System
ROI	Return on Investment $[-]$
RPA	Rocket Propulsion Analysis
SDG	Sustainable Development Goals
STH	Total System Test Hardware $[-]$
UN	United Nations

Constants

μ_E	Standard gravitational parameter of Earth $3.986 \times 10^{14}\,[\text{m}^3/\text{s}^2]$
σ	Stefan-Boltzmann constant $5.670 \times 10^{-8}\,[\text{W}/\text{m}^2/\text{K}^4]$
g_0	Standard gravitational acceleration $9.807\,[\text{m}/\text{s}^2]$

J_2	Second dynamic form factor of Earth 1.082×10^{-3}	[–]

Greek Symbols

α	Angle of attack	[°]
β	Ballistic coefficient	[kg/m^2]
δ	Phase shift constant	[rad]
Δp_p	Required pump pressure rise	[Pa]
Δp_{cool}	Pressure loss in cooling jacket	[Pa]
$\Delta p_{\text{dynamic}}$	Increase in dynamic pressure	[Pa]
Δp_{feed}	Pressure loss in feedlines	[Pa]
Δp_{inj}	Pressure loss in the injector	[Pa]
Δp_{ps}	Max. allowable pressure rise per turbopump stage	[Pa]
ΔV	Change of velocity	[m/s]
ϵ	Emissivity	[–]
ϵ	Expansion ratio	[–]
η_p	Turbopump efficiency	[–]
γ	Flightpath angle	[°]
κ	Thermal conductivity	[W/m/K]
λ	Slenderness ratio	[–]
μ	Dynamic viscosity	[Pas]
μ	Euler-Cauchy damping coefficient	[–]
μ	Half-arc of spherical cap	[rad]
μ	Mass ratio	[–]
ν	Euler-Cauchy frequency coefficient	[–]
Ω	Right ascension of the ascending node	[°]
ω	Cone half-angle	[°]
ω	Oscillation frequency	[Hz]
ϕ	Phase angle	[°]
ρ	Density	[kg/m^3]
ρ	Tangential Meridian	[rad]
ρ_p	Propellant density	[kg/m^3]
σ	Stress	[Pa]
σ_s	Structural ratio	[–]
τ	Pump shaft torque	[Nm]
θ	Polar angle	[rad]
ϑ	Pitch angle	[°]
ξ	Damping coefficient	

Other Symbols

$\ddot{\cdot}$	Second time derivative
$\dot{\cdot}$	First time derivative
*	Normalized value

Roman Symbols

$\dot{m}$	Mass flow	[kg/s]
A	Angle-of-attack constant	[–]
a	Acceleration	[m/s^2]
a	Semi-major axis	[m]
c^*	Characteristic velocity	[m/s]
C_p	Profit retention cost retention factor	[%]
c_p	Specific heat	[W/m^2/K]
C_{DEV}	Development cost	[US$]
C_{FI}	Cost of fees and insurance	[US$]
C_{FM}	Flight model cost	[US$]
C_{ground}	Ground operation costs	[US$]
C_{MAN}	Manufacturing cost	[US$]
C_{OPS}	Operational cost	[US$]
C_{prop}	Propellant cost	[US$]
C_{trans}	Transportation cost	[US$]
C_{unit}	Cost per unit	[US$]
C_A	Axial force coefficient	[–]
C_D	Drag coefficient	[–]
c_f	Specific propellant cost	[US$/kg]
C_L	Lift coefficient	[–]
C_{m_α}	Moment coefficient slope	[–]

$C_{m_q} + C_{m_{\dot{\alpha}}}$	Pitch damping coefficient	$[-]$
C_N	Normal force coefficient	$[-]$
c_{ox}	Specific oxidizer cost	[US$/kg]
C_p	Pressure coefficient	$[-]$
C_X	Force coefficient in X-direction	$[-]$
C_Y	Force coefficient in Y-direction	$[-]$
C_Z	Force coefficient in Z-direction	$[-]$
d	Characteristic length	[m]
E	Energy	[J]
E	Young's Modulus	[Pa]
e	Eccentricity	[°]
h_c	Coolant convective heat transfer coefficient	$[\mathrm{W/m^2/K}]$
H_p	Head pressure rise	[m]
I	Moment of inertia	$[\mathrm{kgm^2}]$
i	Inclination	[°]
I_{sp}	Specific impulse	[s]
I_{xx}	Area moment of inertia	$[\mathrm{m^4}]$
K	Column effective length factor	$[-]$
L	Length	[m]
L^*	Characteristic length	[m]
L_d	Development learning factor	$[-]$
M	Moment	[Nm]
N_r	Pump rotational speed	[rad/s]
n_{legs}	Number of landing legs	$[-]$
p_c	Chamber Pressure	[Pa]
p_i	Pump inlet pressure	[Pa]
p_o	Pump outlet pressure	[Pa]
p_v	Fluid vaporization pressure	[Pa]
P_{req}	Required power from turbine	[W]
Q	Volumetric flow rate	$[\mathrm{m^3/s}]$
q_c	Cooling heat flux	$[\mathrm{W/m^2}]$
q_i	Incident heat flux	$[\mathrm{W/m^2}]$
q_r	Radiative heat flux	$[\mathrm{W/m^2}]$
r	Radius	[m]
R_i	Stress ratio	$[-]$
S	Reference area	$[\mathrm{m^2}]$
s	Stroke length	[m]
t	Thickness	[m]
T_s/T_b	Ratio of coolant channel surface temperature and coolant bulk temperature	$[-]$
u_{ss}	Suction specific speed	[m/s]
V_c	Chamber volume	$[\mathrm{m^3}]$
V_c	Propellant velocity	[m/s]
x/D	Coolant channel characteristic length	$[-]$
Nu	Nusselt number	$[-]$
Pr	Prandtl number	$[-]$
Re	Reynolds number	$[-]$
A	Area	$[\mathrm{m^2}]$
a	Acceleration	[m/s]
IV	Interaction Value	$[-]$
M	Mach number	$[-]$
m	Mass	[kg]
n	Number of stages in turbopump	$[-]$
r	Distance	[m]
SF	Safety factor	$[-]$
T/W	Thrust to weight ratio	$[-]$
T1	Recurring first unit	[US$]
V	Velocity	[m/s]

1 Executive Overview

H_2GO is a project that aims to design a launch vehicle that carries liquid hydrogen to an orbital fuel depot for the use of NTR in upcoming space missions. The launch vehicle, named H_2ERMES, addresses the following need and objective:

Mission Need Statement

> *To enable economical and sustainable space exploration, there is a need to develop infrastructure supporting nuclear thermal rocket propelled spacecraft.*

Project Objective Statement

> *To design a launch vehicle to facilitate in orbit refueling of liquid hydrogen, via orbiting fuel depots in an environmentally and economically sustainable manner.*

The project H_2GO aims to perform its first operational flight by 2032. To achieve this, a brief timeline of the project was drawn and the design aims to be finalized by mid 2026, the manufacturing, testing and integration performed by 2029 and flight test phase ranging until 2032.

In order to evaluate the competitiveness of H_2ERMES compared to the current offer of launchers, a market analysis was conducted. It consisted of identifying the different stakeholders and then performing a SWOT analysis to assess the strengths, weaknesses, opportunities and threats of the launcher. The main takeaways from this analysis is that H_2ERMES aims to address a future market need for more sustainable deep-space exploration at cheap launch rates, thanks to its reusability, after a few years of operations, while incorporating new technologies such as a regeneratively cooled heat shield an engine benefiting from the aerospike effect. Concerns were raised on the current state of research for NTR following budget cuts to NASA which could lead to the termination of the main research project on the topic, project DRACO.

Requirements

The first step of the design process is to establish the requirements that translate into the functions and performance the system must comply to. They were broken down into stakeholder requirements, system requirements and subsystem requirements. The list of stakeholder requirements is given by Table 1.1.

Table 1.1: Stakeholder requirements

Requirement ID	Requirement	Importance
RQ-STK-COS-1	The vehicle shall be developed with a total engineering budget not exceeding US$1.54 billion through its first operational flight.	Driving
RQ-STK-COS-2	The operational cost per launch shall not exceed US$77 million after its first 5 operational flights.	
RQ-STK-COS-3	The total cost of the vehicle shall not change to more than 33 [%] of the initial estimate.	
RQ-STK-PLD-1	The vehicle shall autonomously deliver a payload of at least 10000 [kg] of LH_2.	Driving
RQ-STK-PLD-2	The vehicle shall safely transport LH_2 as a payload to the designated orbit.	
RQ-STK-PLD-3	The vehicle shall transport a total of 500000 [kg] of LH_2 to the depot in a year.	Driving
RQ-STK-PLD-4	The vehicle shall deliver the payload to an orbit of 600 [km] at a 6 [°] inclination.	Driving
RQ-STK-DOK-1	The vehicle shall be responsible for all maneuvering in orbit, while the refueling station remains stationary.	Driving
RQ-STK-DOK-2	The vehicle shall autonomously come within 15.2 [m] of the station.	

continued on next page

Table 1.1 – *continued from previous page*

Requirement ID	Requirement	Importance
RQ-STK-DOK-3	The vehicle shall stay at the targeted distance from the refueling station for 10 [min].	
RQ-STK-RFL-1	The vehicle shall complete the refueling process within 3 [h].	
RQ-STK-RFL-2	The vehicle shall support in-orbit hydrogen refueling via a passive fluid interface provided by the customer.	
RQ-STK-RLV-1	The launch vehicle shall have a turnaround time of two months between consecutive launches.	
RQ-STK-RLV-2	The reusable vehicle shall be capable of at least 25 launches with minimal refurbishment.	Driving
RQ-STK-RLV-3	The first operational launch shall happen before 2032.	
RQ-STK-RLV-4	The mission shall return the vehicle to Earth for refurbishment and re-use.	Driving
RQ-STK-REL-1	The vehicle shall have safety factors when applicable according to industry standards.	Driving
RQ-STK-REL-2	The vehicle shall achieve at least a 95 [%] mission success rate over its first 20 operational launches.	
RQ-STK-SUS-1	The vehicle shall produce at least 25 [%] less emissions throughout its launch compared to current operational rockets.	Driving
RQ-STK-SUS-2	The vehicle shall be compliant with NASA-STD-8719.14C to reduce space debris.	
RQ-STK-SUS-3	The design of the vehicle shall incorporate at least 20 [%] recyclable or reusable materials throughout its construction.	
RQ-STK-REG-1	The vehicle and launch operations shall be compliant with Order Regulating the Operation of Installations of the Guyana Space Center.	
RQ-STK-REG-2	The vehicle shall incorporate safety protocols from SSCMAN91-710 and ECSS-Q-ST-40C Rev.1.	
RQ-STK-REG-3	The vehicle shall use radio frequency spectra in coordination with the International Telecommunication Union.	

Technical Risks

The risk assessment was performed according to the guidelines established in the NASA Risk Management Handbook [1]. The method follows those steps: *Identify, Analyze, Plan, Track and Control the risks*. For each identified risk, the severity and probability scores are assigned based on their impact and chance of occurrence, multiplying them together gives their risk index. Based on this criteria, the magnitude and acceptability of the risks are determined. The risks with unacceptable risk index are mainly linked to structural failure, aerodynamics and handling of LH_2. After mitigation, the main risks are the following:

1. *RI-GNC-6*: Vehicle deviates from the intended re-entry path.
2. *RI-STR-3*: Vehicle experiences resonance leading to structural failure.
3. *RI-STR-1*: Vehicle structurally fails under the acceleration loads.
4. *RI-STR-4*: The presence of manufacturing defects leads to structural failure.

It is also important to mention that some risks have no contingency and therefore must be considered with care.

Trade-Off

Resulting from the trade-off performed during the midterm [2] on both system and subsystem level, the H_2ERMES vehicle features a blunted cone geometry, optimized for aerodynamics and structural integrity. Due to the use of LH_2 with LOX as propellant, it only features two cryogenic tanks: one for the fuel and payload, and one for the oxidizer, both sized and positioned to eliminate the need for insulation from the harsh space environment. Propulsion is provided by a 24 thrust chamber engine which takes advantage of the aerospike effect, situated on top of the regeneratively cooled heat shield, using the onboard propellant as coolant. Recovery is achieved using

four telescopic landing legs, attached to the outside of the main propellant tanks. The vehicle will fly on top of the first stage of Blue Origin's New Glenn launch vehicle, leveraging existing, proven hardware to focus development and refurbishment efforts on the novel reusable second stage. Additional key systems include power by the use of fuel cells, also powered by the stored hydrogen and oxygen, attitude control through hydrogen peroxide monopropellant thrusters, navigation using GPS receivers, communications by use of near Earth architecture with a point-to-point data relay, and docking by utilizing the International Docking System Standard on both the launch vehicle and the orbital depot, the latter of which will perform most of the docking maneuver by grabbing the launch vehicle with a robotic arm. This docking adapter also provides the umbilicals required to perform the refueling operations.

Preliminary Design

Following the functional analysis, a preliminary design of each subsystem was performed. This mainly consisted of developing a tool for sizing the subsystem, making critical design decisions, and outputting the subsystem mass or dimensions when applicable, or other design parameters. The goal by the end was to integrate all the tools to iterate the dry mass of H_2ERMES.

- **Aerodynamics**: H_2ERMES experiences all possible velocity regimes from subsonic (launch, re-entry, and recovery), transonic (launch, re-entry, and recovery) supersonic (launch, and re-entry), to hypersonic (re-entry). Newtonian methods were used for hypersonic calculations, and the RASAero tool for subsonic regimes. The vehicle exhibits a maximum lift-over-drag of 0.2 during the hypersonic regime, and a maximum lift-over-drag of 0.6 during the subsonic regime. The vehicle exhibits damped oscillatory motion at constant velocity conditions, however, it experiences diverging oscillations during deceleration.
- **Tanks**: The tanks are the main structural elements of the second stage; therefore, their outer walls correspond to the outer walls of H_2ERMES following the blunted cone geometry. The LH_2 and LOX monocoque tanks are made out of stainless steel 304L and share a common bulkhead. The pressure inside the tank is initially set to 2 [bar] and 2.5 [bar] respectively using autogenous-pressurization. The tanks were sized taking into account pressure, launch loads, buckling and fatigue which resulted in a thickness of 4.4 [mm] for the LH_2 tank and 5.4 [mm] for LOX. Additionally, one header tank for each propellant is present to limit sloshing during re-entry and landing burns.
- **Active Metallic Heat Shield**: H_2ERMES has a bottom-mounted actively cooled heat shield made of stainless steel 310, using LH_2 circulating through rectangular channels.
- **Propulsion**: The propulsion system consists of one engine with 24 thrust chambers, which takes advantage of the aerospike effect resulting from the interaction between the exhaust plume and the heat shield. One turbo pumps is used to achieve a pressure rise in the LH_2 and another one is used for LOX. The engine uses the expander bleed cycle, where both the LH_2 and LOX pumps are driven by hydrogen which was expanded by traversing the heat shield and combustion chamber's cooling channels. The fuel used to drive the pumps is then dumped overboard.
- **Landing Legs**: The landing legs follow a simple axial telescopic design with a single strut, sized for buckling and yielding under bending. Besides this, the legs feature an oleo-pneumatic shock absorber, pneumatic deployment mechanism, aero-cover to shield the legs from aerodynamic loads, and a mechanical locking mechanism.
- **Nosecone**: The nosecone was designed to withstand the aerothermodynamic loads experienced by the launch vehicle during ascent. The thickness of the cap is 2.22 [mm] while the thickness of the insulation is 2.10 [mm] which results in a design weight of approximately 800 [kg].
- **Power**: H_2ERMES requires high-density power for only three days (including a two-day safety margin), which led to the selection of two Space Shuttle alkaline fuel cells capable of delivering approximately 7 [kW] of continuous power and up to 12 [kW] of peal power at 28 [V] DC.
- **Data Handling**: Data handling uses a triple-redundant RAD5500 main computer running a real-time VxWorks OS capable of handling high sensor throughput and 1080p camera data streams.
- **Communications**: H_2ERMES uses a triple-redundant SDR to handle S-band uplink at 2.11 [GHz] and downlink at 2.29 [GHz].
- **Attitude & Orbital Determination and Control System**: H_2ERMES determines its attitude and orbit using four redundant PODRIX GNSS receivers and controls it with forty Nammo 220 [N] hydrogen-peroxide

thrusters.

- **Docking and Refueling**: The docking and refueling interface, while eventually provided by the customer according to *RQ-STK-RFL-2*, is recommended to follow the International Docking Standard System, which provides both the active and passive docking interfaces, and the locations and sizes for umbilicals for electricity and fluid transfer.
- **Boil-Off Mass Estimation**: The total boil-off mass estimation was calculated by looking at the expected boil-off at each phase of the mission. The external tool BoilFAST [3] was used to calculate the boil-off mass and state properties at different points in the mission.

Integration

Once each sizing tool was completed, a first integration was performed that converged to the first H_2ERMES design. A threshold of 1 [%] between iterations was taken to ensure the values are consistent. Additionally the P&ID (piping and instrumentation diagram), electrical block diagram and data flow chart were drawn. Lastly, the different budgets were established including mass, cost, power, data processing, link and delta V. The main takeaways from those budgets are summarized in Table 1.2.

Table 1.2: H_2ERMES Budget Summary

Characteristic	Value	Characteristic	Value
Wet Mass	300.1 [t]	Data Rate with Margin (70 [%])	56.2 [Mbps]
Dry Mass	39.5 [t]	ΔV Required	6391 [m/s]
Total Boil-Off	4.9-6.6 [t]	ΔV Available	6659 [m/s]
Payload	13.3-15 [t]	Development Cost	939.8M [US$]
Total Power	4890 [W]	Manufacturing Cost	25.3M [US$]
Total Power with Margin (20 [%])	5868 [W]	Operational Cost	70.0M [US$]
Data Rate	33.1 [Mbps]		

Vehicle Overview

The launch vehicle configuration with the subsystems integrated is shown in the figure below:

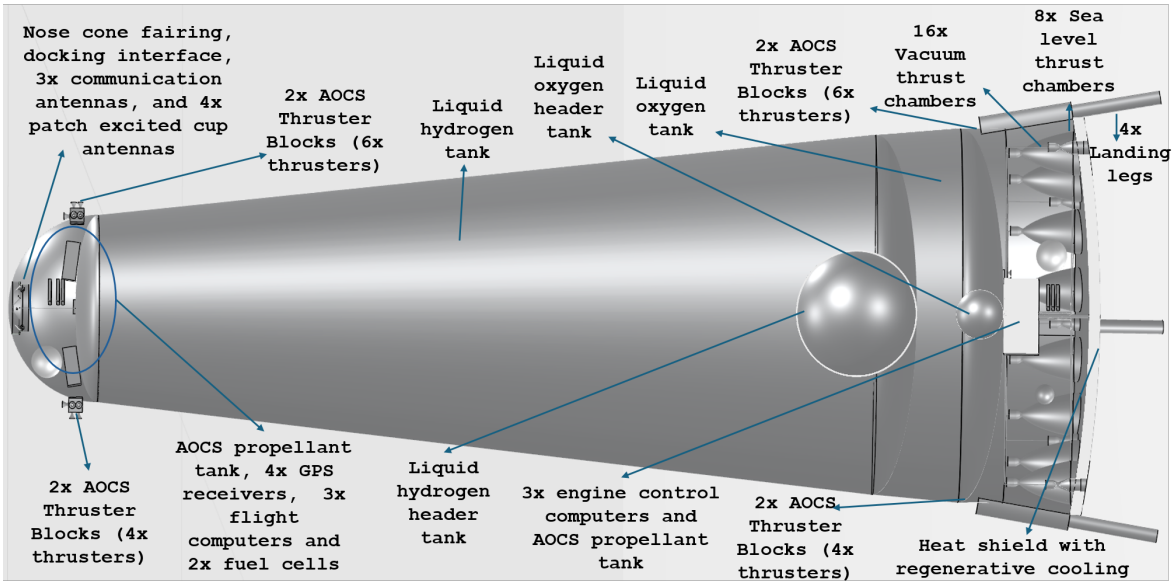

The flight timeline, shown in Figure 1.1, was established, from which it was determined that there will be approximately 150 launch windows per year, which is more than the 36 required for delivering 500 [t] of LH_2 per year.

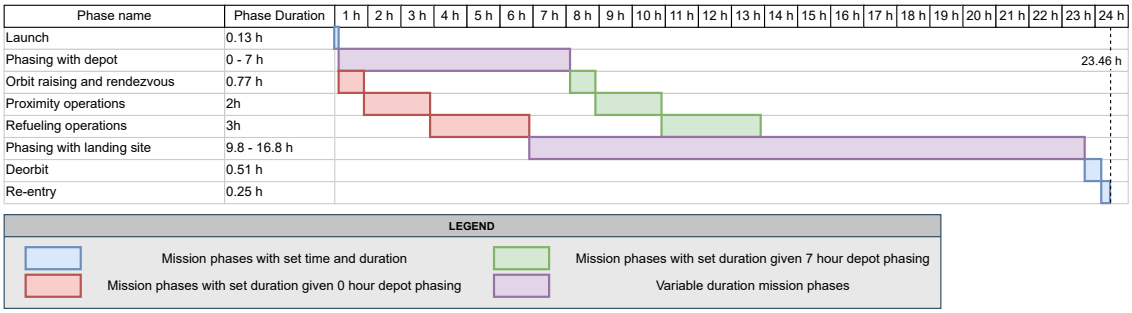

Figure 1.1: Flight timeline

Quality Assurance

It is vital to ensure each part of the design is properly verified and validated. For this, a description of the verification and validation methods for each tools is given, as well as verification of the requirements following one of the methods: Analysis, Inspection, Demonstration or Testing. Validation methods of each subsystems as products are also described. Lastly, the compliance matrix of the stakeholder requirements is given.

Sustainability Assessment

Three key factors of sustainability were identified: economic, social and environmental. These were considered from both a project management and a technical perspective. Moreover, Sustainable Development Goals (SDG's) 5, 7, 8, 9 and 12 of the United Nations were adopted for the H_2GO project. Additionally, a Life Cycle Assessment (LCA) was performed using the European Space Agency (ESA) LCA Handbook. It allows for a quantification of the emissions due to the production, launch and other activities related to H_2ERMES.

2 Introduction

The future of space exploration is rapidly evolving, with nuclear thermal rocket (NTR) propulsion emerging as a promising technology for deep space missions. NTR systems offer significantly higher specific impulse than traditional chemical propulsion, allowing for faster transfer times and more efficient deep space travel. However, despite their advantages in space, NTR suffers from low thrust-to-weight ratios, limiting its practicality for atmospheric launch. As a result, their application is primarily limited to in-space propulsion [4].

A conventional approach envisions spacecraft being launched using launch vehicles propelled through conventional chemical propulsion, with NTR being used only by spacecraft once in orbit. However, this introduces the primary challenge of NTR: its propellants, such as liquid hydrogen (LH_2) have very low densities, making them inefficient to launch in large quantities from Earth, due to the large volume requirements.

One proposed solution is the development of in-orbit refueling infrastructure. By establishing orbital fuel depots, spacecraft can launch with less mass and refuel once in space, reducing launch costs and increasing mission flexibility. The project developed in this report aims to contribute to that vision, by designing a vehicle capable of autonomously transporting LH_2 from Earth's surface to Low Earth Orbit (LEO), where it can dock with an orbital depot for refueling operations. This vehicle, named H_2ERMES, is engineered for autonomous operations from launch to orbital rendezvous and recovery, forming a key component of future deep space logistics.

This report delves into the design of H_2ERMES. The overview of the project is provided in Chapter 3, which then defines the requirements, which are listed in Chapter 4. When designing a new system, the associated risks must be considered, which are illustrated in Chapter 5. To initiate the design, the overview of trade-offs performed in conceptual design is presented in Chapter 6, through which concepts are generated and a final concept is chosen for detailed analysis and design. The analysis and preliminary design are performed in Chapter 8. The detailed subsystems and components are integrated through means discussed in Chapter 9. Once the design of the vehicle is done, the final vehicle overview is presented in Chapter 10. To ensure the validity of the design, quality assurance is performed through the steps outlined in Chapter 13. The operations of the mission are outlined in Chapter 11. The sustainability characteristics of the mission and vehicle design are evaluated in Chapter 12. Finally, the report is concluded with recommendations in Chapter 14.

3 Project Overview

This chapter presents an overview of the project. First, Section 3.1 gives an overview of the mission, followed by a market analysis in Section 3.2. Lastly, Section 3.3 gives the project objectives.

3.1. Mission Overview

The overall goal of the H_2ERMES vehicle is to deliver an LH_2 payload to orbital depots situated in LEO, to which a wide range of missions and customers are able to dock to refuel their spacecraft. Keeping this in mind, the design throughout the project is focused mainly on the second stage of the launch vehicle, ensuring full reusability at every step. The mission need statement and project objective statement are given as follows:

Mission Need Statement

> *To enable economical and sustainable space exploration, there is a need to develop infrastructure supporting nuclear thermal rocket propelled spacecraft.*

Project Objective Statement

> *To design a launch vehicle to facilitate in-orbit refueling of liquid hydrogen, via orbiting fuel depots in an environmentally and economically sustainable manner.*

3.1.1. Relevance

With an increasing need for sustainable space infrastructure, H_2ERMES aims to enable a platform for the use of NTR in upcoming space missions. By allowing cost-effective and environmentally responsible access to refueling of orbital depots, the mission aims to ensure the future of space exploration, either for long-life spacecraft in Earth's sphere of influence or recurrent, high efficiency, deep space missions.

3.1.2. Mission Milestones

The project timeline can be seen in Figure 3.1 and is divided into five main phases: The first phase consists of the work being performed in the context of the DSE which will produce the conceptual design of H_2ERMES presented at the symposium by the end of June 2025.

The second and third phases are the preliminary and final design. At the end of those two phases, the preliminary and critical design reviews are produced.

Following this, the manufacturing, testing and integration phase starts, focusing primarily in producing first iterations of the systems and testing them. By the end, an initial integration for the first flight test shall be performed. At the end of phase four, H_2ERMES can be subjected to a flight readiness review.

The fifth and last phase is the flight test phase, H_2ERMES will be tested in flight and from the data and potential failures observed, final design iterations can be made. Once the design is certified for commercial use, the first operational flight will take place in 2032.

3.2. Market Analysis

The objective of the market analysis is to evaluate the competitiveness of H_2ERMES compared to current offers found on the market. Additionally, the future of the market will be predicted according to existing initiatives and ongoing developments to assess the added value of the proposed technology. This market analysis is conducted using methods such as the Stakeholder Power/Interest Matrix in Section 3.2.1, SWOT analysis in Section 3.2.2, and prediction of the future market in Section 3.2.3.

3.2.1. Stakeholder Power/Interest Matrix

One powerful tool to assess the influence of the different stakeholders on the project is the power/interest matrix, shown in Figure 3.2.

The matrix is divided into four categories, firstly, "Regularly Engage", encompasses the customers, investors, different suppliers and the relevant space agencies. The stakeholders in this category require, as the name indicates, regular engagement and active communication. The second category, "Actively Consult", includes the military

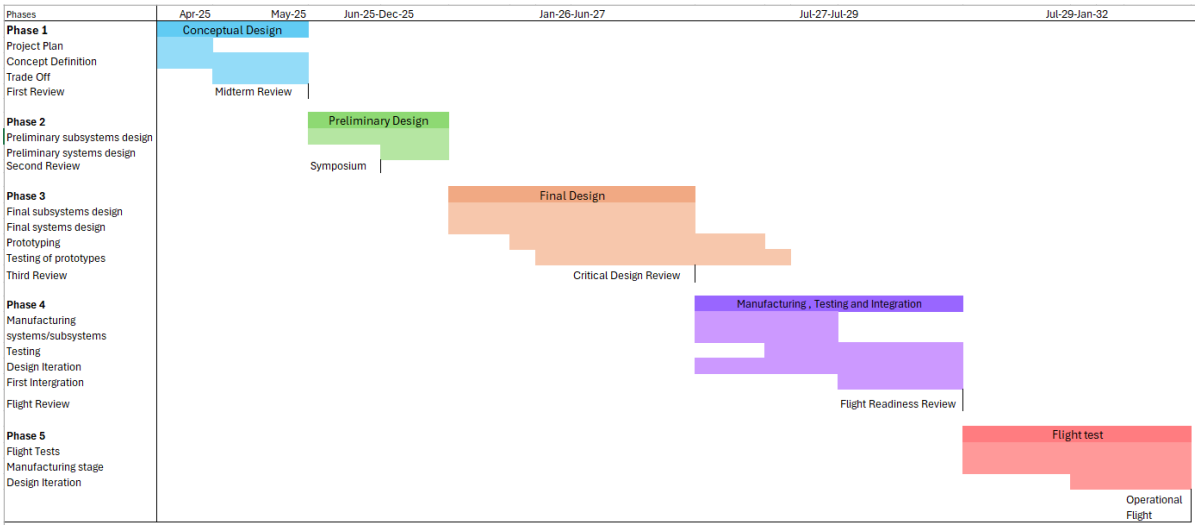

Figure 3.1: H_2ERMES project timeline

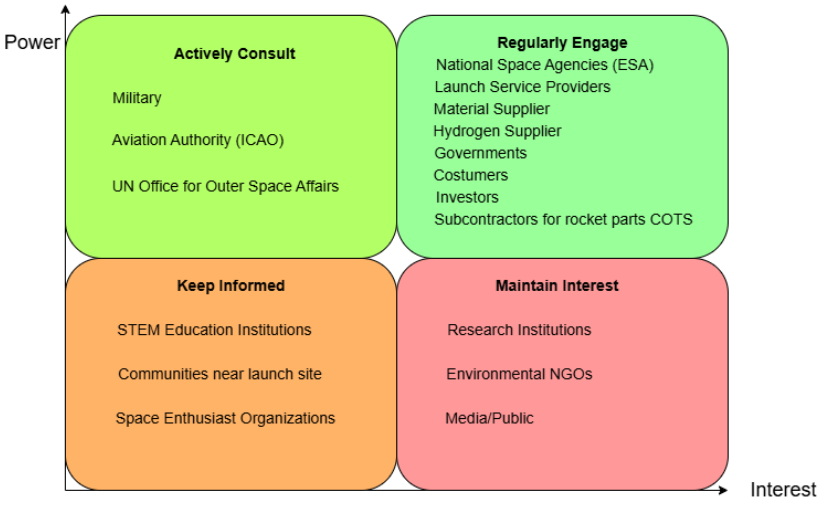

Figure 3.2: Stakeholder Interest/Power Matrix

and relevant authorities. Those institutional bodies are relevant and require consultancy regarding the regulation the product falls under. The stakeholders mentioned in those categories are considered **key** stakeholders of H_2GO.

The third and fourth categories referred to as ”Maintain Interest” and ”Keep Informed” encompass the different stakeholders with relatively low power on the project but that are still kept informed, given their shared interest in the project. Stakeholders with high interest but low power are the media which are critical for public relation purposes, as well as the different environmental NGOs and research institutions such as universities. Lastly, it is beneficial to keep informed stakeholders such as communities living close to the launch site.

3.2.2. SWOT Analysis

The SWOT analysis presented in Figure 3.3 outlines the mission’s strengths, including a novel concept, improved access to liquid hydrogen for nuclear thermal rocket propulsion, rocket reusability, and potential partnerships with existing initiatives. However, challenges include limited research, strong competition, and technical risks related to cryogenic conditions.

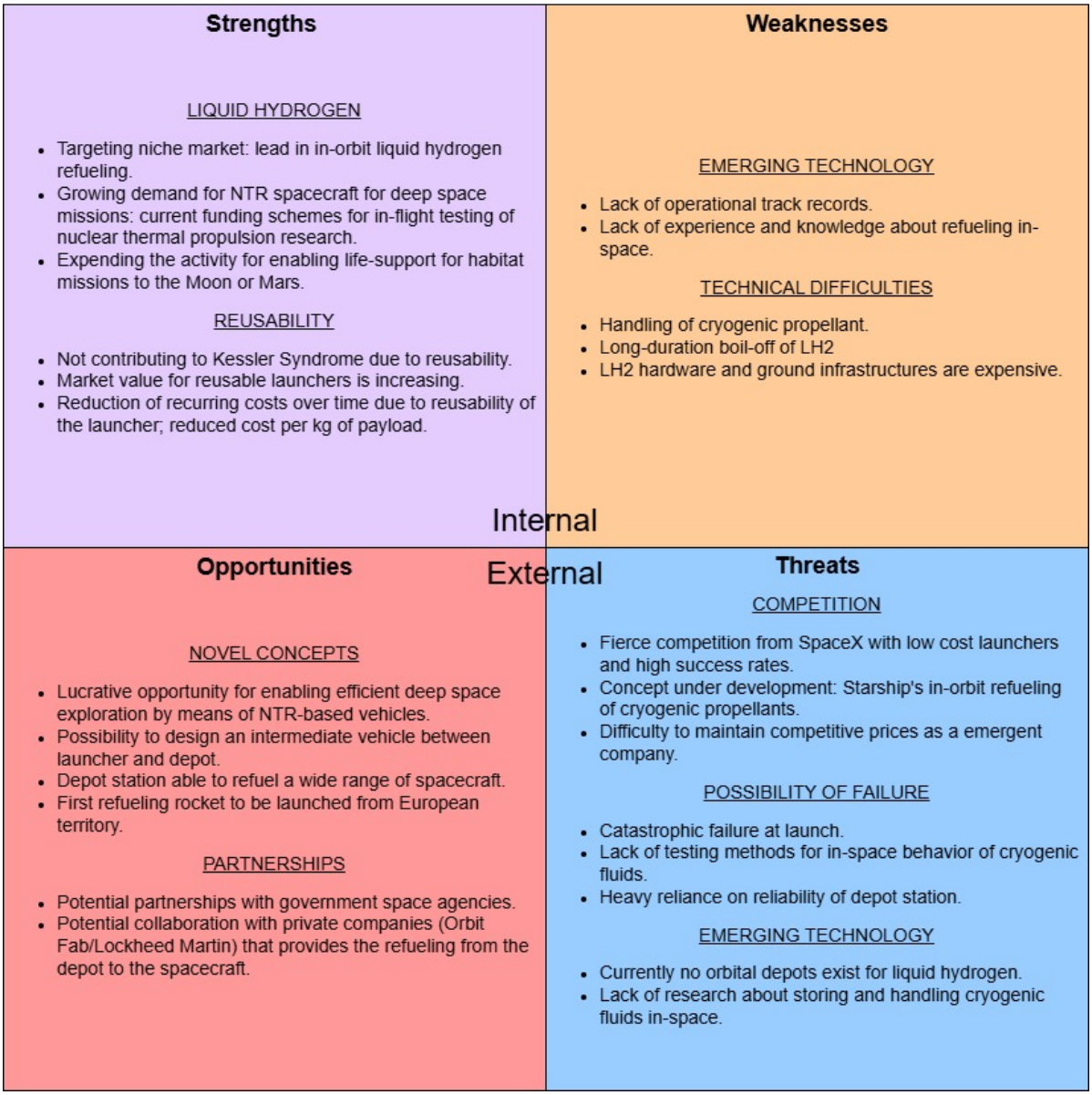

Figure 3.3: Technical SWOT analysis

3.2.3. Predict Future Market

The actors in the predicted future markets can be divided into three categories: the programs actively researching and building nuclear thermal propulsion spacecrafts, the current launchers, reusable or not, able to be adapted for hydrogen transport purposes, and future possible endeavors in the domain of hydrogen refueling from current actors. It is worth mentioning that establishing a hydrogen depot in-orbit will enable, in a relatively near future, further operation of deep-space missions. This will create a new market in which new actors will emerge. The goal of this section however is only to look at impactful recent political decisions, current competitors and existing potential partners.

3.2.4. Nuclear Thermal Propulsion Research Plans

In the 1960s, the Nuclear Engine for Rocket Vehicle Application (NERVA) was a nuclear thermal rocket engine development program that produced several engine prototypes [5]. It was a collaborative project between NASA and the Atomic Energy Commission (AEC) [5]. The program was ended due to funding cuts with no flight tests being conducted. The research on the topic was halted for many years, until a recent surge of interest for crewed missions to Mars and deep space exploration. In 2023, DARPA and NASA announced DRACO (Demonstration Rocket for Agile Cislunar Operations), aiming to demonstrate a working NTP system in space by 2027. *"Using a nuclear thermal rocket allows for faster transit time, reducing risk for astronauts. Reducing transit time is a key component for human missions to Mars, as longer trips require more supplies and more robust systems. Maturing faster, more efficient transportation technology will help NASA meet its Moon to Mars Objectives"*[1]. However, recent proposal from the White House for a budget cut of NASA would lead to a termination of the project [2]. As stated by officials on the most recent NASA budget proposal: *"These efforts are costly investments, would take many years to develop, and have not been identified as the propulsion mode for deep space missions. The nuclear propulsion projects are terminated to achieve cost savings and because there are other nearer-term propulsion alternatives for Mars transit."*, here referring to chemical propulsion. As budgetary efforts are currently shifting toward chemical propulsion, notably the Starship program, it is however acknowledged by scientists and engineers that NTR offers the only realistic path to sustainable transits between Earth and Mars.

Another research focused project is PADME, Power-Adjusted Demonstration Mars Engine, a nuclear thermal propulsion reactor concept developed by Ultra Safe Nuclear Technologies, USNC-Tech[3]. It is still at a conceptual stage, however it has received the support of Blue Origin, General Electric Hitachi Nuclear Energy, and Framatome as well as NASA and the Department of Energy (DOE).

3.2.5. Market Competitor in Launch Services

The three main competitors that are directly aiming at providing refueling services or have knowledge on LH_2 handling are: SpaceX, Blue Origin and ULA.

SpaceX would be the closest competitor, with the Starship tanker variant for methane refueling in the scope of a Mars mission[4]. As SpaceX has demonstrated first stage recovery and second stage re-entry, and aims for full reliability of Starship, they may become a low cost and reliable launch provider for potential in-space refueling in the future, whose activities could expand to enable LH_2 handling.

Blue Origin has developed the heavy-lift launch vehicle New Glenn, whose second stage uses LH_2 as propellant[5]. Therefore, the company have the knowledge to handle cryogenic hydrogen as well as a partly reusable rocket which could be adapted for refueling purposes.

The last main competitor would be ULA, United Launch Alliance, a joint venture between Boeing and Lockheed Martin, which developed ACES, the Advanced Cryogenic Evolved Stage [6]. ACES was a conceptual upper stage for a launcher, and one of its objectives was to enable in-space refueling. However, the project came to a stop in September 2020 as ULA shifted its effort to the development of the Centaur V upper stage for the Vulcan rocket[6].

[1] URL https://www.nasa.gov/news-release/nasa-darpa-will-test-nuclear-engine-for-future-mars-missions/ [cited 2025-05-02]

[2] URL https://arstechnica.com/space/2025/06/some-parts-of-trumps-proposed-budget-for-nasa-are-literally-draconian/ [cited 18-06-2025]

[3] URL https://www.ans.org/pubs/proceedings/article-55812/ [cited 2025-05-02]

[4] URL https://arstechnica.com/space/2024/04/nasa-exploration-chief-lays-out-next-steps-for-starship-development/ [cited 2025-05-09]

[5] URL https://www.futurespaceflight.com/commercial-rockets/new-glenn.html [cited 2025-05-02]

[6] URL https://www.denverpost.com/2015/04/13/america-meet-vulcan-your-next-united-launch-alliance-rocket/ [cited 2025-05-02]

Additional competitors would be Rocket Lab, who is currently developing Neutron, a Medium-lift launcher and stated it is interested in providing refueling services[7]. Relativity Space is likewise currently developing the partially reusable launcher Terran R, which makes substantial use of 3D printed materials, and has a high payload capacity[8]. If successful, Terran R would offer a substantially flexible solution which could adapt to answer a potential LH_2 demand. The last competitor would be Ariane Group with their current Ariane 6[9]. Even though not reusable, the Ariane launchers have been proven reliable, and are able to accommodate a large range of payload. Therefore, the possibility for Ariane group to adapt their launcher for refueling purposes could be an option.

3.2.6. Potential Future Customers

Potential future customers of the refueling service include national space agencies, such as ESA, developing potential deep-space missions, as well as crewed missions to Mars.

Other potential customers could be companies such as Orbital Fab, which is currently offering an in-orbit refueling service called RAFTI, Rapidly Attachable Fluid Transfer Interface, a standardized refueling port to avoid complex docking procedures[10]. The interface currently supports hydrazine but could expand for LH_2 transfer.

Lastly, for refueling of Earth orbiting satellites, services such as Northrop Grumman's SpaceLogistics providing both refueling and inspection services[11] or Astroscale U.S.'s Astroscale Prototype Servicer for Refueling, APS-R, providing refueling for satellites in geostationary orbit[12]. Both services consist of satellites making rendezvous and docking to the satellite to refuel.

3.2.7. Product Consideration

H_2ERMES can now be compared with currently available launcher options. Starting with the reusability aspect: being able to recover H_2ERMES and relaunch it within a certain time window with minimal refurbishment would allow H_2GO to lower the launch cost compared to expendable launch providers. H_2ERMES introduces many new technologies such as a regeneratively cooled heat shield, aerospike engines, currently only in the development stage and not yet used in routine service, and an unconventional second stage vehicle shape optimized for re-entry, with only Stoke Space working on a vehicle with a similar shape. Introducing many new technologies comes with associated risks but also new opportunities.

3.3. Project Objectives

The project aims to develop a sustainable and reusable system for orbital delivery of liquid hydrogen, supporting the establishment of in-space refueling infrastructure for NTR missions. This is achieved through three main objectives.

Liquid Hydrogen Transportation: The primary objective of the project is to design a vehicle capable of accommodating in-orbit refueling of liquid hydrogen by transporting it to in-orbit fuel depots in an environmentally and economically sustainable manner.

Reusability: Develop and validate a reusable system architecture, including the launch vehicle, cryogenic storage tanks, and fueling interfaces. Reusability should be achieved without compromising payload mass efficiency or performance, aiming to reduce launch costs and turnaround times for hydrogen delivery missions.

Sustainability Objective: Incorporate environmental and economical sustainability into every phase of the mission life-cycle.

[7] URL https://www.rocketlabusa.com/launch/neutron/ [cited 2025-05-02]
[8] URL https://www.mvp.vc/company-initations/initiation-report-relativity-space [cited 2025-05-02]
[9] URL https://www.arianespace.com/ariane-6/ [cited 2025-05-02]
[10] URL https://www.orbitfab.com/refueling-services/ [cited 2025-05-02]
[11] URL https://www.northropgrumman.com/space/space-logistics-services [cited 2025-05-02]
[12] URL https://astroscale.com/astroscale-u-s-to-lead-the-first-ever-refueling-of-a-united-states-space-force-asset/ [cited 2025-05-02]

4 Requirements

The first step of any design process is to establish the requirements the design must adhere to. The requirements represent the functions the systems must perform, how the systems must perform, and other considerations dictated by stakeholders. Definitions of the tags used for the requirements is found in Section 4.1, followed by the user, stakeholder, system, and subsystem requirements in Section 4.2, Section 4.3, Section 4.4, and Section 4.5 respectively.

4.1. Requirement IDs

All requirements have a unique identifier assigned to them. Within this identifier, a tag is present to categorize requirements by their responsible system. Besides this, the original given user requirements have a unique tag, and for stakeholder requirements, the tag is also added. Table 4.1 shows all the tags.

Table 4.1: System Requirement IDs

Category	Requirement ID	Category	Requirement ID
User	USR	Stakeholder	STK
Cost	COS	Payload	PLD
Docking	DOK	Refueling	RFL
Reusability	RLV	Reliability	REL
Sustainability	SUS	Regulatory	REG
Propulsion	PRP	Liquid Hydrogen	LH2
Systems	SYS	GNC	GNC
Recovery	REC	Safety	SAF
Communications	COM	Operations	OPS
Materials	MAT	Aerodynamics	AER
Structures	STR	Power	POW
Nosecone Fairing	NSC	Data Handling	DAH

4.2. User Requirements

Table 4.2 below provides the list of the original user requirements as defined in the project assignment. For each requirement, a decision has been made to accept, reject, or negotiate. As indicated in the table, most requirements need to be negotiated. The user requirements are represented by the ID RQ-USR-XX.

Table 4.2: Original user requirements

ID	Requirement	Action
RQ-USR-01	The vehicle shall autonomously deliver a payload of at least 10000 [kg] of LH_2 to a refueling station in a 600 [km] orbit with a 6 [°] inclination in a single launch.	Negotiated
RQ-USR-02	The vehicle shall be responsible for all maneuvering in orbit, while the refueling station remains stationary and does not perform any orbital maneuvers.	Accepted
RQ-USR-03	The vehicle shall achieve at least a 95 [%] mission success rate over its first 20 launches.	Negotiated
RQ-USR-04	The vehicle shall safely transport LH_2 as a payload to the designated orbit.	Accepted
RQ-USR-05	The vehicle shall incorporate automated safety protocols to mitigate risks during launch, flight and landing, with no more than a $\leq$0.01 [%] probability of catastrophic failure per launch adhering to industry safety standards for crewed and uncrewed missions.	Negotiated
RQ-USR-06	The design of the vehicle shall incorporate at least 20 [%] recyclable or repurposed materials throughout its construction.	Accepted

continued on next page

Table 4.2 *– continued from previous page*

ID	Requirement	Action
RQ-USR-07	The vehicle shall produce at least 25 [%] less carbon emissions throughout its launch when compared to current operational rockets.	Accepted
RQ-USR-08	The vehicle shall be developed with a total engineering budget not exceeding US$500 million through its first fully operational prototype.	Negotiated
RQ-USR-09	The design of the vehicle shall ensure that any subsystem's cost does not increase more than 10 [%] compared to the initial estimates from the start of the design up to its initial launch.	Negotiated
RQ-USR-10	The operational cost per launch shall not exceed US$20 million after its first five operational launches.	Negotiated
RQ-USR-11	The internal costs shall be reduced to below US$15 million per launch within five years of the vehicle's debut.	Rejected
RQ-USR-12	The vehicle shall support in-orbit LH_2 refueling operations and complete the refueling process within 12 [h].	Negotiated
RQ-USR-13	The reusable vehicle shall be capable of at least 25 launches with minimal refurbishment.	Accepted
RQ-USR-14	The launch vehicle shall have a turnaround time of one week between consecutive launches.	Negotiated
RQ-USR-15	The vehicle shall meet all international safety and environmental regulations, including National Aeronautics and Space Administration (NASA), European Space Agency (ESA) and European Union Aviation Safety Agency (EASA) requirements, by the design's critical review phase.	Negotiated

4.3. Stakeholder Requirements

The user requirements are converted to the stakeholder requirements, shown in Table 4.3.

Table 4.3: Stakeholder requirements

Requirement ID	Requirement	Importance
RQ-STK-COS-1	The vehicle shall be developed with a total engineering budget not exceeding US$1.54 billion through its first operational flight.	Driving
RQ-STK-COS-2	The operational cost per launch shall not exceed US$77 million after its first 5 operational flights.	
RQ-STK-COS-3	The total cost of the vehicle shall not change to more than 33 [%] of the initial estimate.	
RQ-STK-PLD-1	The vehicle shall autonomously deliver a payload of at least 10000 [kg] of LH_2.	Driving
RQ-STK-PLD-2	The vehicle shall safely transport LH_2 as a payload to the designated orbit.	
RQ-STK-PLD-3	The vehicle shall transport a total of 500000 [kg] of LH_2 to the depot in a year.	Driving
RQ-STK-PLD-4	The vehicle shall deliver the payload to an orbit of 600 [km] at a 6 [°] inclination.	Driving
RQ-STK-DOK-1	The vehicle shall be responsible for all maneuvering in orbit, while the refueling station remains stationary.	Driving
RQ-STK-DOK-2	The vehicle shall autonomously come within 15.2 [m] of the station.	
RQ-STK-DOK-3	The vehicle shall stay at the targeted distance from the refueling station for 10 [min].	
RQ-STK-RFL-1	The vehicle shall complete the refueling process within 3 [h].	

continued on next page

Table 4.3 *– continued from previous page*

Requirement ID	Requirement	Importance
RQ-STK-RFL-2	The vehicle shall support in-orbit hydrogen refueling via a passive fluid interface provided by the customer.	
RQ-STK-RLV-1	The launch vehicle shall have a turnaround time of two months between consecutive launches.	
RQ-STK-RLV-2	The reusable vehicle shall be capable of at least 25 launches with minimal refurbishment.	Driving
RQ-STK-RLV-3	The first operational launch shall happen before 2032.	
RQ-STK-RLV-4	The mission shall return the vehicle to Earth for refurbishment and reuse.	Driving
RQ-STK-REL-1	The vehicle shall have safety factors when applicable according to industry standards.	Driving
RQ-STK-REL-2	The vehicle shall achieve at least a 95 [%] mission success rate over its first 20 operational launches.	
RQ-STK-SUS-1	The vehicle shall produce at least 25 [%] less emissions throughout its launch compared to current operational rockets.	Driving
RQ-STK-SUS-2	The vehicle shall be compliant with NASA-STD-8719.14C to reduce space debris.	
RQ-STK-SUS-3	The design of the vehicle shall incorporate at least 20 [%] recyclable or reusable materials throughout its construction.	
RQ-STK-REG-1	The vehicle and launch operations shall be compliant with Order Regulating the Operation of Installations of the Guyana Space Center.	
RQ-STK-REG-2	The vehicle shall incorporate safety protocols from SSCMAN91-710 and ECSS-Q-ST-40C Rev.1.	
RQ-STK-REG-3	The vehicle shall use radio frequency spectra in coordination with International Telecommunication Union.	

4.4. System Requirements

The system requirements for H_2ERMES have been given in Table 4.4 which apply to most subsystems.

Table 4.4: System requirements

Requirement ID	Requirement	Stakeholder ID
RQ-SYS-1	The vehicle shall be capable of performing unmanned operations.	*RQ-STK-PLD-1*
RQ-SYS-2	Each operational launch shall have a success probability of at least 95 [%].	*RQ-STK-REL-2*
RQ-SYS-3	The vehicle shall comply with ESA regulations.	*RQ-STK-REG-1*
RQ-SYS-4	The vehicle shall comply with EASA regulations.	*RQ-STK-REG-1*
RQ-SYS-5	Critical vehicle components shall be designed to endure at least 25 launches before replacement.	*RQ-STK-RLV-2*
RQ-SYS-6	The vehicle shall comply with safety regulations.	*RQ-STK-REG-1*
RQ-SYS-7	The vehicle shall adhere to regulations set by regional governments.	*RQ-STK-REG-1*
RQ-SYS-8	The vehicle shall comply with the Regulation on Registration, Evaluation, Authorization, and Restriction of Chemicals (REACH) [7].	*RQ-STK-REG-1*

4.5. Subsystem Requirements

Lastly, subsystem requirements are defined for each of the subsystems present in the vehicle, and can be seen in Table 4.5. New requirements are marked with ● in the various requirement tables, changed requirements are marked with ●, and removed requirements are marked with ●. These markings are in relation to the requirements

generated during the conceptual design phase, as the requirements were changed/developed based on further research after discussing with the client.

Table 4.5: Subsystem requirements

	Requirement ID	Requirement	Stakeholder ID
Subsystem: Propulsion			
🟡	RQ-PRP-1	The vehicle's propulsive system shall deliver a delta V (ΔV) of at least 6391.01 [m/s].	*RQ-STK-PLD-4*
🟡	RQ-PRP-2	The vehicle's propulsive system shall deliver at least a thrust-to-weight ratio of 1.2 [−] during launch.	*RQ-STK-PLD-4*
🟡	RQ-PRP-3	The emissions of the propulsion system shall be less than 336 [t] of CO_2 equivalent.	*RQ-STK-SUS-1*
🟡	RQ-PRP-4	The vehicle's propulsive system shall deliver no more than thrust-to-weight ratio of 1.2 [−] at stage separation.	*RQ-STK-PLD-4*
🟡	RQ-PRP-5	The vehicle's propulsive system shall be re-ignitable 10 times.	*RQ-STK-DOK-1*
Subsystem: Liquid Hydrogen Payload			
🟡	RQ-LH2-1	The vehicle shall store at least 56700 [kg] of LH_2.	*RQ-STK-PLD-1*
🔴	RQ-LH2-2	The vehicle shall have a maximum LH2 leak rate of [TBD].	*RQ-STK-PLD-1*
🟡	RQ-LH2-3	The vehicle shall store LH_2 according to Guiana safety standards.	*RQ-STK-PLD-2*
🟡	RQ-LH2-4	All ground tests using LH_2 shall be conducted according to Guiana standards.	*RQ-STK-REG-1*
🟡	RQ-LH2-5	The vehicle shall transport LH_2 according to Guiana safety standards.	*RQ-STK-PLD-2*
Subsystem: Guidance, Navigation and Control (GNC)			
🟡	RQ-GNC-1	The vehicle AODCS shall have an attitude determination accuracy of 0.25 [°].	*RQ-STK-DOK-2*
🟡	RQ-GNC-2	The vehicle ADCS shall have a minimum thruster impulse of 125 [Ns].	*RQ-STK-DOK-2*
🟡	RQ-GNC-3	The vehicle shall provide trajectory control during landing with an accuracy of 3 cm from the launch pad.	*RQ-STK-RLV-4*
🟢	RQ-GNC-4	The vehicle's AODCS shall produce a slew rate of at least 0.5 [°/s].	*RQ-STK-DOK-1*
Subsystem: Refueling			
🟡	RQ-RFL-1	The vehicle shall have a transfer efficiency of at least 10 [%] for LH_2 transfer.	*RQ-STK-RFL-2*
	RQ-RFL-2	The vehicle shall support the LH_2 transfer process passively.	*RQ-STK-RFL-2*
	RQ-RFL-3	The vehicle shall transfer at least 10000 [kg] of LH_2 to the refueling station.	*RQ-STK-RFL-2*
Subsystem: Recovery			
	RQ-REC-1	The vehicle shall perform Earth re-entry.	*RQ-STK-RLV-4*
🟡	RQ-REC-2	The vehicle shall be recovered at the launch site.	*RQ-STK-RLV-4*
	RQ-REC-3	The vehicle LH_2 shall be vented before safe recovery.	*RQ-STK-PLD-2*
🟡	RQ-REC-4	The vehicle shall have a cross range of 200 [km].	*RQ-STK-RLV-4*
🟡	RQ-REC-5	The emissions during re-entry shall be less than 2000000 [$kgCO_2e$].	*RQ-STK-SUS-1*
🔴	RQ-REC-6	The vehicle shall have a probability of recovery of [TBD].	*RQ-STK-REL-2*
🔴	RQ-REC-7	The emissions during crash landing shall be less than [TBD].	*RQ-STK-SUS-1*
🟢	RQ-REC-8	The recovery subsystem shall be able to withstand the loads generated by landing the vehicle	*RQ-STK-RLV-4*
Subsystem: Safety			
	RQ-SAF-1	The vehicle shall possess a flight termination system.	*RQ-STK-REG-1*
	RQ-SAF-2	The vehicle shall have automated safety protocols during launch.	*RQ-STK-REG-2*
	RQ-SAF-3	The vehicle shall have automated safety protocols during landing.	*RQ-STK-REG-2*

continued on next page

Table 4.5 – *continued from previous page*

	Requirement ID	Requirement	Stakeholder ID
	RQ-SAF-4	The vehicle shall have automated safety protocols during flight.	*RQ-STK-REG-2*
●	RQ-SAF-5	The LH_2 shall be transported safely on ground according.	*RQ-STK-REG-1*
●	RQ-SAF-6	The LH_2 shall be stored safely on the ground.	*RQ-STK-REG-1*
●	RQ-SAF-7	The vehicle components shall be assessed after refurbishment.	*RQ-STK-RLV-1*
	RQ-SAF-8	The vehicle shall undergo acceptance testing before each flight.	*RQ-STK-RLV-1*
Subsystem: Communications			
	RQ-COM-1	The vehicle shall communicate with mission control throughout the flight.	*RQ-STK-PLD-4*
●	RQ-COM-2	The vehicle shall adhere to radiocommunication protocols according to International Telecommunication Union.	*RQ-STK-REG-1*
Subsystem: Data Handling			
●	RQ-DAH-1	The vehicle's computers shall provably resolve any process without timing out.	*RQ-STK-PLD-4*
Subsystem: Operations			
●	RQ-OPS-1	The vehicle shall be refurbished within two months.	*RQ-STK-RLV-1*
●	RQ-OPS-2	Launch pad service providers shall be re-evaluated every five years.	*RQ-STK-COS-2*
●	RQ-OPS-3	The vehicle shall be launched from Guiana Space Centre launch site.	*RQ-STK-PLD-4*
●	RQ-OPS-4	Fuel providers shall be re-evaluated every five years.	*RQ-STK-COS-2*
Subsystem: Material			
	RQ-MAT-1	The vehicle shall use at least 20 [%] recyclable materials.	*RQ-STK-SUS-3*
	RQ-MAT-2	The vehicle shall use at least 20 [%] reusable materials.	*RQ-STK-SUS-3*
	RQ-MAT-3	The materials shall withstand cryogenic temperatures of 20 [K] where applicable.	*RQ-STK-PLD-1*
	RQ-MAT-4	The payload tank material(s) shall be resistant to hydrogen embrittlement.	*RQ-STK-PLD-1*
●	RQ-MAT-5	The LH_2 storage tank material systems shall have a heat transfer coefficient of no more than [TBD].	*RQ-STK-PLD-1*
Subsystem: Aerodynamics			
●	RQ-AER-1	The vehicle shall have a drag coefficient of less than 2.	
	RQ-AER-2	The vehicle shall have a ballistic coefficient of less than 5500.	*RQ-STK-PLD-4*
●	RQ-AER-3	The vehicle shall be statically stable	*RQ-STK-PLD-4*
●	RQ-AER-4	The vehicle shall have a pitch damping coefficient of less than zero.	*RQ-STK-PLD-4*
●	RQ-AER-5	The vehicle shall have a lift-over-drag of more than 0.1 [−]	*RQ-STK-PLD-4*
●	RQ-AER-6	The vehicle shall be stable at constant velocities	*RQ-STK-PLD-4*
●	RQ-AER-7	The vehicle shall be stable at decelerating velocities	*RQ-STK-PLD-4*
Subsystem: Structures			
	RQ-STR-1	The vehicle structure shall survive re-entry aerothermodynamics loads.	*RQ-STK-RLV-4*
	RQ-STR-2	The vehicle shall handle the payload mass.	*RQ-STK-PLD-1*
	RQ-STR-3	The vehicle structure shall handle launch loads.	*RQ-STK-PLD-4*
●	RQ-STR-4	The vehicle structure shall withstand acceleration loads of 8 [g].	*RQ-STK-PLD-4*
●	RQ-STR-5	The vehicle structure shall not fail due to fatigue failure within 25 launches.	*RQ-STK-RLV-2*
●	RQ-STR-6	The header tank shall contain 1216 [kg] of LH_2	*RQ-STK-RLV-2*
Subsystem: Power			
●	RQ-POW-1	The vehicle shall provide a minimum power of [TBD] during launch.	*RQ-STK-PLD-4*
●	RQ-POW-2	The vehicle shall provide a minimum power of [TBD] until docking	*RQ-STK-PLD-4*

continued on next page

Table 4.5 – *continued from previous page*

Requirement ID	Requirement	Stakeholder ID
RQ-POW-3	The vehicle shall provide a minimum power of [TBD] throughout refueling	*RQ-STK-RFL-1*
RQ-POW-4	The vehicle shall provide a minimum power of [TBD] during re-entry.	*RQ-STK-RLV-4*
RQ-POW-5	The vehicle shall provide a minimum power of [TBD] during recovery.	*RQ-STK-RLV-4*
RQ-POW-6	The vehicle's continuous power consumption shall not exceed 7 [kW] during any mission phase.	*RQ-STK-RLV-4*
RQ-POW-7	The vehicle's 15 [min] peak power consumption shall not exceed 12 [kW] during any mission phase.	*RQ-STK-RLV-4*
RQ-POW-8	The vehicle shall carry enough reactants to continuously provide power during a mission of 72 [h] length.	*RQ-STK-RLV-4*
Subsystem: Nosecone		
RQ-NSC-1	The vehicle's nosecone shall be able to withstand buckling due to dynamic pressure experienced during ascent.	*RQ-STK-PLD-2*
RQ-NSC-2	The nosecone shall ensure that the maximum temperature of the inner wall will remain lower than the maximum operating temperature.	*RQ-STK-PLD-2*
Subsystem: Payload Tank		
RQ-PLD-1	The payload tank shall contain enough hydrogen so as to atleast deliver 10000 [kg] to the depot assuming a 5 [%] transfer efficiency.	*RQ-STK-PLD-1*
RQ-PLD-2	The payload tank shall ensure that there is at least 3000 [kg] of LH_2 left right before re-entry for heat shield cooling.	*RQ-STK-RLV-4*
RQ-PLD-3	The payload tank shall ensure that the vapor pressure inside will always be higher than 2 [bar].	*RQ-STK-PLD-2*

5 Technical Risks

Technical risks are defined as conditions that result in deviation from desired performance. The definition of performance can be extended to both the schedule (design phase) and the mission. Section 5.1 will cover the method of risk analysis, and the overview of all risks is given in Section 5.2.

5.1. Risk Analysis Method

There are a plethora of methods to define and identify risks, but a specific method for this design should be selected and implemented. Considering the design falls in the field of space engineering, it is a trivial decision to implement risk engineering practices from established organizations such as NASA (National Aeronautics and Space Administration) and ESA (European Space Agency). This method will be discussed in this section.

5.1.1. Risk Discovery

The risk assessment was performed according to the guidelines established in the NASA Risk Management Handbook [1], specifically the CRM (Continuous Risk Management). This method is outlined in the following steps:

1. Identify: Capture concerns regarding performance that affect stakeholder requirements.
2. Analyze: Estimate the probability and severity of risks.
3. Plan: Develop a risk management action plan.
4. Track: Acquire, compile, and report observable data of risk management.
5. Control: Evaluate risk management decisions and adapt as necessary.

The risks discovery process is covered by steps *Identify* and is defined according to the following risk statement.

> *Given that [Condition], there is a possibility of [Departure] adversely impacting [Asset], which can result in [Consequence].*

However, for brevity, the verbosity of the statements is neglected, and only the *Condition* and *Departure* parameters are described.

5.1.2. Risk Categorization

The risk categorization is described by the *Analyze* step of the CRM process. For each risk, the severity and probability scores are given according to the definitions in Table 5.1. The overall threat of the risk is calculated as *probability* $\times$ *severity*, and presented as the risk index. The explanations of each index are provided in Table 5.2.

Table 5.1: Severity and Probability scores definitions for a risk

Severity Score	Impact on Performance	Probability Score	Chance of Occurrence
5	Maximum: Unacceptable, no alternatives exist.	**5**	Maximum: Certain or almost certain to occur at least once. Chance is 100 [%].
4	High: Major reduction, but workarounds available.	**4**	High: Will occur frequently. Chance is 100 - 10 [%].
3	Medium: Moderate reduction, but workarounds available.	**3**	Medium: Will occur sometimes. Chance is 10 - 1 [%].
2	Low: Moderate reduction, some approach retained.	**2**	Low: Will seldom occur. Chance is 1 - 0.1 [%].
1	Minimum: Minimal or no impact.	**1**	Minimum: Will rarely occur. Chance is less than 0.1 [%].

5.1.3. Risk Management

Once the risks are classified a method for managing them also has to be developed. The parts of the CRM process that directly relate to risk management are *Plan*, *Track*, and *Control*. For each risk, a mitigation and contingency strategy is generated. The mitigation strategy reflects the steps taken to prevent the *Condition* from occurring and

Table 5.2: Risk index classification

Risk Index	Magnitude & Acceptability of Risk and Risk Scenario
>20	Maximum (Unacceptable): Maximum disruption/threat to project plan or success.
15 - 20	High (Unacceptable): Maximum disruption to project plan, high threat to project success.
10 - 14	Medium (acceptable): Some disruption/threat to project plan or success; manage risk and consider alternatives
5 - 10	Low (acceptable): Little disruption/threat to project plan or success; some management necessary.
<5	Minimum (ideal): No disruption or threat.

primarily affects the probability of the risk but can also influence the severity. The contingency strategy reflects the steps taken after a *Condition* has been met, and affects only the severity of the risk. The goal of the mitigation and contingency strategies is to reduce the risk index to an acceptable level (<15), and ideally all risks should be at a minimum (<5).

The risk maps for the identified risks pre- and post-mitigation are presented in Table 5.3 and Table 5.4.There are a few risks that have a risk index of >5 post mitigation, and this is primarily due to the associated severity. The severity of this risk cannot be mitigated enough nor can the contingency plan adequately manage the risk. This is reflected in risks where if the condition is met, it leads to extreme consequences - risks such as *RI-STR-1* if occurred have to be accepted. While the risk index for *RI-LH2-7* is within the minimum range it is still rated with a high severity, since similarly, if BLEVE (Boiling Liquid Expanding Vapor Explosion) occurs there are no actions to be taken and the risk is accepted. Such risks are highlighted in Table 5.5 in red.

Table 5.3: Risk map pre-mitigation strategies

Risk Probability						
	5				*RI-AER-3*	*RI-LH2-3* *RI-AER-2* *RI-STR-3*, *RI-STR-4*
	4				*RI-ALL-2* *RI-MAT-4*	*RI-AER-1* *RI-GNC-6*
	3			*RI-ALL-1* *RI-PRP-3* *RI-LH2-4*, *RI-LH2-6* *RI-DOK-1*	*RI-SYS-4* *RI-PRP-2*, *RI-PRP-4* *RI-LH2-1*, *RI-LH2-2* *RI-POW-1* *RI-GNC-1*	*RI-SYS-1*, *RI-SYS-2*, *RI-SYS-3*, *RI-SYS-5* *RI-LH2-4* *RI-MAT-1*, *RI-MAT-2*, *RI-MAT-3* *RI-STR-2* *RI-POW-4*
	2			*RI-POW-2* *RI-POW-3*, *RI-GNC-3*	*RI-SYS-6* *RI-OPS-1*, *RI-OPS-2* *RI-GNC-2*, *RI-GNC-4*, *RI-GNC-5*	*RI-PRP-1* *RI-LH2-7* *RI-DOK-2* *RI-STR-1* *RI-STR-4*
	1					
		1	**2**	**3**	**4**	**5**
		Risk Severity				

Table 5.4: Risk map post-mitigation strategies

Risk Probability						
	5					
	4					
	3	*RI-AER-3*				
	2		*RI-ALL-1*, *RI-ALL-2* *RI-SYS-1* *RI-LH2-2* *RI-DOK-1* *RI-MAT-4* *RI-AER-1* *RI-STR-2* *RI-GNC-1*	*RI-GNC-6*		*RI-STR-3*
	1	*RI-SYS-6* *RI-PRP-3* *RI-LH2-3*, *RI-LH2-5*, *RI-LH2-6* *RI-POW-2*, *RI-POW-3* *RI-OPS-1* *RI-GNC-3*, *RI-GNC-5*	*RI-SYS-2*, *RI-SYS-3*, *RI-SYS-4*, *RI-SYS-5* *RI-PRP-1*, *RI-PRP-2*, *RI-PRP-4* *RI-LH2-2*, *RI-LH2-4* *RI-MAT-1*, *RI-MAT-2* *RI-POW-1*, *RI-POW-4* *RI-GNC-2*, *RI-GNC-4*	*RI-DOK-2* *RI-MAT-3* *RI-AER-1* *RI-OPS-2*	*RI-LH2-7*	*RI-STR-1* *RI-STR-4*
		1	2	3	4	5
		Risk Severity				

5.2. Risk Overview

A set of risks have been identified based on literature, this table is not meant to be treated as an absolute comprehensive list, but rather an overview of the key risk elements that should be considered and evaluated further as the design progresses. This overview is given in Table 5.5

Table 5.5: Technical risks

ID	RD	Risk	Mitigation	Contingency	P *pre→post*	S *pre→post*
RI-ALL-1	All	Low TRL→unexpected failures impacting the reliability	Prioritize use of higher TRL components; maintain backups of high TRL components	Switch to high TRL component	3→2	3→2
RI-ALL-2	All	simulation models improperly constructed→erroneous predictions	Implement validation steps.	Use existing models	4→2	4→2
RI-SYS-1	Systems	subsystems developed independently without integration testing→incompatibility	Implement good systems engineering practices	Evaluate if integration failure can be isolated to a single subsystem and reiterate design.	3→2	5→2
RI-SYS-2	Systems	flight software malfunction→system crashes or incorrect operations	Implement redundancies and fault detection software.	Switch to alternate flight computer	3→1	5→2
RI-SYS-3	Systems	FTS not activate autonomously→inability to safety terminate flight	Implement redundancies	Switch to manual override	3→1	5→2
RI-SYS-4	Systems	vibrations exceed design tolerances→damage to sensitive components	Protection around sensitive components; perform tests	Switch to alternate components	3→1	4→2
RI-SYS-5	Systems, GNC	instruments malfunction→failure of navigation systems	Implement redundancies and fault detection software.	Switch to redundant instruments	3→1	5→2
RI-SYS-6	Systems, GNC, Power	EMI→signal corruption	Implement appropriate shielding	Switch to redundant instruments; Power down systems causing interference	2→1	4→1
RI-PRP-1	Propulsion	Turbopump blades operate at high RPMs→fatigue cracks	Testing; safety margins	Isolate failed pump and switch to redundant flow	2→1	5→2
RI-PRP-2	Propulsion	Propellant valves and seals experience extreme temperature and pressure→leakage	Testing; high TRL components; redundant systems	Detect leaks with dedicated sensors and execute emergency propellant safe-shutdown and line purge	3→1	4→2
RI-PRP-3	Propulsion	Combustion can develop thermo-acoustic instabilities→high-frequency pressure oscillations	Testing; implement design mitigation to dampen oscillations	Abort burn on severe instability detection; initiate controlled shutdown	3→1	3→1
RI-PRP-4	Propulsion	Pressurization subsystems malfunction→over- or under-pressurization causing tank structural failure or propellant feed anomalies	Implement redundancies; testing, and include pressure-relief devices	Vent excess pressure	3→1	4→2
RI-LH2-1	LH_2	Insulation fails→excess heat ingress, causing boil-off	Implement safety factors to insulation structure and validation through on-ground testing	Release excessive boil-off to prevent increase in pressure	3→2	4→2
RI-LH2-2	LH_2, Structures	LH_2 containment fails→hydrogen leakage	Implement safety factors with validation testing for high; implement structures to protect vulnerable systems	Dump LH_2	3→1	4→2
RI-LH2-3	LH_2, Structures	Hydrogen embrittlement→fractures or leaks.	Safety factors; appropriate material selection; coatings; operational controls (pressurization cycles)	Pressure relief devices to reduce strain on tank structure	5→3	5→1

Continued on next page

Table 5.5 – continued from previous page

RI-LH2-4	LH_2, Structures, Materials	Pressure relief systems fail→rupture or explosions.	Implement safety factors and validation through testing; Ensure all personnel are a safe distance away on the ground.	No contingency	3→1	5→2
RI-LH2-5	LH_2, Thermal	Inadequate thermal management→excessive LH_2 boil-off	Thermal management; safety factors for tanks	Unless gas undergo liquefaction, release boil-off to prevent overpressurization	3→1	3→1
RI-LH2-6	LH_2, Operations	LH_2 is handled improperly during storage or transportation→accidents	Follow existing protocols related to LH_2	Follow existing emergency protocols	3→1	3→1
RI-LH2-7	LH_2, Structures	LH_2 is exposed to rapid depressurization→BLEVE	Implement safety factors and validation through testing; Ensure all personnel are a safe distance away on the ground.	No contingency	2→1	5→4
RI-DOK-1	Docking	Vehicle fails to align with the station depot→unsuccessful docking	Docking alignment performed by mechanical arm	Attempt docking procedures again; if complete failure to dock, dump LH_2 and perform return operations.	3→2	3→2
RI-DOK-2	Docking	Vehicle fails to undock→recovery failure.	Implement high TRL docking mechanisms	Attempt undocking again; if fail, dump LH_2 to avoid BLEVE; No contingency	2→1	5→3
RI-MAT-1	Materials, Structures	Materials are exposed to various thermal stresses→structural failure	Safety factors; assess thermal stresses before design	No contingency	3→1	5→2
RI-MAT-2	Materials, Structures	Repeated stress cycles→material failure	Safety factors; assess fatigue cycles before design	No contingency	3→1	5→2
RI-MAT-3	Materials	Insulation materials are flammable→fire	Use fire resistant materials	Fire suppression systems	3→1	5→3
RI-MAT-4	Materials, Structures	Re-entry protection fails→excessive thermal loads	Use tested and validated materials.	Redundant thermal protection systems; No contingency	4→2	4→2
RI-AER-1	Aerodynamic	Gusts→instability	Implement structures to maintain stability for all flight regimes	Attempt control algorithms for correction; FTS in case of extreme divergence from flight path	5→2	4→2
RI-AER-2	Aerodynamic, Structures	Aeroelastic interactions →divergent oscillations	Safety factors; testing and analysis of aerodynamic characteristics	No contingency	5→1	5→3
RI-AER-3	Aerodynamics	Fuel sloshing→instability	Control mechanisms to control sloshing	No contingency in case of excessive sloshing; baffles in tank; soft control	5→3	4→1
RI-STR-1	Structures	Acceleration loads →structural failure	Safety factors; testing for validation	No contingency	2→1	5→5
RI-STR-2	Structures	Stages fail to separate properly→collision	Redundant systems for separation; testing and validation	Control for recovery in case of no separation or to avoid collision; No contingency for collision	3→2	5→2
RI-STR-3	Structures	Resonant frequencies→structural failure	Identification of resonance frequencies; testing and validation	Abort launch; No contingency for structural failure	5→2	5→5
RI-STR-4	Structures	Manufacturing defects→structural failure	Testing and validation	Abort launch; No contingency for structural failure	5→2	5→5
RI-POW-1	Power	Electrical systems fails→power loss	Parallel integration of power systems to ensure the entire system does not fail at once	Power down non-essential components; No contingency for absolute loss of power	3→1	4→2
RI-POW-2	Power	Overheat or short-circuit→fire	Fire resistant materials	Fire suppression systems	2→1	3→1

Continued on next page

Table 5.5 – continued from previous page

RI-POW-3	Power	Power systems generate heat→thermal overload	Implement thermal management systems	Release LH_2 to reduce pressure; power down non-essential components	2→1	3→1
RI-POW-4	Power	Faults in power distribution→subsystem power loss,	Redundant circuitry and protection	Implement software protocols to attempt reset	3→1	5→2
RI-OPS-1	Operations	Ground station instrumentation fails→communication loss	Redundant ground station instruments	Autonomous control measures	2→1	4→1
RI-OPS-2	Operations	Flight communication systems fail→loss of contact	Redundant systems and use of high TRL components	Autonomous control measures	2→1	4→3
RI-GNC-1	GNC	Vehicle deviates from intended flight path→trajectory error	Autonomous control systems to ensure flight control GNC	Flight termination in case of unrecoverable divergence from flight path	3→2	4→2
RI-GNC-2	GNC	Actuators fail→loss of control	Redundant systems and use of high TRL components	No contingency if redundant systems also fail	2→1	4→2
RI-GNC-3	GNC	Clock drift→desynchronized systems	Implement appropriate software protocols and use high TRL components	Switch to redundant systems	2→1	3→1
RI-GNC-4	GNC	Automated tasks are performed incorrectly→erroneous operations	Implement appropriate software protocols and use high TRL components	Switch to redundant systems or manual override where applicable.	2→1	4→2
RI-GNC-5	GNC, Systems	Radiation→bit flips	Implement protective measures	Software protocols	2→1	4→1
RI-GNC-6	GNC	Vehicle deviates from the intended re-entry path,→trajectory error	Autonomous control systems to ensure flight control	Flight termination in case of unrecoverable divergence from flight path	4→2	5→3

6 Concept Trade-Off

This chapter outlines the performed trade-off resulting in the system architecture which will be designed in further detail throughout this report. It starts by elaborating upon the trade-off methodology in Section 6.1, after which the subsystem and final architecture are traded-off in Section 6.2 and Section 6.3 respectively.

6.1. Trade-Off Methodology

To move from the various design options for each of the subsystems to a final architecture to be further developed, first, a trade-off was performed on the multiple subsystems defined. From the results of these trade-offs, multiple full system architectures were generated.

The trade-offs were performed in the following way:

1. First, the various options entering the trade-off were listed out. These are the options from the design option tree, with some discarded due to non-viability.
2. Next, the criteria used in the trade-off were defined, including their weights. In general, these criteria flow from the requirements and risks associated with the subsystem, or from general performance parameters specific to the subsystem.
3. To be able to calculate the trade-off scores, each design option was analyzed in terms of the defined criteria. From this analysis, each parameter was given a score on a 1-5 grading scale, with one being the least favorable option, and five the best.
4. The winner of the trade-off was then determined by calculating the weighted sum of the criteria scores for each concept.
5. Lastly, a sensitivity analysis was done to assess the impact of certain scores, criteria, or criteria weights, and to ensure the trade-off rationale was robust.

An overview of the trade-off process can be seen in Figure 6.1.

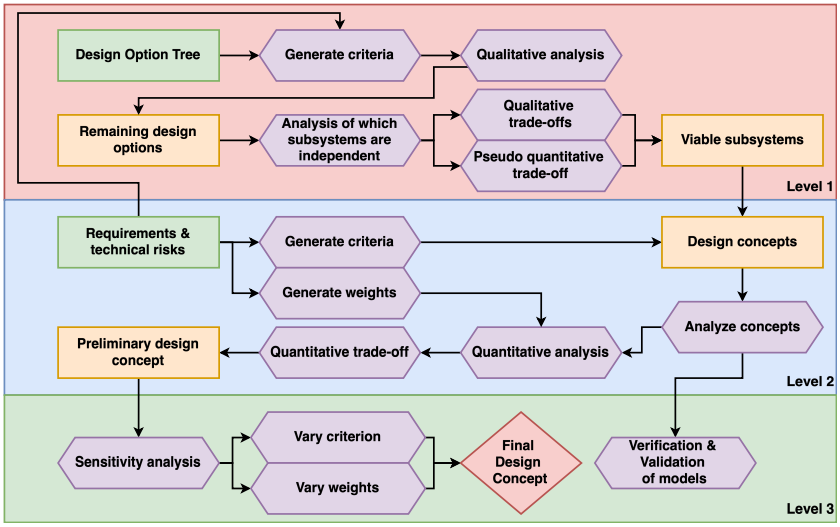

Figure 6.1: Flowchart of the trade-off method

The **Level 1** trade-off in red concerns the subsystem trade-off, moving from the design option tree to remaining options for the subsystems by use of a qualitative and pseudo quantitative trade-off. Then, in the **Level 2** trade-off in blue, the system concepts are generated, analyzed, and traded-off. From there, the sensitivity analysis is performed in **Level 3** in green, and the final system architecture is selected.

6.2. Subsystem Trade-Off

The subsystems for which a trade-off was performed are:

1. First Stage
2. Power
3. Thermal management
4. Propulsion Architecture
5. Propellant
6. Attitude Control System
7. Attitude & Orbital Determination System
8. Communication Architecture
9. Data Dissemination Architecture
10. Re-entry Trajectory
11. Re-entry Vehicle Shape
12. Re-entry Thermal Protection System
13. Recovery Subsystem
14. Tank Material
15. Tank Architecture

In order to perform a robust trade-off for each subsystem individually, the criteria differ between each. Still, due to the stakeholder requirements and general design logic, certain criteria showed up multiple times, as outlined below.

1. **Mass**: Mass showed up in nine out of the 15 trade-offs as a criteria, with an average weight of $0.267\,[-]$. This indicates that mass was generally used as a criteria with a relatively high weight.
2. **Sustainability**: Sustainability is covered in different metrics differing per subsystem, such as emissions, toxicity, or reusability, and assessed in 10 out of 15 subsystems, with an average weight of $0.255\,[-]$, highlighting the importance of sustainability in the design process.
3. **Risk**: For most subsystems, risk is assessed by use of TRL or complexity, which is a criteria for 14 out of 15 subsystems with an average weight of $0.207\,[-]$.

Moreover, examples of other criteria used, which were inherently more specific parameters of the respective subsystems, include I_{sp} for propulsion and ACS, precision for AODS, or storability for the propellant. All trade-offs can be found in the midterm report [2].

Resulting from this level 1 trade-off, the options for each of the subsystems can be found in Table 6.1.

Table 6.1: Subsystem trade-off results

Subsystem	Winning Option	Subsystem	Winning Option
First Stage	New Glenn	Re-entry Trajectory	Gliding
Power	Fuel Cells	Re-entry Vehicle Shape	1. Winged Lifting Body
Thermal Management	No insulation		2. Wingless Lifting Body
Propulsion Architecture	Liquid propellant		3. Blunted Cone
Propellant	1. LH_2/LOX	Re-entry Thermal Protection System	Regenerative cooling
	2. CH_4/LOX	Recovery Subsystem	1. Landing Legs
Attitude Control System	H_2O_2 monopropellant thrusters		2. Runway Landing
Attitude & Orbital Determination System	GPS receivers		3. Tower Catch
Communication architecture	Near Earth	Tank Material	Stainless Steel Alloy 304L
Data Dissemination Architecture	Point-to-point	Tank Architecture	Monocoque

Most interestingly, for the propellant, re-entry vehicle shape, and recovery subsystem, multiple options still emerged as outcome of the trade-off due to very close results.

6.3. Final Architecture Trade-Off

To generate the full system architecture concepts, the subsystems with multiple options remaining were taken as a baseline. First, due to the inherent compatibility and precedent from existing vehicles, combinations were made with vehicle shape and recovery subsystem. These combinations made are found in Table 6.2.

Table 6.2: Combinations of vehicle shape and recovery method for the system architecture trade-off

Combination Concept Name	Vehicle Shape	Recovery Method
Aves	Winged lifting body	Runway landing + Parachute
Ursus	Blunted cone	Landing legs
Cetaceans	Wingless lifting body	Tower catch

Then, for all three of these combinations, two concepts were generated, one using hydrolox as propellant, and the other using methalox, resulting in the six concepts described in Table 6.3.

Table 6.3: System architecture names for the level 2 trade-off

Concept Name	Overarching Concept	Propellant
Penguin	*Aves*	LH_2/LOX
Ostrich	*Aves*	CH_4/LOX
Polar Bear	*Ursus*	LH_2/LOX
Grizzly Bear	*Ursus*	CH_4/LOX
Beluga	*Cetaceans*	LH_2/LOX
Dolphin	*Cetaceans*	CH_4/LOX

6.3.1. Trade-Off Criteria

The criteria used for the level 2 trade-off were taken from analysis of the requirements and the risks. From that, the following criteria and respective weights were selected:

1. **Total Mass (0.3)**: Multiple requirements directly impact the total design of the vehicle, and with that the total mass. Besides this, a lower total mass leaves a larger budget for increase in payload, which can be analyzed in more detail and optimized for. This criterion is assigned a high weight as it is used as the main performance characteristic of the concepts.
2. **Environmental Impact (0.3)**: A large focus of the project is to incorporate sustainability throughout the design. *RQ-STK-SUS-1* and *RQ-STK-SUS-2* highlight the main requirements for the environmental sustainability, and due to the scope of the project, a high weight is assigned to this criterion.
3. **Risk (0.25)**: With the detailed risk analysis outlined in Chapter 5, it was seen that there were still some higher impact risks. Because of this, risk is included in the trade-off with a medium weight to ensure safe vehicles have a higher chance of being developed over less safe ones.
4. **Cost (0.15)**: Requirements *RQ-STK-COS-1* and *RQ-STK-COS-2* highlight the need for an economically sustainable vehicle. Since these requirements are set by the client, it is essential to analyze the concepts for cost to ensure these requirements can be met. A relatively low weight is assigned, as the cost requirements are subject to change, following discussion with and approval from the client.

To be able to properly compare the quantification of these criteria for each of the concepts, a grading scale of one through five was used. For the criteria where a lower score indicates a better result, such as cost, Equation 6.1a was used for the grading, while Equation 6.1b was used for the criteria where a higher value indicates a better score.

$$s = \frac{x_i - min\,(x)}{max\,(x) - min\,(x)} \cdot (-4) + 5 \qquad (6.1a)$$

$$s = \frac{x_i - min\,(x)}{max\,(x) - min\,(x)} \cdot (4) + 1 \qquad (6.1b)$$

In these, s indicates the score, x_i the individual quantification of a certain concept, $max\,(x)$ the maximum value of the quantification of all six concepts, and $min\,(x)$ the minimum value.

6.3.2. Analysis of Concepts

For analysis of the mass, environmental impact, and cost, tools were developed to quantify these criteria for each of the concepts.

The mass was estimated using a multitude of parameters influencing the total mass, including payload mass, structural ratios of similar existing missions, estimating the ΔV for the mission, and from this estimating the total, propellant, and structural masses [8].

The environmental impact was assessed using the IDEMAT database, taking the structural mass of the concepts, and finding the average CO_2 equivalent [kg] of manufacturing and extracting the materials for this, and a similar approach for the propellants. For the concepts using methalox, combustion was also included, but not for the concepts using hydrolox, as the greenhouse gases emitted by these will be negligible after just 9 [d], and are thus assumed to not have a large environmental impact.

The total cost was estimated by taking the sum of operational and engineering cost. The operational cost was estimated using a preliminary hybrid parametric model [9], taking the sum of many factors, such as ground operation costs, propellant costs, and flight & mission costs. The engineering cost was modeled using the dry mass of the concept, and the engineering cost and dry mass of a reference mission.

Lastly, the risk was assessed by the use of assessing the five principal domains of risk and failure. The risks associated with this risk assessment are the primary risks identified from Chapter 5.

6.3.3. Trade-Off Results

While analyzing the different concepts, it was found that the *Aves* concepts would result in non-viable options when looking at the mass. As a result, these two concepts were immediately removed from the trade-off, continuing with the remaining four options. For the trade-off between these, the resulting matrix can be seen in Table 6.4.

Table 6.4: System trade-off matrix

Concept	Total mass (0.3)	Sustainability (0.3)	Risk (0.25)	Cost (0.15)	Total
Polar Bear	4	5	4	3	4.15
Grizzly Bear	1	1	5	1	2
Beluga	5	5	1	5	4
Dolphin	3	3	2	4	2.9

Clearly, the *Polar Bear* concept was the winner, but as the score of the *Beluga* concept was quite close, it was vital to perform a sensitivity analysis on the trade-off to ensure the best concept would come out victorious.

6.3.4. Sensitivity Analysis

The sensitivity analysis was performed in two methods: first, the selective sensitivity analysis assessed the impact of each of the criteria individually, by removing them from the trade-off one-by-one, and seeing their impact. Next, the stochastic analysis assessed a multitude of weights for all of the criteria, to ensure any combination of weights would result in the same outcome. From both of these sensitivity analyses, it was concluded that the *Polar Bear* concept was indeed the winning concept, and was thus selected as the architecture for the H_2ERMES vehicle.

7 Functional Analysis

The functional analysis is required to determine the various operations needed to perform the mission. Section 7.1 shows the overall mission architecture, and Section 7.2 and Section 7.3 show the functional flow diagram and functional breakdown structure, respectively.

7.1. Mission Architecture

A high level mission architecture can be found in Figure 7.1. It is split up into the space segment and the ground segment. The scope of this project is mainly the launcher, and with it bringing the LH_2 payload to the depot. Besides this, the reusability of the launcher is also within the scope, including refurbishment and maintenance.

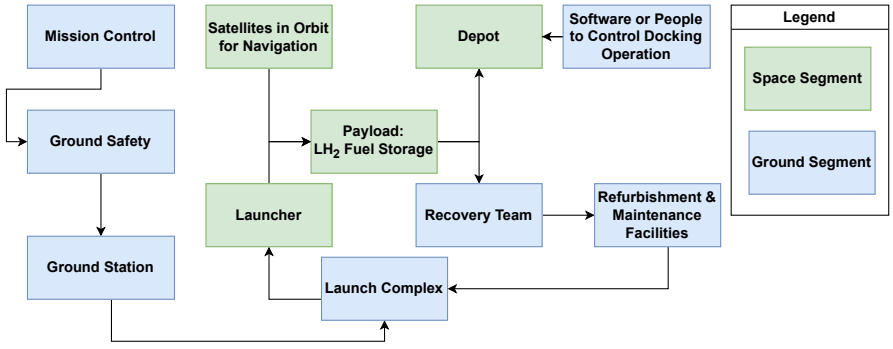

Figure 7.1: High level mission architecture

7.2. Functional Flow

The system shall perform a number of functions before, during, and after its operational life. These functions are split up into the following high level phases:

- Design: From project planning until the final design, ready for production
- Manufacturing: Production of operational vehicles and the acceptance testing performed throughout the process
- Operations: Repeated refueling missions, including pre-launch and post-launch processing
- Decommissioning: Dismantling of the vehicle and sustainable processing and recycling of its parts

The Functional Flow Diagram (FFD) shows all functions that need to be performed to successfully conduct these phases displayed in the logical order in which they have to be performed including any decision points which might lead to different functions being performed depending on the result of previous function. The top level blocks (FN-#) represent the phases and the functions are broken down to level three flight operations as these have individual subsystems performing each function. The design, manufacturing and refurbishment are only shown down to level two as Design planning is covered more thoroughly in previous project phases [2], while manufacturing and refurbishment are covered in Section 11.2 and Section 11.4, respectively. FFD can be seen in Figure 7.2.

7.3. Functional Breakdown Structure

Based on the functional flow as described in Section 7.2, a systemic breakdown of all the functions can also be described in a Functional Breakdown Structure (FBS) shown in Figure 7.3. The FBS contains all functions shown in the FFD, and additional functions are worked out for the parts of operations most relevant for the scope of this project, which are in-orbit operations and re-entry.

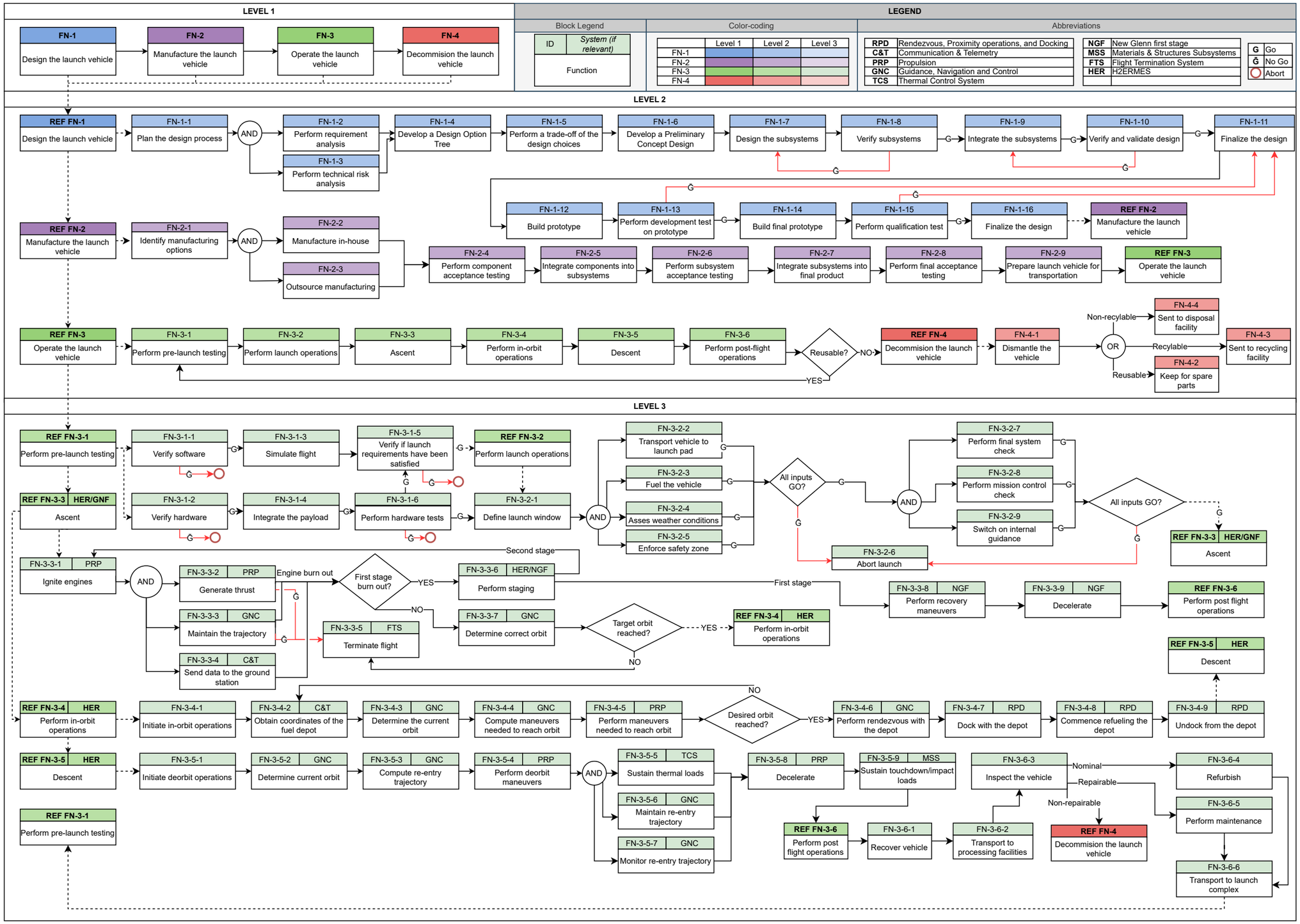

Figure 7.2: Functional Flow Diagram

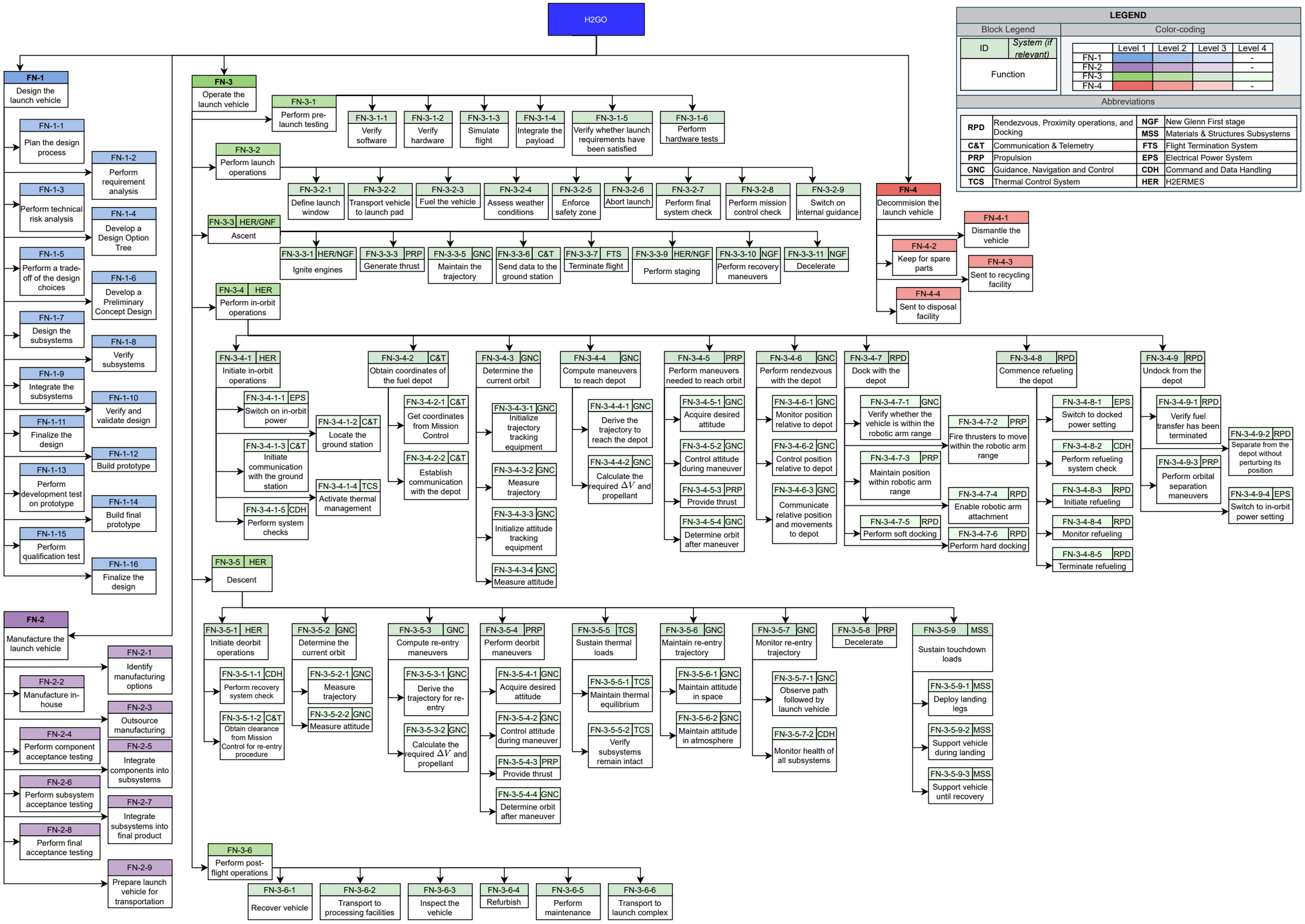

Figure 7.3: Functional Breakdown Structure

8 Preliminary Design

With the system architecture defined, it is possible to design the individual subsystems. First, the design process is presented in Section 8.1. Next, the methodology for the sensitivity analysis on each subsystem is defined in Section 8.2. From that, the method for the design of each of the individual subsystems is given in Section 8.3 through Section 8.17.

8.1. Design Process

To begin with, it is necessary to develop a plan to approach the detailed design phase of the H_2GO mission. The first part of design process involved conducting a detailed literature study on the concept that was chosen in the midterm trade-off. At the end of the research phase, the inputs and outputs to design the subsystem are identified. Then, a tool is developed in order to model the subsystem and obtain key parameters needed to define the subsystem. After obtaining outputs, the tool is verified and validated in order to test the sanity of the tool. This process is followed by every subsystem with the exception of a few where available COTS components were selected. Table 8.1 highlights all of the tools which were developed for design purposes, as well as their function.

Table 8.1: Developed Tools Table

Subsystem	Purpose of Tools Developed
ΔV calculation	Simulating orbit insertion and landing burns
Aerodynamic Calculations	Hypersonic and Stability Modeling
Tank Design	Tank sizing and plotting, header tank sizing and fatigue calculation
Propulsion	Optimizing O/F ratios, calculating the mass of the thrust chambers, finding the most optimal combination of sea level and vacuum thrusters,turbopump mass sizing
Landing Leg Sizing	Landing leg dimensions based on loadings
Nosecone	Design of the nosecone tanking into account the vertical velocity of the launcher at ascent as well as altitudes and tank geometries
Active metallic heat shield	1D heat transfer model using material properties from an existing database, as well as initial coolant properties, to find coolant properties along the channels, and the cooling channel geometry
Power	Reactant consumption modeling, avionics and wiring mass estimations
AOCS	Thruster sizing tool to determine the number and orientation of thrusters
Re-entry trajectory estimation	Calculating the equilibrium and skipping trajectories, as well as control simulation and stability analysis

8.2. Sensitivity Analysis Method

The design process of the H_2ERMES vehicle includes making assumptions, adding margins and calculating final design parameters that need to comply with requirements. To provide confidence to these parameters, a sensitivity analysis was performed on all subsystem designs, as well as for the final system. The analysis varies design inputs and observes the results while commenting on possible mitigation or utilization strategies, if applicable. Each parameter change was then given a sensitivity score as defined in Table 8.2.

Table 8.2: Sensitivity Score Definitions

Sensitivity Score	Description
1	The change makes the design unfeasible and/or requirements are not met.
2	The change reduces margins, but the design is still feasible and/or compliant.
3	The change does not change design feasibility and/or compliance.
4	The change increases margins, making the design more feasible and/or compliant.
5	The change strongly increases margins.

At the subsystem level, the most critical parameters were varied by an appropriate amount determined by the

responsible engineer. At the system level, a programmatic analysis was performed in which all variables could be varied at the same time. This will be further presented in Section 10.5.

8.3. Delta V

To perform the mission outlined in Section 8.4, the propulsion system of H_2ERMES has to provide change of velocity (ΔV) to get into orbit, perform all required in-orbit operations including disturbance compensation and finally land back at the launch site under its own power. First, the individual components of the ΔV budget are going to be covered in Section 8.3.1 to 8.3.3, after which the sensitivity of the performed calculations is discussed in Section 8.3.4.

8.3.1. Orbital Insertion

The ΔV requirement for orbit insertion is determined by means of numerical simulation from the time of separation until the achievement of circular 200 [km] orbit. The simulation works by applying the governing equations Equation 8.1 to 8.7 to propagate state variables in time using Forward Euler scheme (Equation 8.8). The influence of atmospheric drag is considered negligible (*AS-DELV-01*), this is considered acceptable as the density at 80 [km] is only 1.68×10^{-5} [kg/m^3] and decreases rapidly from there and other launch vehicles' second stages such as Saturn V are also considered to have zero drag losses [8].

The pitch angle ϑ is set equal to flightpath angle γ for a gravity turn ascent, however, as perfect gravity turn is only possible with one specific thrust-to-weight ratio, a constant offset from flightpath angle is introduced. This trajectory is not necessarily optimal [8] but it does present a lower conservative limit on the required ΔV, in future iterations a proper trajectory optimization shall be performed. The initial conditions used for the simulation are based on the New Glenn stage separation conditions[1] and can be seen in Figure 8.2.

$$m_i^* = \frac{m_i}{m_0} \tag{8.1}$$

$$(T/W)_{i+1} = (T/W)_0 \cdot \frac{1}{m_i^*} \tag{8.2}$$

$$(a_h)_{i+1} = (T/W)_i g_0 \cos(\vartheta_i) \tag{8.3}$$

$$(a_v)_{i+1} = -\frac{\mu_E}{r_i^2} + (T/W)_i g_0 \sin(\vartheta_i) \tag{8.4}$$

$$\dot{m}^* = (T/W)_0 \cdot \frac{1}{I_{sp}} \tag{8.5}$$

$$m_{i+1}^* = m_i^* - \dot{m}^* \cdot \Delta t \tag{8.6}$$

$$\gamma_{i+1} = \arctan \frac{\dot{r}_i}{r_i \dot{\theta}_i} \tag{8.7}$$

$$s_{i+1} = s_i + \dot{s}_i \cdot \Delta t \tag{8.8}$$

$$\Delta V = I_{sp} g_0 \ln \frac{m_0}{m_{final}} \tag{8.9}$$

Here m^* [$-$] is the mass normalized with the initial mass, m [kg] is the mass, I_{sp} [s] is specific impulse, T/W [$-$] is thrust to weight ratio, $\dot{m}^*$ [/s] is mass flow normalized with initial mass, Δt [s] is simulation time step, r [m] is the distance from Earth center, θ [rad] is radial angle, ϑ [rad] is pitch angle, γ [rad] is flightpath angle, a_v [m/s^2] is vertical acceleration, a_h [m/s^2] is horizontal acceleration and s is any state being propagated. Subscript i denotes i-th iteration and ˙ denotes first time derivative.

The normalized mass and mass flow are used so the initial mass fraction is always one and the entire simulation is independent of the actual mass of H_2ERMES. As such the only design variable influencing the ΔV required for insertion is the thrust to weight ratio, the relation between these values was found by varying the thrust to weight ratio and finding the optimal offset for pitch angle by trial and error until the simulation reached the desired 200 [km] circular orbit. After the simulation concludes the required ΔV is calculated using Equation 8.9, the result is presented in Figure 8.1.

8.3.2. Landing Burn

The landing burn ΔV is determined using equivalent simulation to Section 8.3.1, utilizing the same propagation scheme and governing equations with the addition of acceleration due to drag computed by Equation 8.10.

$$a_D = \frac{1}{2}\rho V^2 \frac{1}{\beta} \tag{8.10}$$

Here a_D [m/s] is the drag acceleration, V [m/s] is the velocity and β [kg/m^2] is the ballistic coefficient.

[1] URL https://www.youtube.com/watch?v=KXysNxbGdCg&t=8363s&ab_channel=BlueOrigin [cited 2025-06-16]

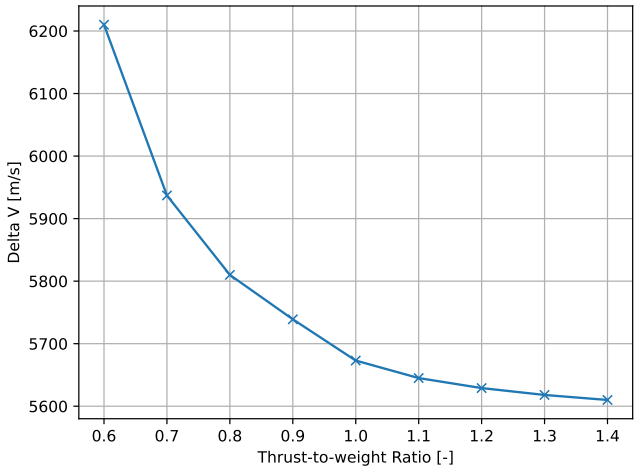

Figure 8.1: ΔV as a function of thrust to weight ratio

Figure 8.2: Initial conditions

Horizontal velocity	2280 [m/s]
Vertical velocity	1040 [m/s]
Altitude	81700 [m]

The simulation will commence with an initial velocity equal to the velocity at the end of re-entry as discussed in Section 8.17 and propagate with the thrust vector directly opposite to the simulated direction of motion until the zero velocity is reached. After the conclusion of the simulation, the ΔV is again calculated using Equation 8.9. The simulation runs with the assumption of purely vertical flight (*AS-DELV-03*), the total ΔV essentially consists of reducing the given initial velocity to zero while compensating for gravity losses, gravity losses are purely defined by the time of the maneuver and the direction of initial velocity does not affect the time, as such this assumption is not expected to have a significant impact. Nevertheless, this assumption shall be verified with more accurate analysis in future design iterations.

An example set of results for varying initial velocity, thrust to weight ratio and ballistic coefficient can be seen in Figure 8.3. It can be seen that increasing thrust to weight ratio and decreasing ballistic coefficient lower required ΔV by decreasing gravity losses through lowering burn time and increasing the desirable decelerating drag, respectively.

8.3.3. In-Orbit Maneuvers

The remaining part of ΔV budget are the various in-orbit maneuvers; the transfer from 200 [km] to 600 [km] orbit, drag compensation and the finally the deorbit burn. For the orbit transfer maneuver and deorbit burn, none of the assumptions used during Conceptual design phase have changed so the same values are retained for further design. The most important relevant assumption is impulsive shot during in-orbit maneuvers (*AS-DELV-02*), since only a few seconds are required for any of the maneuvers and orbital period of H_2ERMES's orbit is in the order of thousands of seconds (Table 10.4), the change of the altitude and angle during the maneuver will not significantly influence the required ΔV. While the drag compensation is partially determined by ballistic coefficient as shown in Equation 8.11 and as such is affected by the design.

$$\Delta V_{\text{atm}} = \frac{1}{2}\frac{\rho V^2}{\beta}t, \tag{8.11}$$

However, since the drag compensation is such a small part of the total ΔV requirement, it was deemed more efficient to continue with the conservative values computed during conceptual design and focus design effort on the more substantial elements. Thus the required ΔV for these elements can be presented in Figure 8.4.

Lastly, as discussed in Section 8.4 it may be necessary to split up the transfer orbit injection and deorbit burn into multiple maneuvers to finetune H_2ERMES's position relative to the depot and landing site, respectively. However, as these multiple maneuvers would still occur at the same altitude, this will not affect the total required ΔV.

8.3.4. Sensitivity Analysis

The sensitivity of the ΔV requirements is presented in Table 8.3. It is performed by varying the major parameters affecting ΔV by approximately 10 [%] compared to the final design values as presented in Chapter 10.

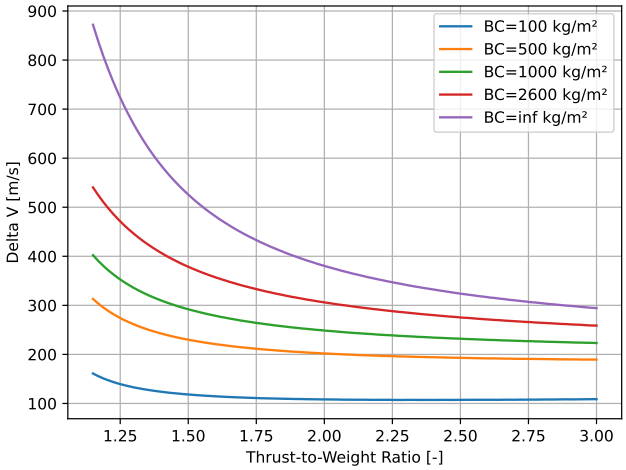

Figure 8.3: Example values for landing burn

Figure 8.4: ΔV requirements retained from conceptual design [10]

Flight stage	ΔV [m/s]
Injection to 600 [km] transfer orbit	114.01
Circularization at 600 [km]	112.34
Deorbit burn	156.66
Atmospheric drag compensation	10

Table 8.3: Sensitivity Analysis ΔV

Parameters:	**Initial vacuum T/W**	**Target orbit altitude**	**Initial sea level T/W**	**Ballistic coefficient**
Change in value	-0.1 [$-$]	$+100$ [km]	-0.1 [$-$]	$+500$ [kg/m^2]
Relative change in ΔV	$+0.25$ [%]	$+1.25$ [%]	$+0.13$ [%]	$+0.07$ [%]
Effect description	Insertion ΔV increases	Transfer and deorbit ΔV increases	Landing ΔV increases	
Requirements affected	*RQ-PRP-1*	*RQ-PRP-1*	*RQ-PRP-1*	*RQ-PRP-1*
Impact:	2	2	2	2

It is clear from Table 8.3 that the ΔV is quite robust in response to small variations so while the margins will be affected, there is little risk of minor changes in specifications making ΔV values unachievable.

8.4. Flight Design

The goal of flight design is to develop a realistic flight timeline which is compatible with all subsystems and fulfills requirements *RQ-STK-PLD-2*, *RQ-STK-DOK-1* and *RQ-STK-RFL-1*, and to ensure that there are sufficient launch windows available so the enough flights per year can be performed to deliver 500 [t] of LH_2 per year to orbit per *RQ-STK-PLD-3*. Due to the boil-off considerations discussed in Section 8.16, it is imperative to perform each flight in as short time as possible. The main factors impacting the flight timeline are orbital alignment with the depot and the launch and landing site at Guiana Space Center (CSG), respectively.

8.4.1. CSG Alignment

For a depot in an undisturbed Kepler of 6 [°] inclination, CSG would pass under its orbital plane once every sidereal day (23.935 [h][2]) while the phase angle changes by 360 [°]. However, the effect of the equatorial bulge will cause a precession of the orbit given by Equation 8.13. As such Equation 8.14 can be used to find the actual time between consecutive CSG passes under the depot's orbital plane and the phase angle change can be found using Equation 8.12, with T being sidereal day. For the given 600 [km] altitude 6 [°] inclination orbit, these evaluate to 23.46 [h] and 353.92 [°], respectively, so these values serve as the total time and cumulative phase angle for each flight.

$$\Delta\phi = 360\frac{t}{T} \tag{8.12}$$

$$\frac{\Delta\Omega}{t} = -3\pi J_2 \left(\frac{R_E}{a(1-e^2)}\right)^2 \cos i \frac{1}{T} \tag{8.13}$$

$$t = \frac{360}{360 - \frac{\Delta\Omega}{t}T_E} T_E \tag{8.14}$$

$$T = 2\pi\sqrt{\frac{a^3}{\mu_E}} \tag{8.15}$$

Here t [s] is the time spend in given orbit, T [s] is the period of the orbit, a [m] is the semi-major axis, μ_E [m^3/s^2] is the standard gravitational parameter of Earth, R_E [m] is Earth radius, e is orbit eccentricity, i [°] is

[2]URL https://nssdc.gsfc.nasa.gov/planetary/factsheet/earthfact.html [cited 2025-06-14]

the orbit inclination, and J_2 [−] is the second dynamic form factor of Earth.

For most flight stages, the time will be primarily determined by operational restrictions and requirements which will be discussed when the final flight timeline is presented in Chapter 10. The phase angle per flight stage in any orbit can be found using Equation 8.12 where T is the orbital period found using Equation 8.15. For the two flight stages that do not take place in orbit; launch and re-entry, the phase angle will be retrieved from their respective simulations in Section 8.3.1 and Section 8.17. The final flight phase angle will then be obtained by summing the individual phase angles and taking the remainder of its division by 360 [°]. The phase angle can be fine tuned by adjusting the orbital parameters after undocking from the depot so the minimum and maximum phase to obtain a range of phase angles, as long as the target value of 353.93 [°] lies between the extreme values, it is possible to fine tune the orbits such that a precise landing can be performed.

8.4.2. Depot Alignment

Before transferring from the initial to the target orbit, H_2ERMES has to first get into proper phase with the depot, in this case, H_2ERMES will traverse 180 [°] in 0.772 [h] during the Hohmann transfer while the depot will traverse 172.32 [°] in the same time as can be seen from Table 10.4 and Equation 8.12, as such H_2ERMES needs to reach the relative angle of −7.68 [°] with respect to the depot.

As mentioned in Section 8.4.1, there is only one possible launch window per 23.46 [h] and so it is usually not possible to launch into this exact phase and phasing operations will have to performed. The worst case phasing time is determined by the synodic period given by Equation 8.16, after which, the relative position of two bodies in orbit repeats, the synodic period is minimized by maximizing the difference between the periods (and therefore semi-major axes by Equation 8.15) of the two orbits.

Since increasing the semi-major axis of the phasing orbit beyond the one of depot would drastically increase ΔV requirements and lowering would expose H_2ERMES to significant levels of atmospheric drag, the most effective phasing strategy is to simply remain in the initial orbit until the required phase angle is reached. Beyond the synodic period, the maximum allowable phasing time may be further constrained by operational requirements, in which case the maximum phase angle that can be covered during phasing stage can be again calculated using Equation 8.12 with T being the synodic period.

$$T_s = \frac{1}{|\frac{1}{T_1} - \frac{1}{T_2}|} \tag{8.16}$$

Here T_s [s] is the synodic period, and T_1 and T_2 [s] are the periods of the two orbits between which synodic period is calculated.

8.4.3. Launch Windows

The change in relative phase angle between the depot and CSG can be once again calculated using Equation 8.12 where T is the depot's orbital period (23.935 [h] (sidereal day) for CSG), and t is the 23.46 [h]. Then the amount of available launch windows can be determined by projecting the relative phase angle using a python program and checking how often is the relative phase angle less than the maximum phasing angle.

8.4.4. Sensitivity Analysis

The sensitivity of the flight design is presented in Table 8.4. It is performed by varying the major parameters affecting the number of available launch windows by approximately 10 [%] compared to the final design values as presented in Chapter 10.

Table 8.4: Sensitivity analysis of flight design

Parameters:	**Initial orbit altitude**	**Target orbit altitude**	**Maximum depot phasing time**	**Target orbit inclination**
Change in value	−20 [km]	+60 [km]	−0.7 [h]	+0.6 [°]
Available launch windows	158	146	135	150
Effect description	Maximum depot phasing angle increases	Flight phasing angle decreases	Maximum depot phasing angle decreases	Timeline is unaffected
Requirements affected	*RQ-STK-PLD-3*	*RQ-STK-PLD-3*	*RQ-STK-PLD-3*	*RQ-STK-PLD-3*
Impact:	4	2	2	3

It can be seen that while the number of available launch windows changes noticeably it nevertheless remains more

than sufficient to enable the mission. The most important change to track are operational and other requirements limiting the maximum depot phasing while an investigation into lowering the initial insertion orbit may open up new launch windows.

8.5. Aerodynamic Calculations

As a re-entry vehicle, H_2ERMES experiences all the possible flow regimes represented by subsonic, transonic, supersonic, and finally hypersonic flow. Designing the vehicle to sustain aerodynamic loads and moments throughout the flight regime requires aerodynamic characterizations for all flight regimes. Generating a model that is capable of processing aerodynamic data over the entire flight regime is a complicated and expensive endeavor, and as such a set of different methods will be used to characterize the vehicle in different regimes. The results of this section are outlined in Chapter 10. The aerodynamic design is performed considering the requirements *RQ-AER-2*, *RQ-AER-3*, *RQ-AER-4*, *RQ-AER-5*, *RQ-AER-6*, *RQ-AER-7*.

In the hypersonic regime the flow over the vehicle is dominated by strong bow shocks and Newtonian pressure distributions. Thus the angle of attack has a first order influence on the aerodynamic coefficients, since the aerodynamic performance is sensitive to small changes in orientation due to shock angles and pressure loads. In contrast, in the subsonic regime, shocks are absent and the flow is smooth and compressible. Aerodynamic coefficients depends more strongly on Mach (M) number and Reynolds number than on the angle of attack. Therefore the aerodynamic coefficients in the hypersonic regimes are analyzed with the angle of attack, and in the subsonic regime the coefficients are analyzed using the Mach number[11, 12, 13].

Once the vehicle reaches the subsonic regime, the vehicle will initiate the use of RCS thrusters to accurately navigate and land, and thus the stability and control characteristics are not of significant concern since the RCS thrusters can be used to control the stability. In the hypersonic regime, RCS thrusters can not be deployed to control the vehicle and such it is important to perform a first order stability analysis. Thus the stability calculations are performed only for the hypersonic regime. Subsonic stability is an analysis to be performed using CFD and wind-tunnels test in conjunction with control tests and characterizations.

This section will present the calculations, methods, and certain considerations for the aerodynamics of the vehicle.

8.5.1. Subsonic Regime

Subsonic flow is defined as flow with $M < 1$. The vehicle will experience this regime in two stages of the flight. During ascent as part of the launch vehicle, and during recovery as part of the final landing stages.

To perform these calculations, the RASAero software package will be used. The RASAero aerodynamic prediction methods and the RASAero software have been calibrated against NACA and NASA wind tunnel model data, free-flight model data and sounding rocket data, missile aerodynamic data, and professional engineering method missile aerodynamic analysis programs, against which in comparison tests RASAero has demonstrated equivalent numerical accuracy. While not explicitly validated for the aerodynamic analysis for capsules and blunt bodies, the subsonic analysis was validated against reference data and first-order hand calculations [14].

8.5.2. Transonic and Supersonic Regime

The transonic regime is defined as $0.8 < M < 1.2$, while the supersonic regime is characterized with $M > 1$. These regions are complex because they concurrently involve subsonic, sonic, and supersonic flow regions which are often separated by shock waves. This leads to mixed elliptical and hyperbolic governing equations around blunt bodies, defying any conventional analytical solutions. In transonic conditions, the presence of shock waves causes rapid variations, and thus unsteady behavior that cannot be reliably captured by first-order approximations, and thus models must be subjected to CFD[15].

Due to this non-linearity and coupling, analytical models for blunt-body flows in these regimes can be complex and/or inaccurate, unlike subsonic or hypersonic cases. The complexity of these flows makes CFD validation essential, as solvers are very sensitive to parameters. Consequently, for this design phase, the transonic flows are approximated using subsonic flow characteristics, and the supersonic flow regime is approximated using low hypersonic characteristics. These assumptions are detailed in *AS-AERO-01* and *AS-AERO-02*.

8.5.3. Hypersonic Regime

The hypersonic regime is conventionally defined as $M > 5$. General flow characterization methods fail in the hypersonic regime due to the physical changes in properties of air such as molecular dissociation and ionization.

There are however a set of analytical models developed by Newton under a set of assumptions to characterize

simple blunt bodies in hypersonic flows [16]. The primary assumptions are as follows are detailed in *AS-AERO-03*, *AS-AERO-04*, *AS-AERO-05*, *AS-AERO-06*, and *AS-AERO-07*. These assumptions lead to a simple pressure law defined by Equation 8.17.

$$C_p = 2\sin^2(\theta) \tag{8.17}$$

Here, C_p [$-$] is the local pressure coefficient, θ [rad] is the local surface inclination angle.

While proven to be unrepresentative of subsonic and supersonic conditions, this method has been validated to be accurate for hypersonic conditions[16, 17]. As such, these methods are used for the H_2ERMES vehicle. The shape that best characterizes the structure of H_2ERMES is the blunt cone shown in Figure 8.5. The loads acting

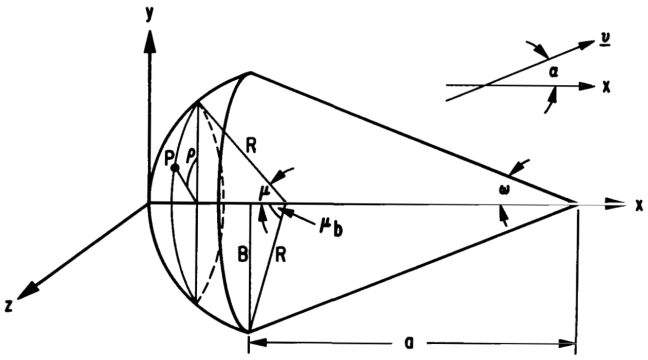

Figure 8.5: Blunted Cone geometry

on the cone are calculated for two sections: the cap or the spherical section, and the conical section. The force coefficients acting on the cap and cone are calculated using Equation 8.18 and Equation 8.19 respectively.

$$C_X = \frac{1}{2}\sin^2\alpha\sin^2\mu_b + (1+\cos^2\mu_b)\cos^2\mu_b \tag{8.18a}$$

$$C_Y = \sin\alpha\cos\alpha\sin^2\mu_b \tag{8.18b}$$

$$C_Z = 0 \tag{8.18c}$$

Here, $C_{X,Y,Z}$ [$-$] are the force coefficients respective to the defined axes, α [rad] is the angle of attack, μ_b [rad] is the half arc angle for the spherical cap.

The force coefficients acting on the cone are calculated only when the angle of attack exceeds or equals the cone half angle.

$$\widetilde{C}_X = -\frac{\sin^2\alpha\cos^2\omega}{\pi}\left[(1+2\cos^2\tilde{\rho})(\pi-\tilde{\rho}) + 3\sin\tilde{\rho}\cos\tilde{\rho}\right] \tag{8.19a}$$

$$\widetilde{C}_Y = \frac{2\sin^2\alpha\cos^2\omega}{\pi}\left[(\pi-\tilde{\rho})\cos\tilde{\rho} + \frac{\sin\tilde{\rho}}{3}(2+\cos^2\tilde{\rho})\right] \tag{8.19b}$$

$$\widetilde{C}_Z = 0 \tag{8.19c}$$

Here, $\widetilde{C}_{X,Y,Z}$ [$-$] are the force coefficients respective to the defined axes, ω [rad] is the cone angle, $\tilde{\rho}$ [rad] defines the tangential meridian on the cone.

8.5.4. Stability Analysis

A critical challenge in designing re-entry vehicles is ensuring both static and dynamic stability across the entire flight regime. The stability requirements vary significantly through subsonic, supersonic, and hypersonic flight regimes; with vehicles that are stable in the hypersonic regime often exhibiting instability in the subsonic regime and vice versa. Consequently, control surfaces or active stabilization mechanisms are often necessary [15, 18].

The aerodynamic stability of re-entry vehicles, particularly blunt bodies, is inherently nonlinear and strongly coupled with the trajectory [19]. While CFD and wind-tunnel tests are standard tools in evaluation, preliminary insights can be gained through first-order stability analysis. There are two main conditions in which a preliminary analysis must be performed: constant velocity and decelerating flight.

Constant Velocity Stability

In constant velocity conditions, a statically stable blunt body may oscillate around its trim point and eventually settle into a limit-cycle oscillation, where the stabilizing and destabilizing moments reach equilibrium. This behavior has been confirmed in both flight data and controlled experiments [20]. The constant velocity analysis can be performed as follows:

An important parameter that defines the stability of a blunt body is the pitch damping coefficient which is derived through the limit-cycle analysis as Equation 8.20[20];

$$C_{m_q} + C_{m_{\dot{\alpha}}} = -\frac{4IC_A}{md^2} \tag{8.20}$$

Here, $C_{m_q} + C_{m_{\dot{\alpha}}}$ $[-]$ is the pitch damping coefficient, C_A $[-]$ is the axial force coefficient, m [kg] is the mass, I [kgm^2] is the moment of inertia, d [m] is the characteristic length.

The pitch damping coefficient should be negative to produce a dynamically stable flight.

The oscillatory motion of the body can be idealized as with constant velocity, free-to-oscillate, with no heave since the flight path angle is assumed to remain constant. This results in a simple harmonic oscillate with damping with the solution in Equation 8.21 [21].

$$\alpha = Ae^{-\xi_1} \cos(\omega t + \delta) \tag{8.21}$$

Here, A [rad] is the angle-of-attack constant, ξ_1 $[-]$ is the damping coefficient, ω [rad/s] is the oscillation frequency, t [s] is the time, and δ [rad] is the phase shift constant.

where:

$$\omega = \sqrt{-\frac{\rho V^2 Sd}{2I} C_{m_\alpha}} \tag{8.22a}$$

$$\xi_1 = \frac{\rho VS}{4m}\left(C_A + (C_{m_q} + C_{m_{\dot{\alpha}}})\frac{md^2}{2I}\right) \tag{8.22b}$$

Here, ρ [kg/m^3] is the density, V [m/s] is the velocity, S [m^2] is the reference area, C_{m_α} [/rad] is the pitching moment slope.

Decelerating Stability

During decelerating flight, the dynamic pressure decreases, weakening the static restoring moments acting on the vehicle. This reduction in the static stability -akin to reducing the stiffness of a spring-mass system- results in a lower oscillation frequency and increased amplitude. Thus, while a blunt body may achieve oscillatory equilibrium in constant velocity flight, it may experience diverging oscillations in decelerating flight. The decelerating problem is represented as an Euler-Cauchy equation and has the following solution given in Equation 8.23 [21].

$$\alpha = At^\mu \cos(\nu \ln t + \delta) \tag{8.23}$$

Here, $\mu[-]$ is the Euler-Cauchy damping coefficient, $\nu[-]$ is the Euler-Cauchy frequency coefficient.

where the Euler-Cauchy coefficients are:

$$\nu = \sqrt{\mu^2 - \frac{8m^2 C_{m_\alpha}}{\pi \rho d I C_A^2}} \tag{8.24a}$$

$$\mu = \frac{md^2(C_{m_q} + C_{m_{\dot{\alpha}}})}{4IC_A} + 1 \tag{8.24b}$$

Here, C_A $[-]$ is the axial force coefficient.

For which the time is assumed to start from infinity and the starting time for the solution is calculated as:

$$t_i = \frac{2m}{\rho S C_A V_i} \tag{8.25}$$

Here, t_i[s] is the initial time, V_i[m/s] is the initial velocity.

Thus, the specific parameters A and δ are calculated as:

$$\delta = \tan^{-1}\frac{\mu}{\nu} - \nu \ln t_i \tag{8.26a}$$

$$A = \frac{\alpha_0}{t_i^\mu \cos(\nu \ln t_i + \delta)} \tag{8.26b}$$

Here, $\alpha_0[°]$ is the trim angle of attack.

In multiple instances, the angle of attack of blunt bodies, such as the Apollo capsule, experiences a deviation of 3 [°] during flight [22]. Thus, the stability analysis is performed for the desired angle of attack α_0 and $\alpha_0 \pm 3$.

8.5.5. Sensitivity Analysis

For re-entry purposes, achieving a maximum lift-over-drag ratio is vital, as such the effect of the geometry is calculated using the equations outlined before. The analysis is presented in Figure 8.6. Calculations are performed for an arbitrary set of geometry data [23, 24]. Increasing both the arc height and the taper ratio reduces the effec-

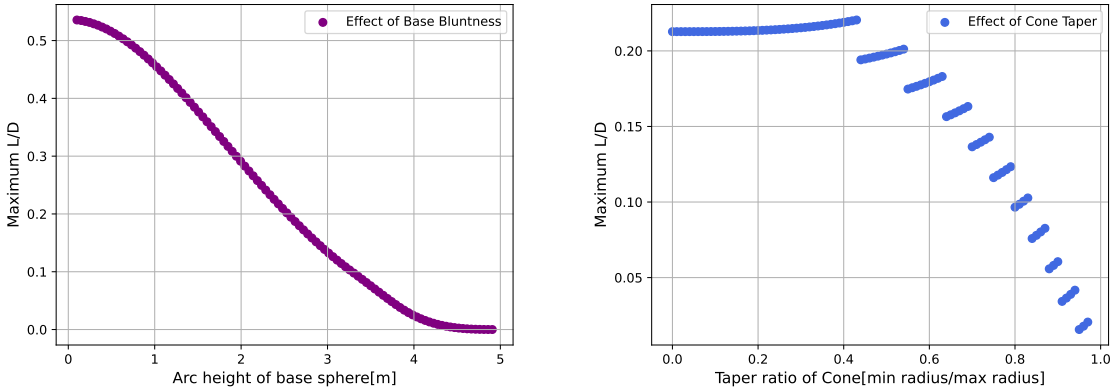

(a) Effect of base-cone bluntness on lift-over-drag

(b) Effect of cone taper ratio on lift-over-drag

Figure 8.6: Effect of geometric properties on aerodynamic characteristics of the vehicle

tive lift-to-drag ratio of the vehicle. From an aerodynamic standpoint, a minimal taper ratio is desirable, however improvements become marginal below a taper ratio of $0.4\,[-]$. Conversely for tank geometry, a cylindrical geometry is preferred. Therefore, the taper ratio of $0.4\,[-]$ is recommended for the vehicle. Correspondingly, the heat shield should be designed with minimal curvature.

The sensitivity analysis of the stability is performed by considering $C_{m_q} + C_{m_{\dot{\alpha}}}$ for angles of attack $\alpha_0 \pm 3$ since that is the expected deviation during flight according to literature [22]. The sensitivity analysis can be found in Table 8.5, and the graphs are given in Figure 8.7 and Figure 8.8.

Table 8.5: Sensitivity Analysis for Aerodynamics Characteristics

Parameters:	**Arc height of base**	**Taper ratio of cone**	**Pitch-Damping Coefficient**
Change in value	$+0.25$ [m]	$+0.1\,[-]$	$\pm 4\,[-]\%$
Effect description	L/D reduction of 8 [%]	negligible change in L/D	negligible change in stability
Requirements affected	*RQ-AER-5*	*RQ-AER-5*	*RQ-AER-7*
Impact:	3	3	3

8.6. Tank

The tanks are the biggest subsystems onboard the rocket in terms of volume and therefore are the most important contributor to the mass of the upper stage. In this section, the design process behind the tank will be explained.

8.6.1. Main Tank Geometry

Due to their sheer size and volume, it was decided that the tanks would be the main structural elements, therefore having the tank walls as the outer walls of HERMES, withstanding the launch loads. As it was settled before, the shape of the vehicle is a blunted cone [10], but the shape needs further refinement.

The tank geometry can be visualized as a truncated cone with two elliptical end caps on the top and bottom. This geometry is then split into the LOX tank at the bottom and the LH_2 tank at the top, separated by a common bulkhead as can be seen in Figure 8.9. It is crucial to locate the LOX tank at the bottom of the LH_2 tank due to

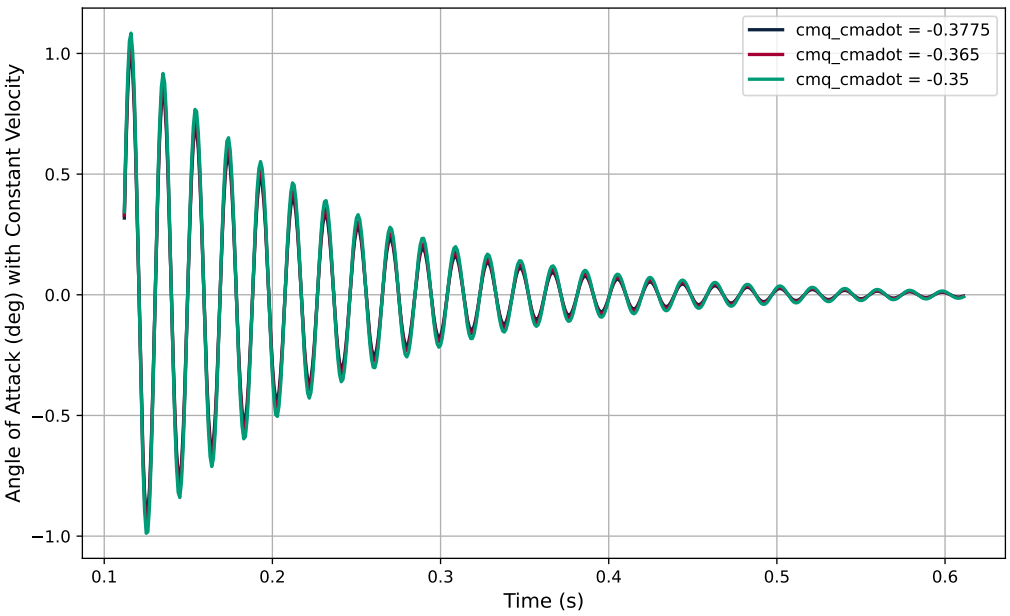

Figure 8.7: Stability analysis for constant velocity

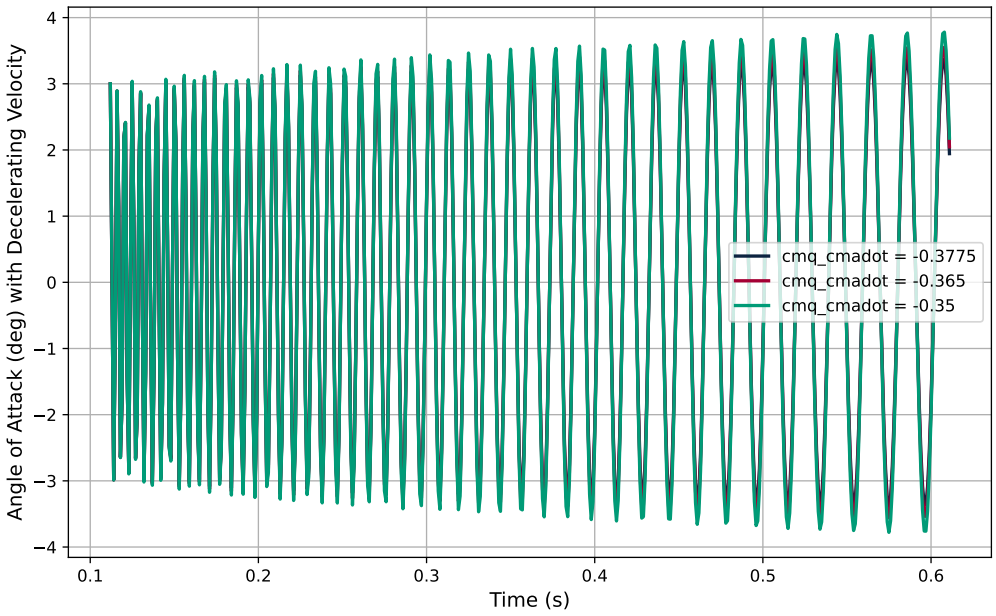

Figure 8.8: Stability analysis for decelerating velocities

their difference in density: having the LOX tank at the top would result in the center of mass located quite high and could result in an unstable behavior.

The overall dimensions of both tanks were determined based on the propellant volume needed with a $10\,[\%]$ margin accounted for ullage. This ullage is a first approximation, most probably overestimated, that heavily depends on the state the LH_2 is stored at. To start sizing it was necessary to constrain some dimensions such as the height of the end caps which is one fourth of the diameter like on cylindrical tanks, the radius ratio between the top and bottom ratio, which was fixed to $0.5\,[-]$ and the tank diameter which was fixed to $10\,[\text{m}]$. Radius ratio of $0.2\,[-]$ is common for capsules; therefore increasing it to $0.5\,[-]$ enabled a balance between aerodynamic and structural considerations.

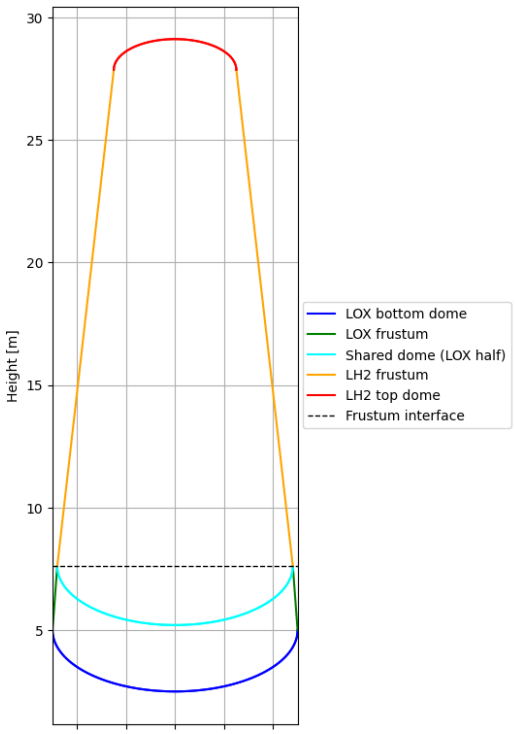

Figure 8.9: H_2ERMES Tank Geometry

8.6.2. Tank Material

As stated in the trade-off section, the choice of material for the tanks is stainless steel 304L. It was chosen for its high strength at cryogenic temperature, 1060 [MPa] [25] from the requirement *RQ-MAT-3*, and its heat capacity which enables the alloy to absorb a lot of heat with minimal rise in temperature making it a great choice against thermal loads during re-entry. It is also performing quite well against hydrogen embrittlement, complying with *RQ-MAT-4*. Stainless steel also comes with its drawbacks being hard to manufacture, weld with and is very dense resulting in a more complex structure. Additionally, stainless steel 304L can be recycle by remelting it and is reusable which complies with *RQ-MAT-1* and *RQ-MAT-2*. It is to be mentioned that as the development carries on, a new alloy, tailored for this application, can be developed for H_2ERMES in the same fashion as for SpaceX Starship.

8.6.3. Main Tank Sizing

The sizing of the tank consists primarily into determining the thickness to withstand the loads the vehicle is subjected to. This will be the driving factor for the mass of the tanks. It is necessary to mention that according to the Guyana Space center regulations [26] a safety factor of $2\,[-]$ is applied directly to the operating pressure, following the Guyana Space Center regulation from *RQ-STK-REG-1*, and a safety factor of $1.5\,[-]$ is used on mechanical loads.

The first step to take to determine the thickness is to determine the loading the structure is subjected to. Starting with the pressure, the latter causes stresses in the structure referred to as hoop and transversal stresses and in the case of conical sections those are expressed as Equation 8.27 and Equation 8.28. The initial pressure in the LH_2

tank is 2 [bar] and can go up to 10 [bar] due to boil-off, at which point pressure is vented off while in the LOX tank the pressure design for is 2.5 [bar] and is assumed constant in flight due to the slower boil-off compared to LH_2.

$$\sigma_{hoop} = \frac{PR_{avg}}{tcos(\phi)} \tag{8.27}$$

$$\sigma_{trans} = \frac{PR_{avg}}{2tcos(\phi)} \tag{8.28}$$

Where σ_{hoop} [Pa] is the hoop stress, P is the pressure inside the tank, R_{avg} [m] is the average radius of the cone, t [m] is the thickness, ϕ [rad] is the half aperture angle of the truncated cone and σ_{trans} [Pa] is the transversal stress.

Another loading acting on the structure is the axial compression cause by the thrust from the engine acting from the base of the tank. The thrust-to-weight ratio of H_2ERMES is estimated to 1.2 [$-$], from this the force can be retrieved and converted to a stress value by Equation 8.29 [27].

$$\sigma_{axial} = \frac{SF \cdot T}{2\pi R_{avg} t} \tag{8.29}$$

Where σ_{axial} [Pa] is the axial stress, SF [$-$] is the safety factor, and T [N] is the thrust.

Lastly, the bending load on the structure is modeled taking into account the maximum lateral acceleration from the New Glenn first stage which is 2 [g]. It was modeled based on $\frac{My}{I}$ as in Equation 8.30. With the moment modeled as a distributed load acting along the length of the cone [28]. For the moment of inertia, the structure was assumed to be a cylindrical by taking the average radius of the truncated cone.

$$\sigma_{bend} = \frac{\frac{m_{fuel}2g}{L} \cdot \frac{L^2}{12} \cdot R_{avg}}{\pi R_{avg}^3 t} \tag{8.30}$$

With σ_{bend} [Pa] the bending stress, m_{fuel} [kg] the mass of LH_2, L [m] the length of the tank, and $\pi R_{avg}^3 t$ [m^4] the moment of inertia of a thin-walled circular cylinder.

Now, knowing all of those stresses act in different directions, they must be combined to ensure that it would not cause the ductile material to yield. For this Von Mises stress technique is used, it is given by Equation 8.31. The stresses in the longitudinal direction σ_θ consist of the hoop stress, where σ_ϕ is a combination of longitudinal stress, bending stress and axial stress.

$$\sigma_{vm} = \sqrt{\sigma_\theta^2 + \sigma_\phi^2 - \sigma_\theta \cdot \sigma_\theta} \tag{8.31}$$

Where σ_θ [Pa] is the stress in the longitudinal direction and σ_ϕ [Pa] is the sum of stresses in the radial direction.

From this, the thickness is determined iteratively until the yield criterion is satisfied.

A check for the buckling of the structure is then made after the estimation of the thickness. This is done following the NASA SP-8019 on the buckling of thin-walled truncated cones [29]. Checks on buckling due to axial loads and bending are considered and are given by Equation 8.32 and Equation 8.33 and both have to be smaller than the axial and bending loads given in Equation 8.32 and Equation 8.30.

$$P_{cr} = \gamma \frac{2\pi E t^2 cos(\phi)^2}{\sqrt{3(1-\mu^2)}} \tag{8.32}$$

$$M_{cr} = \gamma \frac{\pi E t^2 r cos(\phi)^2}{\sqrt{3(1-\mu^2)}} \tag{8.33}$$

Where γ [$-$] is the knockdown factor, E [Pa] the Young's modulus, μ [$-$] is the Poisson ratio, and ϕ [rad] is half aperture angle of the truncated cone.

Lastly a check on the natural frequency against the vibrations produced by the New Glenn first stage need to be performed to ensure the structure does not resonate. Again the simplification of a cylindrical thin-walled shell structure is made for which the first-mode axial and lateral natural frequencies are given by Equation 8.34 and Equation 8.35 [27].

$$f_{ax} = 0.56\sqrt{\frac{EI}{mL^3}} \tag{8.34}$$

$$f_{lat} = 0.25\sqrt{\frac{EA}{mL}} \tag{8.35}$$

Where f_{ax} [Hz] is the natural frequency in the axial direction, f_{lat} [Hz] is the natural frequency in the lateral direction, A [m^2] is the surface area, and m [kg] is the tank and propellant mass.

According to the New Glenn guide [30], to ensure the structure does withstand the vibrations and does not resonate: the first and second natural frequency mode must be greater than 6 [Hz] laterally and 15 [Hz] axially. The results for the LOX and LH_2 are summarized in Table 8.6.

Table 8.6: Natural frequencies main tank

Mode and Tank	Value	Unit
Lateral Mode LOX Tank	181.787	[Hz]
Axial Mode LOX Tank	54.860	[Hz]
Lateral Mode LH_2 Tank	11.022	[Hz]
Axial Mode LH_2 Tank	35.256	[Hz]

Looking at those results, one can see that especially for theLH_2tank the margin is pretty small and this could lead to a potential structural failure. Therefore, as a recommendation, rings or other types of reinforcements could be added towards the top of the LH_2 tank more prone to vibration due to the small cross section.

8.6.4. Main Tanks Sensitivity Analysis

The main inputs to the tank sizing tool are the structural and propellant mass of the stage, the payload mass (the mass of LH_2 to deliver to the depot), the pressures inside the tanks, and the maximum pressure that can be achieve in the LH_2 tank due to boil-off. Varying those parameters results in the sensitivity analysis shown in Table 8.7. Given the sensitivity of the design to pressure, this change can be mitigated by the use of pressure-relief valves and burst discs in the design that ensure the pressure never exceeds its rated value.

Table 8.7: Main tank sensitivity analysis

Parameters:	**Stage structural mass**	**Propellant mass**	**Payload Mass**	**Initial tank pressure**	**Maximum pressure LH_2**
Change in value	+10 [%]	+10 [%]	+10 [%]	+1 [bar]	+10 [bar]
Relative change in sub-system mass	+0 [%]	+14 [%]	+2 [%]	+39 [%] +51 [%]	+27 [%]
Effect description	Structural mass of the stage is minimal compared to propellant mass	Significant change in tank mass with increasing propellant mass	Payload mass impacts the tank mass less than the propellant mass	Very sensitive to a pressure change: the LH_2 being at a lesser pressure at the beginning than LOX, the tank masses scales accordingly	Relatively high impact on the LH_2 tank mass but smaller than the initial pressure impact.
Requirements affected	None	None	*RQ-STR-2*	*RQ-STR-2*	*RQ-STR-3*
Impact:	3	4	3	2	4

8.6.5. Common Bulkhead

Looking at the architecture of common bulkheads on previous missions such as the Centaur V. They consist most of the time of a sandwich structure in which insulation material is fitted to limit the heat flux between the LOX and LH_2 [31] and enables mass and volume savings on the second stage. This however, comes with the drawback of being hard to inspect between launches. A similar design can be applied on H_2ERMES given the sheer amount of area between the two tanks.

8.6.6. Pressurization of the Tank

The pressure in the main tank are assumed to be 2 [bar] in the LH_2 tank, increasing with boil-off, and 2.5 [bar] in the LOX tank. To ensure that pressure stays at those minimum values, the tanks are autogenous-pressurized.

This means that a small part of the oxygen is heated up by the heat produced by the engines and is re-injected to the tank to keep the ullage at the given pressure. Three pressure transducers, to ensure 2 out of 3 readings coincide, are implemented in the design to read the pressure value of the ullage volume and in turn trigger the autogenous-pressurization sequence.

8.6.7. Fatigue Considerations

H_2ERMES will have to be designed by keeping rapid reusability and refurbishment in consideration as per *RQ-STK-RLV-2* and *RQ-STK-RLV-4*. Therefore, the fatigue life of the tanks is an important consideration since these tanks will face massive temperature differences and pressures. These conditions, over time, can negatively influence material properties, increasing the risk of failures. This will expand on the fatigue analysis of the tank and any corresponding considerations.

For this report, it was deemed sufficient to analyze primarily the axial forces and internal pressures acting on the tank. The bending forces present should also be examined for fatigue considerations, however, this analysis is not performed due to resource limitations.

The first step is to calculate the stress environment of the tanks during different stages of flight. Then, two different types of fatigue prediction tools, the Paris crack growth rate and the Miner's cycle rule, will be implemented. This will be followed by a sensitivity analysis. The fatigue prediction is intended to function as a check on the thickness of the tank found from Section 8.6.3. If the structure is predicted to fail, then the thickness of the tank is increased, and the process will be iterated to ensure survival for 25 launches. Then during refurbishment operations, Non-Destructive Evaluation (NDE) technologies can be used to find cracks that are larger than the maximum crack length which the launcher can have before complete crack propagation and failure [32].

Fatigue Stress Environment

Before the tank stress can be calculated, the flight timeline is divided into different stages of varying stress environments. These are summarized in the list below.

- On Launchpad (Before Launch)
- Max Q
- Max thrust firing of H_2ERMES
- Before Refueling
- After Refueling
- During Re-entry
- On Launchpad (After Launch)

Furthermore, three different types of stresses are evaluated: thermal, mechanical and pressure. It is also important to note that as defined in *AS-FATG-01*, the tank will be assumed to be clamped on both ends which induces thermal stresses. This formulation is given by Equation 8.36.

$$\sigma_{thermal} = \frac{E\alpha\Delta T}{\cos(\phi)} \tag{8.36}$$

Where $\sigma_{thermal}$ [Pa] *is the thermal stress,* $\alpha_{expansion}$ $[-]$ *is the thermal expansion of the tank material, and* ΔT [K] *is the temperature gradient of the surface.*

There are two main thermal stress environments that the vehicle will have to survive. The first environment is the temperature difference present between the ambient atmosphere and cryogenic LH_2 temperatures during Max-Q (the moment at which the launch vehicle experiences the highest dynamic pressure) and at the second stage firing. To make a conservative estimate, it will be assumed that at these stages there is an effective ΔT of 280 [K] as per *AS-FATG-05*.

Assuming that the launch vehicle is designed such that it is theoretically unconstrained when the tank is at 20 [K], there will be thermal stresses induced on the tank at the launch pad before LH_2 is pumped into the tank. This is due to the expansion of the tank at room temperatures as LH_2 is pumped in. The second main thermal stress environment occurs around the refueling point. To avoid the boiling of LH_2, the tank vent pressure is set at approximately 10 [bar]. GH_2 absorbs significant amounts of the oncoming heat, thus eventually heating up in the process. These temperatures can reach up to 200 [K]. Thus, a ΔT of 180 [K] will be considered for this point.

Also note that at the launch pad, the tank can experience cryogenic temperatures due to residual LH_2 surrounded by an ambient temperature of 300 [K].

The mechanical stress inside the tank, assumed to act axially, is given by Equation 8.29.

$$\sigma_{mechanical} = \frac{F}{2\pi R_{top} t \cos(\phi)} \tag{8.37}$$

Where F [N] is the axial force acting on the tank. Note that the smallest value of R (R_{top}) will be taken since that leads to a bigger value of mechanical stress.

Note that this is divided by $\cos(\phi)$ since mechanical stresses acts in the direction of the wall, but if it is assumed to be laterally constrained, then the reactive forces will be offset by $\phi[°]$. To calculate the pressure stress inside the tank, the critical axial compressive load for a pressurized conical tank taken from [29], can be treated as a mechanical load acting as a compressive force and then equated to a mechanical stress using Equation 8.37. The critical axial compressive load, as per [29], is given in Equation 8.32 without the impact of pressure. Taking into account the pressure, Equation 8.32 becomes Equation 8.38.

$$p_{cr} = [\frac{\gamma}{\sqrt{3(1-\mu^2)}} + \Delta\gamma] 2\pi E t^2 \cos^2(\phi) + \pi R_{top}^2 P_{tank} \tag{8.38}$$

where $\Delta\gamma$ [−] is taken to be roughly 0.12 [−], and P_{tank} [Pa] is the pressure inside the tank.

It is important to note that the value of $\Delta\gamma$ varies with the tank geometry and pressure, but the peak value of this coefficient is 0.12 [−]. Thus to make a conservative design, $\Delta\gamma$ will be taken to be this peak value (*AS-FATG-02*).

The stress environments for the tanks are now constructed by evaluating these stresses at all loading points discussed at the start. The resulting stress environment is visualized in Figure 8.10 based on the design characteristics outlined in the Midterm report [2].

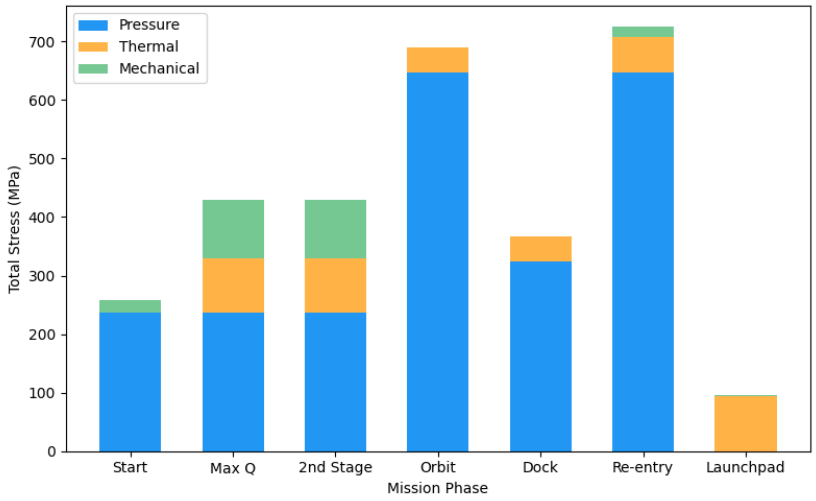

Figure 8.10: Pressure, thermal and mechanical stresses plotted at different loading points.

As can be seen, maximum stress is expected during orbit and re-entry, while the lowest stress is expected when the launch vehicle is on the launchpad. However, since this is a complicated loading history that has multiple different stress ranges, a Rainflow counting algorithm was used to simplify this into stress ranges and stress cycles. Furthermore, as per *RQ-STK-RLV-2*, H_2ERMES is expected to last 25 launches. Thus, the total stress cycle will be the number of launches multiplied by the local stress cycle. The stress ranges and the total stress cycle will then be used for fatigue predictions.

Paris Fatigue Prediction

The Paris crack growth rate can be used to predict fatigue failure due to crack propagation through Equation 8.39.

$$\frac{da}{dn} = C(\Delta K)^m \tag{8.39}$$

$$\Delta K = Y \Delta\sigma \sqrt{\pi a} \tag{8.40}$$

Where $\frac{da}{dn}$ [m/cycle] is the increase in crack growth rate per cycle, ΔK [Pam$^{0.5}$] is the stress intensity factor calculated in Equation 8.40, $\Delta\sigma$ [Pa] is the change in stresses, Y [$-$] is a geometric factor depending on where the crack is, C [$-$] and m [$-$] are Paris crack growth rate coefficients, and a [m] is the depth of the crack.

It is important to note that Y [$-$] is strongly dependent on the crack depth and the thickness of the tank. Thus, this was parameterized to be a function of these two variables [32]. The coefficients of the Paris crack growth rate, C and m were taken from [33]. However, it is important to note that these coefficients are entirely empirical and thus differ with geometry and also greatly depends on the notch location and how the tests themselves were performed. Furthermore, since this is a conical tank, these coefficients will be greatly affected but for the purpose of this analysis, the conical shape will be assumed to have no effect on these coefficients *AS-FATG-03*. In an ideal case, these coefficients would be found experimentally for this specific loading case. However, since at this design stage it is unfeasible to do so, the calculations will be done with these coefficients. This assumption is still valid since this specific paper uses the Paris crack growth rate for a stainless steel 304 tank at cryogenic temperatures which is similar to our actual load case. Furthermore, since these effects are not clearly understood for a conical tank geometry, a safety factor of 2 on the number of cycles will be taken. These coefficients are shown in Equation 8.41 and Equation 8.42 [33].

$$C = 5.131 \cdot 10^{-20} \tag{8.41}$$

$$m = 7.02 \tag{8.42}$$

Next, to use the Paris crack equation, a critical crack depth has to be calculated based on the loading case of the tank such that if the crack were to exceed this size, the tank would lose its load bearing capabilities and fail [32]. This critical crack depth is based on the minimum thickness of the tank that is needed to survive the maximum stress during the flight timeline. This is given in Equation 8.43.

$$a_{critical} = \left(\frac{K_{IC}}{Y\sigma\sqrt{\pi}} \right)^2 \tag{8.43}$$

Where $a_{critical}$ [m] is the critical crack depth, and K_{IC} [Pam] is the fracture toughness of the tank material.

Thus, with the thickness of the tank decided in the previous section, Equation 8.39 will run for every stress cycle expected for the stress ranges calculated with the Rainflow counting algorithm. If the crack depth ever goes beyond the critical crack depth, an iteration process starts by increasing the thickness.

Miner Fatigue Prediction

Miner's rule can also be used to predict failure in materials. It is based on a linear damage rule, which essentially means that every cycle of loading and unloading increases the *damage* count. The Miner's rule is given in Equation 8.44a.

$$D_{damage} = n_{cycle} \frac{\sigma^m}{C} \tag{8.44a}$$

$$m = \frac{-1}{a} \tag{8.44b}$$

$$C = 10^{-\log(b)/a} \tag{8.44c}$$

$$\sigma = \frac{b}{N^a} \tag{8.44d}$$

Where D_{damage} [$-$] is the cumulative damage done to the material, n_{cycle} [$-$] is the number of cycles for a specific stress range taken from the Rainflow algorithm, σ [Pa] here is the stress range also taken from the Rainflow algorithm, m [$-$] and C [Pa^m] are derived from the S-N curve coefficients of the tank material in Equation 8.44b and Equation 8.44c. Here a and b [Pa] are coefficients of the S-N curve as given in Equation 8.44d where N [$-$] is the number of cycles to failure.

Thus, choosing the appropriate coefficients is vital to predicting fatigue behavior. Ideally, as in the case of the Paris crack growth coefficients, the Miner coefficients should also be determined experimentally for the specific load case and tank geometry. However, for this report, the specific S-N curve that will be used is given in [34]. The S-N curve in this paper however, was obtained from a FEM simulation performed in ANSYS at standard temperature and pressure conditions for the AISI 304 steel. While this simulation was performed at standard conditions, the tank will experience its largest load variations at cryogenic temperatures, and material properties

can differ significantly in this regime [35] [25]. For example, as per [25], the yield strength increases by a factor of 2 in the cryogenic regime, which can affect the fatigue properties of stainless steel. Therefore, more testing is necessary to find fatigue-specific coefficients.

Furthermore, since the effects of tank geometry on fatigue are not clearly understood, it will be assumed, as per *AS-FATG-04*, that a safety factor of 2 [−] is taken with respect to the stresses calculated from the different loading phases. The S-N curve a and b coefficients, taken from [34], are listed in Equation 8.45a, and Equation 8.45b while the Miner's C, and m coefficients are listed in Equation 8.45c and Equation 8.45d.

$$a = -0.1555 \quad (8.45a) \qquad C = 1.348 \cdot 10^{21} \quad (8.45c)$$

$$b = 1884 \quad (8.45b) \qquad m = 6.452 \quad (8.45d)$$

Sensitivity Analysis

This section will discuss a sensitivity analysis that was performed for fatigue predictions. The results of this can be seen in Table 8.8.

Table 8.8: Sensitivity analysis for the fatigue prediction tool

Parameters:	**Maximum Pressure in tank**	**Top Radius**	**Cone Angle ϕ**	**Minimum Launches**
Change in value	$\times 1.25$ [−]	$\times 1.25$ [−]	$\times 2$ [−]	$\times 0.5$ [−]
Relative change in subsystem mass	$+30.23$ [%]	$+25.58$ [%]	$+4.65$ [%]	-9.30 [%]
Effect description	Increase in tank thickness to accommodate the increased stress.	Pressure stress increases with radius (Equation 8.38), so thickness and mass increase.	No significant increase in tank mass due to the cosine rule.	Decrease in mass due to lower thickness needed to sustain less cycling.
Requirements affected	None	None	None	None
Impact:	2	2	3	4

The sensitivity analysis in Table 8.8 shows that the mass of the tank is sensitive to an increase in the pressure of the tank and the bottom radius of the cone. The maximum pressure inside the tank has to be set this high to delay the venting point of the hydrogen gas while increasing the bottom radius increases the stress in the walls as per Equation 8.38. Thus, a possile mitigation strategy for both these risks is to use materials which have better fatigue properties which can handle successive pressurization without failing. Furthermore, a detailed study can be done to identify the failure locations due to pressurization of the conical shell tanks such as crack nucleation spots or local pressure high spots. Then, the local thickness in these locations could be increased thereby not adding more mass than is necessary. The other variables, the conical angle and the minimum launches, have a minimal impact on the mass of the tank (on the order of single percentages). Thus, these can be optimized as per other subsystems.

8.6.8. Header Tanks

The header tanks are required to carry the propellant required after the refueling process has completed, for the de-orbit and landing burns. These are spherical tanks located within their respective main fuel tanks. This results in the fact that no insulation is required, as their outside environments are the colder main tanks. Furthermore, these tanks will be non-load-carrying, considering that they are quite small with respect to the main conical tanks. Furthermore, as per *RQ-STK-RLV-2*, a safety factor of 2 [−] was also taken. They are sized with an internal pressure of 10 [bar], which results in the minimum wall thickness found using Equation 8.46a. The volume required for the tanks, and with that the radius R, follows from ΔV calculations. An important note is that 10 [%] of the tank volume will be reserved for the ullage and the temperature of this liquid will be initially kept at 20 [K]. This gives a density of LH_2 of 71.13 [kg/m^3]. The radius of this tank will simply be given by Equation 8.46b.

$$\sigma = \frac{PR}{2t} \quad (8.46a) \qquad R = \sqrt[3]{\frac{3m_{LH2}}{4\pi\rho_{LH2}f_{liquid}}} \quad (8.46b)$$

Where R [m] is the radius of the header tank, R is the header tank thickness, P is the inner pressure. f_{liquid} [−] is the fill level of LH_2 taken to be 0.9 [−], m_{LH_2} [kg] is the mass of liquid hydrogen needed to be stored in the header tank, and ρ_{LH_2} [kg/m^3] is the density of liquid hydrogen.

For this report, this analysis was deemed to be sufficient. However, due to resource constraints, several things had to be omitted from the actual design of the header tank. For example, the header tanks also go through repeated stress ranges which can induce fatigue failure. This was not considered for the sizing of the header tank. This can be improved upon by considering this failure mode. Furthermore, the mass of the connection points between the header tank and the main tank has also not been considered due to time constraints. These are for now, assumed to be negligible as per *AS-HEAD-01*.

8.7. Propulsion

In the following section, the conceptual design of the propulsion system is presented. Carrying over the choice of chamber pressure of 6.1 [MPa], as well as 24 thrust chambers, the propellants LH_2 and LOX, and the igniter selection of a torch igniter. From these, the characteristics of the feed system, particularly the pressurization system concept, turbopump design, and piping specifications are found. Moreover, the engine thrust chamber design is developed, where the choice of chamber pressure is revised, as well as the engine cycle. Furthermore, an optimization of the O/F ratio, as well as the layout of thrusters is performed, and the general engine parameters and performance are estimated. Following this, the mass of the thrust chambers is calculated depending on their geometry. Finally, the final parameters of the design, which were calculated, are listed. Then a sensitivity analysis is performed, and the final thrust chamber profiles and engine bay layout are shown.

8.7.1. Feed System

A key part of the propulsion system is the feed system, which involves delivering the propellant and oxidizer to the combustion chamber. The main design decisions to be made regarding the feed system are: pump-fed or pressure-fed, type of cycle, material and thermal insulation for piping, and type of injector. These decisions are explained in the subsequent paragraphs.

Pressurization of Propellants

Firstly, the propellant and oxidizer will be supplied through a **pump-fed** mechanism. In pump-fed systems, the chemical energy of the propellant and/or oxidizer is used to power turbines that drive pumps which pressurize the propellant before delivering it to the thrust chamber. On the other hand, with pressure-fed systems, the propellant tanks are pressurized before launch. For high-thrust applications such as launch vehicles, pressure-feed systems are not desired because the prior pressurization of such large tanks implies a very high mass penalty [36].

In the case of H_2ERMES, the pump-fed system employs an **expander bleed cycle**. In this configuration, cryogenic propellant is first circulated around the combustion chamber to absorb heat, and, for this application, the liquid hydrogen will be further conducted through the heat shield. The propellant gains heat and vaporizes, which then drives the turbine. Unlike a closed expander cycle, where the heated propellant is injected again into the combustion chamber, the expander bleed cycle vents the propellant after passing through the turbine. This cycle was selected primarily due to the previous decision to use liquid hydrogen for **regenerative cooling** of the thrust chambers and heat shield, which results in the expansion of the LH_2. Given the complexity of the cooling system, which serves both the chambers and heat shield, the associated significant pressure losses make it inefficient to feed the propellant to the thrust chambers again.

Turbopump Design

The feed system will comprise two main high-pressure turbopumps, one for the LH_2 and one for LOX. Both turbines will by driven by LH_2 due to its higher specific heat capacity at cryogenic temperatures compared to LOX [37]. In expander cycles engines, the velocity ratio (defined as the ratio of blade speed compared to flow velocity) is quite high due to the limited pressure drop across the turbine. Consequently, energy extraction must be more efficient and distributed across multiple engines. As a result, **multi-stage reaction turbines** will be employed [36]. Finally, due to the disparity in densities of LH_2 and LOX, the rotational speeds needed for the turbopump of each fluid are quite different, and thus a dual shaft must be employed. To suit system architecture and reduce complexity, the turbines will be placed in parallel instead of in series. The Space Shuttle Main Engine, also operating with LH_2 and LOX, also employed this turbine arrangement [38].

The design of the turbopump is determined mainly by the required rise in pressure through the pump, Δp_p, and the Net Positive Suction Head (NPSH), which is the necessary pressure margin to prevent the propellant from cavitating. The process for estimating turbopump mass is developed in the following paragraphs and equations. This process has been taken from *Space Propulsion Analysis and Design* [36] and adapted to H_2ERMES.

The required pump pressure rise is determined by taking the pressures of LH_2 and LOX at the tanks' outlets and increasing them to the required chamber pressure. This calculation accounts for pressure losses throughout the

feed system, both upstream and downstream of the pump. These pressure losses arise from different sources: the conversion of static pressure into dynamic pressure, and pressure drops in the feed system, the cooling jacket of the regenerative cooling system, and the injector. A schematic of the pressure profile throughout the feed system is shown in Figure 8.11. These losses are given by Equation 8.47, Equation 8.48, Equation 8.49, and Equation 8.50, consequently.

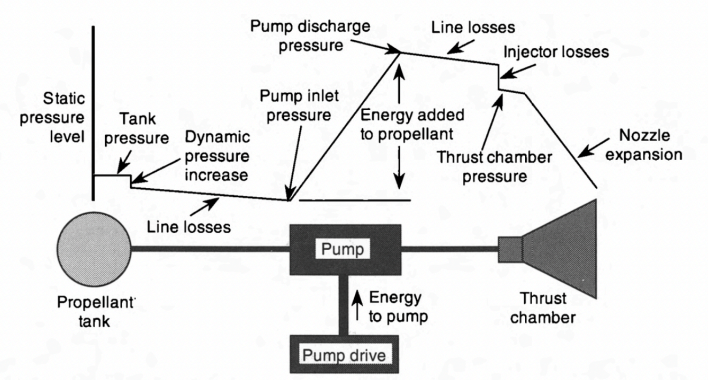

Figure 8.11: Pressure profile across pressure-fed feed system [36]

$$\Delta p_{\text{dynamic}} = \frac{1}{2}\rho_p V_p^2 \tag{8.47}$$

$$\Delta p_{\text{feed}} = 35000 - 50000\text{Pa} \tag{8.48}$$

$$\Delta p_{\text{cool}} = 0.15 p_c \tag{8.49}$$

$$\Delta p_{\text{inj}} = 0.3 p_c \tag{8.50}$$

Here, $\Delta p_{dynamic}$ is the increase in dynamic pressure in [Pa]*, ρ_p is the propellant density in* [kg/m^3]*, V_p is the propellant velocity in* [m/s]*, Δp_{feed} is the pressure drop in the feedlines in* [Pa]*, Δp_{cool} is the pressure drop in the cooling jacket in* [Pa]*, p_{inj} is the pressure drop across the injector in* [Pa]*, p_c is the chamber pressure in* [Pa].

ρ_p is obtained from BoilFAST for a given temperature, and V_p has been set to 10 [m/s] according to Humble [36]. This equation assumes that the fluids are initially at rest in the tank and that the increase in dynamic pressure due to the flow is directly translated to a decrease in static pressure. For Δp_{feed}, a pressure loss of 50000 [Pa] was taken as a conservative estimate. Lastly, p_c is determined in Section 8.7.2.

The pump-inlet pressure is then given by Equation 8.51. The required pump discharge pressure at the pump outlet is given by the chamber pressure and the additional losses downstream of the pump, as can be seen in Equation 8.52. The required pressure rise is then the difference between the inlet pressure and the required discharge pressure, as shown in Equation 8.53, where a 10 [%] margin has been used to account for extra pressure losses that have not been including in the main sources mentioned before and to mitigate uncertainties in the operation of the turbopump.

$$p_i = p_{\text{main}} - \Delta p_{\text{dynamic}} - \Delta p_{\text{feed}} \tag{8.51}$$

$$p_o = p_c + \Delta p_{\text{feed}} + \Delta p_{\text{inj}} \tag{8.52}$$

$$\Delta p_p = 1.1(p_o - p_i) \tag{8.53}$$

Here, p_i is the pump inlet pressure in [Pa]*, p_{main} is the pressure at the main tank, either LH_2 or LOX in* [Pa]*, p_o is the pump outlet pressure in* [Pa].

Once the required pressure rise across the pump has been established, the necessary number of stages can be determined in accordance with Equation 8.54. This is based on the maximum allowable pressure increase per stage, which is 16 [MPa] for liquid hydrogen and 47 [MPa] for liquid oxygen. To ensure operational redundancy, an additional stage is included in both the fuel and oxidizer pumps.

$$n \geq \frac{\Delta p_p}{\Delta p_{ps}} \tag{8.54}$$

n is the number of stages, Δp_{ps} is the allowable pressure rise per stage in [Pa].

Furthermore, the pump rotational speed is given by Equation 8.55. The NPSH can be calculated using Equation 8.56. The power required to drive the pump is given by Equation 8.57, where the pump's head pressure rise in meters, given by Equation 8.58. Lastly, the mass of the turbopump, can be estimated as per Equation 8.60. The pump shaft torque is calculated using Equation 8.59.

$$N_r = \frac{u_{ss}\text{NPSH}^{0.75}}{\sqrt{Q}} \tag{8.55}$$

$$\text{NPSH} = \frac{p_i - p_v}{g_0 \rho_p} \tag{8.56}$$

$$P_{req} = \frac{g_0 \dot{m} H_p}{\eta_p} \tag{8.57}$$

$$H_p = \frac{\Delta p_p}{g_0 \rho_p} \tag{8.58}$$

$$\tau = \frac{P_{req}}{N_r} \tag{8.59}$$

$$m_{tp} = A\tau^B \tag{8.60}$$

Here, N_r is the pump rotational speed in $[\text{rad/s}]$*, u_{ss} is the suction specific speed, which is taken to be* $130\,[\text{m/s}]$ *as per liquid hydrogen, Q is the volumetric flow entering the pump in* $[\text{m}^3/\text{s}]$*, H_p is the pump's head pressure rise in* $[\text{m}]$*, m_tp is the mass of the turbopump in* $[\text{kg}]$*, A and B are empirical coefficients that can be taken as* $1.5\,[-]$ *and* $0.6\,[-]$*, respectively, and τ is the pump shaft torque in* $[\text{Nm}]$.

Piping

The piping will be thermally protected using vacuum-insulated pipes, which consist of an inner and outer pipe separated by a vacuum. Vacuum insulation minimizes heat losses, vaporization, and the appearance of ice [3]. In addition, vacuum insulation provides a more hygienic solution in comparison to the use of insulation materials that can retain moisture and bacterial growth, which is key for the reusability of the vehicle. According to Meyer [39], for LH_2 storage applications, the use of vacuum insulation reduces around $50\,[\%]$ of the boil-off compared to perlite insulation. The pipes will be made out of stainless steel 304L because it is a widely used material for vacuum jacketed piping due to its high resistance to corrosion even without heat treatment.

To determine propellant and oxidizer channel areas and diameters, continuity can be used with the mass flow obtained from the thrust as derived in Section 8.9. This can be seen in Equation 8.61 and Equation 8.62. After the propellant and oxidizer pass through the pump, they diverge into different feed lines that go to each thrust chamber, and since the mass flow is assumed to be constant throughout the propulsion system, the channel areas will be calculated taking into account 1/24 of the total mass flow. Lastly, for all the feed lines, 1/7 of the total mass flow is LH_2 and 6/7 are LOX.

$$A_c = \frac{\dot{m}}{\rho_p v_p} \tag{8.61}$$

$$D_c = 2\sqrt{\frac{A_c}{\pi}} \tag{8.62}$$

where A_c is the channel area in $[\text{m}^2]$ *and D_c is the channel diameter in* $[\text{m}]$*, $\dot{m}$ is the mass flow in* $[\text{kg/s}]$

Injector Choice

A key design requirement for the propulsion system is that it must be throttleable and re-ignitable. This will be done mainly by regulating the mass flow and flow velocities. To regulate the mass flow that goes into the combustion chamber, a **pintle injector** has been selected since it has a variable cross-sectional area. Pintle injectors can be continuous type, multi-hole type and multi-slit type. Experimental studies show that the multi-slit type has a high combustion efficiency and is the most suitable for continuous throttling. This is because the slits allow for controllability of the direction of injection, which allows for regulating the point and velocities at which the fuel and oxidizer combine. Furthermore, if the slits are vertically heightened, the combustion performance can be further improved since the pressure drop across the injector is minimized [40].

8.7.2. Engine Thrust Chamber Design

In the following subsection, the design of the engine thrust chambers is addressed. Firstly, the chamber pressure and engine cycle are selected, according to past concepts and the group's design choices. Following this, the optimal Oxidizer to Fuel (O/F) ratio, which minimizes the total propellant mass, is found. Moreover, the main thrust chamber dimensions and efficiencies are calculated, using CEA and RPA. Next, the optimal configuration of thrusters, which once again results in a lower total mass, is calculated via an optimization. Finally, the mass of each kind of thrust chamber is calculated, according to the dimensions calculated previously.

[3] URL https://cryospain.com/why-choose-vacuum-insulated-pipesabc.com [cited 2025-06-17]

Choice of Igniter

Due to *RQ-PRP-5*, which states that the engine shall be re-ignitable at least five times throughout H_2ERMES' flight, a choice of igniter which can be fired several times must be made. Several different concepts were considered, however only one option completely fulfilled all requirements. Firstly, High Voltage Electrical Spark Plugs were considered, however, these solution would only allow for a small amount of fuel and oxidizer to be ignited at a time, which would make it challenging for full ignition to occur, at the high mass flows in which the engine operates. Following this, a solution involving pyrotechnic detonation was considered. However, this solution also proves ineffective, as it is only able to light the engines once, and does not allow for easy relight capabilities, breaching *RQ-PRP-5*. Finally, the choice of a torch igniter, which injects propellants into a small pre-chamber where a spark igniter imparts the activation energy necessary to start the combustion process, as described by Tinker [41], would be the most effective solution, allowing for multiple re-lights of the engine at a high reliability.

Choice of Chamber Pressure

As per Humble [36], one of the first parameters to be chosen for a rocket engine design is the chamber pressure (P_c). Given the choice of an expander cycle, an engine with a similar cycle was chosen as an analogue for the chamber pressure necessary. The chosen analogue engine was the Vinci, developed by ArianeGroup, which has a chamber pressure of 6.1 [MPa] [4]. The choice of an expander bleed cycle will, moreover, allow for higher thrust levels compared to the Vinci engine, at the expense of lower engine efficiency, as found in an analysis by Sippel [42]. Figure 8.12 illustrates the general layout of the chosen engine cycle. In short, the expander bleed cycle harnesses the heat of the combustion chamber to increase the temperature of the LH_2 and expand it, driving the turbines for each propellant. The bleed cycle comes into effect after part of the propellant has been passed through the turbines, and is expelled overboard. Aside from the previously mentioned advantages, a bleed cycle also decreases the turbine inlet pressure compared to a traditional bleed cycle, as the propellant used to drive the turbines does not need to be fed back to the combustion chamber, reducing the stress experienced by the turbopumps, and consequently their weight. A single shaft pump is not possible due to the large differences in the densities of LH_2 and LOX. Additional information on the particular solution employed for the engine cycle, as well as how it integrates with the rest of the design can be found in Section 9.2.

O/F Optimization

Following the choice of chamber pressure, it was necessary to also choose a ratio of oxidizer to fuel mass flow ratio (O/F) which would minimize the total vehicle mass. The main criteria which governed this choice are engine performance and volume of propellants necessary. Conventionally, the chosen O/F ratio would be the value which resulted in the highest engine specific impulse (I_{sp}), however, LH_2 and LOX have drastically different densities, respectively 67.87 [kg/m^3] at a subcooled temperature of 22.8 [K] and pressure of 2 [bar] and 1305.8 [kg/m^3] at 54.5 [K] and 2.5 [bar], as found through coolprop [44]. As such the effect of increase in volume and structural mass of the tanks with an increase in the fraction of propellant of LH_2 must be accounted for.

An analysis using Chemical Equilibrium with Applications (CEA) [45], which was validated by NASA, has been performed to estimate the performance, more specifically the I_{sp}, of different O/F ratios for a given engine configuration. For this purpose, the RocketCEA [5] Python wrapper for the original NASA FORTRAN CEA code was used.

Solely for the analysis of the impact of different O/F ratios in the overall design, several assumptions were made. Firstly, the structural fraction σ_s, as defined by Equation 8.63, the relationship between the structural mass m_s and the propellant mass m_p was assumed to be constant value of 0.131 [$-$], the most recent estimate of the vehicle at this stage of the design. Moreover, it is assumed that the ΔV to be delivered by the main propulsion system is 6737 [m/s], that there is only one engine burn, and I_{sp} is constant throughout this burn. Additionally, a payload mass of 15 [t] is assumed, which results from the payload mass with margins calculated in the midterm report [2]. Finally, it is assumed that the Expansion Ratio for all thrust chambers is constant at 80 [$-$].

Since the structural ratio is constant, the O/F resulting in the lowest total mass will also result in the lowest propellant mass. As such, the comparison between different values of O/F is performed keeping that value in mind. To calculate the propellant mass, Equation 8.64 was used, which depends on the mass ratio μ, calculated in Equation 8.65. The I_{sp} used to calculate μ is obtained from the previous CEA analysis.

[4] URL http://www.astronautix.com/v/vinci.html [cited 2025-06-24]
[5] URL https://rocketcea.readthedocs.io/en/latest/index.html [cited 2025-06-24]

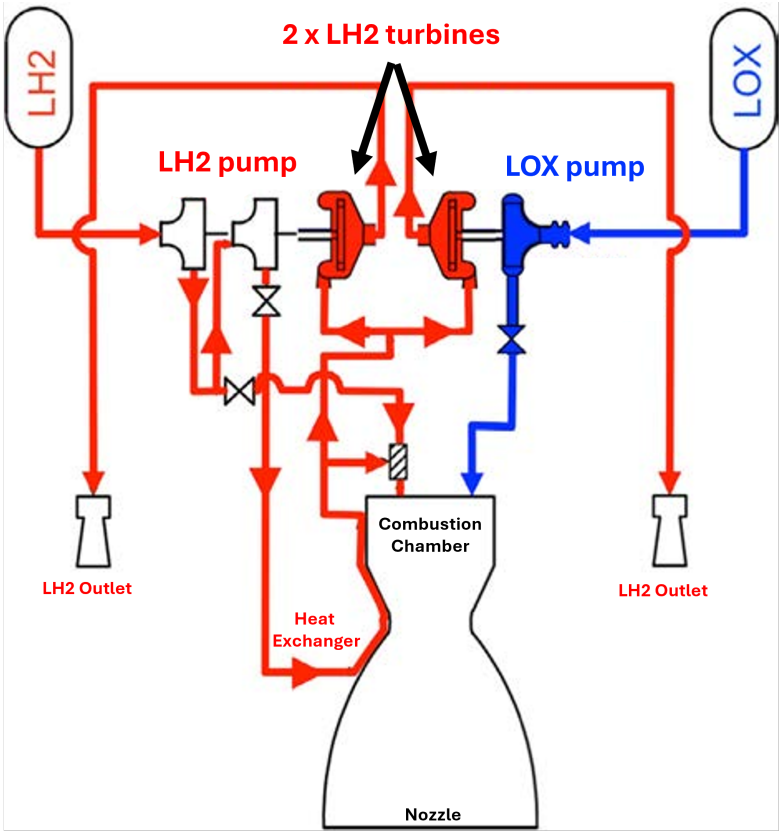

Figure 8.12: Expander Bleed Cycle modified illustration based on research by Paniagua [43]

$$\sigma_s = \frac{m_s}{m_s + m_p} \tag{8.63}$$

$$m_p = m_{PL}\frac{(\mu - 1)(1 - \sigma_s)}{1 - \mu\sigma_s} \tag{8.64}$$

$$\mu = e^{\frac{\Delta V}{g_0 I_{sp}}} \tag{8.65}$$

Figure 8.13 highlights the relation between the O/F ratio and the calculated propellant mass. It can be noted that the optimal O/F ratio, which led to the highest I_{sp}, is $5.06\,[-]$. However, this propellant mass results in a high total volume of propellants of $320\,[m^3]$. Since the structural ratio is assumed to be constant, the increase in the mass of the tanks from an increase in volume is not taken into account in the optimization, and as such, it was decided to use a higher O/F ratio than optimal. Taking into account the propellant masses for an O/F of $6\,[-]$ and $7\,[-]$, it can be seen that the increase in m_p compared to the optimal case is $1.52\,[\%]$ and $6.46\,[\%]$, with a resulting decrease in total volume of the propellants of $9.06\,[\%]$ and $13.2\,[\%]$, respectively. It can be seen, as such, that an O/F of $6\,[-]$ presents an appropriate balance between engine performance and propellant volume.

It should be noted that the values for propellant mass calculated throughout the analysis in this section are not representative of the actual propellant mass for the vehicle, as the relationship between m_p and m_s is not constant in reality, and the analysis regarding ΔV, the expansion ratio and I_{sp} is expanded on the remaining design steps.

General Engine Parameter Modeling (RPA)

One of the main design parameters which is left to determine is the ratio between the nozzle exit area (A_e) and the nozzle throat area (A_t), named the expansion ratio (ϵ). This ratio greatly influences the engine exit pressure (P_e), which in turn influences the thrust (F_t) produced for some given freestream pressure conditions (P_∞), as described by Equation 8.66, where $\dot{m}$ represents the engine mass flow and v_e represents its exhaust velocity. For a given A_t, in vacuum, a larger ϵ will result in a larger thrust for a given mass flow, as well as a larger I_{sp}, however, in sea level conditions, the exit pressure of vacuum optimized engines is lower than the freestream pressure, due to overexpansion, and as such its thrust is reduced greatly.

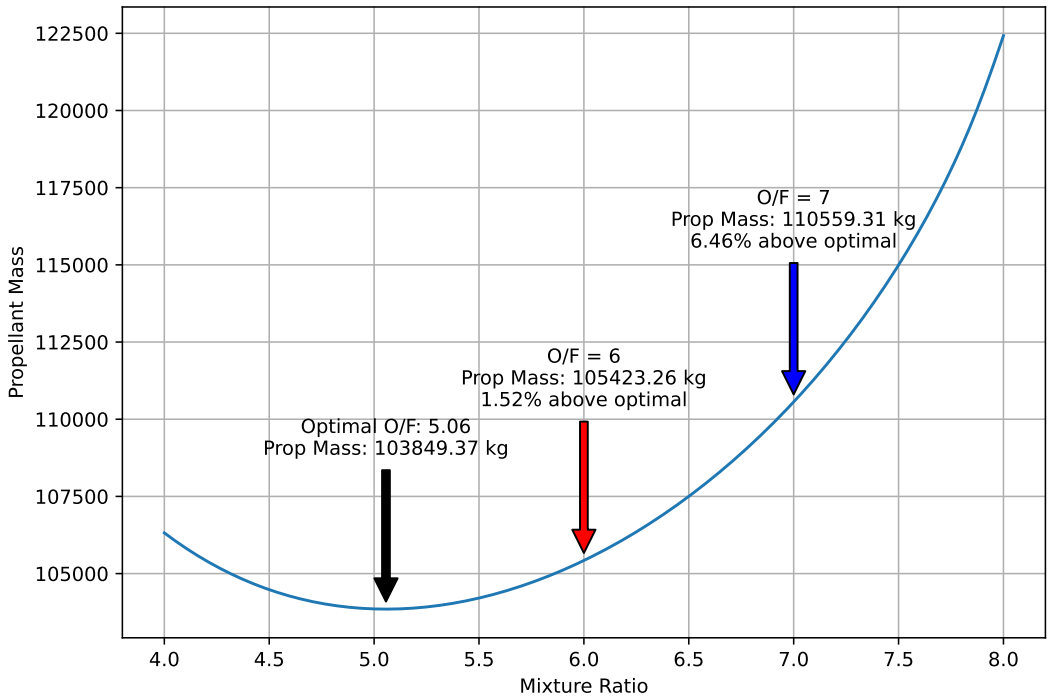

Figure 8.13: Relation between O/F ratio and the propellant mass

$$F_t = \dot{m} v_e + (P_e - P_\infty) A_e \qquad (8.66)$$

$$I_{sp} = \frac{F_t}{\dot{m} g_0} \qquad (8.67)$$

Accordingly, it was decided to have two kinds of thrust chambers for the engine, which would be either optimized for operation in vacuum or sea level. For the vacuum optimized chambers, the largest possible expansion ratio would be ideal, as the theoretical best ϵ at these conditions is infinite. Keeping this aspect in mind, and targeting an exit diameter D_e between 1 and 1.2 [m], to comply with spatial constraints, an ϵ of 80 $[-]$ was chosen for the vacuum optimized engines. On the other hand, for the sea level optimized engines, an expansion ratio of 8 $[-]$ was chosen to ensure sufficient engine performance on sea level.

To approximate the real performance of the engines, the common program Rocket Propulsion Analysis (RPA) was used. RPA was successfully verified by comparison with CEA, as well as by comparison with the performance data of selected historic engines, as per Ponomarenko [46]. For the analysis of each engine, additional parameters need to be calculated, as they are necessary inputs for engine design. Firstly, the throat area A_t is calculated according to Equation 8.68, using a value for the characteristic velocity c^* found by RPA for the current propellant combination of 2271.574 [m/s], a chosen mass flow ratio of 34.9 [kg/s] and the chosen p_c were also taken into account. Finally, a value for A_t of 0.013 [m^2] was found.

$$A_t = \frac{\dot{m} c^*}{p_c} \qquad (8.68)$$

$$L^* = \frac{V_c}{A_t} \qquad (8.69)$$

The final set of design parameters which are the inputs for the design are listed in Table 8.9.

Table 8.9: Design Inputs for RPA Engine Analysis

Input	Value [Units]	Additional Information
Chamber Pressure P_c	6.1 [MPa]	
O/F ratio	6 [−]	Chosen in Section 8.7.2
Fuel/Oxidizer Combination	LOX/LH_2	
Expansion Ratio ϵ	8/80	Depending on sea level or vacuum optimization
Engine Mass Flow Rate $\dot{m}$	34.9 [kg/s]	Dependent on Thrust
Chamber Characteristic Length L^*	1.02 [m]	As stated by Humble [36] for the current propellant combination. Defined in Equation 8.69, V_c assumes a purely cylindrical chamber.
Throat Area A_t	0.013 [m^2]	
Contraction Area Ratio A_c/A_t	3.48 [−]	Estimated using relations from Humble [36].

Following the analysis using RPA, the main performance figures are listed in Section 8.7.3.

Thrust Chamber Configuration Optimization

As discussed in Section 8.7.2, a combination of sea level and vacuum optimized thrust chambers is used. As was previously found in Section 8.3, the ΔV necessary for each engine burn is reduced the higher the thrust to weight ratio during that maneuver. As such, in order to find the distribution between both types of sea level and vacuum thrust chambers which results in the lowest total mass, an optimization was performed.

Firstly, it was assumed, as per *AS-PROP-08*, that at any time the mass flow of all of the thrust chambers was the same. Additionally, it was chosen to only fire the sea level thrust chambers during landing, as the sea level thrust and specific impulse of the vacuum optimized nozzles are substantially lower than optimal. Moreover, both the sea level and vacuum optimized thrust chambers are assumed to be fired throughout any burns occurring in vacuum. Given the previous assumptions, as well as the fact that for the design a total vacuum thrust F_{tot} will be set as per *RQ-PRP-4*, as well as the vacuum specific impulses for either the sea level $I_{sp_{sl_{non-opt}}}$ and vacuum $I_{sp_{vac_{opt}}}$ optimized thrust chambers found in Section 8.7.2, Equation 8.70 and Equation 8.71 can be used, respectively, to calculate the vacuum thrust for sea level $F_{sl_{non-opt}}$ and vacuum optimized $F_{vac_{opt}}$ thrust chambers. In the equation, N_{sl} and N_{vac} are respectively, the number of sea level and vacuum optimized thrust chambers.

$$F_{sl_{non-opt}} = \frac{F_{tot}}{N_{sl} + N_{vac}\frac{I_{sp_{vac_{opt}}}}{I_{sp_{sl_{non-opt}}}}} \tag{8.70}$$

$$F_{vac_{opt}} = \frac{F_{sl_{non-opt}} I_{sp_{vac_{opt}}}}{I_{sp_{sl_{non-opt}}}} \tag{8.71}$$

From the obtained values for thrust, the mass flow of propellant through each thrust chamber can be calculated using Equation 8.67.

Regarding the main optimization, the number of sea level and vacuum thrusters was kept even for symmetry along the roll axis. Following this consideration, the combined I_{sp} in vacuum for a situation where all thrusters were firing was calculated using Equation 8.72, with the previously found coefficients.

$$I_{sp_{tot}} = \frac{F_{sl_{non-opt}} N_{sl} + F_{vac_{opt}} N_{vac}}{(\dot{m}_{vac} N_{vac} + \dot{m}_{sl} N_{sl}) g_0} \tag{8.72}$$

The propellant masses for delivering the ΔV corresponding to the thrust to weight ratio of each of the combinations considered (the value corresponding to a certain N_{sl}) were calculated, in turn, using Equation 8.64. The results of the optimization are presented in Figure 8.14, which identifies that 8 sea level thrusters is the configuration which minimizes the propellant weight. The same assumptions applied in the optimization present in Section 8.7.2 apply here, where the structural ratio is assumed constant, and the displayed propellant masses are not indicative of the final values. The graph additionally lists the increased values of propellant mass, in blue, where it was assumed that vacuum Thrust chambers also fired in the landing maneuver, in sea level. It is clear the drastically lower I_{sp} of these thrust chambers invalidates their use in sea level pressures.

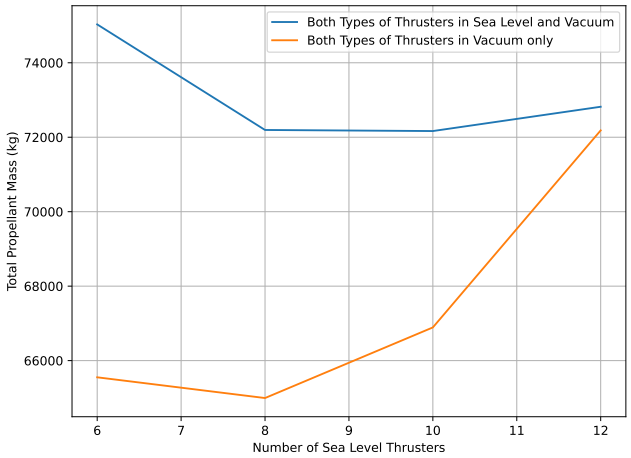

Figure 8.14: Relation between N_{sl} and propellant mass

Thrust Chamber Mass Sizing

In order to calculate the mass of each kind of thrust chamber, the output of the dimensions of the thrust chamber obtained in RPA was used, as well as relations by Humble [36], which assume a conical converging diverging nozzle and cylindrical thrust chamber, as exemplified in Figure 8.15, which also provides a visual for the output geometry variables from RPA. Furthermore, the material chosen for the thrust chamber was Inconel 718, with a density of 8220.931 [kg/m^3], and an ultimate tensile strength σ_{UTS} of 1.151 [GPa].

(a) Nozzle sizing parameters

(b) Combustion chamber sizing parameters

Figure 8.15: Mass relation for each of the components of the thrust chambers, by Humble [36]

In order to calculate the wall thickness t_w necessary for withstanding the chamber pressures, Equation 8.73 taking into account hoop stresses was used, where SF is a safety factor, decided to be four to account for stress concentrations and other stresses not modeled in hoop-stress analysis, and R_c is the inner radius of the combustion chamber.

$$t_w = \frac{P_c \cdot SF \cdot R_c}{\sigma_{UTS}} \tag{8.73}$$

After t_w is calculated, the mass of the simplified nozzle and combustion chamber can be found, respectively, through Equation 8.74 and Equation 8.75, with all of the remaining parameters taken from the performed analysis in RPA.

$$m_{cc} = \pi p_t t_w \left(2 r_{cc} L_{cc} + \frac{r_{cc}^2 - r_t^2}{\tan \theta_{cc}} \right) \tag{8.74}$$

$$m_{noz} = \pi p_t t_w L_n (r_e + r_t) \tag{8.75}$$

8.7.3. Final Propulsion Design Parameters

As a result of the previous design steps, Table 8.10 presents all of the intermediate and final results of the analysis which was performed.

Table 8.10: Final Propulsion Analysis Results

Output	Value [Units]	Additional Information
Chamber Pressure P_c	6.1 [MPa]	Design Choice from Section 8.7.2
O/F ratio	6 [−]	Chosen in Section 8.7.2
Nozzle Exit Diameter D_e	0.367/1.160 [m]	Sea Level/Vacuum Optimized, as calculated in Section 8.7.2
Nozzle Throat Diameter D_t	0.130 [m]	Same value for Sea Level/Vacuum Optimized, as calculated in Section 8.7.2
Expansion Ratio ϵ	8 [−]/80 [−]	As decided in Section 8.7.2
Exit Pressure P_e	0.111/0.005 [MPa]	Dependent on ϵ, respectively for ϵ = 8 and 80
Optimum Expansion Altitude H_{opt}	0/20.306 [km]	Dependent on ϵ, respectively for ϵ = 8 and 80
Sea Level Thrust F_t	123.774/44.817 [kN]	Sea Level/Vacuum Optimized, per chamber
Vacuum Thrust F_t	134.624/153.311 [kN]	Sea Level/Vacuum Optimized, per chamber
Sea Level Specific Impulse I_{sp}	361.645/130.946 [s]	Sea Level/Vacuum Optimized
Vacuum Specific Impulse I_{sp}	393.347/447.948 [s]	Sea Level/Vacuum Optimized
Characteristic Velocity c^*	2271.574 [m/s]	Section 8.7.2 for the propellant combination
Mass Flow Rate $\dot{m}$	34.9 [kg/s]	Same for all thrust chambers
Thrust Chamber Mass m_{eng}	9.666/66.040 [kg]	Sea Level/Vacuum Optimized
N_{sl}	8 [−]	
N_{vac}	16 [−]	
Turbopump mass	587.929 [kg]	
Channel area for propellant A_1	0.113 [m^2]	tanks to turboprop
Channel diameter for propellant D_1	0.379 [m]	tanks to turboprop
Channel area for oxidizer A_2	0.015 [m^2]	tanks to turboprop
Channel diameter for oxidizer D_2	0.137 [m]	tanks to turboprop
Channel area for propellant A_3	0.005 [m^2]	turboprop to thrusters
Channel diameter for propellant D_3	0.077 [m]	turboprop to thrusters
Channel diameter for oxidizer D_4	0.011 [m]	turboprop to thrusters

Figure 8.16 highlights the final hardware resulting from propulsion design, which are the profiles of the Sea Level and Vacuum optimized thrust chamber profiles, as well as the engine bay.

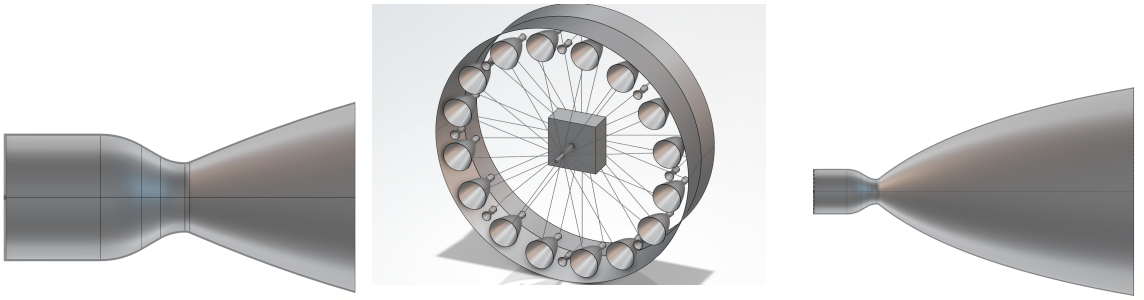

(a) Sea Level Optimized Thrust Chamber Profile

(b) Engine Bay, Including the turbopumps (represented as a parallelepiped)

(c) Vacuum Optimized Thrust Chamber Profile

Figure 8.16: Final products of propulsion design

8.7.4. Sensitivity Analysis

The Sensitivity Analysis for the propulsion system is done independently for the feed system and thrust chambers and nozzles. For the feed system, the following four variables have the largest impact on the turbopump design: pressure in the tanks, velocity of propellant and oxidizer and chamber pressure. For the thrust chamber design, the variables being altered are: area ratio, chamber pressure, O/F ratio and mass flow rate. The results of the sensitivity analysis are presented in Table 8.11.

Table 8.11: Sensitivity analysis of turbopump design

Parameters:	**Chamber pressure**	**Fluid velocity**	**Pressure in the tanks**
Change in value	-10 [bar]	$+20$ [m/s]	-1.7 [bar]
Change in turbopump mass	45.04 [kg]	Complex value	Complex value
Effect description	Reduces pump increase required from pump.	NPSH becomes negative	NPSH becomes negative
Impact:	4	1	1

Feed System

In this sensitivity analysis, the chamber pressure, fluid velocities and pressure in the tanks have been varied significantly. This is because it is key to highlight that the pressure in the tanks must have a minimum value or otherwise the fluids reach the pump inlet with too little pressure to avoid cavitation. The same phenomenon occurs when the LH_2 and LOX have a high velocity: there is a large increase in dynamic pressure and thus a large reduction in static pressure which yields a negative Net Positive Suction Head, making the design unfeasible. In order to account for this, both velocities have been set to 10 [m/s] and the channel areas for the feed lines have been designed accordingly.

To mitigate this potential risk, low-pressure turbopumps could be included upstream of the main turbopumps. These increase the pressure slightly before the flow reaches the high-pressure turbopumps, to avoid cavitation. However, these pumps add considerable additional mass and complexity. Additionally, a depressurization of the tanks could potentially lead to structural collapse of the tanks. This means that below a pressure threshold, the mission must be aborted.

Lastly, if the chamber pressure were to be reduced, this would significantly reduce the requirement imposed on the pump and thus the turbine could be smaller. However, a reduction in chamber pressure affects significantly propulsive performance and thus, will not be reduced.

Thrust Chamber Design

The main parameters affecting the fulfillment of the propulsion subsystem requirements listed in Chapter 4 are the Area Ratio ϵ, chamber pressure p_c, O/F ratio and mass flow rate. With the main parameter being affected by these changes being the thrust F_t, both in sea level and in vacuum, which affects the compliance with *RQ-PRP-4*, concerning the thrust to weight ratio. The current total thrust for the launch vehicle in vacuum, when all of the vacuum and sea level optimized thrust chambers are firing, is 3532 [kN], and for the launch vehicle in sea level, when only the sea level optimized thrust chambers are firing, it is 991 [kN].

Table 8.12: Sensitivity analysis of thrust chamber design

Parameters:	**Area Ratio** ϵ	**Chamber Pressure** P_c	**O/F Ratio**	**Mass Flow Rate** $\dot{m}$
Change in value	$+5$ [$-$]	$+0.5$ [MPa]	-1 [$-$]	$+10$ [kg/s]
Change in Sea Level Thrust F_t	-14.2 [kN]	$+6.98$ [kN]	$+17.2$ [kN]	$+285$ [kN]
Change in Vacuum Thrust F_t	$+44$ [kN]	$+1.59$ [kN]	$+32.8$ [kN]	$+1013.48$ [kN]
Effect description	Decrease in SL thrust, increase in VAC thrust	Slight increase in thrust in both cases	Sizable increase in thrust in both cases	Greatly increased thrust in both cases
Requirements affected	*RQ-PRP-4*	*RQ-PRP-4*	*RQ-PRP-4*	*RQ-PRP-4*
Impact:	4	4	4	5

Regarding the effects observed in Table 8.12, the increase in thrust in vacuum conditions and decrease in thrust in sea level conditions can be attributed to a decrease in the adverse phenomena of underexpansion in vacuum, and an increase in the adverse phenomena of overexpansion in sea level for both kinds of nozzle type. Moreover, an increase in chamber pressure results in an increase in the nozzle exit pressure for the propellants, decreasing the effect of pressure losses as shown in Equation 8.66. With regards to the O/F ratio, a decrease by 1 [$-$] would mean an increase in I_{sp}, since the engine would be operating closer to the optimal O/F ratio of 5.03 [$-$] identified in Section 8.7.2, and for the same mass flow, a higher specific impulse implies a higher thrust, as confirmed by the relation expressed in Equation 8.67. Finally, a substantial increase in thrust is experienced by the engine when the

mass flow rate is increased, as predicted, all other factors being equal, by the relation expressed by Equation 8.67.

8.8. Landing Legs

As a result of the trade-off, H_2ERMES's recovery method will be in the form of landing legs. For this, multiple options exist [47]:

1. Simple telescopic landing legs, similar to those found on Stoke Space's Nova upper stage, as seen in Figure 8.17a. These legs are telescopic in the sense that they only extrude axially, no rotational deployment is present.
2. Telescopic legs with a secondary Y-strut, similar to the landing legs on SpaceX's Falcon 9, shown in Figure 8.17b. These legs also feature a telescopic strut, but extension of this strut allows the secondary Y-shaped strut to be deployed from the sides of the vehicle.
3. Fold-out cruciform legs, as found on a concept for Blue Origin's New Shepard, illustrated in Figure 8.17c, which has a less intuitive deployment mechanism, but with the added benefit of being able to fully conceal the volume taken up by the legs into the shape of the vehicle, reducing the parasitic drag caused by them.

(a) Simple telescopic landing legs[6]

(b) Telescopic landing legs with secondary Y-strut[7]

(c) Fold-out cruciform landing legs[8]

Figure 8.17: Different styles of landing legs

Based on initial calculations of the dry mass, it was found that a secondary strut would not be necessary for H_2ERMES's landing, and for simplicity of the design, the fold-out cruciform configuration was also not considered, since adding more novel concepts into the design would increase the risk, and possibly development time and cost. Instead, simple telescopic landing legs will be present to support recovery of the vehicle. The selection of this style of legs also fits best with the conical vehicle shape, as the angled side profile allows the legs to be deployed at the same angle naturally, increasing the footprint radius of the vehicle, which in turn increases the stability for landing procedures.

These landing legs are made up of the following components:

1. The main strut, which extends from its undeployed position to take up the weight of the vehicle during landing.
2. The shock absorber, which ensures any velocity and acceleration during landing is dissipated to the supporting structure.
3. The deployment mechanism, which ensure the legs are able to move from the undeployed state to the deployed state.
4. The aero-cover, which both connects the landing legs to the rest of the vehicle, but also reduces the parasitic drag by having a more aerodynamically efficient shape, and thermally shields the legs during re-entry.
5. Smaller components, such as the locking mechanism, and integration hardware.

8.8.1. Design of the Main Strut

H_2ERMES is designed in a way where a nominal landing will take place at a velocity of 0 [m/s], i.e. the propulsion system will remove any velocity the vehicle has before landing, slightly hovering before touchdown. Because of this, the landing legs mainly need to be able to statically withstand the loads generated by the landing mass of the vehicle, for which the structural analysis procedure is explained in this section [48].

A free body diagram of a single leg during a nominal landing can be found in Figure 8.18.

From this, the axial force can be found using Equation 8.76a, and the transverse force using Equation 8.76b.

[6] URL https://www.spacex.com/vehicles/falcon-9/ [cited 2025-06-18]
[7] URL https://www.stokespace.com [cited 2025-06-18]
[8] URL https://www.blueorigin.com/new-shepard [cited 2025-06-18]

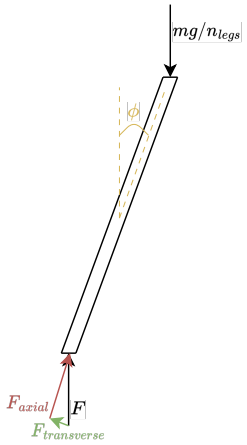

Figure 8.18: Free body diagram of a single landing leg during nominal landing conditions

$$F_{\text{axial}} = F\cos\phi = \frac{mg}{n_{\text{legs}}}\cos\phi \tag{8.76a}$$

$$F_{\text{transverse}} = F\sin\phi = \frac{mg}{n_{\text{legs}}}\sin\phi \tag{8.76b}$$

Here, F is the force [N], *m the dry mass of H2ERMES* [kg], *n_{legs} the number of landing legs* $[-]$, *and ϕ the angle between the landing legs and the vertical* [°].

The transverse force will be used to assess the maximum bending stress created in the leg using Equation 8.77a [49]. While the axial stress can be found using Equation 8.77b [49].

$$\sigma_{\text{bending}} = \frac{My}{I_{xx}} = \frac{F_{\text{transverse}}Lr}{I_{xx}} \tag{8.77a}$$

$$\sigma_{\text{axial}} = \frac{F}{A} \tag{8.77b}$$

Here, $\sigma_{bending}$ is the bending stress [Pa], *M the moment* [Nm], *equal to the force multiplied by the length L of the landing legs* [m], *y the distance from the neutral axis* [m], *in this case equal to the radius of the legs* [m] *as the worst case scenario, and I_{xx} the area moment of inertia of the legs' cross-section* [m^4]. *And σ_{axial} is the axial stress* [Pa], *and A is the legs' cross-sectional area* [m^2].

To ensure the legs are able to withstand the combined loading, the interaction equation Equation 8.78 can be used.

$$\text{IV} = \frac{\sigma_{\text{axial}} + \sigma_{\text{bending}}}{\sigma_{\text{yield}}} \tag{8.78}$$

Here, IV is the value of the interaction equation $[-]$, *which should be less than 1 after incorporating safety factors, which is discussed in Section 8.8.5.*

Besides yielding, another form of structural failure to consider is buckling of the legs. Depending on the geometry of a rod, specifically the slenderness ratio, two buckling modes exist: Euler buckling and Johnson buckling. The slenderness ratio λ of a rod can be found using Equation 8.79a, and the critical slenderness ratio λ_{cr} using Equation 8.79b.

$$\lambda = KL\sqrt{\frac{A}{I}} \tag{8.79a}$$

$$\lambda_{\text{cr}} = \sqrt{\frac{2\pi^2 E}{\sigma_{\text{yield}}}} \tag{8.79b}$$

Here, KL is the effective length of the column [m], *with K set to* 1 $[-]$ *as a conservative approach, as this results in a lower σ_{cr} for both Euler and Johnson buckling. Note that this corresponds to a pinned-pinned connection.*

For slenderness ratios below the critical slenderness ratio, Johnson buckling is leading, while Euler buckling is leading for larger slenderness ratios. The Johnson critical buckling stress is found using Equation 8.80a, while the Euler critical buckling stress is found using Equation 8.80b [49, 50], both not yet including safety factors, which are incorporated later.

$$\sigma_{\text{cr}} = \sigma_{\text{yield}} - \frac{1}{E}\left(\frac{\sigma_{\text{yield}}}{2\pi}\right)^2 \lambda^2 \tag{8.80a}$$

$$\sigma_{\text{cr}} = \frac{\pi^2 E}{\lambda^2} \tag{8.80b}$$

Here, σ_{cr} is the critical buckling stress [Pa], *E the material Young's modulus* [Pa], *and λ the slenderness ratio* [−].

Figure 8.19 shows the Johnson and Euler buckling stresses as a function of slenderness ratio of a rod.

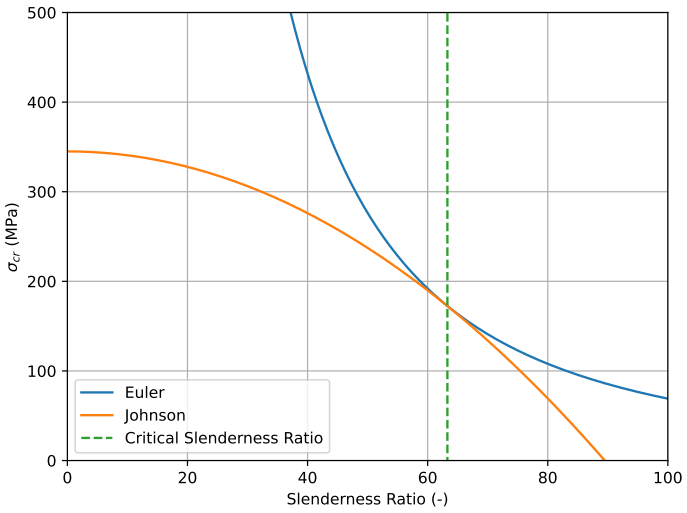

Figure 8.19: Johnson-Euler buckling parabola

Note that the exact values of these graphs depend on the specific material used, however the general shape stays the same. As a result, Figure 8.19 serves as a qualitative illustration of the buckling regimes, rather than an accurate representation of values for which regions a certain type of buckling dominates.

Then from this, it can be assessed which buckling mode is representative for a given rod geometry, and a critical buckling stress can be determined. Next, the alternative interaction equation in Equation 8.81 can be used.

$$\text{IV} = \frac{\sigma_{\text{axial}}}{\sigma_{\text{cr}}} + \frac{\sigma_{\text{bending}}}{\sigma_{\text{yield}}} \tag{8.81}$$

The two interaction equations can be used to determine whether a landing leg will fail under nominal landing conditions, either from general yielding or by buckling.

Besides a nominal landing, it is very likely the vehicle will not be perfectly aligned with the horizontal during landing. As a result, the landing legs need to be able to take up the entire weight of the vehicle, equal to four times the nominal load. For this, again buckling and axial yielding are considered, but with an axial load equal to the full weight of the vehicle, four times the nominal loading.

8.8.2. Design of the Shock Absorber

To take into account uncertainties, it is important to also size for another non-nominal landing, e.g. one where the velocity is nonzero. For this, one can use a shock absorber.

The energy required to be dissipated from such a non-nominal landing can be found using Equation 8.82.

$$E = \frac{1}{2} m V^2 \tag{8.82}$$

Here, E is the total energy to be absorbed [W], *m is the mass per leg* [kg], *equal to the total mass divided by the number of legs, and V is the vehicle velocity* [m/s].

From this, the required stroke length s can be found by rewriting Equation 8.83.

$$E = \int F ds \tag{8.83}$$

The force generated to dissipate this energy F, assumed to be an average, can be modeled using Equation 8.84.

$$F = a_{\text{max}} mg \tag{8.84}$$

Here, F is the average force generated by the shock absorber to dissipate the energy [N], *a_{max} the maximum acceleration for this force* [g], *and g the gravitational acceleration* [m/s^2].

With this, the stroke length and the overall dimensions of the shock absorber can be determined.

8.8.3. Design of the Deployment Mechanism

Next, it is important to consider the deployment mechanism of the legs. This will again be done by a pneumatic system, using the Helium already on-board for pressurization of tanks. Unlike on telescopic legs with a secondary Y-strut, an initial deployment mechanism is not needed, since the deployment does not require a rotation around a hinge in the case of H_2ERMES, simplifying the design. To model the deployment, the actuator is modeled as an internal chamber with a small piston. Since only a single strut is used for the legs, the stroke length of the deployment mechanism is equal to the length of this strut. From this, the dimensions of the deployment piston can be found.

8.8.4. Design of the Aero-Cover

The legs and their mechanisms need to be shielded from aerodynamic loads during launch and re-entry phases of the mission, and need to be attached to the rest of the vehicle. For this, the aero-cover is used, designed as a first order estimate to obtain the total mass of the recovery subsystem. The cover is modeled as a cross-section of half of an ellipse, with the radii scaled from the radius of the main strut. The length of the cover is assumed to be 1.1 times the length of the main strut and the stroke length of the shock absorber combined. The design of the cover is subject to refinement during aerodynamic optimization, to also consider the parasitic drag generated by the attachment of the legs to the outer structure, and assessment of the thermal loads generated on the side profile of the vehicle during re-entry.

8.8.5. Final Design

For the sizing, safety factors in accordance with NASA STD-5001b [51] and ESA ECSS E-ST-32-10C [52] are incorporated for the loads and sizing equations, taking the maximum of the two in case of a discrepancy. For the interaction equations, safety factors are also incorporated, generally by use of Equation 8.85 [53].

$$\text{IV} = \sum_i (SF \cdot R_i) \leq 1 \tag{8.85}$$

Here, R_i are the stress ratios used in the interaction equations [$-$], *and SF is the safety factor* [$-$].

For stability during landing, a choice has been made to use four legs. While the minimum number of legs required for stability is three, it was assessed that due to the sheer size of the vehicle, and with that a high location for the center of gravity, adding this additional leg would largely increase the maximum angle the vehicle could land at without toppling over, while having a negligible effect on the total dry mass.

The material chosen for the legs is the titanium alloy Ti6AlV4, due to its efficient structural properties at sea level temperatures, but also at higher temperatures, which the landing legs will experience due to them being situated relatively closely to the engines.

With the design procedure outlined in Section 8.8.1 through Section 8.8.4, a tool was developed to perform the structural analysis of multiple configurations, consisting of a length L, radius r and thickness t of the main strut, after which the lowest mass configuration is given as the output. This tool was integrated into the integration to automatically update the dry mass based on the current iteration.

8.8.6. Sensitivity Analysis

The sensitivity analysis of the landing leg design is performed in the method described in Section 8.2. The results can be found in Table 8.13, in which the landing dry mass, number of legs, and landing leg material are analyzed.

As seen from Table 8.13, a change in material would highly increase the total subsystem mass, and thus the material selected for the legs will stay Ti6Al4V, mitigating the results of these changes. As discussed in Section 8.8.5, removing one leg would decrease the mass, even though the individual legs would increase in size, but as the recovery subsystem mass was found to be only around 5 to 10 [%] of the total dry mass, a decrease here of 16.63 [%]

Table 8.13: Sensitivity analysis of the landing legs

Parameters:	**Dry Mass**	**Number of Legs**	**Material**	
Change in value	$\times 1.25$ [$-$]	Change to 3 [$-$]	Change to SS304L	Change to AL2024T3
Relative change in subsystem mass	$+22.5$ [%]	-16.63 [%]	$+573.91$ [%]	$+48.98$ [%]
Effect description	Increasing the dry mass also increases the mass of the landing legs to a similar degree	While decreasing the number of legs does reduce the total subsystem mass, it would be a less stable configuration.	While using the same material as for the tanks would be good for compatibility, the mass goes from under 10 [%] to over 30 [%] of the total dry mass, resulting in a non-viable solution.	Use of the widely used cheaper aluminum alloy results in a subsystem mass 1.5 times as high, showing that the use of the titanium alloy is a better choice.
Requirements affected	None	None	None	None
Impact:	3	3	1	2

is quite negligible, while the maximum landing angle is affected quite significantly. Also note that wile no requirements are directly affected, a high increase in the subsystem mass, like when changing the material, would result in the dry mass of the landing legs taking near 25 [%] of the total dry mass, requiring massive redesign for the required propellant, giving a non-viable solution.

Besides the parameters used as inputs for the sizing tool, the main driving factor of the design is the vehicle shape, mainly the angle ϕ and the required clearance height, defined as the distance between the lowest point of the landing legs in stowed position and the lowest point of the vehicle. Generally, it was seen during testing of the tool that the leg length was found to be minimum, while still having the required clearance. Besides this, it was observed that even for smaller angles of ϕ, the bending stress σ_{bending} was often larger than the axial stress σ_{axial} due to the larger clearance height required. However, it was also seen that the total mass of the recovery subsystem did not change too much for large variations in ϕ.

8.9. Nosecone

This section covers the design of the nosecone of H_2ERMES. The main job of the nose cone is to provide adequate protection against the aerodynamic loads and thermal loads experienced during ascent as per *RQ-NSC-1* and *RQ-NSC-2*. To simplify this analysis, the shape of the nosecone was decided to be a thin wall spherical end cap with insulation lining the inside of the nosecone. Furthermore, this section will be split into two subsections that deal with design considerations for heat experienced in Section 8.9.1 and then the aerodynamic loading due to the dynamic pressure in Section 8.9.2. Finally a sensitivity analysis will be performed in Section 8.9.3.

8.9.1. Insulation for Nosecone

The nosecone experiences heating due to the formation of a shockwave at the front of the nose which produces peak heating at the stagnation point. This heat will propagate through the nosecone and, if not kept in check, can heat up all the subsystems kept there through radiation from the surface of the inner wall. This includes all onboard avionic components, the ADCS tank and thrusters, and fuel cells. Thus, the purpose of this section is to determine the thickness of this insulation needed to ensure that the internal temperature will be a maximum of 350 [K]. The type of insulation chosen for this project is based on a high temperature Multi Layer Insulation (MLI) blanket from BeyondGravity specifically made for payload fairings [54]. The insulation properties chosen for this report is given in Table 8.14.

Table 8.14: MLI Insulation properties

Property	**Value**	**Unit**
Thermal Conductivity	4×10^{-4}	[W/mK]
Density	1072.5	[kg/m^3]

To calculate the temperature at the inside of the nosecone, first the heat flux at the stagnation point will be calculated for a blunt nosed body. Then, the outer wall temperature can be calculated from the oncoming heat flux by assuming it to be equal to the radiative equilibrium temperature. This assumption is valid since it assumes that

the external atmosphere does not help with taking the heat away through convection and that the entire heat flux will have to be absorbed by the outer wall. Finally, a simple first order heat conduction equation based model can be built to calculate how the temperature of the inside wall will change with respect to the outer wall temperature.

Firstly, a simplified equation to predict heat flux at the stagnation point of a blunted body is given by Chapman in Equation 8.86.

$$q_{flux} = 1.63 \cdot 10^{-4} \left(\frac{\rho}{R_n} \right)^{0.5} V^3 \tag{8.86}$$

Where q_{flux} [W/m^2] is the heat flux at the stagnation point, ρ [kg/m^3] is the air density, R_n [m] is the nose radius, and V [m/s] is the velocity of the launcher.

The air density experienced by H_2ERMES is a function of the altitude which can be determined by integrating the vertical velocity profile of a launcher. Both these velocity profiles were taken from the Vega Launcher given in since at this stage, these numbers are not available for H_2ERMES. Next, the outer wall temperature can be calculated by using Equation 8.87.

$$T_{surface} = \sqrt[4]{\frac{q_{flux}}{\epsilon \sigma}} \tag{8.87}$$

Where $T_{surface}$ is the temperature of the outer wall surface, ϵ is the emissivity of the nosecone, and σ is the Stefan Boltzmann constant.

Next, a 1D heat conduction equation is used to estimate the propagation of the temperature through the wall of the nosecone. This is a similar mode as shown in Figure 8.20. The exact numerical method equation however, is different. The specific method used in this case is given in Equation 8.88a.

$$T_j^{i+1} = T_j^i + Fo(T_{j-1}^i - 2T_j^i + T_{j+1}^i) \tag{8.88a}$$

$$Fo = \frac{\alpha \Delta t}{\Delta x^2} \tag{8.88b}$$

Where T_j^i [K]is the temperature of the node at location j at time i, and Fo is the Fourier constant calculated in Equation 8.88b where Δt [s] is the time step of the method, Δx [m] is the distance between the nodes, and α [m^2/s] is the thermal diffusivity of the material.

The thermal diffusivity of the material is calculated through Equation 8.89a and Equation 8.89b.

$$\alpha = \frac{k_{eff}}{\rho C_p} \tag{8.89a}$$

$$k_{eff} = \frac{t_{steel} + t_{insulation}}{\frac{t_{steel}}{k_{steel}} + \frac{t_{insulation}}{k_{insulation}}} \tag{8.89b}$$

Where k_{eff} [W/mK] is the thermal conductivity of the interface, C_p [J/kgK] is the specific heat capacity, and ρ [kg/m^3] which is the density of the material. k_{eff} is calculated in Equation 8.89b [55] where t_{steel} and $t_{insulation}$ [m] is the thickness of the nosecone and the insulation respectively, and k_{steel} [W/mK] and $k_{insulation}$ [W/mK] is the thermal conductivity of steel and insulation respectively.

As per the Von Neumann stability analysis, Fo must be less than 0.5 $[-]$ for the method to be numerically stable. It is important to note that the density of the insulation will be negligible compared to the density of the stainless steel. Moreover, it is a conservative assumption that the C_p of the insulation does not affect the C_p in Equation 8.88b since a high C_p negatively impacts the heat propagation. Thus, it will be assumed that the rho and C_p in Equation 8.88b is the same as the material for the nosecone and the only impact having insulation will have is on k_{eff}.

The minimum thickness of the insulation will be found iteratively by varying the value which will directly change k_{eff} in Equation 8.89b.

8.9.2. Aerodynamic Loads

During ascent, the nosecone of a launch vehicle experiences an external dynamic pressure which the nosecone will have to be able to withstand. For the purpose of this report, only buckling due to external pressure will be considered for this analysis. The dynamic pressure experienced by the nosecone can be determined from the launch profile of the Vega launcher as was done in Section 8.9.1. The theoretical maximum critical pressure for a thin-walled hemisphere cap is given by Zoelly [56] in Equation 8.90.

$$p_{critical} = \frac{2E}{\sqrt{3(1-v^2)}}(\frac{t}{R})^2 \tag{8.90}$$

Where $p_{critical}$ [Pa] is the maximum external pressure, E [Pa] is the Young's modulus, v [$-$] is the Poisson ratio of the material, t [m] is the thickness of the cap, and R is the radius of spherical arc.

However, the maximum buckling load is greatly dependent on manufacturing imperfections and thus Equation 8.90 greatly overpredicts the maximum buckling load as it is derived for a perfect hemisphere. Thus, a knockdown factor proposed by Evkin can be used to calculate this value [57]. This is given in Equation 8.91a.

$$\bar{q}_{EBC} = \frac{0.693}{(1-v)^{0.2}\lambda^{0.4}} \tag{8.91a}$$

$$\lambda = (12(1-v^2))^{0.25}(\frac{R}{t})^{0.5}2\sin(\frac{\phi}{2}) \tag{8.91b}$$

Where λ [$-$] is a geometric factor of the hemispherical cap, ϕ [rad] is the induced angle of the cap.

To find the optimum thickness for the nosecone, a python script was written which increases the thickness of the tank until the critical pressure force is higher than the dynamic pressure experienced by the nosecone.

8.9.3. Sensitivity Analysis

A sensitivity analysis is done on the nosecone sizing to evaluate its sensitivity of several variables. This is shown in Table 8.15.

Table 8.15: Sensitivity analysis for the nosecone

Parameters:	$k_{insulation}$	**Radius**	**Velocity of launch vehicle**	**Material**
Change in value	$\times 4$ [$-$]	$\times 1.25$ [$-$]	$\times 1.25$ [$-$]	Change to AL7075-T6 (properties were taken from [58])
Relative change in subsystem mass	$+69.48$ [%]	$+50$ [%]	$+16.94$ [%]	-43.26 [%]
Effect description	An increase in the thermal conductivity of the insulation increases mass of the nosecone.	Increases the area where the stagnation heat flux acts which increases the mass of insulation. More material is needed for the sphere cap.	An increase in the velocity of the launch vehicle causes an increase since the stagnation heat flux and dynamic pressure experienced by the launch rocket increase, thereby increasing mass.	Using Aluminum will decrease the mass by roughly half.
Requirements affected	None	None	None	None
Impact:	2	2	2	4

The sensitivity analysis in Table 8.15 shows how choosing a worse insulating material than the MLI chosen can cause a dramatic increase in the mass of the nosecone. If a worse insulation material is indeed chosen, a possible mitigation strategy is to apply insulation on the components inside the nosecone that need to be kept at certain temperatures, for example the ADCS propellant tank with a max temperature of 373 [K]. Furthermore, increasing the radius of the tank also causes a dramatic increase in the mass of the subsystem. This is because the heat entering the tank has a bigger surface to enter through. If the increase in the nosecone mass is too high, the same mitigation strategy of applying insulation on specific components can be used here as well. This would increase the mass of those subsystems but it would still be lighter than applying insulation on the inside of the tank.

Increasing the velocity of the launch vehicle also has similar but less drastic effects. It should be noted that since the launch vehicle velocity for this analysis was chosen from the Vega launcher which is a smaller rocket, this parameter can be changed which is why the effect of this was studied in this sensitivity analysis. Clearly, increasing it by 25 [%] only increases the mass by roughly 17 [%].

Furthermore, changing the material for a lighter one can cause a dramatic decrease in weight savings. However choosing a different material than the tank can cause unforeseen residual stress environments which can weaken the structure over time leading to failure. However, for future studies, it is recommended that lighter materials

like aluminum 7075-T6 be investigated further albeit with giving proper consideration to how this structure will be joined to the rest of the launch vehicle.

8.10. Active Metallic Heat Shield

This section describes the re-entry protection system employed by the H_2ERMES vehicle. Based on *Stakeholder Requirements* and *Project Objective Statement*, it was decided to use an actively cooled metallic heat shield [2]. Given the rarity of this solution in historical missions, this design presents a unique challenge. No simple analytical methods were found in literature. Instead, research suggested that the best design approach should involve Computational Fluid Dynamics (CFD) or Finite Element Methods (FEM) [59].

However, given the resources available for the H_2GO project, it was not possible to utilize such tools. Instead, a set of relatively simple analytical tools was gradually built up to combine into a comprehensive first-order analysis program that uses similar methodologies used for regenerative cooling analysis inside rocket engine thrust chambers. These tools will be chronologically presented in this section, as well as an overview of the final design program. A sensitivity analysis will also be included.

8.10.1. Heat Transfer

Upon re-entry, the H_2ERMES vehicle will enter Earth's atmosphere and use it to shed its orbital velocity. During this process, large amounts of heat will be generated and an incident heat flux q_i will act on the bottom of the vehicle, where the heat shield is located. Since the vehicle will re-enter bottom first, it is the heat shield that needs to sustain the highest heat flux. To prevent it from melting, it will be cooled with the hydrogen onboard. The first analysis performed aimed to approximate the amount of this coolant needed. An energy balance method was devised and it was found that approximately 9 [%] of the vehicle dry mass would be needed as coolant mass [2].

Knowing that the solution could be feasible (since there is enough ΔV budget to carry this coolant mass), the mechanism of this heat transfer needed to be studied next. There were no readily available programs for this application, so a simple 1-D heat transfer model was created. This model was built using the following assumptions:

- *AS-COOL-01* The heat shield incident heat flux q_i is uniformly distributed across the heat shield surface A_s and is equal to the stagnation point heat flux. This heat flux is defined as a function of time. This assumption is conservative [59].
- *AS-COOL-02* The coolant acts as a bulk fluid, which means the flow properties are averaged across the coolant channel cross-section A_{cs}.
- *AS-COOL-03* The coolant heat flux is determined using the Taylor empirical relationship which is derived for a similar flow regime and has shown an accuracy within 10 [%] [60].
- *AS-COOL-04* The 1-D heat transfer model is sufficiently representative to analyze the heat transfer [61]. The model should be validated.
- *AS-COOL-05* The heat shield material is a stainless steel alloy with a high maximum operating temperature and cryogenic compatibility. Stainless steel was also chosen as the primary structural material for the vehicle [2].

These assumptions are sufficient to develop the first iteration of the heat transfer model. Further assumptions will be introduced in the following subsections.

1-D Heat Transfer Model

The devised 1-D heat transfer model is illustrated in Figure 8.20.

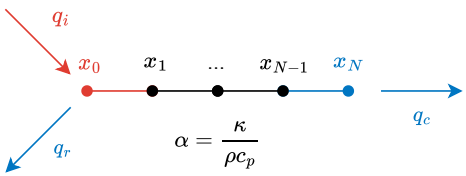

Figure 8.20: 1-D Heat Transfer Node Diagram

The first node x_0 transfers heat in three ways: it experiences some incident heat flux q_i, it radiates heat out through some radiative heat flux q_r and conducts heat into the heat shield wall. The incident heat flux was provided as a function of time by the operations department. The radiative heat flux is given by the Stefan-Boltzmann formula in Equation 8.92. The nodes between the first and last nodes $x_1, ..., x_{N-1}$ conduct heat according to the standard heat equation given in Equation 8.93. The equation will be solved numerically via the forward time-centered scheme (FTCS). All nodes have constant material properties derived from the Granta material database available to TU Delft[9].

The last node x_N is similar to the first node. It receives heat via conduction and transfers heat to the coolant via the coolant heat flux q_c. This flux is dominated by convective heat transfer (Equation 8.94) which is governed by the convective heat transfer coefficient h_c (Equation 8.95).

$$q_r = \epsilon \sigma T^4 \tag{8.92}$$

$$\frac{\partial T}{\partial t} = \alpha \frac{\partial^2 T}{\partial x^2} \tag{8.93}$$

$$q_c = h_c(T_N - T_b) \tag{8.94}$$

$$h_c = \frac{\mathrm{Nu}_b \kappa}{L} \tag{8.95}$$

Here ϵ $[-]$ *is the material emissivity,* σ $[\mathrm{W/m^2/K^4}]$ *is the Stefan-Boltzmann constant,* α $[\mathrm{m^2/s}]$ *is the thermal diffusivity of the material, i.e. the thermal conductivity divided by density and specific heat capacity at constant pressure* $\alpha = \frac{\kappa}{\rho c_p}$, T_N $[\mathrm{K}]$ *is the temperature at the last node* x_N, T_b $[\mathrm{K}]$ *is the bulk coolant temperature,* κ $[\mathrm{W/m/K}]$ *is the thermal conductivity of the wall material,* L $[\mathrm{m}]$ *is the length of the coolant channel and* Nu_b $[-]$ *is the bulk Nusselt number of the coolant.*

The Nusselt number is a dimensionless number that relates the convective heat transfer to the conductive heat transfer across a boundary. It is derived empirically. Most relationships were derived during the Apollo and NERVA programs [4], or lated during the Space Shuttle program [60]. The most applicable relationship is the Taylor relation [60] given in Equation 8.96.

$$\mathrm{Nu}_b = \frac{\text{Total heat transfer}}{\text{Conductive heat transfer}} = 0.023\,\mathrm{Re}_b^{0.8}\mathrm{Pr}_b^{0.4}(T_{ca}/T_b)^{-\left(0.57-\frac{1.59}{z/D_H}\right)} \tag{8.96}$$

Where Nu_b $[-]$ *is the bulk Nusselt number of the coolant,* Re_b $[-]$ *is the coolant bulk Reynolds number,* Pr_b $[-]$ *is the coolant bulk Prandtl number,* T_{ca} $[\mathrm{K}]$ *is the coolant channel contact area temperature,* T_b $[\mathrm{K}]$ *is the coolant bulk temperature,* z $[\mathrm{m}]$ *is the length along the channel w here the Nusselt number is being evaluated and* D_H $[\mathrm{m}]$ *is the coolant channel hydraulic diameter. Generally, the b subscript indicates bulk properties.*

This empirical model is based on the standard Dittus-Boelter equation [60, 62], but adds a temperature and a channel length correction. Essentially, Reynolds and Prandtl numbers account for the flow regime, the temperature ratio accounts for the temperature gradient across the coolant channel contact area A_{ca} and the z/D parameter accounts for the fact that the hydrogen flow develops further along the length of the coolant channel [60].

Now that the heat transfer mechanisms of the 1-D heat transfer model are established, the coolant properties will be investigated next.

Coolant Properties

Liquid hydrogen has excellent thermodynamic properties for regenerative cooling [60, 62]. For example, its specific heat at constant pressure c_p is on average three times higher than the specific heat of water. Crucially, when hydrogen becomes supercritical (the critical point is around 33.2 [K] and 13.3 [bar] [44]), its dynamic viscosity μ drops and the specific heat c_p peaks. Examining Equation 8.96, it is apparent that the decrease in μ causes a stronger cooling as the Reynolds number $\mathrm{Re} = \frac{\rho V_c L}{\mu}$ increases. Some relevant properties are plotted in Figure 8.23.

The coolant is indirectly part of the 1-D heat transfer model. It interacts with the last node x_N by receiving the same coolant heat flux q_c. Then, this energy is assumed to be stored as an increase in its enthalpy H_c (the sum of the internal energy and the pressure-volume product). In practice, the coolant will not gain pressure but rather lose pressure mostly due to friction losses [62]. Before these losses can be estimated, the cross-section of the coolant channel must be established.

[9] URL https://www.ansys.com/products/materials [cited 2025-06-17]

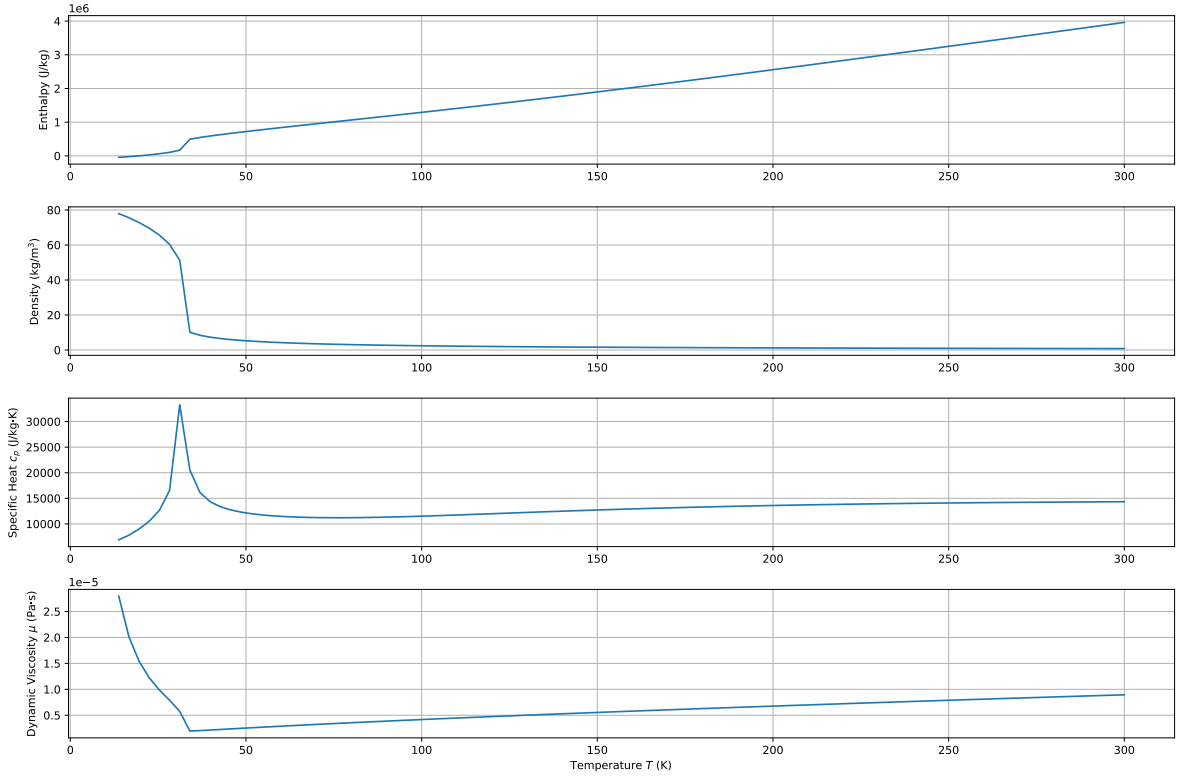

Figure 8.21: Hydrogen fluid properties as a function of temperature at 10 bar [44]

Coolant Channel Shape

The shape of the coolant channels is yet another design choice/degree of freedom that would ideally be analyzed using more advanced tools like CFD. However, in this phase of the H_2GO project, a qualitative assessment is more suitable. Given the expected size of the heat shield with a diameter of 10 [m], manufacturability and mass are the main concerns when choosing the shape of the channel. Therefore, a rectangular flat coolant channel shape was chosen and is illustrated in Figure 8.22.

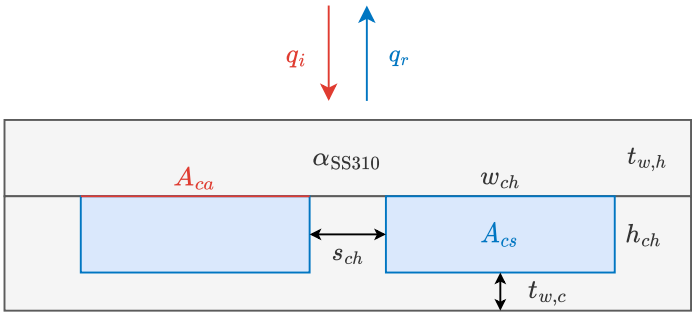

Figure 8.22: Heat Shield Cooling Channels Cross Section

This shape minimizes the thicknesses of the hot wall $t_{w,h}$ and the cold wall $t_{w,c}$ while still providing enough cross-sectional area A_{cs}. A_{cs} is defined by a channel height h_{ch} and a channel width w_{ch}. This shape also provides a significant contact area A_{ca} for the coolant and hot wall. Individual channels are spaced by a distance of s_{ch}. The three-dimensional layout is not required for this analysis, but will be mentioned later in the section.

Pressure Drop

Knowing A_{cs}, the coolant pressure drop can be evaluated. This is conventionally evaluated using the Darcy-Weisbach equation [63] given in Equation 8.97.

$$\frac{\Delta p}{L} = f_D \frac{\rho_b}{2} \frac{v_b^2}{D_H} \tag{8.97}$$

where Δp [Pa] *is the pressure drop,* L [m] *is the length of the given channel section,* f_D $[-]$ *is the Darcy friction factor,* ρ_b [kg/m^3] *is bulk coolant density,* v_b [m/s] *is bulk coolant speed and* D_H [m] *is the hydraulic diameter.*

The hydraulic diameter is defined as $D_H = \frac{4A}{\chi}$ [63], where A is the cross-sectional area of the coolant channel and χ is the wetted perimeter of the coolant cross-section. For a rectangular cooling channel, this corresponds to $D_H = \frac{4w_{ch}h_{ch}}{2w_{ch}+2h_{ch}}$.

The bulk coolant speed will be derived from the cross-sectional area A_{cs} and the necessary coolant mass flow. Lastly, the friction factor f_D depends on the flow regime. If the flow is laminar, $f_D = \frac{64}{\text{Re}}$. However, it is expected that the flow will be mostly turbulent (Re > 3000, so the Gnielinski correlation will be used: $f_D = (1.82 \log \text{Re} - 1.64)^{-2}$ [64].

Note that these relationships are conventionally used for incompressible fluids. However, the Gnielinski relation promises to give a good approximation [64]. Nevertheless, this is tracked as an assumption:

AS-COOL-06: The pressure drop inside the coolant channels can be estimated with the Darcy-Weisbach equation [63].

Combining the above with fluid properties [44], first results for the coolant can be observed in Figure 8.23 for initial coolant conditions of 20 [K] and 50 [bar], the coolant geometry of $w_{ch} = 10$ [mm], $h_{ch} = 2$ [mm] and the coolant mass flow of $\dot{m}_c = 2$ [g/s] in the channel.

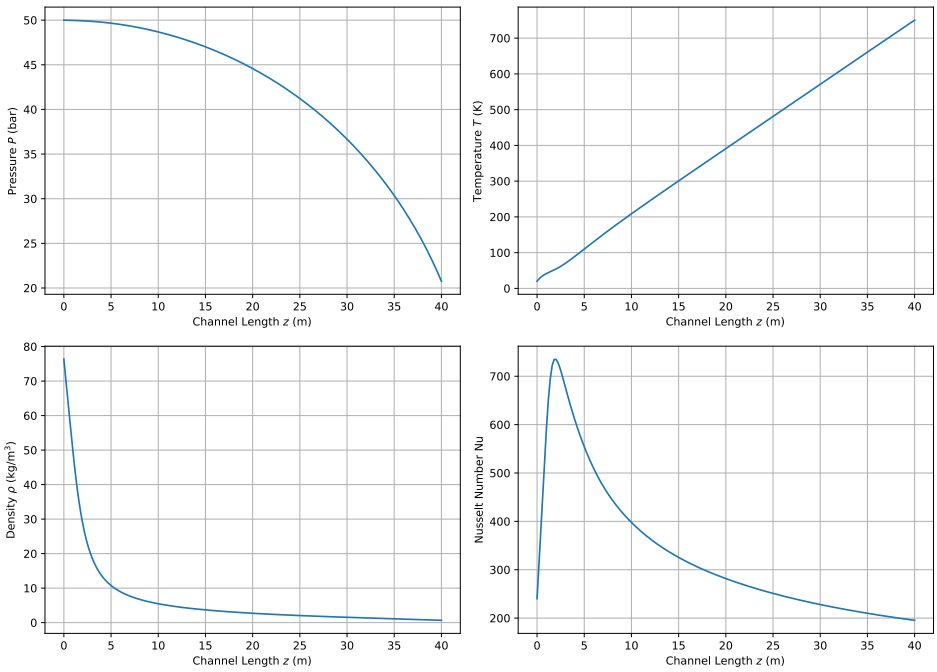

Figure 8.23: Change in fluid properties along the length of the coolant channel

It can be seen that for these initial conditions, the coolant channel should not be longer than 50 [m] as it would become too hot and lose too much pressure towards the end. This channel length limit is critical for the heat shield sizing in the next subsections.

First Results

Bringing all of the above together, the first initial 1-D heat transfer simulation is performed. First, the initial conditions are defined: coolant inlet properties (pressure and temperature); coolant channel geometry; coolant mass flow; initial temperature of the nodes (assumed 20 [K]); and the nodes are initialized with a uniform spacing Δx across an assumed wall thickness of 4 [mm]. Next, a constant heat flux of 200 [kW/m^2] is applied for 15 [min] to study the steady state.

To maintain numerical stability, a maximum time step must satisfy the numerical condition $\Delta t_{max} < \frac{(\Delta x)^2}{2\alpha}$. Once the time step is known, the simulation starts time-marching and temperature distribution across the heat shield wall is obtained. The results are presented in Figure 8.24.

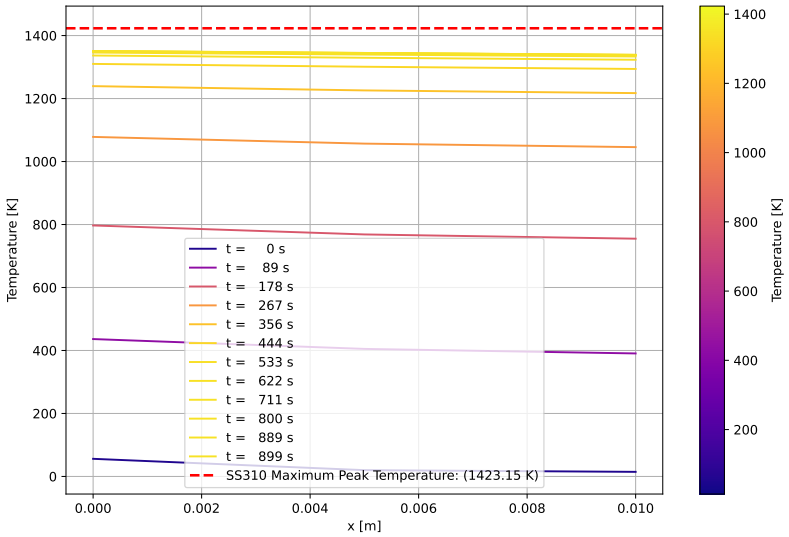

Figure 8.24: Simple Heat Transfer Temperature Profiles

It can be seen that the heat shield heats up rather slowly, as it takes almost 10 [min] to reach the steady state. Surprisingly, the thermal mass of the stainless steel heat shield appears to be a significant benefit to the design problem. When steady state is reached, the radiative heat flux q_r balances the incident heat flux q_i and cooling q_c. Note that it scales with $q_r \propto T^4$.

In summary, the first iteration of the 1-D heat transfer model suggests that it is possible to regeneratively cool a metallic heat shield under expected heat loads. Not only is there some amount of coolant that can compensate for the total heat load, but there is a cooling solution that can handle the peak heat flux. However, the model is still simplistic. Next, the material for the heat shield will be discussed in more detail.

8.10.2. Materials

Taking into account the results in Figure 8.24 and the *Stakeholder Requirements*, it is apparent that the heat shield material should have the following properties:

- High-temperature ceiling
- Good cryogenic performance at 20 [K] and good compatibility with LH_2
- High emissivity ϵ
- Good weldability etc. for convenient manufacturing
- Competitive pricing

During the midterm, the tank material was selected as stainless steel [2]. A similar trade-off was performed for the heat shield material while optimizing for the above properties. After several alloys were considered, it quickly became apparent that for such a demanding material application with tight margins, it would not be feasible to simply order an off-the-shelf material stock with a readily available material properties list.

Instead, development must be performed by working with the material supplier, establishing careful quality control (QC) and quality assurance (QA) policies, and gradually testing the material properties under various condi-

tions while ensuring that they are consistent. For example, finding material properties as a function of temperature from 20 [K] to 1400 [K] already significantly limits the number of materials that can be evaluated at this stage of the project.

Therefore, the materials were evaluated largely on the basis of qualitative literature research and available data. The main source was the Granta database from Ansys [10]. In studying the database, two alloys were identified as the most promising. Haynes 230 (UNS N06230) and SS310 (1.4845). Haynes 230 is a nickel-based superalloy that has excellent high-temperature thermal properties. However, even the Granta database has limited information on its cryogenic performance. The second material was the SS310 stainless steel alloy, typically used in industrial furnaces. This metal is similar to the main structural alloy SS304L, but performs better at higher temperatures.

As discussed above, simply taking values from a datasheet can lead to an incomplete understanding of a material. For example, stainless steel properties are different across different stock shapes (beam stock, sheet stock, bar stock, etc.) and across different manufacturing techniques (wrought, cast, additively manufactured, etc.). However, for the purpose of a preliminary analysis, it will be assumed that this is a good enough approximation.

AS-COOL-07: The material database data for SS310 is a good enough approximation for realistic material performance on the heat shield.

SS310 properties were adapted and digitized using the WebPlotDigitizer tool [11]. The results are shown in Figure 8.25.

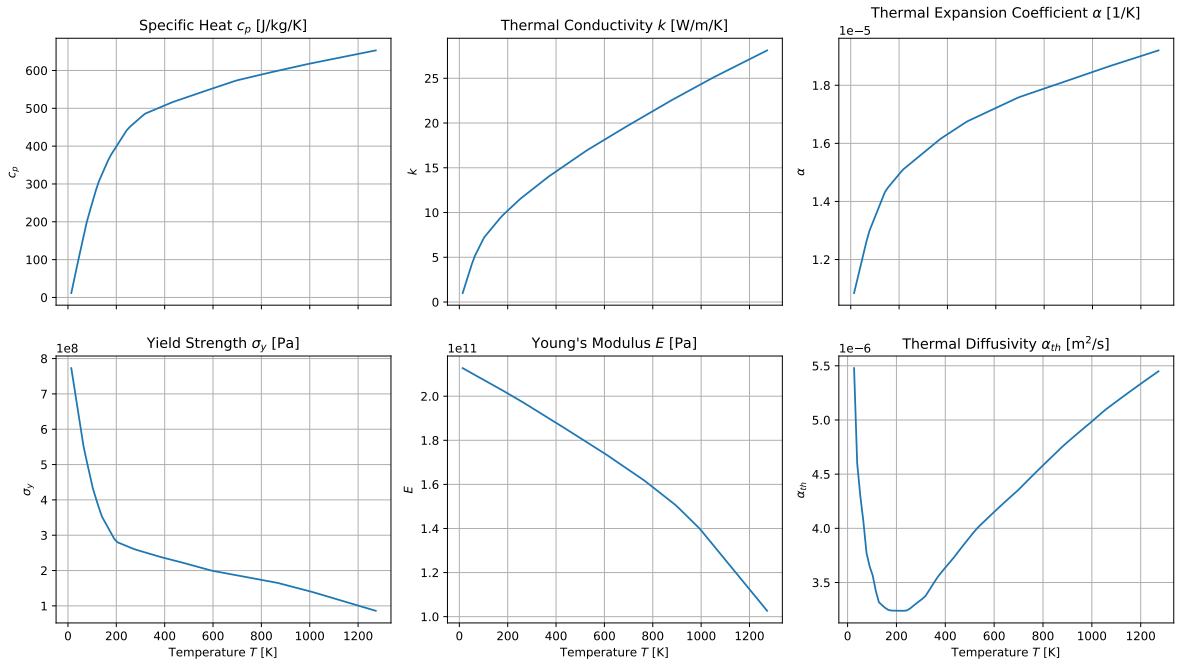

Figure 8.25: SS310 Properties [12]

Material emissivity ϵ is not readily available from the datasheet as it generally depends on the surface finish of the steel. As illustrated in Figure 8.16, the SS310 can have an emissivity anywhere from 0.07 to 0.97. Such high emissivity is achieved by purposely leaving the material exposed to a high-heat oxygen-rich environment for several minutes or hours to oxidize. As shown in Figure 8.26, the Andromeda2 vehicle from Stoke Space (which is also expected to use a stainless steel heat shield) seems to have severely oxidized heat shield tiles.

As discussed earlier, the high emissivity can be significantly beneficial in minimizing the maximum temperature seen by the heat shield. However, the oxidized layer will have weaker material properties. From this discussion,

[10] URL https://www.ansys.com/products/materials [cited 2025-06-17]
[11] URL https://automeris.io [cited 2025-06-24]
[12] URL https://www.ansys.com/products/materials [cited 2025-06-17]

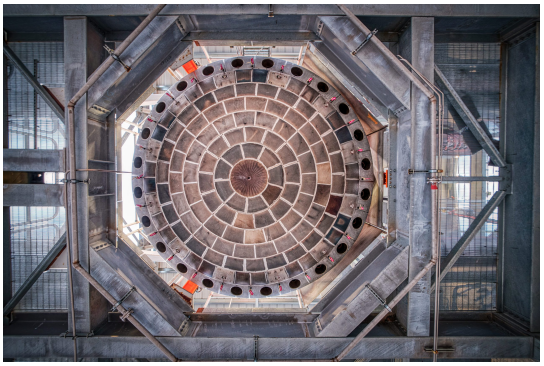

Figure 8.26: Oxidized metallic heat shield of the Andromeda2 by Stoke Space[13]

Table 8.16: Emissivity values for some metals, adapted[14]

Metals	**Emissivity Range** $[-]$
Stainless Steel	
polished	0.07
type 310, oxidized from furnace service	0.90-0.97
Tin, bright	0.06
Tungsten filament, aged	0.03-0.35
Zinc	
commercial pure, polished	0.05
galvanized sheet	0.21

Figure 8.27: Oxidized stainless steel and typical SS310 emissivity value

two more assumptions were derived.

AS-COOL-08: The heat shield will oxidize on the surface and have an emissivity of at least 0.9 $[-]$.

AS-COOL-09: The first 100 $[\mu m]$ of the heat shield wall thickness will be neglected in structural calculations to account for its reduced material properties.

After these considerations, the material properties were implemented in the 1-D heat transfer simulation. At each time step, material properties were re-evaluated for each node based on its current temperature. The results are shown in Figure 8.28 for a 20 $[mm]$ and a 4 $[mm]$ wall thickness.

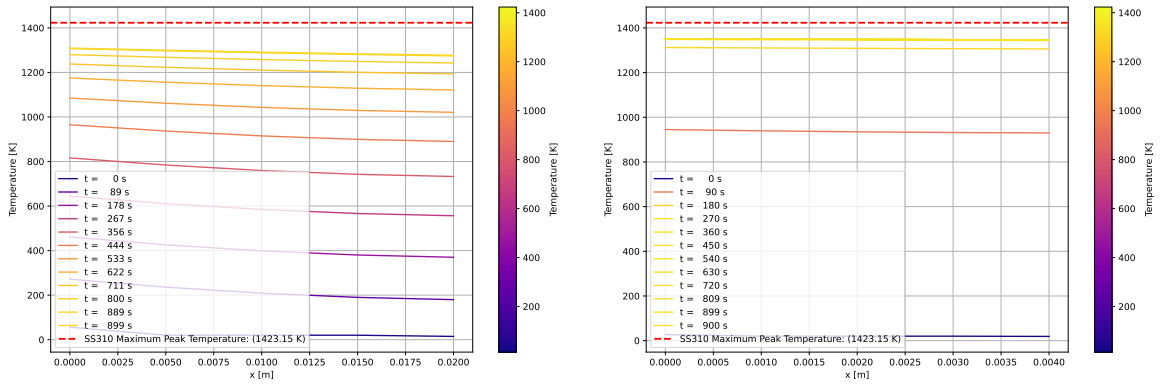

(a) 20 [mm] wall thickness

(b) 4 [mm] wall thickness

Figure 8.28: Improved simulation results

Given the low c_p values at cryogenic temperatures (indicated in Figure 8.25), Figure 8.28b now shows a much faster initial temperature increase for conditions otherwise identical to those of Figure 8.24. This is a critical difference. Given the transient nature of the incident heat flux, it is apparent that the regenerative cooling system could be optimized to handle the peak heat flux only temporarily relying on the heat shield itself acting as a heat sink. The extreme case of this is illustrated in Figure 8.28a. The 20 $[mm]$ heat shield wall thickness carries so much thermal mass that the steady state is not reached even in 15 $[min]$. Of course, this is not accurate since such mass would significantly increase the incident heat flux q_i in the first place, however, it is useful to illustrate this extra thermal effect of the heat shield. It is another factor that needs to be considered during optimization, which is discussed in the next subsection.

[13] URL https://cdn.prod.website-files.com/60757a01065b4ef4ebb38328/6140abe81bbee55789709868_TN-2021-69-EN-V0.pdf [cited 2025-06-18]

[14] URL https://www.stokespace.com/introducing-andromeda/ [cited 2025-06-18]

8.10.3. Cooling Optimization

The previous two subsections introduced the 1-D heat transfer model, hydrogen coolant properties, aspects of the coolant channel geometry, and variable material properties. All basic building blocks are now in place to start the optimization process.

Due to the number of possible variations, it was not possible to implement a programmatic optimizer within the preliminary design stage of the H_2GO project. There are roughly 7-8 key parameters influencing the simulation with most of them encapsulating several more parameters. For example, the channel geometry is defined by w_{ch}, h_{ch}, s_{ch} and has a corresponding empirical pressure drop model that can also be varied.

So instead of a programmatic optimizer, a procedure was devised to run the final set of programs and find the optimal design by hand:

1. Perform the 1-D heat transfer analysis on a sample area and find the ratio of the area covered by the coolant channels vs. the heat shield area.
2. Based on the total coolant channel contact area, calculate the total coolant loop volume based on the cross-sectional geometry of the channel.
3. Assume a primed coolant loop and integrate coolant mass flow in time during the re-entry phase to get the total coolant mass needed.
4. Iterate by varying the mass flow and search for minimal heat shield dry mass and coolant mass combination while staying within a narrow temperature envelope.

Note that this process essentially decouples the space-time simulation. That is, the coolant properties along the channel length can be approximated independently of the time-marching heat transfer simulation.

After varying all the parameters, the simulation result in Figure 8.29 was obtained.

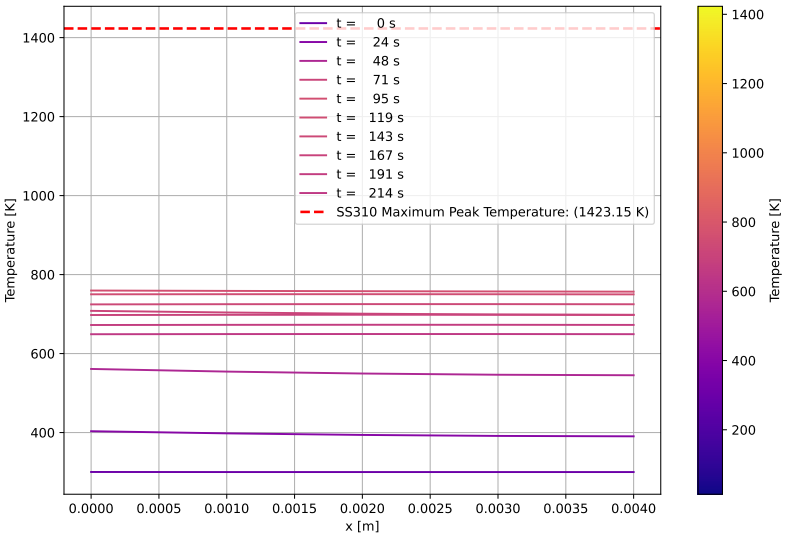

Figure 8.29: Heat Shield Temperature Profiles

In the plot, a relatively narrow temperature range from 300 [K] to approximately 800 [K] can be observed. This is deemed beneficial for the thermal cycling aspects of the design. This was achieved with constant mass flow rate through the coolant loop. In the future, the coolant mass flow rate could be throttled (similarly to throttling the main engines) to further optimize the temperature range of the heat shield as well as the coolant mass needed for re-entry.

The required coolant mass estimate was considered not reliable enough to replace the previous conservative estimate of 3000 [kg], so that parameter carried the same value into subsystem integration. Once a more accurate number is found, the payload mass budget can be increased on behalf of this coolant mass budget.

8.10.4. Structural Considerations

The heat shield will need to sustain thermal and pressure cycling as well as the loads induced by the re-entry deceleration. Given the scope of the H_2GO project, the resulting stress and fatigue for the heat shield were not evaluated. Instead, a highly conservative estimate was made based on the fatigue considerations discussed in Section 8.6.7.

The minimum hot wall thickness $t_{w,h}$ was selected as $4\,[\text{mm}]$, similar to the tank wall thickness. This results in a relatively heavy heat shield, but should provide enough margin to handle pressure and thermal stresses as well as fatigue. Thermal cycling could be severely mitigated by further optimization of the coolant loop (as highlighted above), and the pressure cycling is not different from the cycling that the feed system lines need to sustain. These problems have been successfully solved in the past [62], so it is expected that a design that could sustain at least 25 re-entry flights is feasible.

The parts of the vehicle without active cooling will also experience some incident heat flux. However, using the radiative heat flux equation, it is found that approximately $51\,[\text{kW/m}^2]$ can be radiated out at a temperature of $1000\,[\text{K}]$ and emissivity of $0.9\,[-]$. Since the peak heat flux at the stagnation point is predicted to be less than $140\,[\text{kW/m}^2]$ for the current configuration of the vehicle, this is also not an issue [59].

Lastly, note that by assuming a conservative constant heat flux across the heat shield, the localized heat flux increase over sharp edges is not considered. According to literature [59], this effect could cause problems on the engine nozzle edges, however it is expected that some coolant will be routed through the engines themselves as well during re-entry to mitigate this problem. Further recommendations for future analysis will be provided in Chapter 14.

8.10.5. Sensitivity Analysis

The sensitivity of the heat shield design was assessed by varying the heat shield wall thickness and observing the effects on operating temperature and mass. An increase of $1\,[\text{mm}]$ is considered a realistic increase to account for the additional structural strength needed for fatigue or larger coolant channel cross section. Next, the coolant channel geometry was also varied to change the cross-sectional area. The channel area was doubled to decrease the channel pressure drop. Lastly, the incident heat flux was varied to understand how the design would be affected in case the vehicle would become lighter or would otherwise re-enter with lesser aerodynamic heating.

As a baseline, the heat shield wall thickness was set at $4\,[\text{mm}]$. The results of the analysis are presented in Table 8.17.

Table 8.17: Sensitivity analysis of the actively cooled heat shield design

Parameters:	**Heat shield wall thickness**	**Heat shield wall thickness**	**Coolant channel area** A_{cs}	**Incident heat flux** q_i
Change in value	$+1\,[\text{mm}]$	$+1\,[\text{mm}]$	Doubled area	Doubled heat flux
Relative change	$+25\,[\%]$ mass	$-8\,[\%]$ peak heat shield temperature	No change in temperature if constant mass flow is maintained, slight decrease in mass	$+80\,[\%]$ increase in peak heat shield temperature
Effect description	The heat shield mass scales linearly with thickness. The default dry mass is 2200 [kg], so $+1\,[\text{mm}]$ is extra 550 [kg]	Since the heat shield acquires more heat sink mass, the peak temperature is lower	Negligible effect	Strong effect on peak temperature, hazardous for the heat shield lifetime
Impact:	2	4	3	1

As seen in the table, the heat shield is in delicate thermodynamic balance. This is necessary to best optimize the dry mass of the subsystem, as well as the coolant mass. It is imperative that the incident heat flux is understood well before the first flight and that more advanced design tools are used to validate the 1-D heat transfer model.

For example, it is realistic that at the nozzle edges (where the engine nozzles and the heat shield wall intersect), the local incident heat flux could be twice the theoretical heat flux at the stagnation point due to localized flow effects [59]. In the table, this resulted in a sensitivity score of 1 since such high heating would most likely start melting the material. This could be mitigated by locally widening the coolant channels or reducing the wall thickness for more effective cooling.

8.11. Power

The large number of electronic equipment onboard H_2ERMES require energy to function during all phases of the mission. This mandates an onboard source of power. Afterwards, the generated electricity needs to be distributed to all electronics onboard, converted to their respective operating parameters.

8.11.1. Power Plant

In the subsystem trade-off [10], fuel cells were selected as the preferred method to generate electricity. They are very uncommon in space applications, as virtually all launch vehicles use batteries and spacecraft opt for solar panels [27]. However, the unique mission characteristics of H_2ERMES, being simultaneously a launch vehicle and a spacecraft in function, proves them to be the most suitable system. Batteries become very heavy beyond a few hours of operation for missions with large power needs, due to their low specific energy density. Solar panels are also comparatively heavy for missions only a few days long, and there are unsolved problems with stowability. Fuel cells came out on top in the trade-off due to their very good specific power and energy density and high reliability. The closest design reference in operational profile, the reusable Space Shuttle, also opted to use fuel cells [65].

Since there has been very little new development in terms of space fuel cell technology since the Space Shuttle, it was decided to use the cell technology from that vehicle. The vast operational history of the Shuttle fuel cells allows for high trust in their reliability. H_2ERMES has no external payload, and therefore it requires less power in comparison. Two fuel cells were deemed satisfactory to provide power for all subsystems, with redundancy to finish the mission in case of the failure of one cell. Similarly to the Shuttle, no backup batteries or other power-generating systems are used. In nominal operating conditions, each cell contributes around half of the generated power.

The alkaline fuel cells generate electricity from a chemical reaction between oxygen and hydrogen at over 70 [%] efficiency [66]. The byproduct of the reaction is water, which is occasionally purged from the cells and routed to flow outside the vehicle. This also takes care of waste heat from the cell. Reactants are drawn from the header tanks and consumed in proportion to the needed power production, which is governed by the main flight computer. The mass of reactants consumed was based on Shuttle parameters [67], calculated from embodied energy.

One fuel cell can output 7 [kW] continuously and 12 [kW] for short 15 [min] periods [65]. This is reflected in *RQ-POW-6* and *RQ-POW-7*. To maintain the 93 [°C] operating temperature, heaters switch on should the power draw fall below a certain level. The fuel cells output direct current (DC) electricity at 28 [V], which is distributed through the main power bus.

8.11.2. Power Distribution and Control

From the nose cone, where the fuel cells are located, the main power bus runs across the entire length of the H_2ERMES vehicle. It connects all electronic equipment to the power plant. Near the bottom of the vehicle, the main power bus links to the propulsion bus. This has extra shielding to withstand the extreme heat and vibrational conditions near the main engine, and provides electricity to the engine control computers and all individual thrust chambers.

Some loads, such as the transmitting antennas, require alternating current (AC) to function, in which case an inverter is also included just before the load to transform electricity from DC to AC. Any required voltage conversion is also done in a distributed, localized manner.

8.12. Data Handling

RQ-SYS-1 states that the vehicle shall operate autonomously. To continuously process information from the environment and make decisions, an onboard computer system is required, which acts upon data received from sensors and sends commands to actuators.

The most extreme operating conditions determine the design of this subsystem. The space environment poses critical radiation damage risks. The powered landing guidance maneuver during the final mission phase requires very rapid computation of control algorithms many times per second to land safely.

8.12.1. Processing Units

Centralizing most computing tasks allows for pooling of computing resources and reducing overall part count. The main flight computer serves as the brain of the vehicle, responsible for most processes. As computers weigh only a small fraction of a percent of the overall vehicle mass, they are often triple-redundant on aerospace vehicles

for better reliability and accuracy [68] [15]. With the three computers performing majority voting among themselves, any momentary errors or inaccuracies arising from one of them can be filtered out.

Similarly to the Space Shuttle and Falcon 9, it was decided to delegate overseeing the engines to specialized engine control computers [68]. This enables swift responses to the quickly evolving engine conditions and to avoid overly large amount of wiring. Sending a signal from each of the 24 individual engines along the entire length of the rocket would be an unfeasible design choice.

To comply with the previously mentioned risk of radiation, space-grade radiation-hardened computing hardware was chosen. The main flight computers use the RAD5500 single-board computer from BAE Systems [16], their newest design in their radiation-hardened product line, owing to the high computational power needs. In turn, the engine control computers require less performance, so the simpler RAD750 was chosen for them [17]. All computers use the common PowerPC architecture, and run a hard real-time operating system to strictly, mathematically provably avoid timing out of computational processes within the milliseconds required for rapid control loops. This ensures compliance with *RQ-DAH-1* The widely used VxWorks operating system by Wind River Software was chosen as the best option for performance [18].

8.12.2. Data Streams

Data is routed to the computing units through space-grade signal lines that connect to all electronics onboard. Most data is carried from sensors and to actuators. Additional sensors, three cameras streaming at 1080p resolution, 60 frames per second were also selected to be used. This is not part of any particular subsystem, or is essential to successful operations. But it is very commonplace on modern launch vehicles, with the Falcon 9 streaming every launch [19], and can prove useful for a wide variety of purposes. A video feed can help characterize damage suffered by the vehicle, oversee engine plume expansion, assist and speed up docking operations with the depot, and even prove useful for public outreach and marketing. As other sensors mostly just report time series numerical data, while cameras return full color images, they are responsible for most of the data throughput that is sent to the computers and later in telemetry to Earth.

8.13. Communications

Though the H_2ERMES vehicle is designed for autonomous operations in line with *RQ-SYS-1*, a method of exchanging information with the target orbital depot and ground operating personnel is also mandatory, indicated in *RQ-COM-1*. The main goal of this is the safety and transparency of operations, in the case of both a successful flight and a failure. For this purpose, the communications subsystem is responsible, comprising of both hardware and software.

8.13.1. Communication Signal

A two-way telecommunications link is established between H_2ERMES and the ground segment of mission operations. Data sent from the spacecraft to the ground is telemetry or downlink, data sent in return are telecommands or uplink. Owing to the autonomous design of the vehicle, continuous ground station command is not necessary. Direct communications with the orbital fuel depot is also possible, but the exact transmission and reception characteristics of the depot are unknown. Based on [69], the uplink frequency is 2.11 [GHz] and the downlink frequency is 2.29 [GHz] on the S-band.

A modern software-defined radio (SDR) is responsible for transforming the digital data signal into a radio-frequency signal with flexible, easily modifiable parameters. This component takes care of modulation and demodulation, encoding and decoding, etc. No specific part has been selected as of yet, but a radiation-hardened or tolerant design is essential. It is also triplicated for redundancy.

8.13.2. Antennas

For the ground station, the decision to use the ESTRACK network was maintained from the midterm report [2]. Ground stations which lie in the track of the near-equatorial orbit of H_2ERMES are Kourou (also used during

[15] URL https://web.archive.org/web/20131203204735/http://www.aviationweek.com/Blogs.aspx?plckBlogId=Blog%3A04ce340e-4b63-4d23-9695-d49ab661f385&plckPostId=Blog%3A04ce340e-4b63-4d23-9695-d49ab661f385Post%3Aa8b87703-93f9-4cdf-885f-9429605e14df [cited 2025-06-17]

[16] URL https://web.archive.org/web/20180922173654/https://www.baesystems.com/en/download-en/20170403144601/1434594567983.pdf [cited 2025-06-17]

[17] URL https://www.baesystems.com/en-us/product/radiation-hardened-electronics [cited 2025-06-17]

[18] URL https://www.windriver.com/products/vxworks [cited 2025-06-17]

[19] URL https://www.spacex.com/launches/ [cited 2025-06-18]

launch), Malindi, South Point and Dongara [70].

Facing extreme aerodynamic, thermal, and vibrational conditions during launch, orbit, and re-entry, a search for antennas designed specifically for use on launch vehicles was made. Primarily, the antenna needed to be flush with the vehicle's body to eliminate aerodynamic forces. Due to the vehicle being made from steel for its high melting point, mounting the antennas inside was not an option as the conducting metal would act as a Faraday cage, heavily attenuating the signal.

The Flexislot antenna from Haigh-Farr was selected as the winning option [20], which can be seen in Figure 8.30a. This fulfills all the above requirements with a very small size and mass factor. The maximum 40 [W] of sustained transmission power is used for the antenna. However, it can only transmit and receive linearly polarized signals. This is compatible with the ground station's right-hand circularly polarized signal [70], but results in a 3 [dB] signal strength loss.

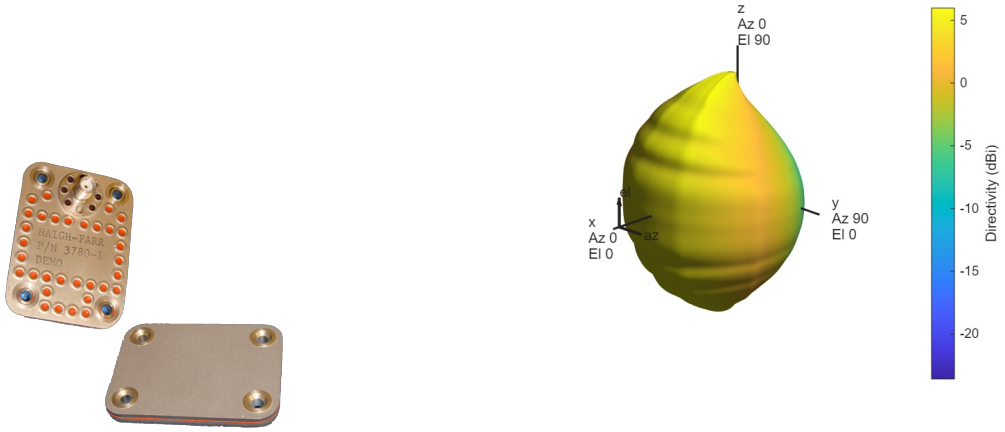

(a) Haigh-Farr Flexislot antenna

(b) Reconstructed three-dimensional gain pattern

Figure 8.30: Flexislot Antenna Characteristics

The antenna has 0 [dBi] to 5 [dBi] gain on the roll axis between -60 [dBi] to 60 [dBi] and 5 [dBi] to 8 [dBi] gain on the pitch axis between -90 [dBi] to 90 [dBi], from the Flexislot data sheet. Though no three-dimensional gain pattern was provided by the manufacturer, it was reconstructed from the two-dimensional roll and pitch patterns using Matlab's `patternFromSlices` function. This pattern can be seen in Figure 8.30b. Analyzing this pattern reveals that by using three Flexislot antennas on the vehicle's cylindrical body, with each antenna spread 120 [°] apart, full spherical coverage can be achieved with positive gain in every direction. This arrangement was chosen as final. To save power, only the antennas facing Earth are operational, and the ones pointing towards space are powered off. A radio switch performs this function.

8.14. Attitude & Orbital Determination and Control System

The attitude & orbital determination and control system (AODCS) plays a vital role in allowing the spacecraft to perform its tasks in orbit. With respect to the H_2ERMES launch vehicle, this subsystem is responsible for performing attitude correction maneuvers, determining the orbit, countering disturbance loads and maintaining trajectory during re-entry. This chapter deals with the detailed design of the AODCS.

8.14.1. Attitude and Orbit Determination

With regard to the determination aspect of the AODCS, GPS receivers will be used to determine the attitude and orbit of H_2ERMES. This instrument acquires information from at least four GPS satellites in low Earth orbit (LEO) to determine its attitude and orbit. The trade-off performed in the midterm report yielded GPS receivers as the best option due to their high accuracy in orbit determination along with their lower mass and costs. Moreover, these devices are commonly used in LEO applications, which is the intended orbit range for the H_2GO mission. Due to the lack of time and resources, it was decided that a commercial off-the-shelf (COTS) product would be integrated into the launch vehicle. Hence, the 2023 E. Gill paper [71] was used as a reference to research about

[20] URL `https://www.haigh-farr.com/docs/default-source/products-data-sheets/general_flexislot-antennas_revb.pdf?sfvrsn=9627fd56_2` [cited 2025-06-17]

currently available GPS receivers on the market. The search was further filtered to only include options which were manufactured in Europe as it would facilitate compliance with regulations, transportation and integration with the launch vehicle. Out of the available options, the PODRIX GNSS receiver was chosen as the best option for this mission. This was due to its relatively higher position accuracy compared to the other options, lower mass and compatibility with spacecraft that were operated in LEO. The antenna for this receiver is spherical in shape with a diameter of 0.2 [m], height of 0.087 [m], a mass of 0.735 [kg] and an operational temperature range between -120 [°C] and 120 [°C]. To allow attitude determination using the GPS receivers, multiple antennas are required and will be placed in opposite positions of the launch vehicle's geometry. Hence, four antennas will be used for attitude determination with additional redundancy.

Table 8.18: GPS receiver characteristics

Characteristics of the PODRIX receiver	
Mass	3 [kg]
Average power	15 [W]
Operating temperature range	-30 [°C] to 60 [°C]
Dimensions	$280 \times 241 \times 81$ [mm^3]
Position accuracy	< 1 [m] 3D root mean square (RMS)
Receiver Time	< 50 [ns]

(a) PODRIX GNSS receiver

(b) Antenna for the PODRIX receiver

Figure 8.31: Images of the chosen GPS receiver and antenna[21]

8.14.2. Attitude & Orbital Control System

Having looked at the AODS, the detailed design of the attitude & orbital control system (AOCS) of the H_2ERMES rocket will be described. In the trade-off performed in the midterm report [10], monopropellant thrusters powered by hydrogen peroxide was chosen for the AOCS. Hence, COTS thrusters which comply with the requirements of the mission were considered. Similar to the research process for GPS receivers, only COTS thrusters made in Europe were considered. After careful analysis of system requirements and similar past missions, the Nammo high-test peroxide (HTP) monopropellant thruster was selected. The Nammo engine is powered by HTP with an 87.5 [%] concentration of hydrogen peroxide and uses a silver catalyst to decompose HTP into steam and oxygen. The catalyst is heated using electrical power to start the decomposition as silver is not a spontaneous catalyst. As the process is exothermic, the heat released is used as an impetus to produce thrust. This engine is currently under development and is being prepared for the upper stage of the Vega-C rocket. Once the thruster is selected, it is necessary to determine the number of thrusters required and quantify the mass and power requirements for the launch vehicle. Section 8.14.2 describes the in-house tool developed to perform sizing of the AOCS. For this analysis, the thrust will be assumed to be 250 N with a specific impulse of 160 seconds. This value was obtained from the datasheet of the thruster which is a value dependent on the fuel flow, thrust force and the burn time of the rocket engine.

Sizing the AOCS

As described earlier, a tool had to be developed to determine the number of thrusters along with their positions around the launch vehicle. To begin with, the tool takes in a set of inputs to determine the number of thrusters, the total mass and power requirements of the AOCS including that of the hydrogen peroxide propellant tank. The steps taken by the tool to produce these outputs have been stated below:

[21] URL https://www.beyondgravity.com/sites/default/files/media_document/2024-04/BG_PODRIX_GNSS_Receiver%20spaceborne_Satellite_RX_V1.0.pdf [cited 2025-06-16]

- Step 1: The tool takes the launch vehicle's mass moment of inertia (MMOI), dimensions of launch vehicle's geometry, slew rate of the launch vehicle, maneuver time of the AOCS along with a dictionary containing information on the thrusters as inputs.
- Step 2: The centroid of the launch vehicle is computed by computing the midpoint of the geometry using standard formulas.
- Step 3: The four main disturbance loads that act on the launch vehicle in orbit are defined using formulas from the new edition of the SMAD textbook [27] and calculated using the dimensions, MMOI and specific constants for each disturbance load.
- Step 4: The angular acceleration experienced by the launch vehicle is calculated by dividing its slew rate by the maneuver time, or the burn time of the thruster. This is then multiplied by the MMOI to obtain the torque. The highest disturbance load is then added to the torque in each axis.
- Step 5: The total torque is then divided by the lever arm of each thruster and the thrust required in each direction is computed. This thrust is multiplied by two to account for rotation in both directions. Then, the number of thrusters required for each thruster type is calculated by diving the total thrust by the thrust of each option. The output is multiplied by a redundancy factor to account for thruster failure.
- Step 6: The total dry mass is computed by multiplying the total number of thrusters by the dry mass of the thrusters. the total power requirement is computed by multiplying the peak power required by each thruster by the total number of thrusters.
- Step 7: The propellant mass is then calculated using the following relation:

$$M = \frac{F_{thrust} t_{burn}}{I_{sp} g_0} \tag{8.98}$$

where F_thrust is the thrust, t_burn is the burn time of the thruster, I_{sp} is the specific impulse of the thruster and g_0 is the gravitational acceleration experienced at sea level on Earth. The resulting value is multiplied by the number of thrusters to get the required total propellant mass.

- Step 8: The volume of propellant required is computed by multiplying the total propellant mass by the highest density of HTP in the stipulated storage temperature range. The propellant tank is assumed to a sphere and the radius of the tank is obtained through this standard formula for volume of a sphere:

$$V = 4/3\pi r^3 \tag{8.99}$$

The volume V is used to compute the radius r of the spherical tank.

- Step 9: Once the radius was obtained, the stress equation for a sphere is used to calculate the thickness of the tank:

$$\sigma = \frac{pr}{2t} \tag{8.100}$$

where p is the internal pressure in the tank, r is the radius of the tank and t is the thickness of the tank.

The stress is equated to the yield stress of the material that will be used on the tank. The code accesses a dictionary containing properties of materials compatible with HTP to get its yield stress. Then, an optimal pressure value is chosen for which the thickness is a valid number.

- Step 10: Once the thickness is obtained, the volume of the tank is calculated in terms of the thickness and multiplied with the density of the material which yields the lowest mass. This mass value is then added to the combined thruster mass to obtain the total mass of the AOCS and is returned as an output by the code.

Final Results

After running the AOCS sizing tool with the most updated dimensions of the H_2ERMES launch vehicle, the total mass and the number of thrusters that will be required were found. The positions of the thrusters were determined during integration of all the subsystems such that it allows manuevering and three-axis control without affecting the performance of the launch vehicle. 40 thrusters with a thrust range between 100 - 250 [N] will be placed around the launch vehicle along with two propellant tanks to power the thrusters. The propellant tanks are made from Aluminum AA6000 T6 series due to their record in handling HTP. The entire system's mass was calculated to be 922 [kg] and a detailed list of the system characteristics can be found in Table 8.19.

Table 8.19: System characteristics of the AOCS

Characteristics of the AOCS	
Number of thrusters	40 [−]
Slew Rate	3 [°/s] [72]
Total dry mass of thrusters	59.2 [kg]
Total propellant mass	765 [kg]
Tank mass	98.9 [kg]
Average power	1000 [W]

8.14.3. Sensitivity Analysis

The sensitivity analysis will be performed for the AOCS in the method described in Section 8.2. This analysis was not performed for the AODS as it was selected qualitatively without a specific tool. Table 8.20 lists the results of the analysis in which the MMOI, dimensions and the slew rate of the launch vehicle are varied to observe the change in subsystem mass. It can be noticed from the table that the MMOI has a severe impact on the design. A mitigation strategy would be to optimize the geometry such that the MMOI is minimized.

Table 8.20: Sensitivity analysis of the AOCS

Parameters:	Mass Moment of Inertia	Burn Time	Slew Rate
Change in value	×1.5 [−]	×0.5 [−]	×0.5 [−]
Relative change in subsystem mass	+48 [%]	2.4 [%]	−50 [%]
Effect description	An increase in the mass moment of inertia causes a 50 [%] rise in the total mass of the subsystem	Reducing the burn time by 50 [%] did not inflict a massive change in the total subsystem mass	Reducing the slew rate halves the subsystem mass, but is ineffective to perform maneuvers with this vehicle
Requirements affected	None	None	None
Impact:	1	3	2

8.15. Docking and Refueling

In order to properly deliver the payload to the orbital depot, it is important to consider the interface required for docking with the depot, and for transferring the payload from H_2ERMES. As specified in *RQ-STK-RFL-2*, the refueling will be done using a passive fluid interface, as provided by the customer, however, a suggestion for a system is given below, in order to have a more detailed design.

To be able to scale the vehicle to other operations at a later date, it is recommended to use a standard defined interface for docking and refueling. This makes it so that the vehicle can be adapted to more missions, even for other customers' orbital depots, at a later moment in time, without needing massive redesign. Because of this, the docking and refueling interface will be based on the International Docking Standard System (IDSS)[22], as seen in Figure 8.32.

This standard provides both the dimensions of the docking system, and the locations for the umbilicals for fluid and electronic data transfer. The main performance characteristic of the docking and refueling interface important at this stage of the design is the total amount of time required to complete the refueling process, as stated in *RQ-STK-RFL-1*.

In order to calculate this this, first the total area of the fluid transfer interface needs to be found. Assuming circular vacuum insulated pipes with a insulation thickness of 12 [mm] [23], and using all six larger available umbilicals, to use the smaller ones for electronic data transfer for system checks during the docking and refueling process, this comes out to 0.071 $[m]^2$. Assuming a flow velocity of 0.5 [m/s], which has been tested for cryogenic fluid transfer in space [74]. From this, the total fluid transfer time can be calculated using Equation 8.101.

$$t_{\text{Refuel}} = \frac{m_p}{\dot{m}} = \frac{m_p}{\rho A V} \tag{8.101}$$

[22] URL https://www.internationaldockingstandard.com [cited 2025-06-15]
[23] URL https://www.opwces.com/content/dam/ces/catalogs/Acme_VJP_Systems_Catalog.pdf [cited 2025-06-24]

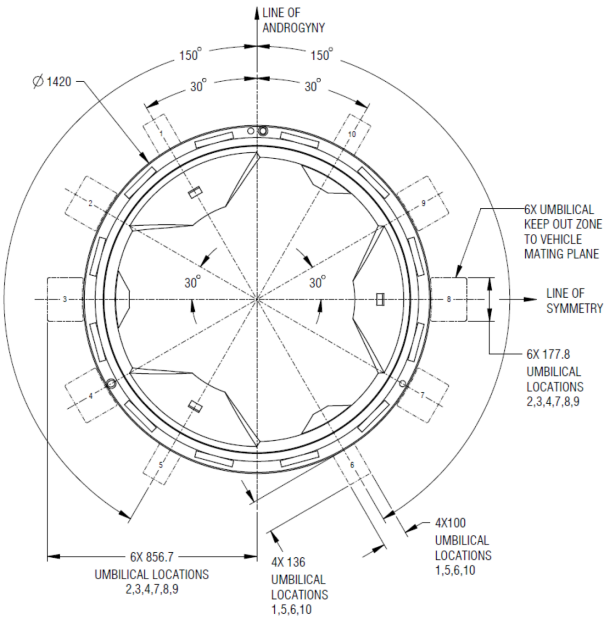

Figure 8.32: Technical drawing of the IDSS, with the umbilicals highlighted [73]

Here, t_{Refuel} is the time to refuel in [s]*, and m_p the payload mass to be transferred in* [kg]*, $\dot{m}$ is the mass flow in* [kg/s]*, ρ the fluid density in* [kg/m^3]*, A the area in* [m]^2 *as calculated above, and V the flow velocity* [m/s].

The entire system is estimated to have a mass of 370 [kg] [75].

8.16. Boil-Off Mass Estimation

When cryogenic liquid is held in an environment that is a lot warmer than the temperature of the fluid, it can result in boil-off of the liquid. This is essentially the liquid vaporizing and turning into vapor. LH_2 is notorious for this specific effect and as there is no insulation for the main tanks, the amount of LH_2 lost to vaporization must be calculated. This is also important to know before since as per *RQ-STK-PLD-1*, atleast 10000 [kg] must be delivered to the depot. Therefore, this section will lay out the methodology to estimate how much boil-off of LH_2 is to be expected during mission operations.

Before any calculations can be done, it is important to first divide the flight into different phases. The mass of boil-off can then be found over each phase, and then summed in the end to find the total boil-off mass. The following phases are considered:

- **Launch to Orbital Insertion**: Refers to the time between being on the launchpad and the moment the orbital insertion has been completed.
- **Orbital to Docking**: The time from orbital insertion to completing docking.
- **Docking to Refueling**: The time spent between docking and refueling is finished. For the purpose of this section, this phase will be approximated as instantaneous.
- **Refueling to Re-entry**: The time spent right after refueling and before re-entry is about to be performed.

An important note is that the orbital launch to orbital insertion phase will be assumed to be instantaneous as per *AS-BOIL-05*. This is a valid assumption for the case of launch pad to orbital insertion phase as orbital insertion only takes a few minutes when compared to the rest of the flight timeline and it also allows some simplifications in Section 8.16.2. Furthermore, as per *AS-BOIL-01*, the refueling process will not cause any boil-off. This is because to get the exact boil-off mass during fuel unloading, an extensive computational modeling software will be needed to model the thermodynamic environment in the tank. Making this assumption allows a simplification of the analysis performed as well. By incorporating the refueling time in the orbital to docking phase, the heat entering the tank during this stage can be accounted for.

The boil-off mass and the change in state variables during phases will be calculated by using an external tool called

BoilFAST developed by the University of Western Australia [3]. This tool has also been extensively validated with experimental data [76]. To set up the tool, an array of inputs needs to be set (akin to a CFD software), and one of the most important inputs is heat load entering the tank. This analysis will be done in Section 8.16.1. After the heat load has been determined, Section 8.16.2, Section 8.16.3, Section 8.16.4, and Section 8.16.5 will discuss the expected boil-off during the four phases, and finally, a sensitivity analysis will be performed in Section 8.16.6.

8.16.1. Boil-Off Heat Flux

To estimate the total heat load entering the tank, an external software called ESATAN-TMS was used. This software has been extensively validated and has been often used in industry to estimate the thermal environment of space for the design of satellites [77]. Furthermore, it will be assumed that the total heat load entering the tank will all be external radiation from planetary (Earth), albedo (Earth) and solar as per *AS-BOIL-03*. Since this analysis was also done in the midterm report [2], the same values for the planetary heat flux, albedo heat flux and solar heat flux can be used as they are valid for a circular orbit of 600 [km]. These are summarized in Table 8.21.

Table 8.21: Incident heat flux on launch vehicle.

Type of Radiation	**Symbol**	**Value** $[\mathrm{W/m^2}]$
Planetary Heat Flux	$q_{planetary,incident}$	355.21
Albedo Heat Flux	$q_{albedo,incident}$	187.34
Solar Heat Flux	$q_{solar,incident}$	1863.26

These incident heat fluxes can then be converted into heat load absorbed by the tank by using Equation 8.102,

$$Q_{absorbed} = \alpha A_{view} q_{incident} \tag{8.102}$$

where $Q_{absorbed}$ [W] is the heat load absorbed due to an incident heat flux, α [−] is the surface absorptivity, A_{view} is the surface area visible to the heat flux, and $q_{incident}$ [W/m^2] is the incident heat flux.

As per assumption *AS-BOIL-04*, A_{view} will be considered to be the same as the projected area of a truncated cone, $A_{projected}$ with elliptical end caps as shown in Equation 8.103.

$$A_{projected} = (r_{top} + r_{bottom})h_{cone} + \frac{\pi}{4}(r_{top}h_{top} + r_{bottom}h_{bottom}) \tag{8.103}$$

where r_{top} [m] is the radius of the top section, r_{bottom} [m] is the radius of the bottom section, h_{cone} is the height of the cone, h_{top} [m] is the height of the top elliptical cap, and h_{bottom} [m] is the height of the bottom elliptical cap.

For the purpose of this analysis, the absorptivity α of the tank wall will be taken to be $0.2\,[-]$. It is important to note though that the α for polished stainless steel is only $0.4\,[-]$ [78]. However, by applying a coating on the outside surface of the wall, the absorptivity can be brought down to around $0.1\,[-]$ depending on the type of coating used (Mylar, Kapton or Teflon among other) [78]. Detailed research will need to be done on the specific considerations of using such a coating on the outer tank wall. For example, during re-entry or ascent, this coating can be damaged which could dramatically increase the heat absorbed by the tank. However, for the purpose of this report, it will be assumed that are no additional considerations regarding applying a coating on the tank wall as per *AS-BOIL-07* but it is a recommendation for future studies to improve the model to estimate heat load acting on the tank and to study the viability of applying a coating on the outer stainless steel wall.

8.16.2. Launch to Orbital Insertion

At the end of the orbital insertion, a significant amount of liquid hydrogen has been used by the propulsion system. This will cause a change in the state variables and must be analyzed since the pressure at any point during launch cannot drop to below the 2 [bar] required to support the structure. Thus, this analysis will be done by assuming that the pressure inside the tank will be constant since it has to be kept above the launch pressure of 2 [bar] (*AS-BOIL-08*).

The Van Der Waals equation will be used for this analysis. This is given in Equation 8.104.

$$(P + a\frac{n^2}{V^2})(V - nb) = nRT \tag{8.104}$$

Where P [Pa] is the pressure, n [mol] is the number of moles, V [m^3] is the volume, R [J/mK], T [K] is the temperature, and a and b [$-$] are the van der Waals coefficients.

Furthermore, as per *AS-BOIL-02*, it will be assumed that the temperature of the vapor is constant and equal to the liquid temperature. This is done to simplify the process for isolating variables in Equation 8.104. Thus, rearranging Equation 8.104 for pressure and number of moles can then be equated at the point right after orbital insertion phase is completed. These points will be shown as subscripts in Equation 8.105.

$$m_{GH_2,end-of-insertion} = \frac{V_{GH_2,end-of-insertion} m_{GH_2,start-of-launch}}{V_{GH_2,start-of-launch}} \tag{8.105}$$

$$n = \frac{m_{GH_2}}{M_{mol,H_2}} \tag{8.106}$$

Where m_{GH_2} [kg] is the mass of hydrogen, M_{mol,H_2} 0.002 [kg/mol] is the molar constant of hydrogen, and n [mol] is the moles of GH_2.

This gives the total mass of gaseous hydrogen that is in the tank after orbital insertion. Since this GH_2 cannot be used as propellant or for delivery to the depot, this mass will be considered as the boil-off mass of LH_2 during launch. The value for $m_{GH_2,start-of-launch}$ and $V_{GH_2,start-of-launch}$ depends on the density of $GH_2$and on the total mass of the hydrogen that has to be in the tank (including LH_2 and GH_2). Since the density and temperature of LH_2 is known for a specific vapor pressure (of 2 [bar]), and since the temperature of $GH_2$is assumed to be the same as LH_2 during orbital insertion, exact values of density can be known. This process can be done on BoilFAST as it allows setting a specific liquid volume, tank pressure, liquid temperature, tank volume, and vapor temperature which will give the exact mass of both LH_2 and GH_2. This process can then be iterated by changing the initial liquid volume to find a combination of the total mass which is equal to the mass of hydrogen brought onboard.

Furthermore, $V_{GH_2,end-of-insertion}$ can be calculated by using the density of LH_2 at start of launch and the mass of LH_2 needed for orbital adjustments, payload delivery, and expected boil-off. Note that for the very first iteration, 3000 [kg] will be assumed which was calculated during the Midterm report [2]. $V_{GH_2,end-of-insertion}$ can then be simply calculated by using the total tank volume and the aforementioned volume of LH_2 needed at end of insertion.

8.16.3. Orbital Insertion to Docking

The change in the state variables during this phase will be calculated using BoilFAST. However, to use BoilFAST effectively, the inputs and outputs must be consistent throughout the different phases. The inputs that are directly decided by Section 8.16.2 are given in Table 8.22,

Table 8.22: BoilFAST inputs during orbital insertion to docking phase

Parameter	Value	Unit	Justification
Initial Surface Pressure	2	[bar]	The pressure was assumed to be constant through orbital insertion (*AS-BOIL-08*).
Vapor Temperature	Same as Liquid	[K]	The temperature was assumed to be constant through orbital insertion.
Initial Liquid Volume	$V_{LH_2,end-of-insertion}$	[m^3]	The initial volume will be iterated upon.
Time	$t_{insertion-to-docking}$	[s]	The initial volume will be iterated upon.

The outputs of this phase that will be needed for the next section Section 8.16.4 are summarized in Table 8.23,

Table 8.23: BoilFAST outputs during orbital insertion to docking phase

Parameter	Value	Unit	Justification
Pressure	$P_{end-of-docking}$	[bar]	Can be taken from BoilFAST pressure vs time plot.
Final Gas Volume	$V_{GH_2,end-of-docking}$	[m^3]	Can be taken from BoilFAST volume vs time plot.
Gas Mass	$m_{GH_2,end-of-docking}$	[kg]	Can be taken from BoilFAST quantity vs time plot.
Gas Temperature	$T_{GH_2,end-of-docking}$	[K]	Can be taken from BoilFAST temperature vs time plot.

It is important to note that boil-off for this phase will only happen if the pressure release valve is opened. Thus, if

$p_{end-of-docking}$ never reaches the 10 [bar], both the $GH_2$and LH_2 will essentially just get warmer but still remain in their respective phases.

8.16.4. Docking to Refueling

As per *AS-BOIL-01*, it will be assumed that there is no boil-off during this process. However, since a significant amount of LH_2 leaves the tank, it will cause a change in the state variables. A similar analysis like Section 8.16.2 can be done for this phase. Firstly, it will be assumed that the mass and temperature of GH_2 will be kept constant ($m_{GH_2,end-of-docking}$ and $T_{GH_2,end-of-docking}$) as per *AS-BOIL-02*). Instead, pressure will change with respect to the change in volume. The change in volume comes from H_2ERMESrefueling the depot which decreases the LH_2 volume and increases the GH_2 volume. Rearranging Equation 8.104 to relate the state of pressure and volume of GH_2 at two different points, is shown in Equation 8.107 [79].

$$(P_1 + a\frac{n^2}{V_1^2})(V_1 - bn) = (P_2 + a\frac{n^2}{V_2^2})(V_2 - bn) \tag{8.107}$$

Substituting the proper terms and isolating $P_{end-of-refueling}$ gives Equation 8.108[79].

$$P_{end-of-refueling} = \frac{(P_{end-of-docking} + a\frac{n_{GH_2}^2}{V_{GH_2,end-of-docking}^2})(V_{GH_2,end-of-docking} - bn_{GH_2})}{V_{GH_2,end-of-refueling} - bn_{GH_2}} - a\frac{n_{GH_2}^2}{V_{GH_2,end-of-refueling}^2} \tag{8.108}$$

The values of $V_{GH_2,end-of-docking}$, and $P_{end-of-docking}$ can be directly taken from Table 8.23 while n_{GH_2} is the number of moles of gaseous hydrogen which can be found from $m_{LH_2,end-of-docking}$ in Table 8.23 by rearranging Equation 8.106. The value of $V_{GH_2,end-of-refueling}$ will be iterated upon in Section 8.16.5 and is dependent on the next section. However, for the first iteration a standard value can be assumed. The outputs of this section can be summarized in Table 8.24.

Table 8.24: Output for docking to refueling calculation

Parameter	Value	Unit	Justification
Pressure	$P_{end-of-refueling}$	[bar]	Taken from Equation 8.108
Final Gas Volume	$V_{GH_2,end-of-docking}$	[m^3]	Can be taken from BoilFAST volume vs time plot.
Mass of Gas	$m_{GH_2,end-of-docking}$	[kg]	Can be taken from BoilFAST mass vs time plot.

8.16.5. Refueling to Re-Entry

This phase is when the pressure inside the tank will reach the vent relief pressure causing loss of LH_2 due to boil-off. Since boil-off is expected, BoilFAST can be used to determine the exact parameters. In this case, the new inputs for the next phase refueling to re-entry is shown in Table 8.25.

Since BoilFAST does not allow to directly set $m_{LH2,end-of-re-entry}$ to 3000 [kg], this process can be done iteratively by increasing $V_{LH2,end-of-refueling}$ by a set amount. It also has to be noted that for these new values of $V_{LH2,end-of-refueling}$, a new value for $P_{end-of-refueling}$ will have to be computed as per Equation 8.108. This can then be fed again as inputs in **??**. This will be done until $m_{LH2,end-of-re-entry}$ is within $\pm 1\%$ of 3000 [kg]. Once this iteration has converged to a solution, the total boil-off mass can be calculated by subtracting $m_{LH2,end-of-re-entry}$ from $m_{LH2,end-of-refueling}$ and then adding $m_{GH_2,end-of-insertion}$ (since the conversion to gas makes the boiled off gas useless for the main mission purpose). Furthermore, this entire process will be run again for different $t_{insertion-docking}$ and $t_{refueling-re-entry}$ within a specified range, and then a simple linear regression analysis can be performed on those data points to get an empirical relationship between $t_{insertion-docking}$ and expected boil-off mass. It must also be noted that since the inputs for this section are quite extensive and closely interlinked with the launch timeline, this analysis will be done at the end at Section 9.5.1.

8.16.6. Sensitivity Analysis

A rough sensitivity analysis was performed on the boil-off estimation on the amount. This is shown in Table 8.26.

Table 8.25: BoilFAST inputs during Refueling to Re-entry phase

Parameter	Value	Unit	Justification
Pressure (Initial Surface Condition)	$P_{end-of-refueling}$	[bar]	The pressure is taken from Table 8.24.
Vapor Temperature	$T_{GH_2,end-of-docking}$	[K]	The temperature was assumed to be constant through orbital insertion.
Initial Liquid Volume	$V_{LH_2,end-of-refueling}$	[m^3]	The initial volume will be iterated upon such that the final mass of LH_2 is 3000 [kg].
Time	$t_{refuel-to-re-entry}$	[s]	Time between the two different phases as decided by ΔV calculations.

Table 8.26: Sensitivity analysis for the boil-off mass prediction

Parameters:	**Pressure Vent (Valve release pressure)**	**Heat Load**	**Increased Mission Duration (from refueling to re-entry)**
Change in value	$\times 1.25$ [$-$]	$\times 1.2$ [$-$]	$\times 1.2$ [$-$]
Relative change in subsystem mass	-7.4 [%]	$+24.41$ [%]	$+31.22$ [%]
Effect description	No noticeable impact on the boil-off mass, which is dominated by the large heat flux entering the tank.	Dramatic increase in boil-off mass since more energy goes into the tank.	Dramatic increase in boil-off mass since the tank is exposed to external heating for longer.
Requirements affected	None	*RQ-STK-PLD-1*	*RQ-STK-PLD-1*
Impact:	4	2	2

As can be clearly seen in Table 8.26, the vent pressure of the tank causes a small change in the boil-off mass calculation. But as per Guiana regulations [26], the burst pressure of the tank must be twice the max operating pressure. Increasing the structural thickness of the tank to handle a roughly 50 [%] increase in pressure can undo any savings in boil-off mass due to increasing the vent pressure.

The boil-off mass is also very sensitive to the resultant heat load acting on the spacecraft as well as increasing the mission duration. Increasing it by 20% (for both cases) results in even less LH_2 being delivered to the depot but it still does not go below the 10000 [kg] set by *RQ-STK-PLD-1*.

Since for the purpose of this report, the heat load was calculated very conservatively, the actual heat load acting on the spacecraft can dramatically decrease with further analysis. For example, it was assumed that the area incident to the flux's discussed in Section 8.16.1 is the area projected by a truncated cone (*AS-BOIL-04*) which takes the worst case scenario. However, this heat load is only possible by applying an external coating to decrease the surface absorptivity. This coating can get damaged during ascent which can increase the local absorptivity of the region dramatically increasing the heat load. The application of this coating also slows down the refurbishment process since it must be inspected to evaluate any resultant damage from the flight. These factors should be considered at a more advanced stage and due to time constraints, were not considered at this stage.

A simpler solution involves the ADCS subsystem. The launch vehicle can be moved, with the ADCS thrusters, so that the heat shield faces the sun instead. This would decrease the heat load entering the tank but would add some requirements on the ADCS subsystem which can increase the mass of the ADCS fuel carried on board. This would require a slight redesign of the ADCS tank as they will need to be larger but the resultant savings from the reduction in boil-off mass (on the order of 1000 [kg]) can easily justify the additional mass of the ADCS subsystem.

8.17. Re-Entry Trajectory

In the following section, the procedure to design a re-entry trajectory is presented in Section 8.17.1. First, the models that are needed in order to have an accurate simulation need to be decided upon, decision which is justified in Section 8.17.2. Furthermore, in Section 8.17.3 a method is described that would allow to check whether a gliding trajectory can be achieved. Once that is checked, the methods in Section 8.17.4 and Section 8.17.5 can be used to calculate the equilibrium glide conditions, and to design a proper entry corridor. Lastly, in Section 8.17.6 a sensitivity analysis is performed to identify possible issues with the design.

8.17.1. Background and Methodology

During the trade-off, it was decided that the vehicle shall attempt to perform a gliding re-entry conditions trajectory. Gliding offers advantages by lowering thermo-mechanical loads, and by providing more control in regards to the landing site.

When designing the re-entry conditions trajectory of a vehicle, models need to be developed in order to perform simulations of the states the vehicle experiences during re-entry conditions. These can range from highly simplified to complex, depending on the level of accuracy required by the analysis. Once the models are set up, the entry conditions need to be assessed in order to ensure compatibility with gliding. The next step is designing a preliminary re-entry conditions trajectory by calculating the possible entry conditions corridor and footprint of the maneuver. Once all of the above are known, a more detailed analysis can be performed on the guidance method of the vehicle.

8.17.2. Models

As previously mentioned, in order to simulate the re-entry conditions motion, models need to be used to simplify computations and enable the use of analytical methods. The models should be selected and implemented in such a way that they are simple enough to run without excessive computational power, but should also provide enough complexity to the simulation so that it actually describes the scenario close enough to what can be expected in reality. The models that were needed to describe the environment are a planetary model, and a model of the flight dynamics.

Planetary Model

Since re-entry conditions are dependent on the conditions of the planetary system it enters, a planetary model needs to be described. This consists of three aspects: shape, gravitational field and atmosphere. Since H_2ERMES is supposed to bring fuel from the Earth to LEO, the only planetary body that was considered for the analysis was Earth.

In terms of shape, a spherical, non-rotating Earth is assumed for the preliminary re-entry conditions trajectory calculation. For the gravity field model, when calculating the first iteration of re-entry conditions parameters, gravity is assumed to be constant. However, when simulating the motion of the vehicle, the entry conditional-field definition should be used instead, as seen in Equation 8.109, which describes the gravitational acceleration between two point masses [59].

$$g = \frac{\mu}{R^2} \tag{8.109}$$

Here, g [m/s^2] is the gravitational acceleration, μ [m^3/s^2] is the geocentric conditions gravitational constant, and R [m] is the distance between point masses.

For the atmospheric model, an exponential model was used for the preliminary analysis. The exponential model assumes that the atmosphere is an ideal gas, and hence is governed by Equation 8.110a [59]. In order to reach an exponential model, R is considered to be constant, with a value of 287 [J/kgK], even though in reality it varies with altitude. Additionally, it is assumed that the atmosphere is in hydrostatic equilibrium. These assumptions lead to the final formula governing the exponential atmosphere model, which is Equation 8.110b.

$$p = \rho RT = \rho \frac{R^\star}{M} T \tag{8.110a}$$

$$\frac{\rho_0}{\rho} = e^{-\frac{h}{H_s}} \tag{8.110b}$$

Here, R [J/kgK] is the gas constant for an ideal gas, $R^\star$ [J/kmolK] is the universal gas constant, M [kg/mol] is the molecular mass of the atmosphere, p [Pa] is the pressure, ρ [kg/m^3] is the density, T [K] is the temperature, and H_s [1/m] is the scale height of the model.

As previously mentioned, the exponential atmosphere is a good first estimate. However, when simulating the exact motion of the vehicle, differences in density can have a strong impact. Therefore, for the numerical simulations of the re-entry motion, the commonly used United States Standard Atmosphere released in 1976 was chosen as an alternative [80]. Since it's based on empirical data, it provides a good estimate to be used in the following analysis [59].

Dynamic Model

When it comes to the dynamic behavior of the vehicle, some relevant parameters are the reference frames and the state variables used. The reference frames commonly used during the simulation procedure are inertial planetocentric, rotating planetocentric and vehicle-centered vertical, body, aerodynamics and trajectory frames. Each reference frame can be assigned state variables. These would be either cartesian or spherical position variables, or attitude angles. The attitude angles can be aerodynamic, trajectory-related, or dynamic. Due to the fact that forces encountered during flight act on different reference frames, transformations need to be performed in order to develop a set of equations that would describe the complete motion of the vehicle. The equations resulting from the calculations are too complex, and will be simplified in order to create the entry corridor.

8.17.3. Entry Conditions

When returning from space, the entry conditions are some of the most important factors determining the re-entry possibilities. That is due to the fact that a vehicle has to make sure it has just the right conditions to not overshoot or undershoot the entry. An overshoot is caused by entering at conditions that do not provide enough atmospheric drag to start slowing down. On the other hand, during an undershoot, the vehicle would experience excessive loads [81]. The entry requirements are visualized in Figure 8.33.

The entry conditions of H_2ERMES are influenced by the orbital mechanics at de-orbit. More specifically, at a given entry altitude, the entry velocity can be calculated using Equation 8.111, which then also returns the entry flight path angle.

$$V^2 = \mu\left(\frac{2}{r} - \frac{1}{a}\right) \tag{8.111}$$

Once these conditions are known, if the entry velocity is equal or larger than the circular velocity, it needs to be checked whether the trajectory is discontinuous and could result in a skip or oscillatory trajectory. According to literature [81], this can be done by computationally checking if there exists a solution for.

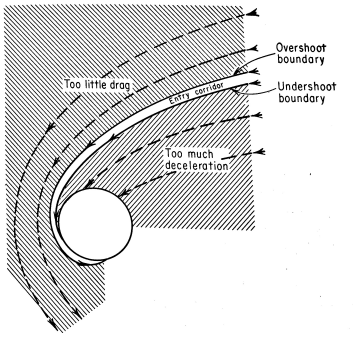

Figure 8.33: Entry Corridor

$$-\theta_f = \frac{0.5(\frac{L}{D})\ln\frac{\frac{V_e^2}{gR_0}}{\frac{V_0^2}{gR_0}}}{\frac{(\frac{gR_0}{V_0^2})-1}{\beta R_0(\cos\theta_f - 1)} - 1} \quad (8.112a) \qquad e^{-\beta y_0} - e^{-\beta y_f} = \frac{1 + (\frac{1}{\beta R_0})(\frac{gR_0}{V_{\theta=0}^2} - 1) - \cos\theta_f}{\frac{1}{2}(\frac{L}{D})(\frac{C_D A}{m\beta})\rho_0} \quad (8.112b)$$

8.17.4. Trajectory Specifications

Starting from the equations mentioned in Section 8.17.2, some assumptions can be made to create a first-order estimate of the trajectory. By assuming a spherical, non-rotating Earth, with an atmosphere at rest, and a vehicle with a flat trajectory plane, Equation 8.113a, Equation 8.113b and Equation 8.113c describe the general two-dimensional motion of a re-entry vehicle.

$$m\frac{dV}{dt} = -D - mg\sin\gamma \quad (8.113a) \qquad mV\frac{d\gamma}{dt} = L - mg\cos\gamma(1 - \frac{V^2}{V_c^2}) \quad (8.113b)$$

$$\frac{dR}{dt} = V\sin\gamma \quad (8.113c)$$

In gliding flight, for preliminary calculations, a few more simplifications can be considered. It can be assumed that $d\gamma/dt$ changes slowly with time, hence it can be approximated to 0. Additionally, the value of γ is considered to be small enough that $\sin\gamma \approx 0$. Therefore, the final equations for gliding flight are Equation 8.114a and Equation 8.114b.

$$m\frac{dV}{dt} \approx -D \quad (8.114a) \qquad 0 = L - mg(1 - \frac{V^2}{V_c^2}) \quad (8.114b)$$

On the basis of these equations, key parameters of the equilibrium glide can be calculated using the formulae depicted in Table 8.27.

Table 8.27: Equilibrium Glide Formulae

Parameter	Notation	Formula
Velocity ratio	$\frac{V}{V_c}$	$\sqrt{\frac{1}{2}\rho_0 e^{-\beta h}V_{c,0}^2 + \frac{W/S}{C_L}} = f(h)$
Equilibrium glide angle	$\bar{\gamma}$	$-\frac{1}{\beta R_e}\frac{2}{L/D}\frac{V_c^2}{V^2}$
Glide range	R_f	$-R_e\frac{1}{2}\frac{L}{D}\ln\left(1 - \frac{V_E^2}{V_c^2}\right)$
Glide time	t_f	$\frac{1}{2}\frac{V_c}{g}\frac{L}{D}\ln\left(\frac{1+V_E/V_c}{1-V_E/V_c}\right)$

continued on next page

Table 8.27 *– continued from previous page*

Parameter	Notation	Formula
Stagnation heat flux	q_c	$c_1 \frac{1}{R_N^n} \left[2 \frac{W/S}{C_L} \left(\frac{1}{V^2} - \frac{1}{V_c^2}\right)\right]^{1-n} V^m$
Loads	$\frac{a}{g}$	$+\frac{D}{W} + \sin\gamma = +\frac{D}{L}\left[1 - \frac{V^2}{V_c^2} - \frac{2}{\beta R_e}\frac{1}{V_c^2}\right]$

8.17.5. Entry Corridor and Footprint

Once the equilibrium glide is calculated, the entry corridor can be designed. An entry corridor should include the following limits:

- Overshoot and undershoot boundary
- Glide trajectory for maximum allowable heat flux
- Glide trajectory for maximum allowable loads

Lastly, starting form the formulae from Table 8.27, the lateral range of the glide trajectory can be calculated by maintaining a constant angle of attack and varying the bank angle. According to literature [59], the optimal bank angle for maximum lateral range is around $45\,[°]$. Therefore, once the stability of the vehicle is calculated, it should be tested what maneuvers it can perform.

8.17.6. Sensitivity Analysis

In order to perform a sensitivity analysis, the method described in Section 8.2 was used. The findings of the sensitivity analysis are documented in Table 8.28. As can be seen from the table, most controllable inputs do not

Table 8.28: Sensitivity analysis of the re-entry trajectory

Parameters:	**Dry Mass**	**Entry Velocity**	**Lift-to-Drag Ratio**	**Atmospheric Model**	**Lift Coefficient**
Change in value	$\times 1.25\,[-]$	$\times 1.25\,[-]$	$\times 0.75\,[-]$	Changed to exponential model	$\times 0.25\,[-]$
Relative change in maximum heatflux	$17\,[\%]$	$0.5\,[\%]$	$0\,[\%]$	$0\,[\%]$	$-0.58\,[\%]$
Relative change in maximum loads	$0\,[\%]$	$0\,[\%]$	$25\,[\%]$	$0\,[\%]$	$0\,[\%]$
Relative change in range	$0\,[\%]$	$66\,[\%]$	$-20\,[\%]$	$-0.02\,[\%]$	$-0.2\,[\%]$
Effect description	Max heat flux remains within margins.	The range does increase, which adds flexibility	A lower lift to drag is detrimental to the mission	The change is almost negligible.	No significant impact.
Requirements affected	None	None	None	None	None
Impact:	3	3	2	3	3

change the performance characteristics too much. The main worry is the possible change of the lift-to-drag ratio, also because that is the most possible change to happen in a real-life scenario. In order to prevent a situation where lower lift-to-drag ratio is induced, either control surfaces can be added to provide more lift, or the vehicle should have some maneuvers that could induce lift.

9 Integration

The individually designed subsystems in Chapter 8 need to be integrated for a coherent final design. Section 9.1 presents the methodology for this integration. Next, Section 9.2 presents the piping and instrumentation diagram of the vehicle, followed by the electrical block diagram in Section 9.3, and the data flow block diagram in Section 9.4. Lastly, the vehicle budgets are given in Section 9.5.

9.1. Methodology

The integration of H_2ERMES was performed in several steps, first, the initial design values were calculated manually to provide inputs into the iteration. For the iteration, a tool was written to iterate the mass values until convergence. This was done by calling each of the tools developed in Chapter 8 in turn and using the values from previous iterations as inputs for the tools. By repeating the iteration until the difference between wet mass between iterations is less than 0.1 [%] it is ensured that all mass values are internally consistent as shown in Figure 9.1.

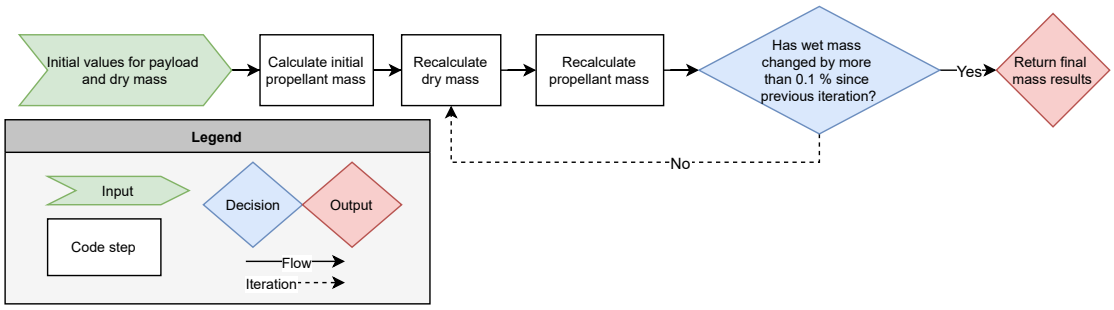

Figure 9.1: Integration code flowchart

The initial values used as a start of the iteration are presented in Table 9.1 while the final resulting values are presented in Section 9.5.1. After the mass convergence was achieved, all mass values were checked once more by the person responsible for each subsystem to ensure that all mass values are consistent and valid. Mostly this was the case, except for the boil-off calculation where the original estimation did not extrapolate well to the new values and the boil-off mass was vastly overestimated at 11855 [kg] and as such it was manually recalculated and the new values of 4897 - 6600 [kg]. Fortunately, both payload and boil-off come from the same tank of LH_2 and so the overestimated mass of boil-off can be simply assigned to increase in payload mass as presented in Table 9.4.

Table 9.1: Integration inputs

Input	Value	Input	Value
Payload mass	8000 [kg]	Insertion ΔV	5800 [m/s]
Dry mass	20642 [kg]	OF ratio	6 [−]
Wet mass	246684 [kg]	Vaccum T/W	1.2 [−]
Boil-off mass	1000 [kg]	Clearance height	2.5 [m]
Vacuum thrust	2.903×10^6 [N]	LH_2 design pressure	2×10^5 [Pa]
LH_2 for power generation mass	15.6 [kg]	LOX design pressure	2.5×10^5 [Pa]
LOX for power generation	132.8 [kg]	Boil-off design pressure	10^6 [Pa]
ACS propellant	765 [kg]	Landing leg material	Ti6Al4V
Re-entry coolant	3000 [kg]	Tank material	SS304L
Sea level I_{sp}	361.65 [s]	Re-entry g-forces	8 [−]
Vacuum I_{sp}	429.75 [s]	Launch g-forces	6 [−]
Sea level thrust chambers	8 [−]	Base radius	5 [m]
Vacuum thrust chambers	16 [−]	Cone half angle	10 [°]

continued on next page

Table 9.1 – *continued from previous page*

Input	Value	Input	Value
Landing ΔV	500 [m/s]	Radius of common bulkhead	4.8 [m]
Deorbit ΔV	210 [m/s]	Hydrogen tank height	12.65 [m]
Circularization ΔV	113 [m/s]	Top tank radius	2.5 [m]
Orbit raising ΔV	114 [m/s]		

After the mass distribution was finalized, the final positioning of all subsystems and their integration was performed. This is presented in a series of diagrams and budgets in the remainder of this chapter.

A maximum total mass target was defined based on a preliminary sizing estimation of New Glenn's second stage total launch mass, since no public data is available concerning this stage. The preliminary mass analysis utilized the only public cross section provided by Blue Origin [30], shown in Figure 9.2. It was assumed that the diameter was 7 [m], as per public data in the same document, and an estimation of the total tank volume for the second stage of 707 [m^3] was taken, by graphical measurements. Due to the further lack of public data regarding New Glenn's upper stage engine, it was assumed that the mixture ratio for the BE-3U engine was 5.5 [−], and a density of 1141 [kg/m^3] and 71 [kg/m^3], respectively for LOX and LH_2 was also assumed. As such, a volume for LOX and LH_2 of respectively 117 [m^3] and 530 [m^3] was found, meaning a total propellant mass of approximately 240 [t]. Assuming a propellant ratio of 0.9 [−], which is correspondent to historical data for similar second stages, once again due to the lack of publicly available data for New Glenn, a total wet mass of 267 [t] is found, adding to this the payload values for New Glenn present in its User's Guide [30], of 45 [t], the total mass at launch of the second stage of Neg Glenn with its payload is estimated to be 312 [t]. To account for the uncertainties in the presented calculation, a conservative total mass at the launch pad limit of approximately 300 [t] was set for the following iterations of the design of H_2ERMES.

9.2. Piping and Instrumentation

In Figure 9.3, the piping and instrumentation diagram (P&ID) is presented, which shows a detailed schematic of the layout and interconnection of all of the different elements constituting the feed system of the rocket's various fluids systems. In the diagram, three main systems are detailed. Firstly the helium feed system lines are represented in orange, these are used for delivering the pressurizing gas which deploys the stage's landing legs and actuates the pneumatic ball-valves. The H_2O_2 lines, represented in green, feed the reaction control system (RCS) which is used to orient and control the spacecraft, feeding a set of thruster blocks. Finally, the LH_2 and LOX lines, represented in red and blue, respectively, feed the main propellants to the turbopumps and to the thrust chambers. Additionally, the LH_2 line also feeds into the regeneratively cooled heatshield.

Regarding the general layout of the feed system, some common elements exist. In particular, the fill lines for all of the main, helium and H_2O_2 tanks have a quick disconnect for ease of interfacing, a filter to prevent the introduction of foreign object debris (FOD) in the tanks, as well as a main ball valve to regulate the filling of the

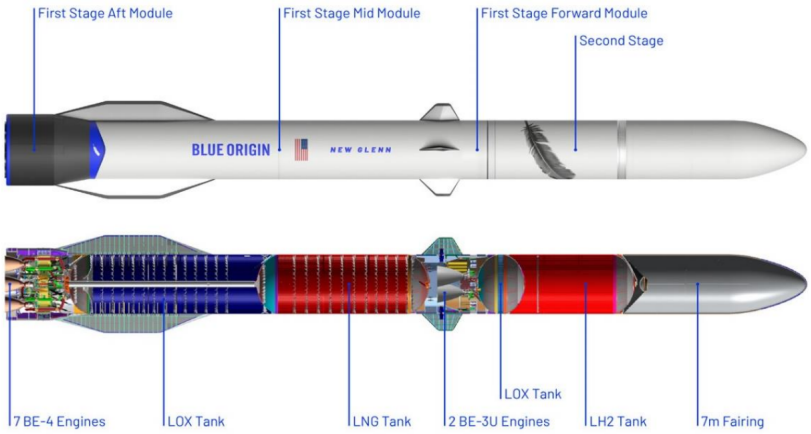

Figure 9.2: New Glenn Cross Section [30]

tanks. The LH_2, LOX and H_2O_2 tanks are filled from the bottom up to allow for easy draining of propellants in case of a launch scrub. Moreover, every tank has temperature and pressure sensors to ensure nominal conditions. In addition, the LH_2 and LOX main tanks have a pressure relief valve for venting the pressure in the case of a less drastic overpressure effect, and a burst disk to prevent bursting in the event of drastic overpressure.

Regarding the helium lines, two lines exit the tank at an adequate set pressure controlled by pressure regulators. To handle splitting of the helium lines for actuating the valves, manifolds are employed. Aside from a pressurizing gas, for the ball valves an electrical connection to a central engine control unit (ECU) is also necessary but not represented, as the actuation of these valves is controlled by a small solenoid valve within each actuator.

Concerning the H_2O_2 line, a pressure regulator is also used downstream of the tank to set a pressure adequate for the thruster blocks. A main valve in this line is also used to control the flow of fuel to each block.

Concerning the main LH_2 and LOX lines, the main tanks are connected to the header tanks by a valve, the latter tanks feed propellants to the turbopumps, and are separated by a filter, to ensure additional redundancy in preventing FOD in the turbopump area. After a pressure rise in the turbopumps, the propellants are fed into the thrust chambers, with a portion of the LH_2 being routed to the heatshield and to drive the turbines for both propellants, being expelled to the exterior after this phase. A valve is placed in between the heatshield and the LOX turbopump, which can be closed off during re-entry, as only the LH_2 turbopump is necessary in the aforementioned flight phase.

9.3. Electrical Block Diagram

In Section 8.11, the components and overall layout of the power subsystem was presented. In this section, the connections of the power network are presented graphically in Figure 9.4. The separation between the power generation and the power distribution part is clearly shown.

In the power plant section, the parallel configuration of the fuel cells is illustrated, so that failure of one of them does not influence the operation of the other, as the reactant distribution system reroutes it. This system is also responsible for the control of the reactant flows. To save on weight, there is no separate tank for the waste water, instead it directly leaves the system when the fuel cells are purged.

The power distribution and control section shows that the main power bus takes the output of the fuel cells, is regulated at $28\,[\mathrm{V}]$ and has direct current. Current conversion via inverters and voltage conversion via buck converters is done in a distributed manner. The specific power draw of each electronic equipment is detailed later in Section 9.5.2. One breakout circuit is the propulsion bus, which provides power to the lowest part of the vehicle, keeping the $28\,[\mathrm{V}]$ from the main power bus.

9.4. Data Flow

As an autonomous vehicle, H_2ERMES needs to detect signals from the environment, process them and decide a way to act. The exact procedures for this have not been developed for this report, but the interconnectedness of the vehicle's various subsystems have been illustrated with two diagrams. These will guide further development of software interfaces and data buses.

The first diagram, Figure 9.5 groups the electronic equipment by function: sensors which convert environmental, physical signals into digital data, processors which store and execute various programs to perform computations on the data, and actuators which affect the vehicle and the environment. Between these groups, a control loop appears: data to commands to physical effects to data again. Some data and commands are bidirectionally connected to the first stage, and through the telecommunications link, the ground segment. Telemetry includes the onboard camera stream and the various sensor values and housekeeping data to monitor the vehicle's health.

The second diagram, Figure 9.6 distributes the flow of data based on source and destination among the various systems interfacing with the vehicle's computer units. The directionality of the data flow is also shown. The data througput, measured in kilobits per second (Kbps) was calculated in Section 9.5.3.

9.5. Budgets

Having performed a first iteration of the design, the mass, power, data processing, link and ΔV budget can be established in the next sections.

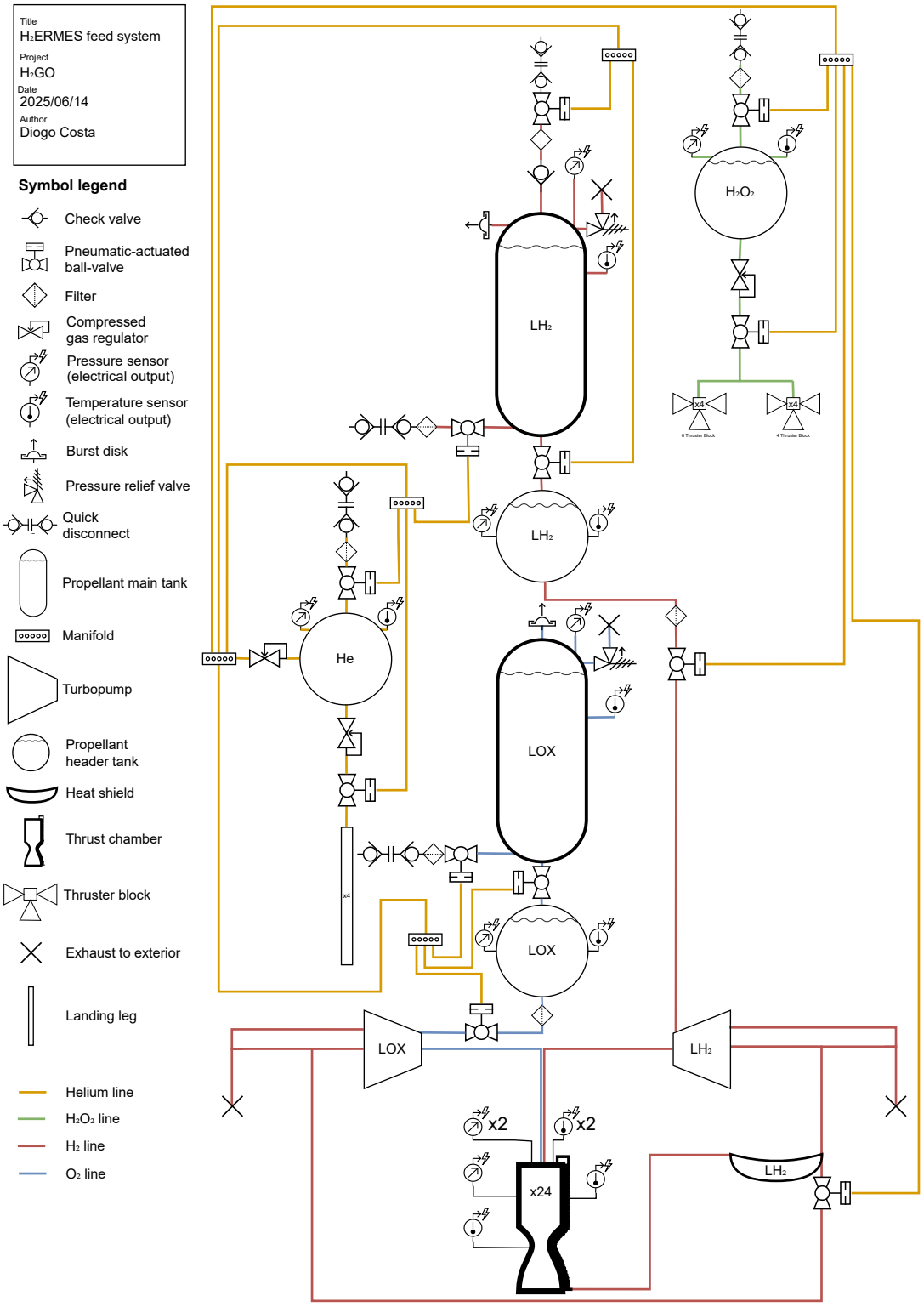

Figure 9.3: Piping and instrumentation of H_2ERMES

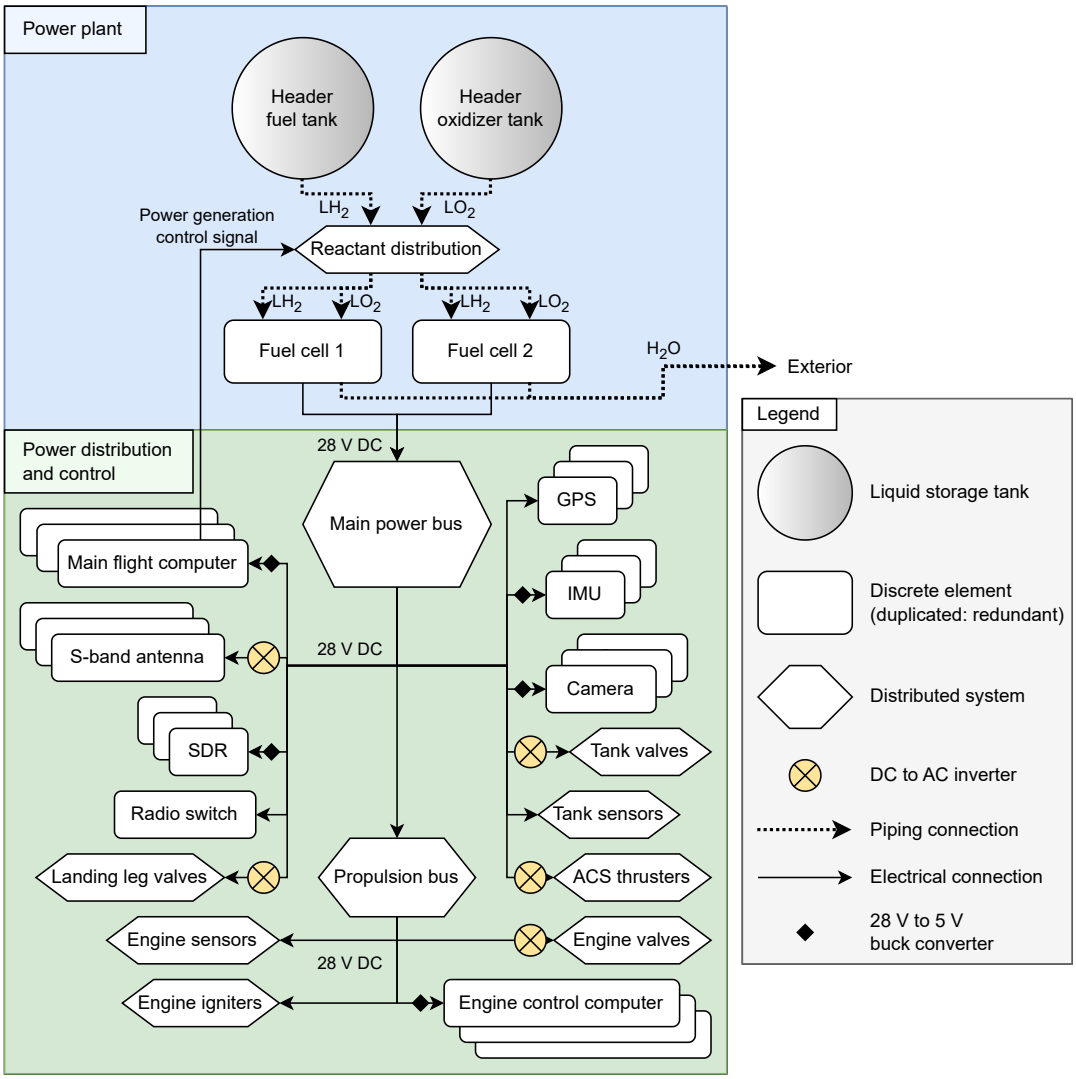

Figure 9.4: Electrical block diagram of H_2ERMES

9.5.1. Mass Budget

This section presents the final mass budget as calculated by various tools presented in Chapter 8. Table 9.2 presents the over all mass budget split between the dry mass of H_2ERMES and all consumables based on their purpose, Table 9.3 presents the split of main propulsion propellant mass by mission stage and Table 9.5 presents the split of dry mass by subsystem. Lastly, Table 9.4 shows the split of boil-off during different mission stages and the mass of hydrogen remaining to be transferred to the depot, as discussed in Section 8.4, this split depends on the specific flight profile.

9.5.2. Power Breakdown

For the sake of redundancy and fail-safe design, it states that H_2ERMES needs to be able to finish its mission even with only one operational fuel cell. As mentioned in Section 8.11, this poses an upper limit on continued power consumption of 7 [kW]. Following evaluation of component specifications, a list of power-consuming electrical equipment was tabulated, with a format based on a similar document from the Space Shuttle [68]. An additional 20 [%] margin is applied in the end to account for components that would be added later during detailed design. The results can be seen in Table 9.6. Lines in bold indicate a subsystem and their total power sums up all components within that subsystem.

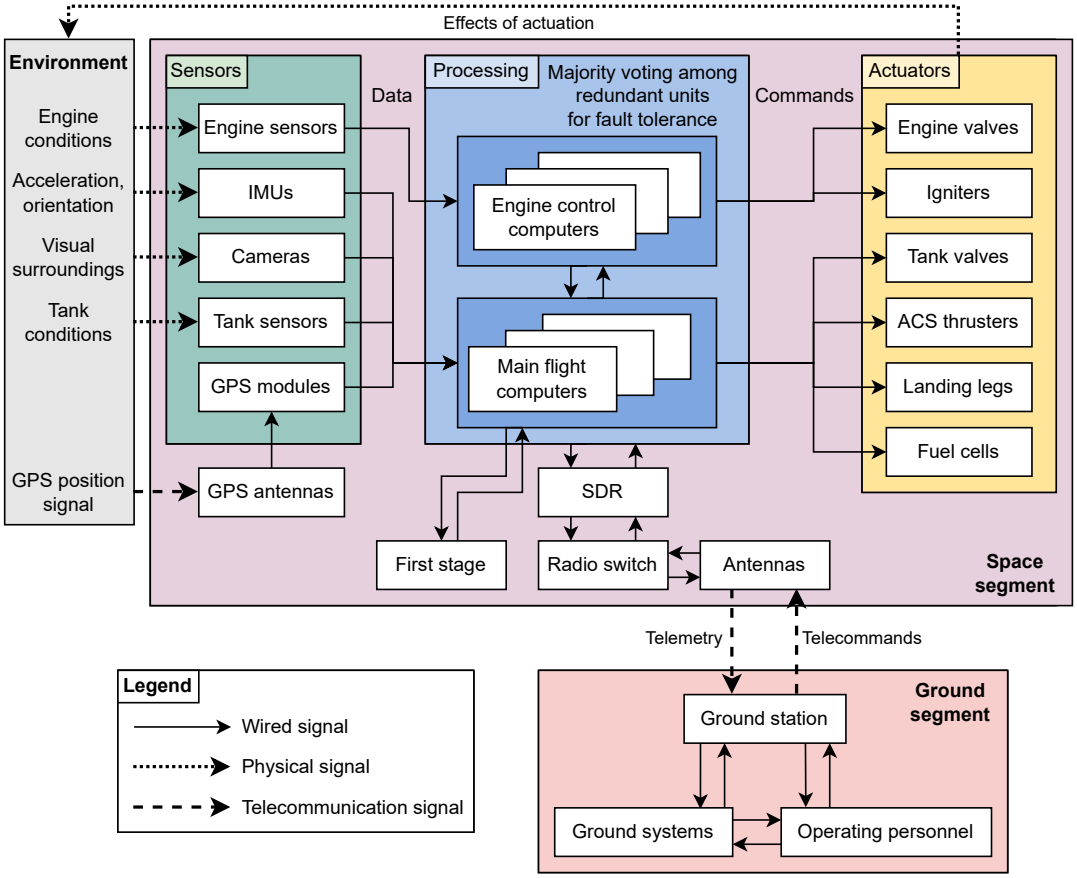

Figure 9.5: Communication flow diagram of H_2ERMES

Table 9.2: Top level mass budget

	Mass [kg]
Dry	39529
Main engine propellant	236806
ACS propellant	765
Re-entry coolant	3000
Power generation reactants	149
Boil-off + payload	19855
Pneumatic system Helium	1.79
Total (Wet mass)	300106

Table 9.3: Main engine propellant budget

	Mass [kg]
Insertion	224322
Transfer to target orbit	3974
Deorbit	2525
Landing	5985
Total	236806

Table 9.4: Boil-off and payload budget

	Mass [kg]
Boil-off during launch	1350
Boil-off before docking	0
Boil-off during refueling	698-787
Boil-off after undocking	4552 - 2760
Total boil-off	4897 - 6600
Payload	13255 - 14958

Table 9.5: Dry mass budget

	Mass [kg]		**Mass [kg]**
Main hydrogen tank	20287	**Docking system**	370
Main oxygen tank	9483	**Nose cone**	850
Header tanks	771	**Power**	231
Landing legs structure	1753	**Avionics**	361
Propulsion	2066	**Wiring**	322
ACS	158	**Interstage**	462
Heat shield	2200	**Pneumatic system**	215
Total	39529		

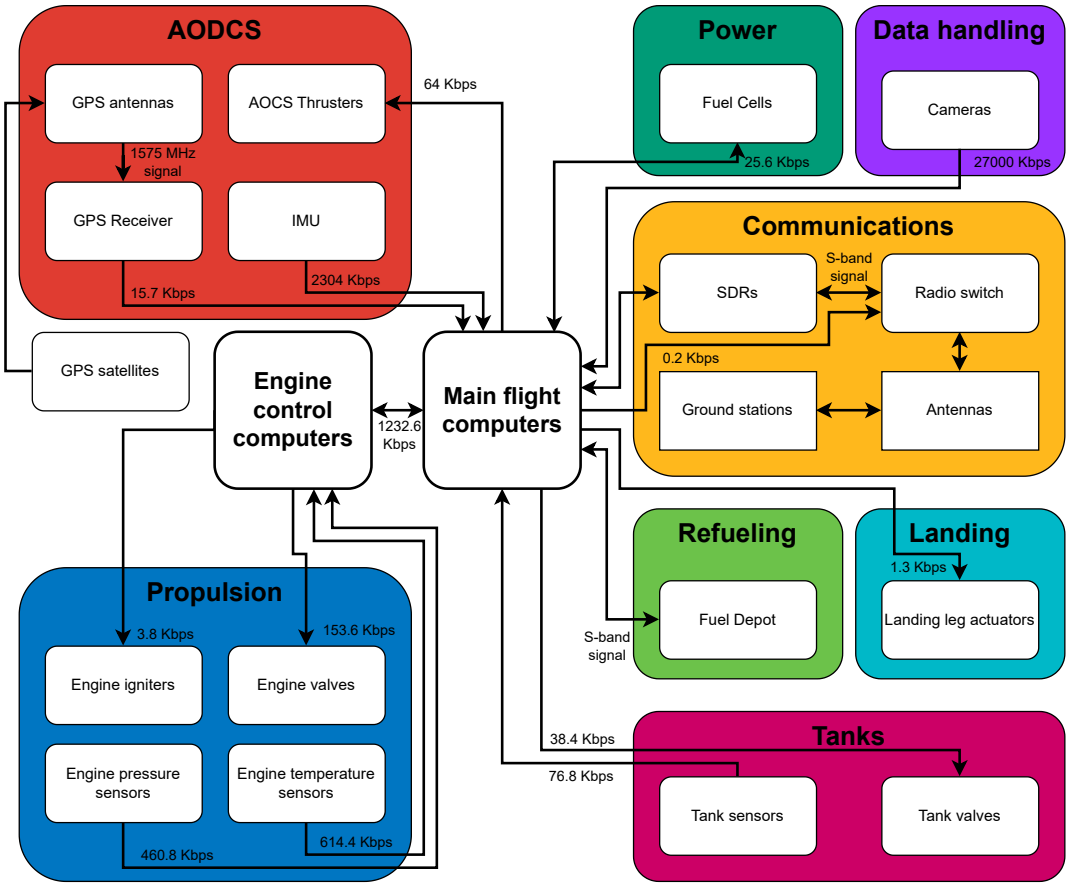

Figure 9.6: Subsystem data handling diagram of H_2ERMES

Table 9.6: Power breakdown

Component	Amount	Current	Voltage [V]	Power [W]	Total power [W]
AODCS					**1150**
GPS module	4	DC	28	15	60
IMU	3	DC	5	30	90
ACS thruster	40	AC	28	25	1000
Propulsion					**1584**
Engine pressure sensor	72	DC	28	3	216
Engine temperature sensor	96	DC	28	3	288
Engine valve solenoid	96	AC	28	5	480
Engine igniter	24	DC	28	25	600
Power					**800**
Fuel cell	2	DC	28	400	800
Communications					**400**
SDR	3	DC	5	50	150
Radio switch	1	DC	28	10	10
Antenna	3	AC	28	80	240
Data handling					**740**
Cameras	3	DC	5	20	60
Main flight computer	3	DC	5	100	300
Engine control computer	3	DC	5	100	300
Tanks					**156**
Tank sensor	12	DC	28	3	36
Tank valve solenoid	24	AC	28	5	120
Recovery					**80**
Landing leg solenoid	8	AC	28	10	80
Total					**4890**
Margin for future growth	20 [%]				978
Total with margin					**5868**

9.5.3. Data Processing Breakdown

In order to properly design for the downlink, the onboard flow of data needs to be quantified. The vehicle's electronics are the ones that generate information, therefore the list of equipment in this tally is the same as in the above Power Breakdown. The exception is the removal of the antenna, which is a passive element. Message size in bits refers to the estimated size of one packet of data sent to the flight computers, and polling rate is how many times it is sent per second. For the GPS, the message size is counted as 6 channels of 64 [b] floating point numbers each (latitude, longitude, altitude, speed, course, accuracy) and for the IMU, 12 channels of 64 [b] each (acceleration, orientation, angular velocity, magnetic field). For the computers, the data rate shown is the system housekeeping data that provides information about ongoing processes. The results of these calculations is presented in Table 9.7.

Table 9.7: Data processing breakdown

Subsystem	Amount	Message size [b]	Polling rate [Hz]	Data rate [Kbps]
AOCS				**2383.68**
GPS module	4	392	10	15.68
IMU	3	768	1000	2304
ACS thruster	40	16	100	64
Propulsion				**1232.64**
Engine pressure sensor	72	64	100	460.8
Engine temperature sensor	96	64	100	614.4

continued on next page

Table 9.7 – *continued from previous page*

Subsystem	**Amount**	**Message size** [b]	**Polling rate** [Hz]	**Data rate** [Kbps]
Engine valve solenoid	96	16	100	153.6
Engine igniter	24	16	10	3.84
Power				**25.6**
Fuel cell	2	128	100	25.6
Communications				**768.16**
SDR	3	256	1000	768
Radio switch	1	16	10	0.16
Data handling				**28536**
Cameras	3	150000	60	27000
Main flight computer	3	256	1000	768
Engine control computer	3	256	1000	768
Tanks				**115.2**
Tank sensor	12	64	64	76.8
Tank valve solenoid	24	16	16	38.4
Recovery				**1.28**
Landing leg solenoids	8	16	16	1.28
Total				**33062.56**
Margin for non-useful telemetry data	20 [%]			6612.512
Margin for future growth	50 [%]			16531.28
Total with margin				**56206.352**

9.5.4. Link Simulation

The pass of H_2ERMES over the ESTRACK Kourou ground station was simulated using Matlab's Satellite Scenario [1] with the parameters previously mentioned or cited in this report or the midterm report [2]. This produced a 3D view of H_2ERMES's orbit, which can be seen in Figure 9.7a. The antenna gain pattern visualization confirmed the full spherical coverage obtained from the Flexislot antennas and their positioning.

The telecommunication link's margin shows an inverted V-shape, which is clearly explained by the distance decreasing, then increasing as the vehicle passes over the ground station. At all times, the signal is routed through the antenna facing the ground station. The visible dip in signal strength near the top indicates a change in the antenna used by the radio switch. Overall, the margin is very large and difficulties in detecting the signal should not be expected. The uplink margin produced similar results, with an even larger margin owing to the powerful ground station transmission power. Though this tool did not provide a detailed breakdown of gains and losses, the conditions were recreated in the Matlab Satellite Link Budget app used for the midterm report [2], which verified the simulation's results.

9.5.5. Delta V Budget

The total delta V budget is formed by performing the orbit insertion and landing burn simulations for the final design values as presented in Table 9.8 and combining them with the values taken from conceptual design and it can be seen in Table 9.9.

[1] URL https://nl.mathworks.com/help/satcom/gs/satellite-scenario-overview.html [cited 2025-06-18]

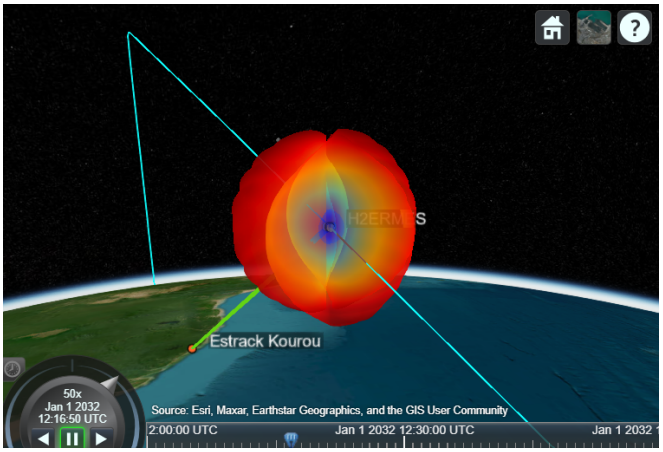

(a) Satellite scenario visualization with antenna gain pattern

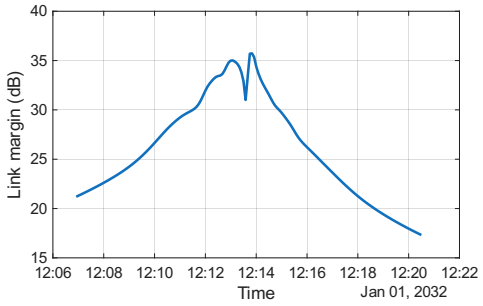

(b) Link margin for the downlink

Figure 9.7: Satellite antenna gain visualization and link margin for downlink.

Table 9.8: ΔV simulation inputs

Input	Value
Initial vacuum T/W	1.2 [−]
Initial sea level T/W	2.26 [−]
Ballistic coefficient	5044 [kg/m^2]
Velocity after re-entry	250 [m/s]

Table 9.9: ΔV budget

Flight stage	**Required** ΔV [m/s]	**Available** ΔV [m/s]	**Margin** [%]
Initial orbit injection	5629		
Injection to 600 [km] transfer orbit	114	6006	2.57
Circularization at 600 [km]	112		
Deorbit burn	157	192	22.56
Landing burn	369	450	21.95
Atmospheric drag compensation	10	11	10
Total	6391	6659	4.19

The ΔV margin is combined for orbit injection, transfer orbit and circularization as the inert mass of the vehicle does not change. Due to uncertainties, margins for the other maneuvers are high, mainly due to initial aerodynamics considerations, which were later refined, lowering the required ΔV. This represents a potential for later optimization. Even though the margins up to orbit circularization are low for preliminary design, the sensitivity analysis in Section 8.3.4 showcases that ΔV is not very sensitive to design changes. Therefore, these margins are considered acceptable.

10 Vehicle Overview

This chapter outlines the final vehicle overview, starting with the layout in Section 10.1. Which is followed by an overview of system characteristics in Section 10.2. Next the vehicle dynamics are given in Section 10.3, and the flight profile in Section 10.4. Section 10.5 shows the sensitivity analysis of the design.

10.1. Vehicle Layout

Once the subsystems have been designed, the internal configuration of the various systems is designed. This overview of the internal configuration is given in Figure 10.1.

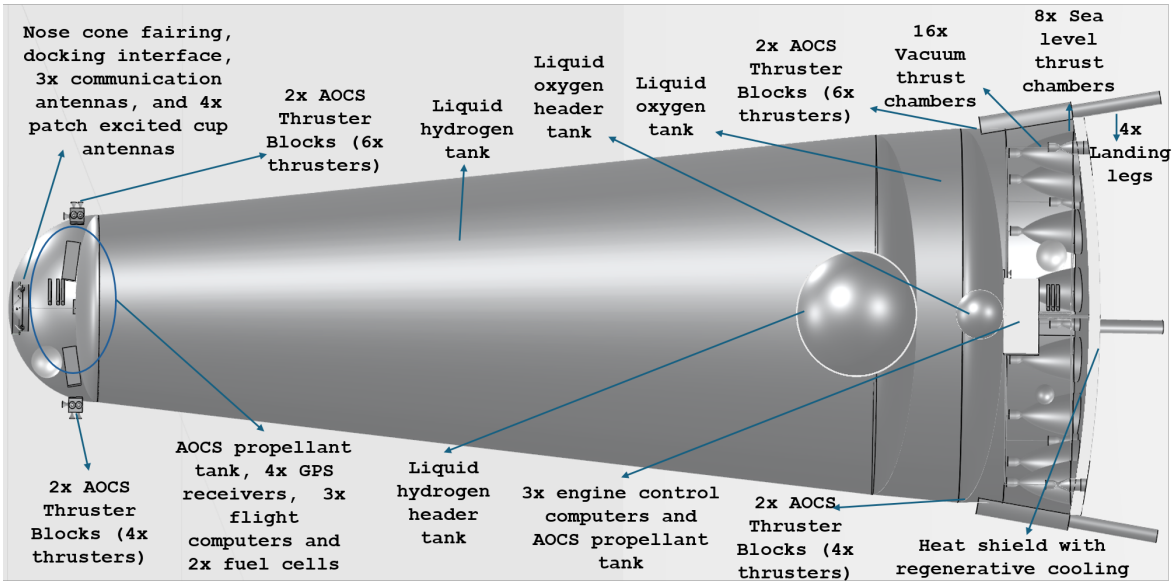

Figure 10.1: Configuration layout of H_2ERMES launch vehicle

Due to the volume occupied by the propellant tanks, a significant portion of the subsystems are situated in the nose cone. The bottom of the vehicle contains the propulsion systems, additional AOCS thruster blocks, and the heat shield.

10.2. System Characteristics

The section will discuss the system characteristics for H_2ERMES. These system characteristics are the result of the analysis done in Chapter 8 and Chapter 9. This will be done in Table 10.1.

Table 10.1: System characteristics for H_2ERMES

System	System Sizing	
AODCS	No. of thrusters	40 [−]
	Max thrust	250 [N]
	Slew rate	3 [°/s]
	Specific Impulse	160 [s]
Boil-Off	Boil-off during launch	1350 [kg]
	Average boil-off during orbit	3565 [kg]
	Average boil-off during transfer	743 [kg]
	Total boil-off	5749 [kg]

continued on next page

Table 10.1 *– continued from previous page*

System	Parameter	Value
Communications	Downlink Bit rate	56.2 [Mb/s]
	Power	40 [W]
Cooling	Coolant channel geometry	Rectangular
	Coolant channel dimensions	10×2 [mm^3]
	Temperature envelope	300-800 [K]
	Material	Stainless Steel 310
Landing Legs	Length	2.6 [m]
	Radius	0.18 [m]
	Thickness	1 [mm]
	Materials	Titanium alloy Ti6Al4V
Mission Design	Flight time	23.46 [h]
	Launch windows / year	150 [–]
Nosecone	Radius	2.5 [m]
	Thickness (steel)	2.22 [mm]
	Thickness (insulation)	2.10 [mm]
Power	Peak power	24 [kW]
	Continuous power	14 [kW]
	Dimensions of 1 fuel cell box	36x38x102 [cm^3]
Propulsion	Total sea level thrust	990.192 [kN]
	Total vacuum thrust	3529.968 [kN]
	Compound sea level specific impulse	361.645 [s]
	Compound vacuum specific impulse	429.748 [s]
	Total mass flow	837.6 [kg/s]
Hydrogen Main Tank	Total Volume	793 [m^3]
	Main tank hydrogen mass	55485 [kg]
	Thickness	4.4 [mm]
	Height	21.74 [m]
	Cone angle Φ	6.07 [°]
	End cap geometry	Elliptical
	End cap height (top)	1.25 [m]
Hydrogen Header Tank	Total Volume	14.5 [m^3]
	Header tank hydrogen mass	1116 [kg]
	Radius	1.66 [m]
	Thickness	2 [mm]
Oxygen Main Tank	Total Volume	161 [m^3]
	Main tank oxygen propellant mass	195815 [kg]
	Thickness	5.4 [mm]
	Height	2.4 [m]
	Cone angle Φ	4.58 [°]
	End cap geometry	Elliptical
	End cap height (bottom)	2.5 [m]
Oxygen Header Tank	Total Volume	5.4 [m^3]
	Header tank oxygen propellant mass	7295 [kg]
	Radius	1.19 [m]
	Thickness	2 [mm]
Vehicle Geometry	Max diameter	10 [m]
	Min diameter	5 [m]
	Total length	30 [m]

10.3. Vehicle Dynamics

This section will discuss the vehicle dynamics for H_2ERMES, specifically focusing on the control and stability characteristics of the vehicle.

10.3.1. Aerodynamic Characteristics

The aerodynamic characteristics of the vehicle calculated according to the methods outlined in Section 8.5.

Hypersonic Aerodynamic Coefficients

The aerodynamic coefficients for the hypersonic regime are given in Figure 10.2.

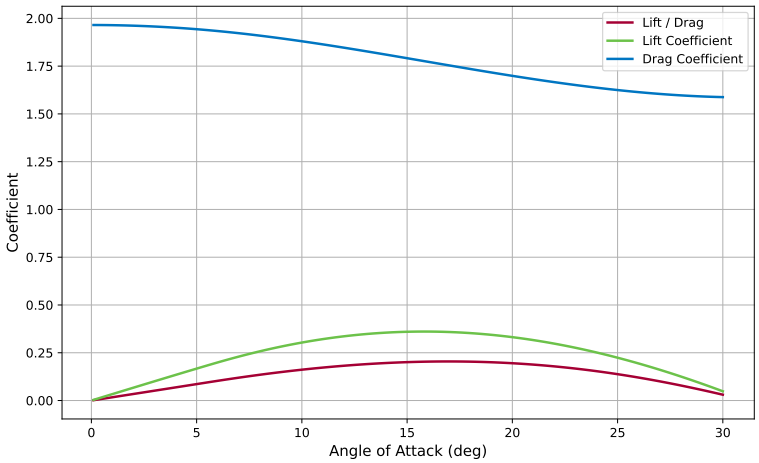

Figure 10.2: Hypersonic Aerodynamic coefficients for H_2ERMES

The maximum L/D occurs at an angle of attack of 17 [°]. Considering that there is an expected deviation of ± 3 [°], the aerodynamic parameters are identified for the desired angle of attack and the extreme cases of deviations.

Table 10.2: Hypersonic (Supersonic) Aerodynamic parameters for $\alpha_0 = 17 \pm 3[°]$

Aerodynamic Parameters	α_0**-3**	α_0	α_0**+3**
L/D	0.196	0.204	0.195
C_L	0.355	0.358	0.331
C_D	1.81	1.753	1.699
C_A	1.842	1.782	1.710
C_N	0.093	0.169	0.269

Subsonic Aerodynamic Coefficients

The subsonic aerodynamic coefficients during launch and re-entry are given in Figure 10.3 and Figure 10.4 respectively.

During the launch the lift-over-drag is negative, however this is not a problem since the first stage will dominate flight characteristics.

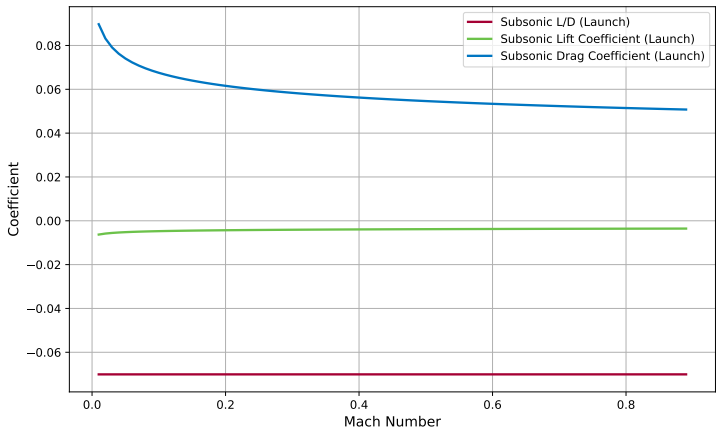

Figure 10.3: Subsonic Aerodynamic coefficients for H_2ERMES during Launch

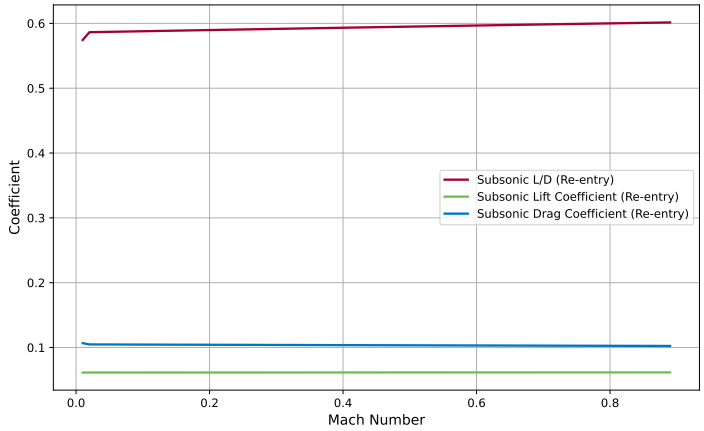

Figure 10.4: Subsonic Aerodynamic coefficients for H_2ERMES during Re-entry

The summarized aerodynamic parameters for the subsonic (and also the transonic regime) are provided in Table 10.3.

Table 10.3: Subsonic (Transonic) Aerodynamic parameters for $\alpha_0 = 17\,[^\circ]$

Aerodynamic Parameters	Nose first (launch)	Base first (re-entry)
L/D	-0.055	0.600
C_L	0.005	0.050
C_D	0.060	0.100

10.3.2. Vehicle Stability Characteristics

Stability with Constant Velocity

For the stability calculations the values for a_0 will be applied since the model assumes constant coefficients. However the pitch-damping coefficient is varied for $\alpha_0 \pm 3$, and the results for stability in constant velocity conditions is presented in Figure 10.5.

The pitch-damping coefficient is negative for all evaluated conditions and thus the system is always dynamically stable at constant velocities.

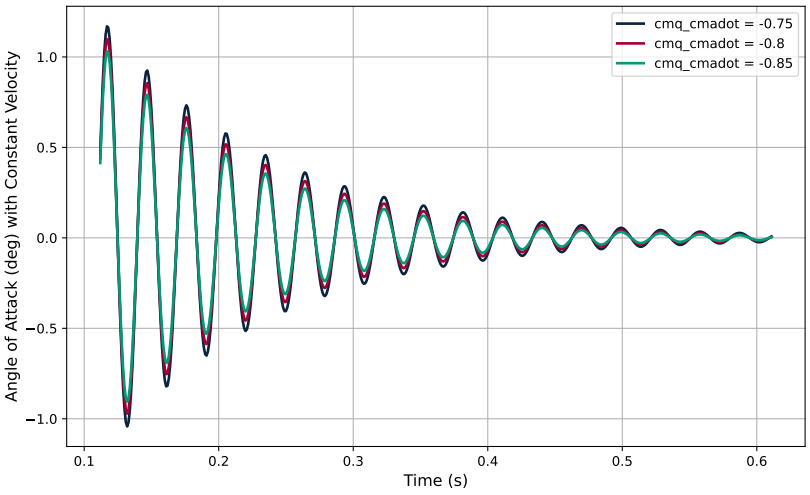

Figure 10.5: Stability for constant velocity H_2ERMES during Re-entry

Stability with Decelerating Velocity

The stability calculations for decelerating conditions is presented in Figure 10.6. The vehicle is not dynamically stable at decelerating velocities. This is a consequence of the pitch-damping coefficient not being large enough. Thus in further iterations the vehicle will require control surfaces or reconfigurations in the layout to ensure dynamic stability. As presented in Section 8.5.4, the dynamic stability of decelerating vehicles is calculated by Equation 8.23, where an increasing axial force coefficient C_A decreases the Euler-Cauchy damping coefficient. However an increasing C_A increases the pitch-damping coefficient as presented in Equation 8.20. Therefore ensuring the dynamic stability of the vehicle is presented as an optimization problem of realizing the optimal force coefficients.

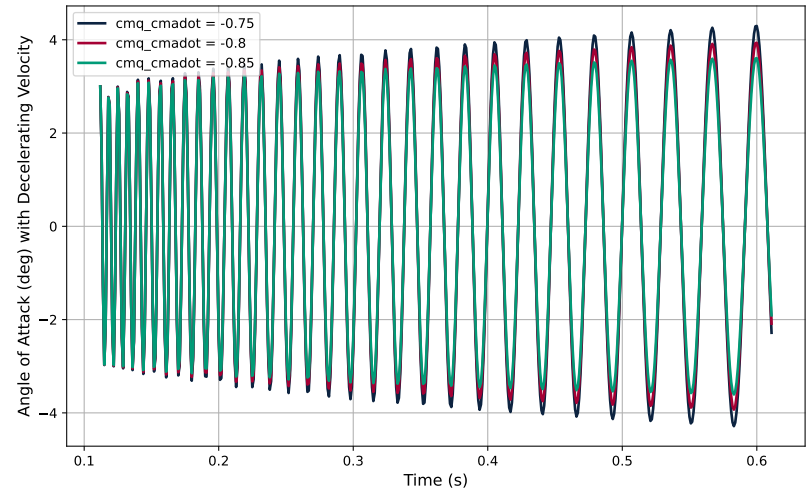

Figure 10.6: Stability for decelerating velocity H_2ERMES during Re-entry

10.4. Flight Profile

In this section, the flight profile and the associated timeline and trajectory are presented. First, time and phase angle associated with each mission stage is discussed based on the methodology presented in Section 8.4 to ensure

that H_2ERMES can reliable reach the required phase angle of 353.93 [°] in 23.46 [h] which were determined as flight limits in Section 8.4.1.

- **Launch:** During this stage H_2ERMES lifts off from CSG and is brought to suborbital trajectory by New Glenn first stage and continues to until it reaches a circular orbit at 200 [km] in altitude. This stage consists of the 190 [s][1] burn time of the first stage and 270 [s] burn time of the second stage for a total of 460 [s] or 0.13 [h], with the phase angle of 10.42 [°] retrieved from Section 8.3.1.
- **Phasing with the depot:** During this stage H_2ERMES will remain in the initial orbit until it reaches the required relative angle of -7.68 [°] (Section 8.4.2). The maximum time available to orbit phasing is limited the ability to also achieve the proper phase angle with the landing site at the end of the mission and was determined to be 7 by trial and error. Thus during this stage H_2ERMES will traverse between 0 and 1709 [°].
- **Orbit raising and rendezvous:** At this stage the orbit is raised from 200 [km] to 600 [km] and circularized at the target orbit. Due to the aforementioned orbit phasing this can be done such that H_2ERMES is now within 30 [km] of the depot and in approximately the same orbit, this is considered as concluding rendezvous. As this is done using a Hohmann transfer precisely 180 [°] are traversed.
- **Proximity operations:** Now very small propulsive burns and ACS thrusters are used to gradually approach the depot and maintain a close position to it so H_2ERMES can be captured by the depot's robotic arm and docked. The time allocated for this stage is 2 [h] as a middle value between 3 [h] taken by SpaceX Dragon[2] and 1 [h] taken by Soyuz[3]. During which the both spacecraft are considered to have the same orbital characteristics for the purposes of calculating phase changes, this is considered reasonable as the relative speed at this stage is measured in less than a [m/s] while the absolute speed is 7.558 [m/s].
- **Refueling operations:** With the payload Mass defined, the time for payload transfer can be calculated using Equation 8.101. This results in a total time of 1 [h], 31 [min], and 16 [s] for the maximum payload Mass. From this, also taking into account margins for system checks and uncertainties, the refueling time used for operational calculations is set to 3 [h], to still comply with *RQ-STK-RFL-1*.
- **Phasing with the landing site:** Equivalently, to phasing with the depot H_2ERMES has to reach a proper phase with the landing site back at CSG, however, the end of this stage is precisely constrained by the time CSG passes under the orbital plane. Reaching a lower orbit to "catch up" to the landing site can be done at no additional cost in ΔV as the orbit will eventually need to be lowered anyway for landing, while reaching a higher orbit to "slow down" with respect to CSG can be done if necessary although this will increase the ΔV. The range of phase angles is presented in Table 10.6.
- **Deorbit:** After arriving into the correct phase H_2ERMES is able to lower its perigee to 50 [km] altitude to initiate re-entry.
- **Re-entry:** Re-entry decelerates H_2ERMES from orbital velocity and allows it to land back at the launch site. The time and phase angle for this are retrieved from the re-entry calculation Table 10.7.

Table 10.4: Orbital parameters

Orbit	**Perigee altitude** [km]	**Apogee altitude** [km]	**Semi-major axis** [km]	**Period** [h]
Initial	200	200	6578.14	1.475
Target	600	600	6978.14	1.611
Transfer 200 **to** 600 [km]	200	600	6778.14	1.543
Re-entry	50	600	6703.14	1.517

It can be seen from Table 10.6 that for both immediate intercept and maximum depot phasing time, the minimum achievable phase is lower than the target of 352.93 [°] while the maximum one is higher. As such by finetuning the perigee of the phasing orbit it is always possible to ensure that H_2ERMES can re-enter and return back to the launch site. The final flight timeline and and example trajectory are presented in Figure 10.7 and Figure 10.8

[1] URL https://www.youtube.com/watch?v=KXysNxbGdCg&t=8363s&ab_channel=BlueOrigin [cited 2025-06-14]
[2] URL https://spaceflightnow.com/2022/04/27/crew-4-mission-timeline/ [cited 2025-06-14]
[3] URL https://spaceflightnow.com/2016/07/06/soyuz-ms-01-launch-to-docking-timeline/ [cited 2025-06-14]

Table 10.5: Set duration mission stages

Mission phase	Time [h]	Phase shift [°]
Launch	0.13	10.42
Orbit raising and rendezvous	0.77	180
Proximity operations	2	446.80
Refueling operations	3	670.20
Deorbit and re-entry	0.76	180
Total	6.66	1487.42

Table 10.6: Limit values for variable duration mission stages

	Immediate intercept		Longest depot phasing time	
	Minimum phase	**Maximum phase**	**Minimum phase**	**Maximum phase**
Phase shift [°]	3754	3922	2190	2288
Total phase shift [°]	201.59	8.97	346.37	84.03

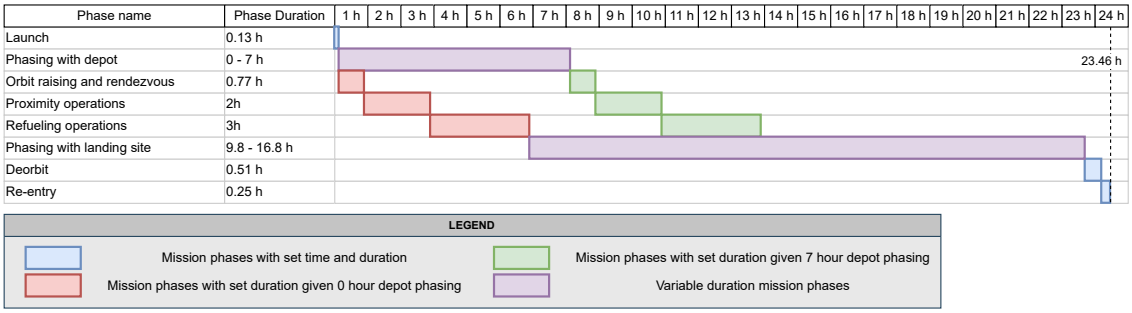

Figure 10.7: Flight timeline

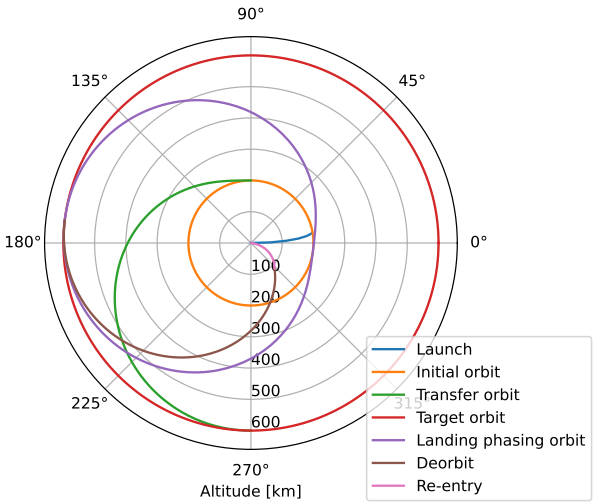

Figure 10.8: Mission trajectory

Furthermore, with the seven hour maximum waiting time, using Section 8.4.3 it can determined that there will be approximately 150 launch windows per year , this is significantly more than the 35.45 required to deliver 500 [t] of LH_2 per year (*RQ-STK-PLD-3*) given 14107 [kg] per launch. Of course, the actual launch cadence will be further limited by launch vehicle availability; nevertheless, when a launch vehicle is ready, it will have about three available launch windows per week.

Given that and the fact that within the roughly 24 [h] window, boil-off decreases with increasing phasing time before docking, these launch windows can be targeted so that the middle value of 14407 [kg] of LH_2 can be

conservatively used as an average payload for planning purposes.

In terms of re-entry, given the methodology described in Section 8.17, the entry conditions are be used to check whether an initial oscillation is present, the preliminary calculations of the equilibrium glide are performed, and en entry corridor is designed.

10.4.1. Initial Entry Conditions

The current initial entry conditions have been calculated based on the available de-orbit delta V and the orbital properties of the vehicle. The following values were used to check the skipping condition:

- $V_{entry} = 7974\,[\mathrm{m/s}]$
- $\gamma_{entry} = -1.35\,[^\circ]$
- $\frac{L}{D} = 0.2\,[-]$

The results showed that an initial oscillation is present, which ultimately leads a velocity at the beginning of the glide trajectory of $6052\,[\mathrm{m/s}]$

10.4.2. Equilibrium Glide

Based on the conditions at the beginning of the glide, Table 10.7 documents the preliminary results of the trajectory. An important note is that the values only reflect the time and ranges of the equilibrium glide, so it doesn't take into account the range and time of the oscillating part of the trajectory.

Table 10.7: Equilibrium Glide Results

Parameter	Value
Longitudinal glide range [km]	700
Lateral glide range [km]	500
Glide time [s]	178
Maximum stagnation heat flux [$\mathrm{kW/m^2}$]	14.4
Maximum loads [g]	4.7

10.5. Sensitivity Analysis

To perform a system-level sensitivity analysis, a program was written that could vary all design input parameters by a specified margin, connect to all design tools, and rerun these tools with the adjusted inputs. Some results of this analysis will be presented in the following tables. The first is the influence of the landing burn ΔV on the Mass budgets presented in Table 10.8.

Table 10.8: Sensitivity of Mass budgets to landing burn ΔV, sampled from $+5\,[\%]$ to $-50\,[\%]$

Landing Delta V [m/s]	**Gross Mass** [kg]	**Dry Mass** [kg]	**Hydrogen Mass** [kg]	**Oxygen Mass** [kg]
525	303077	39727	57212	205374
456.25	291227	38543	55267	196652
387.50	281227	37592	53638	189232
318.75	271454	36649	52027	182014
250	262711	35827	50590	175529

This ΔV budget was varied up by only $+5\,[\%]$ since it was already a very conservative estimate, hence why it was varied down by $-50\,[\%]$. As indicated in the table, a great potential performance increase is available if the landing burn ΔV budget can be minimized. Next, the sea level I_{sp} was varied in Table 10.9.

The value was varied by $\pm 10\,[\%]$ since a larger variation is most likely unfeasible based on literature [62], the flight profile and the atmospheric model which influences the engine performance. Next, the vacuum I_{sp} was varied and the results are presented in Table 10.10.

Table 10.9: Sensitivity of Mass budgets on sea level I_{sp}, sampled from -10 [%] to $+10$ [%]

Sea Level I_{sp} [s]	**Gross Mass** [kg]	**Dry Mass** [kg]	**Hydrogen Mass** [kg]	**Oxygen Mass** [kg]
325.48	308178	40216	58042	209155
361.65	300123	39533	56704	203121
397.81	291078	38535	55244	196534

Table 10.10: Sensitivity of Mass budgets on vacuum I_{sp}, sampled from -10 [%] to $+10$ [%]

Vacuum ISP [s]	**Gross Mass (**[kg]	**Dry Mass** [kg]	**Hydrogen Mass** [kg]	**Oxygen Mass** [kg]
425.55	311751	40549	58633	211804
436.75	280420	37616	53478	188560
447.95	255251	35256	49351	169878
459.15	239056	34171	46610	157511
470.35	226064	33431	44392	147476

This variation is again within realistic margins [62]. For example, one of the RD-0146 engine variants has demonstrated I_{sp} of 470 [s][4]. The results of this performance increase show an astounding decrease in gross mass. In comparison, the LH_2 mass needed for fuel cells was varied in Table 10.11.

Table 10.11: Sensitivity of Mass budgets on LH_2 needed for fuel cells, sampled from -20 [%] to $+20$ [%]

H2 Power Mass [kW]	**Gross Mass** [kg]	**Dry Mass** [kg]	**Hydrogen Mass** [kg]	**Oxygen Mass** [kg]
15.6	300123	39533	56704	203121
19.5	300166	39536	56715	203149
23.4	300132	39530	56710	203127

The hydrogen mass needed is well predictable because fuel cells are an established technology from the Space Shuttle program. A variation of ± 20 [%] is conservative. And yet, there is no meaningful impact on the gross mass.

Given the total count of inputs that can be varied, not all results of the sensitivity analysis program will be presented here. It is obvious that the H_2ERMES vehicle can be very sensitive to variations in parameters. This is line with literature and many previous missions [82].

It must be noted that, due to the highly coupled aspects of launch vehicle design, studying the results of one parameter change is merely indicative of a trend. For example, to get higher I_{sp}, the engines would most likely have to become heavier (as they would have to carry a heavier nozzle), they would require more volumetric budget, stronger (and thus heavier) mounting etc. The snowball effect is everpresent in launch vehicle design.

To mitigate potential issues with budgets (mass, ΔV, etc.), sufficient margins were built into the design of the H_2ERMES vehicle. For example, *RQ-STK-PLD-1* requires the vehicle to carry at least 10000 [kg] of payload, but the current design carries at least approximately 13000 [kg] as described in Table 9.4.

[4] URL https://www.russianspaceweb.com/rd0146.html [cited 2025-06-18]

11 Operational Assessment

Operational assessment covers the operational considerations of H_2ERMES. Firstly, Section 11.1 describes how the project will get to operational status, while Section 11.2 explains all the manufacturing and related considerations, Section 11.3 covers how H_2ERMES will interface with ground infrastructure. RAMS characteristics are covered in Section 11.4 and the cost and market are covered in Section 11.5 and Section 11.6, respectively

11.1. Design and Development Logic

The Design Synthesis Exercise (DSE) only covers the design phase of the project. To successfully execute the mission a further activities would have to be performed after the conclusion of the DSE. An initial overview of these activities is shown in Figure 11.1.

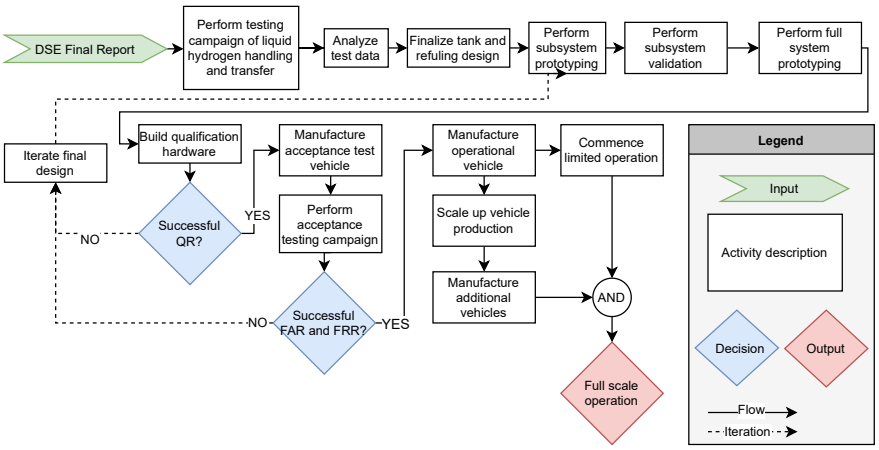

Figure 11.1: Project design and development flow diagram

The most crucial and uncertain part of the design that has to be validated before detailed design can commence is the handling and transfer of LH_2, therefore, the first step of post-DSE activities will have to be an extensive test campaign of this aspect of the vehicle. Afterwards, the prototyping and validation will be performed for individual subsystems and the integrated vehicle, respectively. When the prototyping is concluded, qualification and subsequently acceptance, hardware will be manufactured and tested. If Qualification Review (QR), Flight Acceptance Review (FAR), and Operational Readiness Review (ORR) are successfully passed, a first operational vehicle will be manufactured and launched.

As given by requirement *RQ-STK-RLV-3*, the first operational launch shall occur no later than 2032 and it will mark the beginning of limited operations. After the first operational launch, the production will need to be scaled up to produce additional launchers which can be used to reach the necessary launch cadence to deliver a sufficient amount of hydrogen to satisfy *RQ-STK-PLD-3*, at which point the full operation shall commence.

11.2. Manufacturing, Assembly, and Integration Plan

This section presents the Manufacturing, Assembly and Integration Plan (MAI plan). In addition, the main tests to be performed and the pre-launch operations have been included. The information for this plan has been compiled from various sources explaining the activities prior to launch, for example, the assembly activities for Ariane 6[1], engine testing from Skyrora[2] or pre-launch testing of NASA's Space Launch System[3].

[1] URL https://www.esa.int/Enabling_Support/Space_Transportation/Ariane/Assembling_Ariane_6_for_launch [cited 2025-06-18]
[2] URL https://skyrora.com/rocket-engine-testing-what-how-and-why/ [cited 2025-06-18]
[3] URL https://www.youtube.com/watch?v=Om6zyUS1330 [cited 2025-06-18]

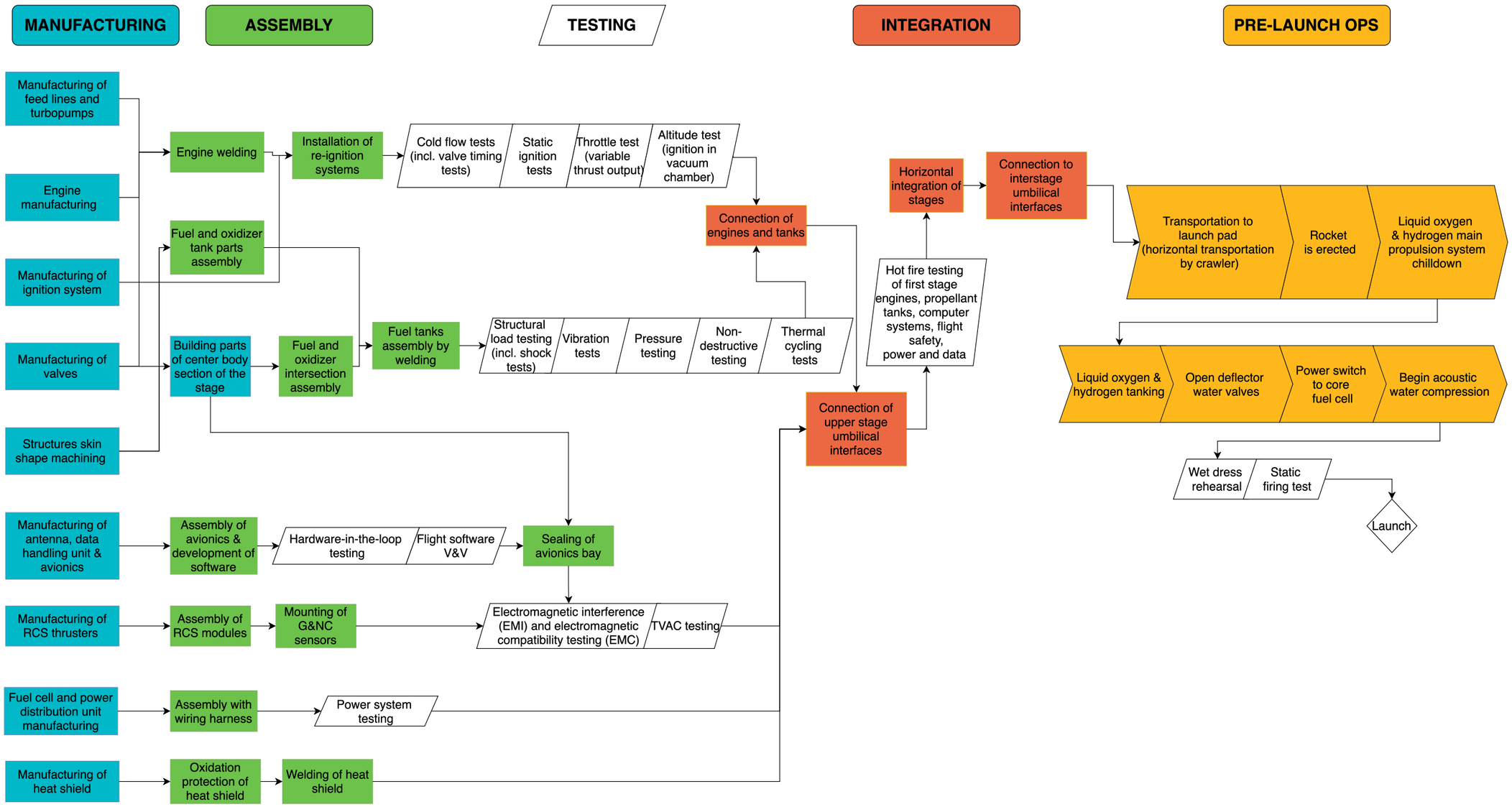

Figure 11.2: Manufacturing, Assembly, and Integration Plan flowchart

11.3. Operational and Logistical Concept

This section aims to outline the operations of the vehicle and its interaction with the surrounding infrastructure. The overview of the operations can be seen in Figure 11.3.

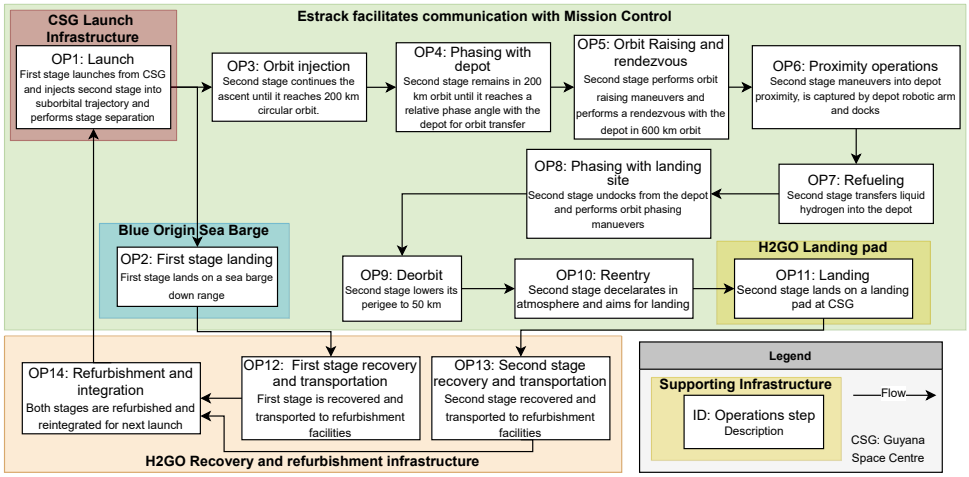

Figure 11.3: Operational flow diagram

The operational flow diagram shows all mission phases as presented in Section 8.4, and the infrastructure necessary to support them, which is further split between existing infrastructure and infrastructure that will need to be developed as a part of this project:

Existing infrastructure

- **Guiana Space Centre launch infrastructure:** There are several options for adapting existing CSG infrastructure to support this launch. The launch complexes Ensemble de Lancement Multilanceurs (ELM) and Ensemble de Lancement Soyouz (ELS) are currently being repurposed to support multitude of commercial launch vehicles[4][5], by cooperating with these other launch vehicle programs, the costs of adapting the launch complex would be minimized. Alternatively, the currently inactive Ensemble de Lancement Ariane-2 (ELA2) could be rebuilt in cooperation with Blue Origin, allowing for greater flexibility in the design and use of the launch complex while leveraging Blue Origin's experience in rebuilding Launch Complex 36 at Cape Canaveral[6].
- **Estrack:** ESA's ground station network will enable communication with H_2ERMES throughout the mission as it is uniquely fit for the purpose, it includes LEO communication ground station around the world including one in Kourou specifically to facilitate communications during launch[7].
- **Blue Origin Sea Barge:** Lastly, the Blue Origin's Landing Platform Vessel 1[8] or equivalent will be used to serve as an off shore landing platform for the New Glenn first stage and will subsequently bring it back to Port Kourou for refurbishment and reuse.

Project specific infrastructure

- **Landing pad:** To enable the landing back at the launch site a landing pad will be constructed close to the launch complex similar to SpaceX's Landing Zones at Cape Canaveral[9] and Vandenberg Space Force base[10]. Since the total sea level thrust of H_2ERMES is comparable to that of one Merlin engine used for Falcon 9 landings[11], a comparable simple pad made of heat resistant concrete is considered sufficient to support landings.

[4] URL https://europeanspaceflight.com/pld-space-likely-to-be-the-first-to-use-new-launch-complex-in-kourou/ [cited 2025-06-14]
[5] URL https://europeanspaceflight.com/maiaspace-tapped-to-take-over-soyuz-site-in-french-guiana/ [cited 2025-06-14]
[6] URL https://www.blueorigin.com/new-glenn [cited 2025-06-16]
[7] URL https://www.esa.int/Enabling_Support/Operations/ESA_Ground_Stations/Estrack_ESA_s_global_ground_station_network [cited 2025-06-16]
[8] URL https://www.bairdmaritime.com/work-boat-world/other-workboats/vessel-review-landing-platform-vessel-1-booster-recovery-platform-to-support-blue-origins-commercial-spaceflight-programs [cited 2025-06-17]
[9] URL https://www.faa.gov/space/stakeholder_engagement/SpaceX_Falcon_SLC_40_EA [cited 2025-06-16]
[10] URL https://spaceflightnow.com/2015/02/17/spacex-leases-property-for-landing-pads-at-cape-canaveral-vandenberg/ [cited 2025-06-16]
[11] URL https://www.spacex.com/vehicles/falcon-9/ [cited 2025-06-17]

- **Recovery and refurbishment infrastructure:** Similarly to the other infrastructure, these facilities are nothing new as both SpaceX[12] and Blue Origin[13] have built them and are currently operating. The processes performed in these facilities are further discussed in Section 11.4.2.

11.4. Reliability, Availability, Maintainability and Safety

The Reliability, Availability, Maintainability, and Safety (RAMS) characteristics of a system are a set of tools that ensure that a system fulfills the mission for which it was designed [83, 84, 85]. These keywords are defined as;

- **Reliability**: Ability to perform a specific function.
- **Availability**: Ability to keep a functioning state in the given environment.
- **Maintainability**: Ability to be timely and easily maintained.
- **Safety**: Ability not to harm people, the environment, or any assets during a whole life cycle.

These characteristics are expanded upon in the respective subsections.

11.4.1. Reliability and Availability

The reliability function is theoretically defined as the probability that a product performs its intended function for a specified mission profile. Performing a reliability analysis is critical to understanding component failure mechanisms and integrated systems failures, which are then worked upon. The availability is intrinsically tied to the reliability analysis since a system's ability to maintain a functioning state in the given environment directly implies that it performs the intended function. For this RAMS characterization, these two parameters will be treated as one and investigated together.

This analysis is performed using methods outlined by the Flight Aviation Authority (FAA) [86]. This method is exceedingly comprehensive and relies on a highly detailed system design in order to investigate the system's reliability. Considering a similar approach, the reliability of the system for H_2ERMES will be analyzed using the assumptions made and the potential impact on the performance of the system. The assumptions are graded according to the rubric in Table 11.1. The assumptions and their reliability assessments are given in Table 11.2;

Table 11.1: Reliability assessment score for assumptions

Score	Reliability	Assumption Validity	Design Reliability and Considerations
5	Very high reliability	Assumptions are robust and well-validated	Design is highly reliable; deviations have low or negligible impact on performance.
4	High reliability	Assumptions are mostly validated or based on solid precedents, but not fully proven in the current context.	Design is reliable; minor deviations may cause modest performance impacts.
3	Design is reliable	First order estimates or simplified models are used; some assumptions are unverified or generalized	Design is acceptable; performance is noticeably impacted by deviations
2	Moderate reliability	Assumptions are weakly justified; significant uncertainty exists.	Design is only conditionally reliable; performance is highly sensitive to deviations.
1	Low reliability	Assumptions are speculative or untested.	Design is not reliable; cannot proceed without further validation and detailed analysis.

[12] URL https://www.nasaspaceflight.com/2014/11/pad-39a-spacex-groundwork-falcon-heavy-debut/ [cited 2025-06-16]
[13] URL https://www.blueorigin.com/new-glenn [cited 2025-06-16]

Table 11.2: Assumptions

ID	Assumption	Potential Impact/Failure	Mitigation	Reliability
AS-AERO-01	Supersonic aerodynamic characteristics are demonstrated by low hypersonic characteristics.	Uncontrolled instability.	Perform CFD and wind-tunnel tests for design validation and further iterations.	1
AS-AERO-02	Transonic aerodynamic characteristics are demonstrated by subsonic characteristics.	Uncontrolled instability.	Perform CFD and wind-tunnel tests for design validation and further iterations.	1
AS-AERO-03	There is no shock formation in the hypersonic regime.	Inaccurate aerodynamic coefficients.	Perform CFD and wind-tunnel tests for design validation and further iterations. Proven method for hypersonic calculations.	3
AS-AERO-04	There is no tangential pressure or shear in the hypersonic regime.	Inaccurate aerodynamic coefficients.	Perform CFD and wind-tunnel tests for design validation and further iterations.	3
AS-AERO-05	Inviscid and collision less flow of particles in the hypersonic regime.	Inaccurate aerodynamic coefficients.	Perform CFD and wind-tunnel tests for design validation and further iterations.	3
AS-AERO-06	H_2ERMES vehicle is characterized by the blunt cone geometry.	Inaccurate aerodynamic coefficients.	Perform CFD and wind-tunnel tests for design validation and further iterations.	3
AS-AERO-07	The base cap is fully illuminated by incoming particles.	Inaccurate aerodynamic coefficients.	Perform CFD and wind-tunnel tests for design validation and further iterations.	4
AS-AERO-08	Drag coefficient remains constant through flight.	Inaccurate stability calculations.	Perform CFD and wind-tunnel tests for design validation and further iterations.	3
AS-PROP-01	The O/F ratio does not change throughout the flight.	Performance of the engine throughout ascent.	Optimize the O/F ratio to work well throughout all phases of flight.	3
AS-PROP-02	There are no combustion instabilities in the thrust chambers.	Loss in performance or at worst explosion in the engines.	Making smaller thrust chambers alleviates combustion instabilities, they mostly happen in larger engines, like in first stages.	4
AS-PROP-03	All of the components of the thrust chambers are able to withstand re-entry.	Loss of mission.	Testing the components in re-entry conditions (test flights), or more detailed re-entry heating calculations for those areas.	2
AS-PROP-04	The pintle injectors used for the thrust chambers can throttle from 100 [%] to 30 [%] of max thrust.	Higher Accelerations than projected due to inability to modulate thrust.	Test the injectors and hotfire the engines in land.	3
AS-PROP-05	Non-viscous, incompressible, steady flow for both propellant and oxidizer.	Slight mismatch in real channel areas of the feed system.	Add a safety margin in the channel diameters in case of viscous effects.	2
AS-PROP-06	Assumes tank pressure does not decrease from design pressure.	Non-functional feed system.	Add pressure sensors in tank and abort mission if pressure drops below a threshold because there is risk of mission failure.	3
AS-PROP-07	Fluids are initially at rest in the tanks and the increase in dynamic pressure directly translates into a decrease in static pressure.	It is a conservative assumption. If there's a slight flow at the tanks, the decrease in static pressure would be smaller than assumed.	CFD inside tank.	4
AS-PROP-08	The mass flow of all the thrust chambers is the same.	Potential unpredicted balances in thrust from each chamber due to mass flow variations.	Test the functioning of the entire propulsion system thoroughly on ground, to ensure that the feed system design can ensure stable mass flows.	3
AS-ADCS-01	Impulsive shots during maneuvers.	Delayed arrival at required orientation/position.	Simulations for faulty maneuvers.	4
AS-ADCS-02	Thrusters fire at maximum thrust.	Thruster fails to produce maximum thrust.	Add thrusters for redundancy to perform maneuvers with a lower thrust level.	3
AS-ADCS-03	Slew rate is averaged to be 3 [°/s].	Slew rate is not enough to perform maneuvers in orbit.	Use simulations to replicate extreme maneuvers with chosen slew rate.	3
AS-COOL-01	The heat shield incident heat flux is uniformly distributed across the heat shield surface.	Localized peak heat fluxes melting parts of the vehicle or oversized heat shield.	Hypersonic wind tunnel testing and CFD to better predict the incident heat flux.	2
AS-COOL-02	The coolant acts as a bulk fluid.	Worse cooling performance than expected, heat shield melting.	Validating the model, making better models (CFD), testing heat transfer and coolant properties of LH_2.	4
AS-COOL-03	The coolant heat flux is determined using the Taylor empirical relationship which is derived for a similar flow regime.	Worse cooling performance than expected, heat shield melting.	Validating the model, making better models (CFD), testing heat transfer with LH_2.	4
AS-COOL-04	The 1-D heat transfer model is sufficiently representative to analyze the heat transfer.	Worse cooling performance than expected, heat shield melting.	Validating the model, making better models (CFD), testing heat transfer with LH_2.	3
AS-COOL-05	The heat shield material is a stainless steel alloy with a high maximum operating temperature and cryogenic compatibility.	Different material might result in different performance and/or mass.	Contacting a material supplier, material qualification tests.	4
AS-COOL-06	The pressure drop inside the coolant channels can be estimated with the Darcy-Weisbach equation.	Higher pressure drop, insufficient cooling, heat shield melting.	More analysis of the coolant flow inside the channels (CFD) and extensive ground testing with LH_2.	2
AS-COOL-07	The material database data for SS310 is a good enough approximation for realistic material performance.	Structural failure of the heat shield.	Contacting a material supplier, establishing QA and QC procedures, material qualification tests.	3

continued on next page

Table 11.2 *– continued from previous page*

Assumption ID	Assumption	Potential Impact/Failure	Mitigation	Importance
AS-COOL-08	The heat shield will oxidize on the surface and have an emissivity of at least 0.9 [−].	If the surface cannot be oxidized and/or has a low emissivity, more coolant will be needed.	Contacting a material supplier, running oxidation and heat radiation measurements.	4
AS-COOL-09	The first 100 [µm] of the heat shield wall thickness will be neglected for structural calculations to account for its reduced material properties.	Structural failure of the heat shield because of the reduced material properties due to oxidation.	Contact a material supplier, running structural tests of the oxidized material.	3
AS-LAND-01	Shock absorber force calculations are averaged.	Shock absorber force might be underestimated, leading to a possible underestimation of the required stroke length.	Safety factors are added. For future, more detailed analysis of the internal force, and updating the model to use this accordingly.	3
AS-LAND-02	Aero covers do not consider aerodynamics.	Increased parasitic drag, possible thermal issues.	Safety factors for sizing are implemented. Future: consider aerodynamic loads and optimize the shape. Won't impact the mass/landing subsystem, but will impact aero.	2
AS-LAND-03	Main strut assumed to be pinned-pinned connection.	Buckling analysis slightly off. Based on the sizing, should not impact too much as the rod is not close to critical slenderness ratio, otherwise other buckling failure mode should be used (both are present in the sizing).	Pinned-fixed connection was analyzed, pinned-pinned is more conservative. Safety factors should otherwise take it into account, which have been applied.	4
AS-TANK-01	Buckling stress over structure.	Buckling assumed to act over the entire structure, not considering local buckling.	Make a reliable FEM model to model local buckling accurately and add extra reinforcement if necessary.	2
AS-TANK-02	Manufacturing defects are translated by the use of knockdown factor.	Assuming the local imperfections within the structure can be translated into a conservative buckling estimation	Experiment to quantify the effect of defects on stress concentration and take it into account in design iteration.	3
AS-TANK-03	Ullage assumed to 10 [%]	Ullage volume overestimated, based on first order sizing.	Refine boil-off calculation to find the ullage needed.	4
AS-TANK-04	Shear due to aeroelasticity is not considered in the sizing process.	In accordance to the aerodynamic assumptions, shear due to aeroelasticity is not considered in sizing. It would introduce extra stress in the structures.	Perform wind tunnel test to estimate this effect.	3
AS-FATG-01	The tank will be clamped at both ends.	Overestimates the stress caused due to thermal stresses since vehicle can expand longitudinally.	Use FEM software to more effectively model thermal stress due to shifts between cryogenic temperature and ambient temperature.	3
AS-FATG-02	The delta gamma coefficient will be assumed to be 0.12 [−] since this leads to a conservative estimation.	Conservative assumption to calculate pressure inside conical tank. Oversizes the tank for fatigue.	Use experiments to get right coefficients to model pressure loading in conical tanks.	3
AS-FATG-03	The effect of the conical tank geometry on Paris crack growth coefficients will not be considered for now. A safety factor of 2 will be taken.	Tank failure since the crack growth rate for conical tanks has not been researched with the same level of detail as cylindrical tank.	Experiments to evaluate crack growth rate characteristics for conical tanks. Take safety factor for preliminary design stage.	1
AS-FATG-04	The effect of the conical tank geometry on Miner's cycle coefficients will not be considered for now. A safety factor of 2 will be taken.	Tank failure since the fatigue for conical tanks has not been researched with the same level of detail as cylindrical tank.	Experiments to evaluate fatigue characteristics for conical tanks. Take safety factor for preliminary design stage.	1
AS-FATG-05	To make a conservative estimate, it will be assumed that at these stages there is an effective ΔT of 280 [K]	Conservative assumption to calculate thermal stresses inside tank and oversizes the tank to handle thermal stress which makes it more robust.	Use FEM software to better understand thermal expansion of conical tank.	3
AS-HEAD-01	The mass of the struts holding the header tank will be assumed to be negligible.	Increase in dry mass.	Take a margin of 10 [%] to account for this increase.	3
AS-BOIL-01	Refueling operations will not cause boil-offs.	Decrease in payload mass delivered to depot.	Create a FEM model to accurately model the thermodynamic environment in the tank when fuel is actively unloaded.	1
AS-BOIL-02	Hydrogen temperatures remain constant during refueling and launch.	Decrease in boil off mass since decrease in temperature means it can absorb more heat before reaching vent pressure.	Create a FEM model to accurately model the thermodynamic environment and temperature of gas in the tank when fuel is actively unloaded for refueling operations.	3
AS-BOIL-03	The heat flux entering the tank will be comprised of solar, albedo and planetary.	Marginal increase in boil off.	Take a safety factor.	4
AS-BOIL-04	The area incident for the heat flux is the projected area of a truncation cone when viewed from the front.	Assumes the worst case scenario. In reality, it will always be smaller than this.	Create a thermal environment model that accounts for vehicle attitude and the incident fluxes.	4
AS-BOIL-05	The orbital insertion phase will be considered to be instantaneous.	Increase in boil off mass which leaves less payload to be delivered.	Create a FEM model to accurately model the thermodynamic environment in the tank when fuel is actively unloaded.	2
AS-BOIL-06	The effect of heat generated on board will be considered to be negligible.	Marginal increase in boil off mass which leaves less payload to be delivered.	Create active thermal environment model of components that cause heat to be generated.	3
AS-BOIL-07	The final absorptivity of the tank wall will be 0.2 [−].	Increase in boil off mass which leaves less payload to be delivered.	Investigate the effect of applying coating on tank wall and refurbishment concerns due to this coating during ascent and reentry.	1

continued on next page

Table 11.2 *– continued from previous page*

Assumption ID	Assumption	Potential Impact/Failure	Mitigation	Importance
AS-BOIL-08	The pressure inside the tank will remain constant at 2 [bar] during the orbital insertion phase.	The pressure inside the tank will not fall below 2 [bar] which is required for structural safety during launch.	Keep an internal heater inside the hydrogen tank to ensure the pressure is held at 2 [bar].	3
AS-TRAJ-01	A spherical, non-rotating Earth is assumed for the preliminary re-entry conditions trajectory calculation.	Ignoring effect of rotation can lead to big difference in skipping behavior prediction.	Perform calculations using the second order approximation method as described in Re-entry Systems book.	3
AS-TRAJ-02	The exponential model assumes that the atmosphere is an ideal gas.	Slightly less accurate calculations, not very relevant for the preliminary re-entry calculations.	Compare with calculations using US 1976 model for the atmosphere. If difference is too big, use US 1976.	4
AS-TRAJ-03	It is assumed that the atmosphere is in hydrostatic equilibrium.	Slightly less accurate calculations, not very relevant for the preliminary re-entry calculations.	Compare with calculations using US 1976 model for the atmosphere. If difference is too big, use US 1976.	4
AS-TRAJ-04	During gliding flight, the flight path angle varies very slowly with time, and the variations are very small.	Calculations become incorrect in areas of flight where flight path angle encounters high variations.	Use non-simplified equations of motion for the areas where assumption might not hold.	3
AS-DELV-01	Drag is negligible during orbit insertion.	Increase in ΔV required for insertion.	Perform an insertion simulation with high fidelity atmospheric model.	3
AS-DELV-02	Impulsive shots for in-space maneuvers.	Negligible increase in ΔV required for in-orbit maneuvers.	Modest margins on in-orbit ΔV budget.	5
AS-DELV-03	Purely vertical flight for landing burn calculation.	Increase in ΔV required for landing.	Perform the landing burn simulation in 2D.	2
AS-NOSE-01	The stagnation heat flux is assumed to act over the entire area of the nosecone.	Conservative assumption and oversizes the nosecone to handle this aerodynamic load.	FEM or CFD to model the stagnation heat flux over the nosecone geometry and during different stages of flight.	3
AS-NOSE-02	The launch profile of the Vega Launcher will be considered to be representative of the actual launch profile.	Nosecone failure due to buckling affecting the ascent trajectory due to unexpected change in shape.	Propulsion and atmospheric model to evaluate the launcher velocity for the case of H_2ERMES.	2

11.4.2. Maintainability

Maintainability is defined as the probability that a product can be restored to an operable state under specified conditions and time. Designing a system to be maintainability requires the system to be subjected to a process that encourages maintainability. This process is outlined in Figure 11.4.

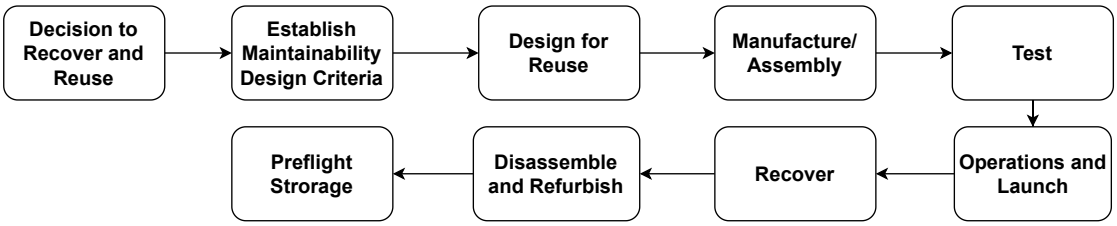

Figure 11.4: H_2ERMES Maintainability Design Process

The decision to recover and reuse is established by the client. The maintainability and design criteria are outlined in the stakeholder requirements in Table 4.3. The system has various considerations for reusability such as using an actively cooled heat shield to avoid the environmental and maintainability impact of ablatives. The compliance of this requirement requires the vehicle to be designed with extreme robustness and ease of maintenance and refurbishment. The refurbishment plan is outlined in Figure 11.5.

11.4.3. Safety

Safety is a key consideration with every space mission. It is vital to consider the safety of the environment and the individual affected by the mission. These risks are often outlined in various guidelines. In accordance with the requirements, the vehicle is designed considering the guidelines outlined in the Order Regulating the Operation of Installations of the Guyana Space Center[26].

Design Safety

- Crew safety: Systems and interfaces are designed to minimize operator error during assembly, fueling, and launch activities. All handling operations are paired with standardized procedures.
- Redundancy and fault tolerance: Critical subsystems are designed with redundancy and safety factors in consideration as mitigation strategies presented in the risk analysis in Chapter 5.
- Hazard analysis: Ongoing Failure Mode and Effects Analysis (FMEA) and Hazard and Operability (HAZOP) investigations.

Operational Safety

- Cryogenic Safety: Cryogenic handling and safety is covered in accordance with the Ames Procedural Requirements[87].
- Launch and Flight Safety: Before the launch the vehicle trajectory and flight corridors are performed to ensure they fall within accepted ranges. Emergency services and security forces are deployed to ensure public safety and minimal interference with operations. Weather and environmental conditions also are validated to ensure the launch is not affected.

Regulatory and Environmental Safety

There are a set of regulations regarding operational, human, and environmental safety that must be adhered to as well. Some are listed below;

- Order Regulating the Operation of Installations at the Guiana Space Center: Covers ground and launch operational safety when using the Guiana Space Center. Outlines risk zones, public and worker safety, emergency services, range safety, and emergency response protocols[26].
- ECSS-Q-ST-40C: Standard defining the safety technical requirements aiming to protect flight and ground personnel, the launch vehicle, associated payloads, ground support equipment, general public, property, space system and environment[88].
- Regulation on Registration, Evaluation, Authorization, and Restriction of Chemicals (REACH): Primary law in the European Union to protect human health and the environment from the risk of chemical exposure.

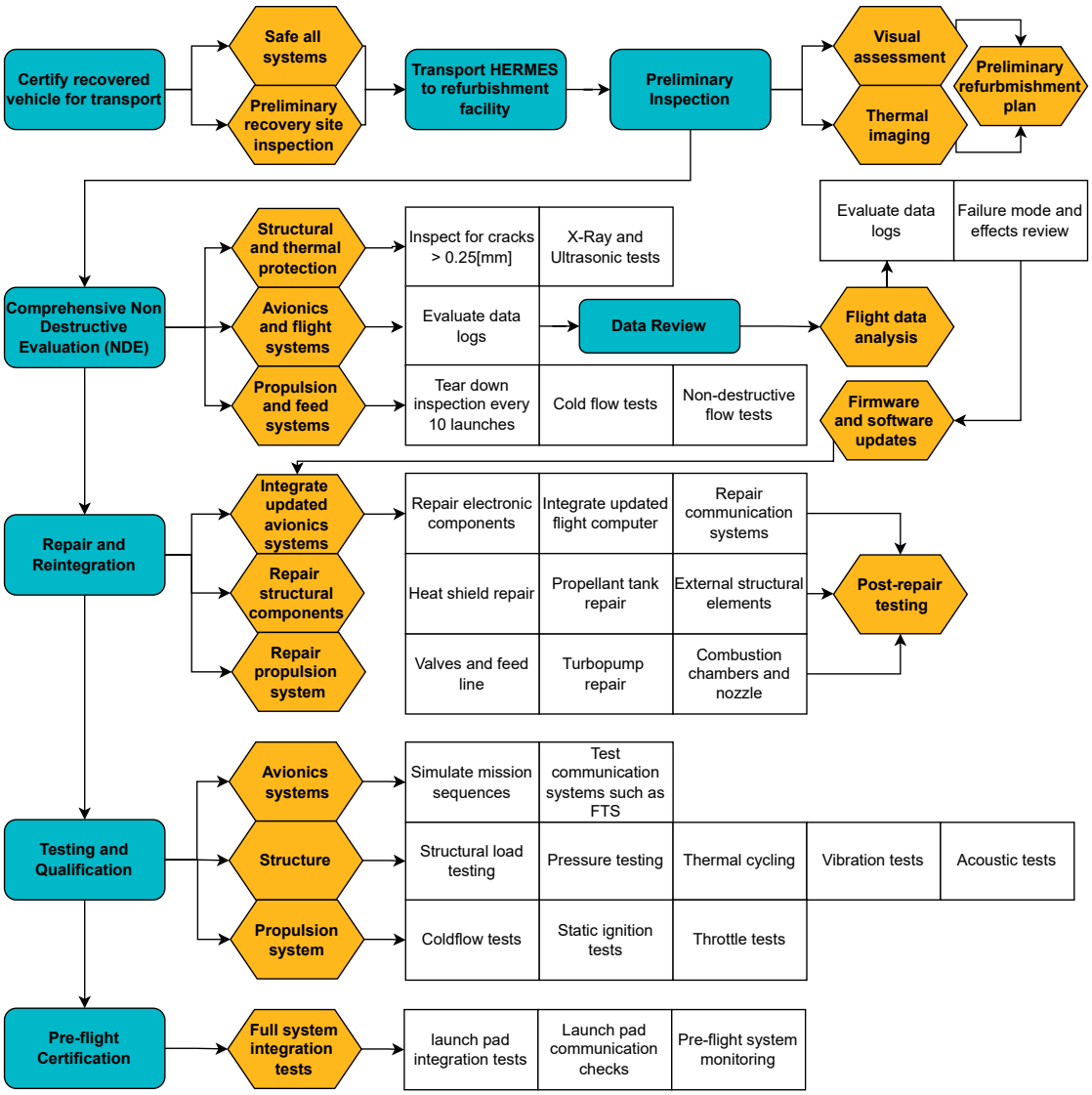

Figure 11.5: H_2ERMES Refurbishment Plan

In compliance with requirements, the design uses green propellants (LH_2 and LOX) which have a minimal impact on the environment as explored in Chapter 12[7].

- UN COPOUS Space Debris Mitigation Guidelines: Outlines guidelines for the safe management of space debris during mission planning, design, manufacturing[89].

Safety Management

- Safety and risk management is performed in accordance with the methods outlined in the NASA Risk Management Handbook[1].

This comprehensive safety framework addresses end-to-end risks, from handling cryogenic LH_2 on the ground to flight termination, debris avoidance, and reuse. By integrating best practices and rigorous regulatory compliance the design ensures mission, personnel, public, and environmental safety.

11.5. Project Cost Breakdown

The project's cost breakdown will be divided into three main components: the cost of development, the cost of manufacturing and the operational cost per flight. Development costs encompass Project Office (PO) (engineering (ENG), management and production assurance (M/PA)) and Manufacturing, Assembly, Integration, Test (MAIT); manufacturing costs include the cost of production; and the operational costs include Direct Operating Costs (DOC) and Indirect Operating Costs (IOC), as defined by N. Drenthe in *Small Orbital Launch Systems, a Tentative Initial Cost Estimate* (SOLSTICE) [90]. DOC includes ground operations, propellant cost, flight and mission operations, and fees and insurance costs (IOC). IOC includes personnel cost, marketing activities, and technical support.

Section 11.5.1, Section 11.5.2 and Section 11.5.3 include the methodology to estimate these costs and Section 11.5.4 presents the cost breakdown of the project. This cost estimation model was found in [9] and arises from different sources such as the *TRANSCOST* model by D.E. Koelle [91], SOLTICE [90] and internal ESA sources. The inherit assumptions to the model can be obtained from the mentioned sources.

11.5.1. Development Cost

Drenthe's model first constructs the recurring first unit (T1), from which, the engineering cost can be estimated according to the cost estimation relationships (CERs) in *NASA Air Force Cost Model* (NAFCOM) [92]. This is denominated T1 Equivalent Method, and its reliable applicability is proven in ESA's *Standard Parametric Information for Cost Engineering* (SPICE) Model. [93]

The engineering cost (CENG) can be estimated by Equation 11.1. Cp is the profit retention cost reduction factor, calculated with Equation 11.2. The rest of the symbols in the equations correspond to costs for different elements in the project. ENG stands for Engineering; MAIT for Manufacturing, Assembly, Integration and Test cost; M/PA% for the percentage of the theoretical first unit (T1) that corresponds to Management and Product Assurance; FM1 to the First Flight Model; STH is the total system test hardware; L_d is the development learning factor; and, HW is the number of times a sub-system is re-used.

$$\mathrm{CENG} = \mathrm{Cp}\left((\mathrm{ENG} + (\mathrm{MAIT} + \mathrm{ENG}) \cdot \mathrm{M/PA\%}) + (\mathrm{FM1} \cdot \mathrm{STH} \cdot \mathrm{L_d} \cdot \mathrm{HW})\right) \tag{11.1}$$

$$\mathrm{Cp} = \frac{s_{\mathrm{COM}} \cdot q + 1}{s_{\mathrm{BAU}} \cdot q + 1} \tag{11.2}$$

FM1, STH, ENG and MAIT can be obtained from Equation 11.3, Equation 11.4, Equation 11.5, Equation 11.6, respectively. In Equation 11.4, DM stands for Development Model, EM stands for Engineering Model and PFM for Proto Flight Model. In Equation 11.5, DD' is the Design and Development that arises from including a delta in Technology Readiness Level (TRL): DD' = DD + ΔTRL. ΔTRL represents the change in TRL required to get a current technology to a TRL of 9. This is measured according to the standard 9-level TRL scale used in the aerospace industry[14].

$$\mathrm{FM1} = \mathrm{T1} - \mathrm{M/PA\%} \tag{11.3}$$

$$\mathrm{STH} = \mathrm{DM} + \mathrm{EM} + \mathrm{PFM} \tag{11.4}$$

[14]URL https://www.nasa.gov/directorates/somd/space-communications-navigation-program/technology-readiness-levels/ [cited 2025-05-16]

$$\text{ENG} = \text{DD'} \cdot \text{FM1} \tag{11.5}$$

$$\text{MAIT} = \text{FM1} \cdot \text{STH} \cdot \text{L}_\text{d} \cdot \text{HW} \tag{11.6}$$

The initial step to estimate the engineering cost is to determine the First Flight Unit Cost Estimate (T1), which estimates the cost of the main equipment (C) as a function of the mass (M) according to Equation 11.7. a is the initial value and b is the growth factor describing the cost-per-kg. These values are obtained from Drenthe[90] NAFCOM[92] by means of regression fitting and normalization of historical data.

$$\text{T1} = a \cdot M^b \tag{11.7}$$

Once the T1 cost is obtained per element, the following development cost relationships can be applied.

- Design and Development Cost: DD' = 3.0 T1 + ΔTRL
- Development Model: DM = 0.3 T1
- Engineering Model: EM = 1.3 T1
- Qualification Model: QM = 1.3 T1
- Proto Flight Model: PFM = 1.5 T1

11.5.2. Manufacturing Cost

When multiple launch vehicles are going to be manufactured, as is the case for H_2ERMES, the manufacturing cost is slightly reduced in comparison to a single unit being manufactured. This is included in the cumulative learning factor, L_c, which can be calculated according to Equation 11.8, where L_m is the manufacturing learning factor. The manufacturing cost can be estimated as per Equation 11.9.

$$L_c = \sum_{i=1}^{n} L_m \tag{11.8}$$

$$C_{MAN} = c_p \cdot (FM1 \cdot L_c + M/PA\%) \tag{11.9}$$

11.5.3. Operational Cost

The operational costs can be calculated from the sum of the direct operation costs (DOC) and indirect operation costs (IOC). This can also be expressed as the sum of the ground operation costs (C_{ground}), propellant costs (C_{prop}), flight & mission costs (C_{FM}), transportation costs (C_{trans}) and fees & insurance costs (C_{FI}). These can be estimated, in k€ according to the following equations, where the meaning and value of each symbol is presented in Table 11.3. The parameters with undefined values are variable per concept. The values of the other parameters are taken from [9] and arise from different sources such as the *TRANSCOST* model by D.E. Koelle [91], SOLSTICE [90] and internal ESA sources. The inherit assumptions to the model can be obtained from the mentioned sources. Lastly, these equations predict the operational cost up to post launch activity of clean-up, but do not include refurbishment activities. An additional 13 M$ will be added to the operational cost per launch to account for component recovery and refurbishment, as per SpaceX's cost per refurbishment. [15]

$$C_{OPS} = C_{DOC} + C_{IOC} = C_{ground} + C_{prop} + C_{FM} + C_{trans} + C_{FI} + C_{IOC} \tag{11.10}$$

$$C_{ground} = \frac{(W \cdot 8 \cdot M_0^{0.67} \cdot LpA^{-0.9} \cdot N^{0.7} \cdot f_c \cdot f_v \cdot L_0 \cdot f_8 \cdot f_{11})}{1000} \tag{11.11}$$

$$C_{prop} = \frac{\left(\frac{M_p}{r+1} c_f + \left(M_p - \frac{M_p}{r+1}\right) c_{ox} + M_{press} c_{press}\right)}{1000} \tag{11.12}$$

$$C_{FM} = \frac{(W \cdot 20 \cdot Q_N \cdot LpA^{0.65} \cdot L_0 \cdot f_8)}{1000} \tag{11.13}$$

$$C_{trans} = T_s \cdot M_0 \tag{11.14}$$

$$C_{FI} = \frac{I + F + (c_{payl} \cdot P)}{1000} \tag{11.15}$$

$$C_{IOC} = \frac{(40 \cdot S + 24) \cdot LpA^{-0.379} \cdot W}{1000} \tag{11.16}$$

[15] URL https://www.ark-invest.com/newsletters/issue-335#:~:text=1.-,The%20Turnaround%20Time%20In%20Rocket%20Reuse%20Suggests%20That%20The%20Cost,In%20The%20Last%20Five%20Years&text=As%20Director%20of%20Research%2C%20Sam,Autonomous%20Technology%20and%20Robotics%20team. [cited 2025-06-18]

Table 11.3: Parameters for estimating operational costs

Parameter	Symbol	Value	Units	Parameter	Symbol	Value	Units
Assembly and Integration Factor	f_c	0.85	[−]	Country Productivity Factor	f_8	1	[−]
Launch Vehicle Type Factor	f_v	1	[−]	Vehicle Complexity Factor	Q_N	0.8	[−]
Commercial Factor	f_{11}	0.55	[−]	Average Learning Factor Operations	L_0	0.64	[−]
Work-Year Costs	W	301200	[k€]	Number of Stages	N	2	[−]
Fuel and Oxidizer Mass	M_p	-	[kg]	Gross Take-Off Weight (GTOW)	M_0	-	[t]
Pressurant Mass	M_{press}	-	[kg]	Mass Mixture Ratio	r	-	[−]
Public Damage Insurance	I	100	[M€]	Payload Mass	P	12500	[kg]
Payload Charge Site Fee	c_{payl}	5.51	[€/kg]	Launch Site Fee	F	1220	[k€]
Specific Transportation Cost	T_s	5.365	[€/kg]	Percent of Work Subcontracted Out	S	20	[%]
Launches per year	LpA	50	[−]				

11.5.4. Cost Breakdown

Once the development, manufacturing and operational costs have been calculated, a 25 [%] margin has been added to include the possible deviation from the estimations. Additionally, the added margin will ensure the compliance with *RQ-STK-COS-3*, which sets the allowable variation of the total cost to 33 [%] from the initial estimate. Furthermore, the above-mentioned cost engineering model performs the estimations in euros, but the stakeholder requirements are in US dollars and thus the estimated costs have been converted. The cost breakdown of the project is shown in Figure 11.6.

11.6. Market Considerations

The market considerations consist of evaluating the return on investment. The latter refers to the balance between the profit made and the total cost of H_2ERMES, given by Equation 11.17.

$$ROI = \frac{P_{Market} - C_{flight}}{C_{flight}} \tag{11.17}$$

Where ROI is the return on investment, P_{Market} is the market price, and C_{flight} is the total price of one launch.

Knowing the cost of the launcher from Section 11.5, the total price of the product can be estimated. For a first iteration of the price, the development cost is assumed to be covered over the first 25 launches or equivalently 5 years of operations. The total price of one launch is given by Equation 11.18.

$$C_{\text{flight}} = C_{\text{OPS}} + \frac{C_{\text{MAN}}}{25} + \frac{C_{\text{DEV}}}{25} \tag{11.18}$$

Where C_{OPS} is the operational price, C_{MAN} is the manufacturing cost, and C_{DEV} is the development cost.

As the market for in orbit refueling is still in the conceptual state, estimating the market price of the a launch is tough. A solution to this is to, from a given return on investment common to the aerospace sector, find the necessary launch rates. It is common in the aerospace industry to offer rates of around 18 [%] [16] as of January 2025 so adjusting the launch rates per kg of propellant delivered to 8900 [US$/kg] the return on investment is 15.54 [%]. It is to be noted that once the initial development cost has been covered, the launch rates are predicted to decrease significantly leading to a total lower price and possibility to raise the profit on each launch.

[16] URL https://pages.stern.nyu.edu/~adamodar/New_Home_Page/datafile/mgnroc.html [cited 17-06-2025]

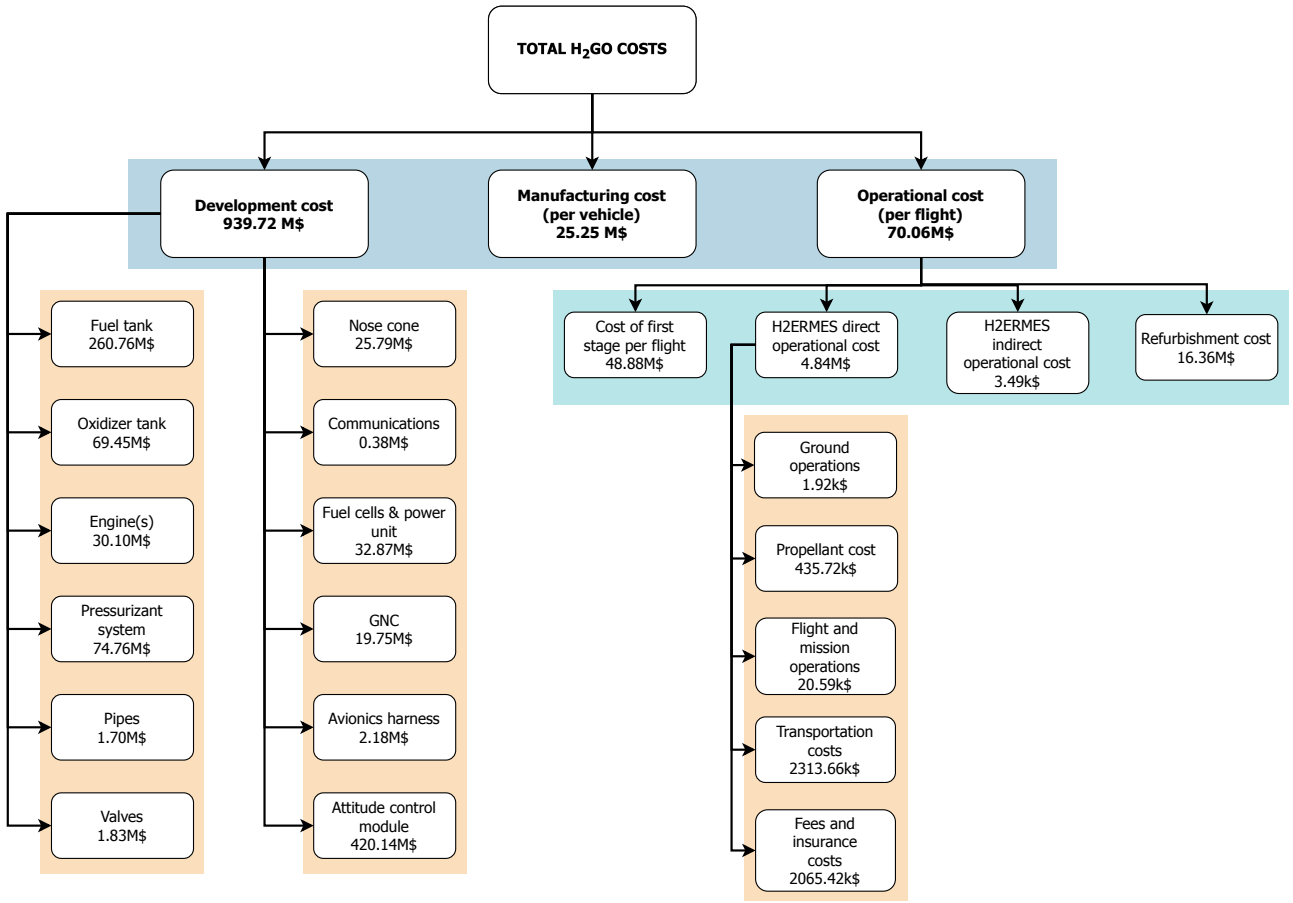

Figure 11.6: Cost breakdown structure

Table 11.4: Market Considerations Results

Cost	Value	Unit
Development Cost	939.7M	[US$]
Operational Cost	70.06M	[US$]
Manufacturing Cost	25.24M	[US$]
Total Cost per Flight	108.66M	[US$]
Payload Mass	14106	[kg]
Launch Rates	8900	[US$/kg]
Market Price	125.54M	[US$]
Return on Investment	15.54	[%]

12 Sustainability Assessment

This chapter describes the sustainable development strategy of the project. Section 12.1 describes the prior decisions taken in relation to sustainability. Section 12.2 outlines the organizational methods implemented in the project management phase. Lastly, Section 12.3 presents the Life Cycle Assessment performed in order to monitor environmental impact.

12.1. Background

Sustainable development is defined as "a process of change in which the exploitation of resources, the direction of investments, the orientation of technological development and institutional change are all in harmony and enhance both current and future potential to meet human needs and aspirations" [94]. Given the scope of the project, sustainability should be assessed from both an organizational and a technical perspective. For the organizational strategy, the focus will be on creating internal working methods and market value. For the technical sustainability assessment, a Life Cycle Assessment (LCA) will be used, in order to ensure compliance with *RQ-STK-SUS-1* and *RQ-STK-SUS-3*.

According to literature, sustainable development can be divided into three main areas: economic, social and environmental [95]. The economic pillar deals with job creation and security, profitability, and ensuring a sustainable balance between profit and resource use. The social aspect encompasses actions such as policy-making, community building and involvement, ensuring health and safety of the population and dealing with social issues. Lastly, environmental sustainability includes the use of natural resources, maintaining the planet's biodiversity and minimizing pollution.

In order to address these three areas in a holistic and meaningful way, the United Nations (UN) 2030 Agenda for Sustainable Development[1] and the Sustainable Development Goals (SDGs) were used as a starting point.

The SDGs that would impact the project have been documented in Table 12.1, together with the impacted area of interest. The number of each SDG represents the number assigned by the UN 2030 Agenda for Sustainable Development. Goals #5 and #8 were chosen in order to ensure the organizational activities of the group create positive societal and economical impact. The other three goals, #7, #9, and #12, were selected due to their connection with the technical research of H_2GO.

Table 12.1: Sustainable Development Goals

#	Goal	Organizational	Technical
5	Achieve gender equality and empower all women and girls.	✓	
7	Ensure access to affordable, reliable, sustainable and modern energy for all.	✓	✓
8	Promote sustained, inclusive and sustainable economic growth, full and productive employment and decent work for all.	✓	
9	Build resilient infrastructure, promote inclusive and sustainable industrialization and foster innovation.	✓	✓
12	Ensure sustainable consumption and production patterns.	✓	✓

12.2. Organizational Perspective

In recent years, as more interest has been shifted towards sustainable development, it has become apparent that sustainability can only be achieved if all levels of an organizational structure and its operations are considered. Therefore, sustainability is impacted both by the ways in which internal work gets carried out, and by the priorities chosen when planning the development of a product. In order to establish approaches the team would follow throughout the project, the three pillars of sustainability mentioned in Section 12.1 were complemented by project management aspects that could relate to H_2GO [96]:

[1] URL https://sdgs.un.org/2030agenda [cited 16/06/2025]

1. **Economic:** stakeholder management, engagement and innovation, economic performance, value chain, quality management
2. **Social:** decision-making, learning, collaboration, communication, commitment
3. **Environmental:** legislation, environmental policies

Therefore, by implementing the SDGs from Table 12.1 into the project management aspects described above, the team could develop guidelines of behavior and priorities to take into account when creating the final product. In terms of internal working methods, especially when it comes to decision-making, collaboration and communication, based on Goal #5 and Goal #8, additional importance was given to ensuring all voices were being listened to, regardless of gender. To achieve this, two safe people were assigned, who could be approached by any team member in case any interaction caused them discomfort or if they felt discriminated against. Additionally, by creating a safe and inclusive space within the team, as the project would be up scaled down the line, jobs could be created where people could be engaged, motivated, and heard. As such, stable workplaces could be created, which can impact also the economical sustainability of H_2GO. The rest of the project management aspects relate mostly to stakeholder satisfaction, market position, and external legislation. As the project aims to develop a reusable second stage, sustainability is a significant part of the value proposition of the product, and has been a leading factor when negotiating requirements, and when imposing additional standards of quality. Since one of the requirements also contains the use of recyclable materials, Goal #12 has been prevalent during the material selection process, the philosophy behind which will be described in the following section.

12.3. Life Cycle Assessment

According to the International Organization for Standardization (ISO), standard ISO 14044:2006, LCA is defined as ”compilation and evaluation of the inputs, outputs and the potential environmental impacts of a product system throughout its life cycle”. LCA has emerged in the last years as a reliable tool to quantify environmental impact all throughout the life cycle of a product or service. Using this method ensures that the full environmental impact is considered [97].

The general methodology for performing an LCA, as described in ISO 14044:2006, includes defining the goal and scope of the assessment, inventory analysis, impact assessment and results interpretation. Each step will be presented in the following subsections. In order to ease the future comparisons with other space missions, the ESA LCA Handbook [98] will be used as a main reference when performing the assessment.

12.3.1. Goal and Scope Definition

Before performing the LCA, the goals and the scope need to be identified. This part of the LCA can be split into two parts: goal and scope.

LCA Goal

The goal includes the reasoning behind performing an LCA, divided into the following details:

- **Purpose:** LCA was performed to measure environmental impacts of the mission throughout the entire life-cycle of the developed product (research to disposal)
- **Application:** Assessment shall serve as an aid in ensuring compliance with stakeholder requirements
- **Audience:** The assessment will be given to the client, and possibly used to create market value
- **Comparison:** Comparison will be carried out to assess level of compliance with *RQ-STK-SUS-3*

LCA Scope

The scope of an LCA generally gives more detailed information about what the assessment will include, from functional unit to system boundaries. For H_2GO, these have been chosen as such:

- **Functional unit:** One launch of a reusable second stage that transports 14000 kg of liquid hydrogen into Low Earth Orbit.
- **System boundaries:** To easily compare the impact to other European missions, the system boundaries were chosen in alignment with the ESA LCA Handbook [98] and have been documented in Figure 12.1
- **Cut-off criteria:** A subsystem, component or input can be ignored if its mass is less than 5% of the component and:
  - there is no available data about the environmental impact of the input

  - input not associated with high environmental or health risk as established by relevant European Commission directives [7]
  - input not included in REACH Annex XIV "Authorization List" or identified by the EU as a critical raw material (CRM) [7]

- **Data:** Most of the data will be acquired from the Industrial Design & Engineering MATerials database (IDEMAT) [2]. Some data for emissions during launch and re-entry will be taken from two tools, the Launch Emission Assessment Tool (LEAT) [3], and the Re-entry Emission Assessment Tool (REAT) [4]. The IDEMAT data is highly reliable, based on literature studies. The two other tools are not as rigorously documented, so the information should be treated with some precaution.
- **Limitations:** Normally the LCA inventory is created using professional tools, like ecoinvent [5]. However, that is a paid platform. Therefore, IDEMAT is considered a good enough alternative, but it does have some limitations in terms of which data is available there. Additionally, the emissions calculated during launch and re-entry rely on detailed information about other commercially-available launchers. Unfortunately, not a lot of information is available, especially for reusable launchers.

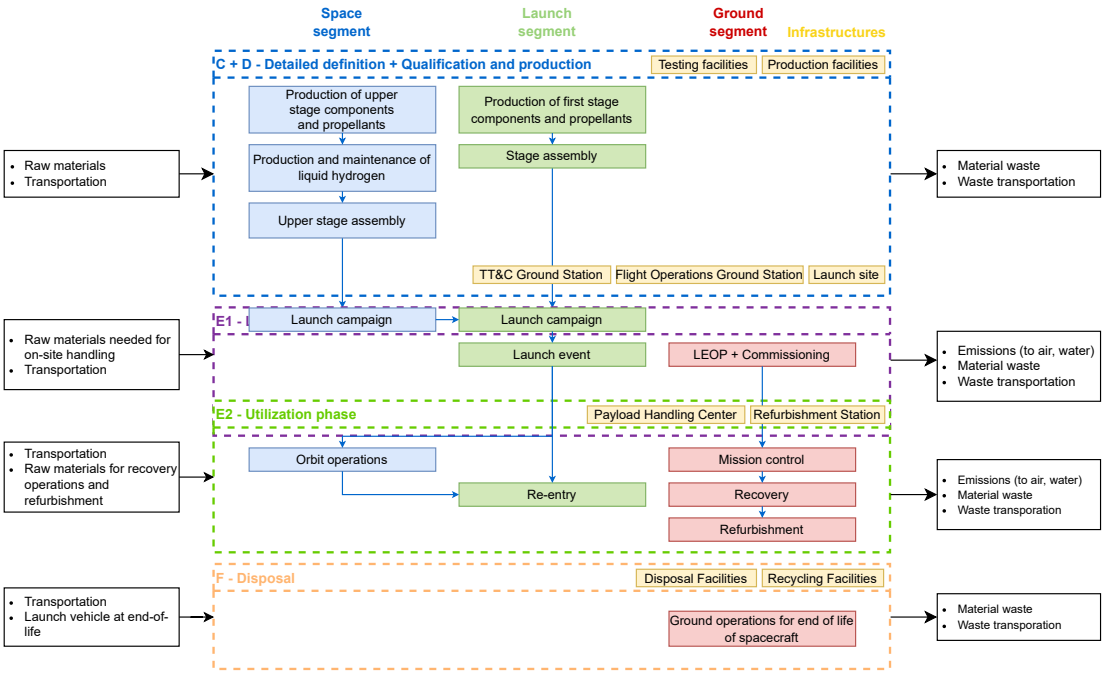

Figure 12.1: Life Cycle Scope

12.3.2. Life Cycle Inventory

A Life Cycle Inventory (LCI) consists of all the inputs and outputs that relate to a system. These have also been documented in Figure 12.1.

12.3.3. Impact Assessment

When performing an LCA, the impact assessment consists of selecting environmental impact categories that can properly communicate the results of the assessment. As mentioned, the chosen database was not one of the classic LCI databases. Hence, some of the widely used impact categories were not available for all data points. However, the database included a very thorough analysis in terms of eco-costs, a methodology developed at TU Delft [99]. Eco-costs are defined as the amount of marginal costs that would need to be incurred in order to balance out the negative environmental impacts. The environmental and social categories of eco-costs are: circular economy, biodiversity, carbon footprint, and human health.

[2] URL https://www.ecocostsvalue.com/data-tools-books/ [cited 16/06/2025]
[3] URL https://github.com/lcasts/LEAT [cited 21/05/2025]
[4] URL https://github.com/lcasts/REAT [cited 16/06/2025]
[5] URL https://ecoinvent.org/ [cited 2025-06-16]

12.3.4. Results

Based on the methodology described in the previous sections, an LCA has been conducted, and the emissions during launch have been calculated. The results have been documented in Table 12.2 and Table 12.3. The values related to manufacturing have been divided by the number of launches, such as to reflect the emissions per launch that stem from material extraction, production, and manufacturing. For the emissions during launch, they have been normalized with mass carried into space. From the results, it was clear that even compared to different rocket, H_2ERMESdoes have lower emissions. Additionally, all of the materials that contribute in larger percentages to the production emissions are recyclable, which does comply with *RQ-STK-SUS-3*.

Table 12.2: LCA Results

Sub-system	**Eco-costs** [€]	**Emissions** [$kgCO_2e$]
Tanks	526	2244
Cooling	40	171
Landing legs	1450	207
Nosecone	16	66
Propulsion	336063	220746
Payload	9304	32995
AODCS	278	1873

Table 12.3: Launch Emissions

Configuration	**Launch Emissions**
H2ERMES	0.711 [$kgCO_2e/kg$]
Falcon 9	0.982 [$kgCO_2e/kg$]
Ariane 5	1.101 [$kgCO_2e/kg$]

13 Quality Assurance

It is vital to ensure each part of the design is properly verified and validated. For this, first the verification and validation methods of tools developed during the design are presented in Section 13.1, followed by verification and validation of the design. Lastly, the requirement compliance matrix is given in Section 13.3.

The V-model is a standard systems engineering tool to ensure V&V happens throughout the development process.

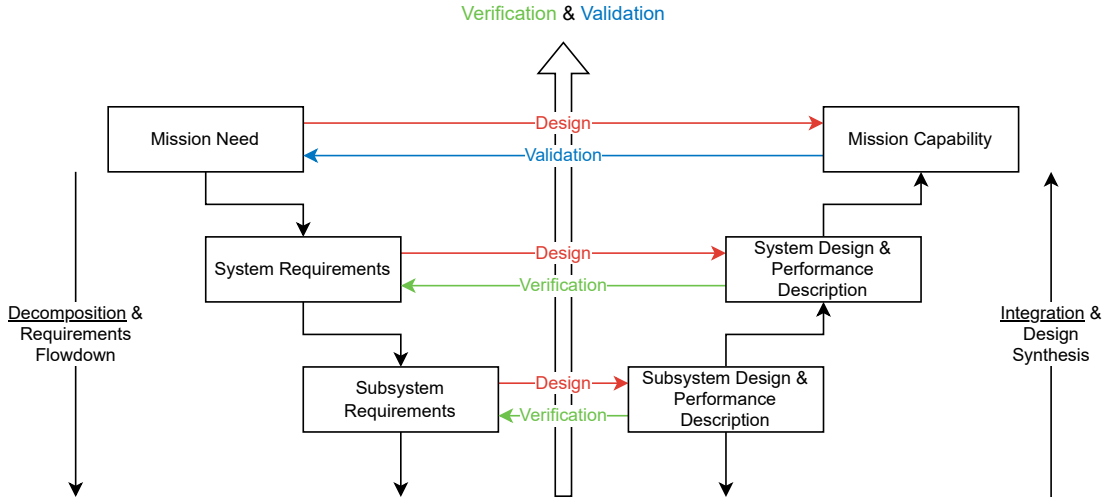

Figure 13.1: V-model

13.1. Verification and Validation of Tools

13.1.1. Aerodynamics

The aerodynamics model used is primarily the Newtonian methods for characterizing hypersonic aerodynamics for blunt body shapes, and the RASAero program. The tool developed using the Newtonian methods has been validated using information available for the Apollo capsule. The RASAero program has been validated extensively by various organizations. However, it has once again been validated using the Apollo capsules and general hand calculations.

13.1.2. Heat shield

In order to model the loads that will act on the heat shield, an in-house tool was developed. The model will be validated using:

1. Experience: During literature research, an existing readily available model for a similar case was not found. To validate the model, further research needs to be done or some existing model can be adapted and used to validate this model.
2. Analysis: Separate elements of the model can be analyzed and validated with more advanced design tools such as CFD or FEM. Although some verification is performed through unit tests, this analysis will focus on the validation part of the V&V procedure.
3. Comparison: As the analysis performed so far is only a first-order approximation, the results may be validated with CFD analysis by considering two existing validated tools used on existing designs.

Note that this is a plan for the future of the project. Currently, there are no resources available to perform this V&V procedure. The tool was verified with software testing, but not validated.

13.1.3. Delta V Calculation

In order to compute the ΔV required for each phase of the mission, a calculation tool was developed. The V&V procedure for this tool has been stated below.

Orbit Insertion

The simulation was verified using a set of unit tests in which simplified scenarios, such as in-orbit movement with no thrust, powered and unpowered vertical flight were simulated and the results were compared to manually performed analytical calculations.

The actual insertion trajectory ΔV estimate was validated by comparison to the Saturn V's second stage as presented in [8], in terms of total ΔV as well as gravity and steering losses.

Landing Burn

The landing burn simulation was again verified with a series of simplified scenarios with analytical solutions. It was additionally validated by simulating the landing burn for Falcon 9 first stage and checking that the velocity, time and consumed propellant closely tracked the actual available values[1].

13.1.4. AOCS Thruster Sizing Tool

The thruster sizing tool was verified by performing unit tests which gave inputs with known outputs and checked if the function returns a similar result. This was complemented by performing hand-calculations with the parameters and then verifying the result with the output of the function. The tool was validated by using the geometry, loads and engine parameters for the command module of the Apollo spacecraft and checking if the number of thrusters calculated matches the number of thrusters used by the Apollo spacecraft.

13.1.5. Landing Legs

The landing legs of the H_2ERMES rocket were modeled by developing an in-house tool. The tool is verified using unit tests, where the individual components, such as stress calculations, are performed by hand, and the results are cross-checked. Validation is done using reference masses of landing gear, and ensuring they equal a similar relative weight. Besides this, finite element methods (FEM) will be employed to cross-check structural results.

13.1.6. Nosecone Sizing Tool

The nosecone dimensions were modeled by an in-house tool. Since this tool only considers the aerodynamic load and the thermal load, it requires to be validated by using FEM on external software such as ANSYS as was done by [54]. Moreover, this tool was verified by performing hand calculations and comparing the outputs with each other.

13.1.7. Tanks

The tank was designed by developing an in-house tool. The tool will be validated by constructing a FEM model with the dimensions of the designed tank, an equivalent pressure and loads and comparing the stress results to the predicted ones. Furthermore, the predicted vibration frequencies will be validated by comparison to existing stainless steel structures.

13.1.8. Fatigue Prediction Tool

The fatigue prediction tool was developed as an in-house tool. The tool was verified by hand calculations and validated with the use of online fatigue calculators [100]. However, these were also simple fatigue prediction tools based on the same equations as used in the domestic in-house developed tool.

13.1.9. Header Sizing Tool

This tool was verified by performing hand calculations and was further verified with online programs that can also calculate the dimensions of a sphere based on a given volume. The part of the tool that sizes the thickness of the tank will be validated by comparing it with an existing data set.

13.1.10. Boil Off Mass Estimation Tool

The mass of the boil-off gas of hydrogen was estimated by using an externally validated software called BoilFAST developed by the University of Western Australia [3]. Moreover, the thermal loads estimation for the input of BoilFAST was also performed with an externally validated tool called ESATAN-TMS [77]. Furthermore, an in house tool was developed to process the inputs and outputs for these tools. These tools were verified by hand

[1] URL https://www.youtube.com/watch?v=KfG-qfVzjwY&ab_channel=NASASpaceflight [cited 2025-06-17]

calculations and validated by comparing predicted outputs with outputs from BoilFAST (for example, mass of the gaseous hydrogen in the tank is an output of BoilFAST. This output was the same when compared to the value predicted by the in-house tool).

13.1.11. Cost Estimation Tool

Since the availability of publicly accessible reliable cost data is limited or even non-existent, any validation performed in this study would be invalid. However, N. Drenthe [90] has performed validation in his report with internal data from ESA.

For example, for the prediction of operational costs, the model has been validated with two approaches. Firstly, the results from the model were compared against reported operating costs in *NASA's Exploration Systems Architecture Study* [101] and *TRANSCOST* [91]. Secondly, the results are validated against an estimate of the Pegasus rocket post per flight to see how the model predicts the variation of operational cost with LpA (launches per annum), and how the cost per flight varies with LpA. Drenthe found that the change in cost per flight arising from a change in LpA is accurately represented by the change in operational costs from the model.

13.2. Verification and Validation of Design

In terms of the design, V&V plays an important role in determining the compatibility of the design to the requirements and checks the sanity of the design. In the midterm report [10], an initial set of verification procedures were defined for all stakeholder and system requirements. Since then, several new requirements have been identified from the design process. This section states the verification plan for the requirements along with a planned set of validation procedures for each subsystem.

13.2.1. Verification

The verification procedure to check compliance with the requirements consists of four methods: inspection, analysis, demonstration and testing. In the first method, the design is compared with the design documentation to check if the requirement is satisfied. In analysis, a mathematical model or any other analysis technique is used to check if the requirement is complied with. Demonstration uses operation, adjustment or reconsideration of the design to check compliance with the requirement. Testing, as the name suggests, puts the design in mission representative conditions to check compliance with the requirement. Table 13.1 contains a list of all the requirements along with the method and description of the verification procedure for each one of them. The names of the methods have been abbreviated in the main table as follows: A for analysis, I for inspection, D for demonstration and T for testing.

Table 13.1: Requirement verification methods

Requirement ID	Method	Details
RQ-STK-COS-1	A	Perform cost budgeting to estimate the total cost of the mission.
RQ-STK-COS-2	A	Develop cost budgets for the total operational cost over 5 missions.
RQ-STK-COS-3	A	Perform a stochastic sensitivity analysis to see whether the costs remain within range.
RQ-STK-PLD-1	D	Load the specified amount of LH_2 to the tank while simulating flight conditions.
RQ-STK-PLD-2	T	Verify LH_2 tank storage through structural testing.
RQ-STK-PLD-3	A	Analyze mission schedule to assess whether the requirement is feasible.
RQ-STK-PLD-4	A	Analyze that vehicle sensors and actuators are sufficient to follow the trajectory.
RQ-STK-DOK-1	T	Test fire ACS thrusters and measure produced thrust.
RQ-STK-DOK-2	T	Simulate orbit conditions and test the maneuvering systems of the launch vehicle.
RQ-STK-DOK-3	A	Develop simulations of launch vehicle proximity operations.
RQ-STK-RFL-1	T	Test refueling operation in a ground based facility.
RQ-STK-RFL-2	D	Verify whether docking interface matches with the adapter of the fuel depot.
RQ-STK-RLV-1	A	Estimate time required by analyzing refurbishment needed after a test flight.
RQ-STK-RLV-2	A	Approximate time needed for 25 launches by acquiring the refurbishment time after one flight.
RQ-STK-RLV-3	A	Develop a schedule to determine if the requirement can be met.
RQ-STK-RLV-4	D	Perform a test flight to assess the re-entry protection of the launch vehicle.
RQ-STK-REL-1	I	Verify that all safety standards are complied at every stage of the design process.
RQ-STK-REL-2	A	Simulate whether the launch vehicle can operate amid failure scenarios.

continued on next page

Table 13.1 - *continued from previous page*

Requirement ID	Method	Details
RQ-STK-SUS-1	T	Measure emissions from test fires.
RQ-STK-SUS-2	A	Mitigate failure modes in the space segment to avoid debris formation.
RQ-STK-SUS-3	I	Verify that sustainable materials are incorporated in design and manufacturing.
RQ-STK-REG-1	I	Ensure all launch and vehicle related procedures happen according to the launch site regulations.
RQ-STK-REG-2	I	Verify that all safety standards are complied at every stage of the design process.
RQ-STK-REG-3	I	Inspect the design frequencies of the selected communication equipment.
RQ-PRP-1	A	Develop delta-V budgets to verify compliance with the requirement.
RQ-PRP-2	A	Analyze the design thrust and gross vehicle mass.
RQ-PRP-3	T	Measure emissions during engine testing.
RQ-PRP-4	A	Analyze the design thrust and vehicle dry mass.
RQ-PRP-5	T	Test re-ignition of the engine in ground tests.
RQ-LH2-1	D	Demonstrate that the tank's structure withstands the proposed amount of LH_2.
RQ-LH2-3	I	Perform inspections to verify all safety standards are complied.
RQ-LH2-4	I	Develop checklists to ensure all safety regulations are followed during ground tests.
RQ-LH2-5	I	Perform intensive checks to ensure the launch vehicle meets all safety standards related to transport and storage of liquid hydrogen.
RQ-SYS-1	I	Run software tests to verify mission activities are performed appropriately.
RQ-SYS-2	A	Simulate failure scenarios to determine the launch vehicle success rate.
RQ-SYS-3	I	Develop a checklist to meet guidelines.
RQ-SYS-4	I	Develop a checklist to meet guidelines.
RQ-SYS-5	A	Ensure design process emphasizes on the durability of the launch vehicle.
RQ-SYS-6	I	Make a checklist to meet guidelines imposed by the French Guiana spaceport.
RQ-SYS-7	I	Review the safety regulations proposed by the regional government.
RQ-SYS-8	I	Review guidelines imposed on environmental impact.
RQ-GNC-1	T	Verify sensor accuracy by testing them in simulated mission conditions.
RQ-GNC-2	T	Fire thrusters and measure the impulse.
RQ-GNC-3	A	Analyze the attitude control system in a trajectory simulation model.
RQ-GNC-4	T	Fire ADCS thrusters to verify the angular velocity that is achieved.
RQ-RFL-1	T	Test refueling operations to deduce efficiency of fuel transfer.
RQ-RFL-2	I	Inspect whether docking interface matches with the adapter of the fuel depot.
RQ-RFL-3	T	Perform structural tests to verify that the tank is able to hold the required amount of payload after undergoing boil-off in orbit conditions.
RQ-REC-1	T	Subject the re-entry protection to expected heat loads.
RQ-REC-2	A	Simulate the launch vehicle return to the specified location.
RQ-REC-3	T	Test venting procedures of the launch vehicle in a test facility.
RQ-REC-4	A	Develop a trajectory simulation to verify that there is no danger posed to settlements or other habitats on ground.
RQ-REC-5	A	Estimate the emissions caused during re-entry of the vehicle using simulations.
RQ-REC-6	A	Simulate the possibility of failure during recovery by replicating failure scenarios.
RQ-REC-7	I	Inspect what pollutants will be released in case of crash landing.
RQ-SAF-1	I	Ensure there is a flight destruction program which is developed and installed in the launch vehicle's on-board computer.
RQ-SAF-2 to *RQ-SAF-4*	I	Inspect the launch vehicle procedures in case of disturbances during launch, flight and landing.
RQ-SAF-5	I	Verify all safety standards are followed by the transportation vehicle.
RQ-SAF-6	I	Verify all safety standards are followed by the launch vehicle.
RQ-SAF-7	D	Develop a checklist of requirements to be checked according to the specifications.
RQ-SAF-8	D	Ensure testing is performed according to the safety standards.
RQ-COM-1	D	Demonstrate that the launch vehicle is able to communicate with the ground station by testing the instruments.
RQ-COM-2	I	Ensure that the instruments comply with the established protocols.
RQ-OPS-1	D	Demonstrate capability of ground facilities to refurbish the launch vehicle within the specified time.

continued on next page

Table 13.1 - *continued from previous page*

Requirement ID	Method	Details
RQ-OPS-2	I	Check whether the service provider still complies with the needs of the mission.
RQ-OPS-3	I	Ensure that the launch provider has agreed to allow launching at the desired site.
RQ-OPS-4	I	Ensure that fuel provider still complies with requirements attributed to LH_2.
RQ-MAT-1	I	Verify that recyclable materials are included in the material selection process.
RQ-MAT-2	I	Verify that reusable materials are included in the material selection process.
RQ-MAT-3	T	Verify performance of material by testing at specified cryogenic temperature.
RQ-MAT-4	I	Inspect possible embrittlement of the structure when loaded with hydrogen.
RQ-AER-1	T	Perform wind tunnel tests to assess the drag coefficient.
RQ-AER-2	A	Simulate actual flight conditions to determine the ballistic coefficient.
RQ-AER-3	A	Use flight dynamics equations to estimate the static stability of the launch vehicle under the specified atmospheric conditions.
RQ-STR-1	A	Develop a thermal loads simulation to assess whether the launch vehicle is capable of withstanding the loads.
RQ-STR-2	T	Load the vehicle under the given loads to test its integrity.
RQ-STR-3	T	Apply launch loads to vehicle in dedicated vibration test facilities.
RQ-STR-4	D	Apply acceleration loads to vehicle in dedicated vibration test facilities.
RQ-NSC-1	T	Test structure by applying the max dynamic pressure of the launch vehicle.
RQ-NSC-2	T	Test structure by applying an external heat flux and measuring temperature of the inside surface.
RQ-PLD-1 to *RQ-PLD-3*	D	Test payload tank by applying an similar mission representative heat flux unload fuel as per required by flight timeline for different subsystems. Measure pressure and mass of LH_2at different points during this test for compliance with different requirements.

13.2.2. Validation

Validation refers to the process of checking whether the final design performs its purpose according to the expectations of the stakeholder. This process applies both to the requirements and the product itself. Hence, this is an important step that needs to be completed to have a flawless execution of the H_2GO mission. With respect to the requirements, each and every requirement was assessed based on five criteria which are commonly abbreviated together as VALID (Verifiable, Achievable, Logical, Integral, and Definitive). Hence, every requirement mentioned in the report has been thoroughly validated before being accepted. The validation procedure for the main design is stated below:

Mission timeline

The mission timeline details all the phases that occur in the mission, beginning from launch till landing of the launch vehicle. As it is difficult to validate the timeline in the ground, a test mission with mock objectives will be launched to check whether the launcher is capable of completing all the objectives within the slotted time.

Delta V

For the estimated Delta V (ΔV) of the mission, the thrust level, mass flow, and specific impulse of the propulsion system will be tested. These parameters shall then be used to validate the computed ΔV value.

Aerodynamics

The scope of aerodynamics mainly concerns the ascent and re-entry phases of the H_2GO mission, where the latter is heading downward at hypersonic speeds. Hence, CFD analysis and wind tunnel tests will be performed in order to validate the aerodynamics of the launch vehicle.

Heat shield

As described earlier, the launch vehicle faces immense thermal loads when re-entering the atmosphere at hypersonic speeds. The H_2ERMES rocket uses a heat shield complemented by active cooling and is located below the main engine of the rocket. To safely overcome the re-entry phase without damage, a validation procedure has been planned for the heat shield. Firstly, inspection is employed by establishing careful quality assurance and quality control measures for the heat shield material supply chain. This is important as the material's performance directly influences the performance of the heat shield. With regard to testing, it will be done both on every single tile and the entire heat shield. The validation process for a single tile is detailed below:

1. The material properties across the qualification temperature range will be validated.

2. Fatigue and thermal cycling will be conducted over the heat shield tile.
3. Yield strength testing will be performed and the stress-strain curve for this specimen will be derived.
4. The emissivity of the tile will be assessed under oxidized conditions.
5. The tiles will then be heated whilst being cooled by liquid hydrogen to test effectiveness of regenerative cooling.

When conducting tests, it is necessary to place margins by defining a wider envelope for the incident heat flux than what is nominally expected during re-entry.

Landing legs
After completing re-entry, the vehicle needs to safely land back on the ground so that it can be refurbished for the next mission. The soft landing of the H_2ERMES rocket is performed using landing legs that extend outward using hydraulic actuators. The landing legs take on the loads during touchdown and reduce the impact on the launch vehicle. Hence, a detailed validation procedure has been planned to test the landing legs for this mission. The procedure has been listed below:

1. The deployment mechanism for the landing legs will be tested repeatedly to check that it works effectively.
2. A static load equivalent to the entire assumed weight of the launch vehicle is applied on each leg. The test checks whether the leg yields under the load and validates the design for the possibility of the launcher landing on a single leg.
3. The landing legs will be subjected to drop tests which simulate a non-nominal landing which would induce a landing velocity. This test will aim to validate the shock absorbers which are supposed to dissipate energy generated due to the induced velocity.
4. The locking mechanism is tested by first applying loads to the legs when they are locked. For it to be validated, the legs need to unlock manually and then be able to stow back so that it returns back to launch configuration.

Power
With regard to power, it is to be noted that the H_2ERMES vehicle will be using fuel cells as its only power source. Although the use of fuel cells has been demonstrated by space shuttles, it is necessary to validate it after system integration. Tests will be run on the power distribution bus, which includes testing redundancy in case of cell failure and fail-safe cell restartability in case of power overdraw.

Propulsion
The H_2ERMES rocket will be powered by an engine taking advantage of the aerospike effect, containing two turbo pumps and 24 thrust chambers. Eight of these thrust chambers are sea-level thrusters while the rest are vacuum thrusters. Several tests will be conducted to validate this engine and have been listed below:

1. The engine will be tested at sea level for different durations and at different thrust levels to measure real engine characteristics.
2. The engine will be reignited several times to validate the reignitability characteristic of the engine.
3. The turbo pump will be tested with the heat shield to compare the drop in pressure with the results of the model and validate that the entire propulsion system works accordingly.
4. Vibrations tests will be conducted to check if the structure is able to handle the vibrations produced by the engine.
5. The thrust structure will be tested to ensure it can handle the propulsion loads.

AODCS
With respect to the AODCS, both the determination and the control segment of the subsystem needs to be validated to ensure flawless performance of the subsystem. The H_2ERMES vehicle contains GPS receivers for AODS and HTP monopropellant thrusters for AOCS respectively. The following tests will be conducted to validate the AODCS:

1. AOCS thrusters shall be tested using hot fires to check the effectiveness of the engine.
2. The AOCS thrusters shall be placed in the chosen configuration around a test setup and fired in various combinations in order to test its effectiveness in attitude control.

3. A GPS signal simulator shall be used to check if the GPS receiver is able to pick up the signal and determine the spacecraft's position.

Tank design
Tank design concerns the design of the main propellant tanks holding LH_2 and LOX. The function of this propellant is not to merely produce thrust, but are also used by fuel cells to produce power. Furthermore, as the main payload is LH_2, its preservation is a crucial aspect of the mission. In order to validate the design of the tanks, the following tests will be performed:

1. The tanks will be filled with cryogenic fuel in order to observe boil-off and pressurization rates
2. An integrated hot-fire of the engine will be performed to demonstrate that the tanks, feed system and the pressurization system work properly under thrust loads.
3. A test environment replicating flight conditions will be created to measure the effect of vibrations, sloshing, and thermal stresses on the tanks.
4. Fatigue tests will be conducted to assess the durability of the tanks when exposed to cyclic loads.

Docking/Refueling interface
With regard to the H_2GO mission, the fuel depot is a separate entity present in low earth orbit and its design is not covered in the scope of this project. However, an interface was created for this black box and a validation procedure has also been planned. The interface that will be used is a standard docking system which has been validated. However, the following steps will be undertaken in order to validate the system for the sake of this mission:

1. The docking process will be validated by docking a mock orbital depot and a model of the spacecraft to check if the interface connects the two elements properly. Undocking will also be validated in the same manner but in reverse order.
2. Partial misalignment tests will be conducted to see how the interface handles the misalignment.
3. Refueling can also be tested using the docking testing as the umbilical is a part of the docking interface which allows the transfer of LH_2 once the connection is made between the launch vehicle and the depot.
4. Apart from these large tests, smaller tests such as leak and pressure tests will be conducted to validate the docking/refueling interface.

13.3. Requirement Fulfillment

Table 13.2 shows the requirements compliance matrix for the stakeholder requirements. Here, the *Compliance* column states whether the design complies with the requirement, with a short explanation found in the *Details* column. The *Sensitive* column indicates the sensitivity of the compliance:

- Sensitive indicates that the performance characteristic in the requirement is subject to change in later detailed design, and as a result, the requirement might not be able to be complied with at that later stage.
- Insensitive indicates that the requirement will be complied with, no matter what changes happen in the later detailed design stages.
- Lastly, N/A indicates that the sensitivity of the compliance is not applicable, such as for those requirements for which compliance is not assessed at this point.

Regarding those requirements marked as Intend to Comply in Table 13.2, compliance can not be assessed at this point in time. For these, later design procedures will ensure that these requirements are complied with, and up to this point they are possibly partially complied with, such as *RQ-STK-REG-1*, where the safety factor for the tank pressure design is obtained from the GSC regulations.

Table 13.2: Stakeholder requirements compliance matrix

Requirement ID	Compliance	Details	Sensitive
RQ-STK-COS-1	Compliant	As outlined in Section 11.5, the total development cost is lower than the total engineering budget set by the customer.	Sensitive

continued on next page

Table 13.2 – *continued from previous page*

Requirement ID	Compliance	Details	Sensitivity
RQ-STK-COS-2	Compliant	Section 11.5 calculates the operational cost per launch, which was found to be lower than the budget set for it by the customer.	Sensitive
RQ-STK-COS-3	Intend to Comply	More detailed cost analysis is required to identify this. However, currently margins of 25 [%] are included to intend for compliance.	Sensitive
RQ-STK-PLD-1	Compliant	Section 9.5.1 shows the values for the final design after integration and iteration, from which it can be seen that the vehicle will be able to deliver a payload larger than 10000 [kg] per launch.	Insensitive
RQ-STK-PLD-2	Compliant	The vehicle is designed with safety in mind. As such, it complies with safety regulations, and is thus assumed to be able to transport LH_2 safely to the orbital depot.	Insensitive
RQ-STK-PLD-3	Compliant	With the payload mass, around 33 launches are required per year in order to achieve this goal, which is a realistic operational concept as outlined in Chapter 11.	Insensitive
RQ-STK-PLD-4	Compliant	All design calculations regarding orbital parameters are done with these parameters in mind, as can be seen in Section 8.3.	Insensitive
RQ-STK-DOK-1	Compliant	The vehicle features an ADCS subsystem, as outlined in Section 8.14, which takes care of the maneuvering in orbit.	Insensitive
RQ-STK-DOK-2	Intend to Comply	This will be assessed at a later point in the design phase, once it can be tested using a representative system.	Insensitive
RQ-STK-DOK-3	Intend to Comply	This will be assessed at a later point in the design phase, once it can be tested using a representative system.	Insensitive
RQ-STK-RFL-1	Compliant	As given in Chapter 11, the refueling process will take less than the 3 [h] specified by the customer.	Insensitive
RQ-STK-RFL-2	Compliant	While the vehicle docking and refueling interface was up until this point not specified by the customer, a suggestion for such a passive system has been outlined in Section 8.15.	Insensitive
RQ-STK-RLV-1	Intend to Comply	The exact time required for refurbishment is assessed at a later design phase.	Insensitive
RQ-STK-RLV-2	Compliant	The tanks, assumed to be the limiting factor, are sized in such a way that fatigue is not an issue before the 25 launches.	Insensitive
RQ-STK-RLV-3	Compliant	The project timeline given in Section 3.1.2 shows that the first operational launch is still planned for 2032.	Insensitive
RQ-STK-RLV-4	Compliant	The vehicle is designed with reusability in mind, and features components for re-entry and recovery such as the heat shield and the landing legs.	Insensitive
RQ-STK-REL-1	Compliant	Safety factors are taken into account in each subsystem design, from sources like NASA STD-5001, ESA ECSS Safety Factor Standards, and more.	Insensitive
RQ-STK-REL-2	Intend to Comply	This will be assessed further into the design and development phase.	Insensitive
RQ-STK-SUS-1	Compliant	The emissions compared to Falcon 9 v1.2 are 27 [%] lower, as shown in Section 12.3.4.	Insensitive
RQ-STK-SUS-2	Intend to Comply	This will be assessed further into the design and development phase.	Insensitive

continued on next page

Table 13.2 – *continued from previous page*

Requirement ID	Compliance	Details	Sensitivity
RQ-STK-SUS-3	Compliant	As mentioned in Section 8.6.3, the tank material is able to be recycled and reused. Since the tanks make up most of the total dry mass, this requirement is complied with.	Insensitive
RQ-STK-REG-1	Intend to Comply	This will be assessed further into the design and development phase.	Insensitive
RQ-STK-REG-2	Intend to Comply	This will be assessed further into the design and development phase.	Insensitive
RQ-STK-REG-3	Intend to Comply	This will be assessed further into the design and development phase.	Insensitive

As can be seen in Table 13.2, 18 out of 25 stakeholder requirements are complied with, while the remaining seven can not be assessed for compliance at the current stage in the design phase. However, for these seven, all are intended to comply with, and will be taken into account once the vehicle is developed further.

14 Conclusion & Recommendations

This chapter will aim to conclude the design report and illustrate further recommendations for the design and the design process.

14.1. Conclusion

This report aimed to design a reusable launcher as a response to concerns regarding deep space travel, specifically the usage of nuclear thermal propulsion. The key problem faced by this technology is the absolute volume and mass of the propellants required to be carried to space before being used. A proposed solution is to produce an orbiting refueling infrastructure that involves an orbiting fuel depot and an accompanying vehicle to transport fuel to the depot. The objective of this paper is to present a preliminary report on the design of such a vehicle.

In addition to the primary objective of transporting fuel, reusability and sustainability are key objectives to be fulfilled in the design. Considering the prevalence of companies such as SpaceX in the market for reusable first stages, a design choice was made to focus on the second stage, since this is a technological challenge that remains unfulfilled. Therefore, this report also presents the design of a reusable and sustainable second stage reusable vehicle for space transportation.

The primary goal as established by the client is to transport a total of 500 metric tonnes of liquid hydrogen to a $600\,[\text{km}]$ low Earth orbit at a $6\,[^\circ]$ inclination. This requirement is to be fulfilled by carrying at least 10 metric tonnes per launch, while reducing emissions by $25\,[\%]$ compared to current operational rockets.

After performing an analysis on current first stage vehicles capable of transporting the required payload, New Glenn produced by Blue Origin was chosen. As such, the design is anchored around the requirements posed to launch with the New Glenn rocket. A similar analysis was performed for the aeroshape of the vehicle; the result of this was to design a blunted cone. This was primarily due to its good balance between aerodynamic and structural properties. Potential configurations using alternative shapes were also considered; however, after evaluation using the predicted total mass, the environmental impact, the total risk, and the associated cost, the blunted cone remains the ideal choice.

The preliminary design was performed for a broad set of vehicle subsystems, which led to certain critical design choices. The system uses an actively cooled heat shield, straying from the conventional ablative method to increase maintainability and sustainability. The heat shield contributes to an aerospike effect generated by 24 main thrusters angled slightly inward. Similarly, the timeline of the missions allows the main tanks to carry cryogenic liquid without insulation. The timeline of the mission also allows for the use of fuel cells, against the more common batteries or photovoltaic cells.

To ensure adaptability, the vehicle uses the standardized space docking system to dock with the orbiting depot. Considering aerodynamics and thermal loads during re-entry, the vehicle will be entering base first using a gliding trajectory. The vehicle uses differential thrust to control itself during landing, where it uses four telescopic landing legs. The vehicle does not utilize active or passive control systems while maintaining static stability and dynamic stability in constant velocity conditions. However, the slender shape of the vehicle contributes to instabilities during decelerating flight. A rendering of the vehicle is provided in Figure 14.1.

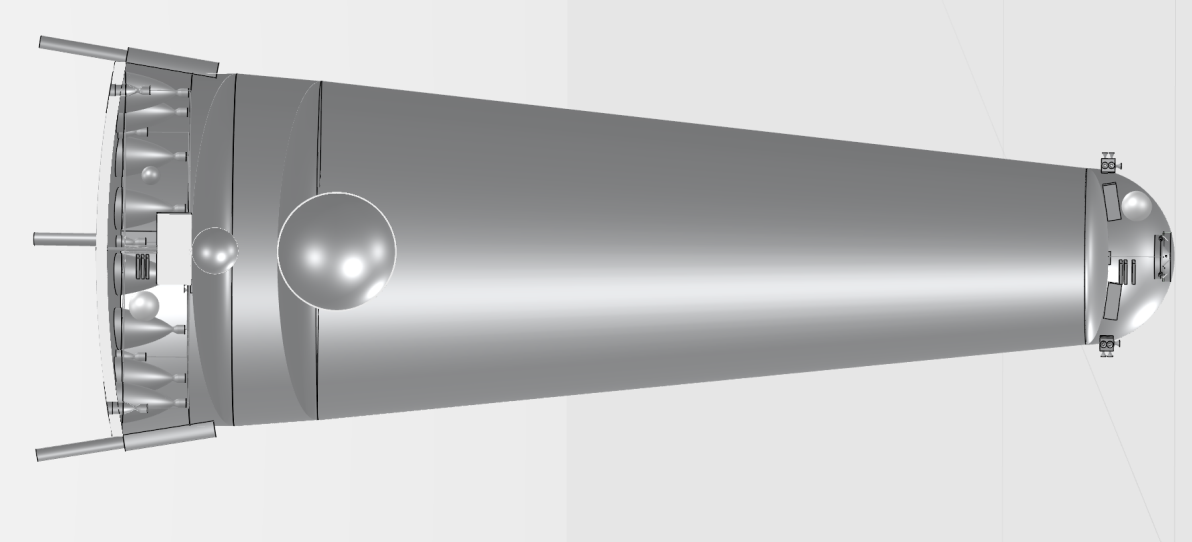

Figure 14.1: Vehicle Render

The main characteristics for the final design are presented in Table 14.1.

Table 14.1: H_2ERMES Vehicle Characteristics

Characteristic	Value	Characteristic	Value
Max Diameter	10.6 [m]	Data Rate	33.1 [Mbps]
Min Diameter	5 [m]	Data Rate with Margin (70%)	56.2 [Mbps]
Total Length	29.8 [m]	ΔV Required	6391 [m/s]
Fuel	Liquid Hydrogen	ΔV Available	6659 [m/s]
Oxidizer	Liquid Oxygen	Hypersonic L/D	0.2 [−]
Wet Mass	300.1 [t]	Subsonic L/D	0.6 [−]
Dry Mass	39.5 [t]	Pitch-damping Coefficient	−0.8 [−]
Total Boil-Off	4.9-6.6 [t]	Trim Angle of Attack	17 [°]
Payload	13.3-15 [t]	Development Cost	939.8M [US$]
Total Power	4890 [W]	Manufacturing Cost	25.3M [US$]
Total Power with Margin (20%)	5868 [W]	Operational Cost	70.0M [US$]

14.2. Recommendations

Having concluded the preliminary design, as presented in this report, it is clear that many areas of the design deserve a deeper investigation than was possible within the limits of the current project. As such, in this section, recommendations that need to be addressed in future iterations or for another team of engineers looking into a similar project are presented on a per-subsystem basis.

Delta V

The ΔV required for orbit insertion was calculated assuming a simple gravity turn, while this is generally a good trajectory, it is not necessarily the most optimal, so a proper trajectory optimization should be performed to optimize payload capacity. Furthermore, aerobraking maneuvers could be investigated for the deorbit and re-entry phase of the flight to again save some ΔV.

Flight Design

Currently, the flight design was performed under the assumption that H_2ERMES is to launch and land at the same site; however, this severely restricts the flight timeline. It may be possible to significantly reduce the time and so the boil-off by reexamining the possibility of sea barge landing or an alternative launch site. The economic benefit of increased payload is weighed against the additional costs of this infrastructure.

Additional timeline flexibility could also be achieved by introducing inclination-changing maneuvers. In this case, the balance will be between the additional payload and the higher ΔV requirements.

Aerodynamics
It is recommended to perform a high fidelity CFD simulation and wind tunnel testing of H_2ERMES through all phases of its atmospheric flight to accurately characterize its aerodynamic behavior, as the analytical models used in the preliminary design do not possess the required accuracy.

If these simulations confirm that the current configuration of H_2ERMES is unstable in decelerating flight, it will be necessary to investigate mitigation strategies. Either by the addition of control surfaces at the cost of additional mass or by adjusting the overall shape of the vehicle, as the analysis indicated a shorter vehicle would be more stable. Furthermore, adjustments to the re-entry path should be investigated as they could also be used to control the aerodynamic forces and moments on the vehicle.

Tank Design
Validating the tank design results by performing a FEM analysis is recommended to accurately model the buckling of the structure under the launch loads and inner pressure. Additionally, adding some reinforcements may make the structure more resistant to vibrations.

Furthermore, regarding fatigue prediction in the main tanks, it is strongly recommend to use FEM to create an S-N curve for the Miner's rule as was done in [34] and the crack growth rate coefficients used for the Paris crack growth rate equation as was done in [33]. The case of bending and the impact of lateral loads was not considered on fatigue due to time constraints. Additionally, the fatigue prediction tool was done for a cylindrical geometry. Since the current tank geometry is a truncated cone with elliptical caps, it is recommended that experimental data be obtained for the specific loading case of H_2ERMES.

Propulsion
It is recommended to perform firing tests of experimental versions of the thrust chambers to better characterize the temperatures of the propellants throughout the cooling loop, as well as to better characterize the performance of the engine. Another key aspect that should involve further testing is the aerospike effect created by the 24 thrust chambers firing slightly angled toward the heat shield. Since quantification of this effect was not possible throughout the preliminary design, further testing could inform potential design decisions for the detailed design.

Landing Legs
While at this stage the tanks are considered driving for fatigue, a fatigue analysis should also be performed for the landing legs. Besides this, aerodynamic and thermal design for the aero-cover can be more detailed to result in a more properly defined subsystem.

Nosecone
The impact of fatigue should be taken into account since H_2ERMES has to survive at least 25 launches for a more comprehensive analysis of the nosecone. Furthermore, the heat propagation while in orbit due to external fluxes should also be considered since all the avionics are kept in the nosecone along with the AODCS propellant tank, which needs an operating temperature of below 100 [°C]. [54] presents a multi disciplinary approach on how to size the nosecone by considering external heat flux (during ascent and orbit) and the aerodynamic loads (during ascent) by using FEM. Therefore, for future studies, it is recommended to base the this approach on sizing the nosecone.

Active Metallic Heat Shield
It is recommended to develop more advanced design tools utilizing CFD and FEM methods. The change to a 3-D transient in time heat transfer model will allow validation of the 1-D model as well as analysis of localized heat fluxes. In addition, it is recommended to contact material engineering specialists and consider developing a specialized alloy for the heat shield application. Concerning that, the manufacturability of the heat shield should be considered in detail for the material chosen. If resources are limited, it is recommended to first validate the 1-D heat transfer model and create a programmatic optimizer for the model that could explore all design variations (different coolant channel geometries, channel layouts, coolant properties, different empirical models, etc.).

Power
The new development of modern, more efficient fuel cells suitable for space allocations would allow for further weight savings, both in cell mass and reactant mass. The progress of such technology should be monitored or even invested in.

Data Handling
The use of radiation-tolerant rather than radiation-hardened electronics would allow greater flexibility in computing capability upgrades.

Communications
A move away from the expensive, bureaucratic, government agency-maintained ESTRACK network should be investigated. The very large link budget allows for downsizing ground stations and switching to a simpler, cheaper, commercial service provider. Another communications architecture change worth investigating is satellite relay communications, through Internet satellites like Project Kuiper or Starlink. Uniquely, this would also permit transmitting data throughout re-entry, where the plasma sheath surrounding the vehicle on all sides except in its wake strongly attenuates all electromagnetic waves.

Attitude & Orbital Determination and Control Subsystem
The determination system could use a combination of instruments rather than solely relying on GPS receivers. This would have greatly improved the redundancy on the subsystem. For the thruster sizing, the translational maneuvers required for docking were not quantified due to time constraints, this should be remedied to validate the number of thrusters selected.

Boil-off
It is recommended that FEM be used to develop the thermodynamic environment inside the tank which can then be used to model the effect of fuel unloading on the state variables (such as vapor pressure, temperature of gas and liquid, and mass of gas and liquid). Furthermore, a full thermal environment should also be made to predict the heat load entering the tank due to external fluxes. Additionally, considerations of having a coating to decrease the incident heat fluxes should also be investigated, as this can also dramatically decrease the heat load. However, this coating has refurbishment considerations and can also get damaged during ascent, impacting its performance. Furthermore, it should be investigated how the AODCS subsystem can be used to maneuver H_2ERMES to decrease the heat flux entering the tank by pointing the heat shield towards the sun at all points during the mission. This will however increase the AODCS propellant mass and the dry mass. But this must be investigated further since any reduction in the heat load can greatly affect the boil-off mass as was seen in Table 8.26.

References

[1] Dezfuli, H. et al. *NASA Risk Management Handbook*. Nov. 2011.

[2] Group 7. *H2GO Midterm Report*. Tech. rep. TU Delft, 2025.

[3] Kumar, L. and Sleiti, A. K. "Modeling and Analysis of Effect of Various Tank Geometries and Relief Pressure on Liquid Hydrogen (LH2) Boil-Off Losses". In: (2024).

[4] Thomas, D. "Nuclear thermal propulsion – Progress and potential". In: *Journal of Space Safety Engineering* 11.2 (June 2024), pp. 362–373. ISSN: 24688967.

[5] Esselman, W. "NERVA Nuclear Rocket Program (1965)". In: (1965).

[6] Le Bar, J. and Cady, E. "The Advanced Cryogenic Evolved Stage (ACES)-A Low-Cost, Low-Risk Approach to Space Exploration Launch". In: *Space 2006*. San Jose, California: American Institute of Aeronautics and Astronautics, Sept. 2006. ISBN: 978-1-62410-049-9.

[7] *Regulation (EC) No 1907/2006 of the European Parliament and of the Council of 18 December 2006 concerning the Registration, Evaluation, Authorisation and Restriction of Chemicals (REACH), establishing a European Chemicals Agency, amending Directive 1999/45/EC and repealing Council Regulation (EEC) No 793/93 and Commission Regulation (EC) No 1488/94 as well as Council Directive 76/769/EEC and Commission Directives 91/155/EEC, 93/67/EEC, 93/105/EC and 2000/21/EC (Text with EEA relevance)*. Legislative Body: OP_DATPRO. Apr. 2025.

[8] Edberg, D. *Design of Rockets and Space Launch Vehicles, Second Edition*. 1st ed. Reston: American Institute of Aeronautics & Astronautics, 2022. ISBN: 978-1-62410-642-2.

[9] Elferink, P. M. F. "Prototype X: A Cost-Based Design Optimization of an Upper Stage Liquid Propulsion Module with Green-Storable Propellants". MA thesis. Delft, Netherlands: TU Delft, Dec. 2022.

[10] Group 7. *H2GO Baseline Review*. Tech. rep. TU Delft, 2025.

[11] Leishman, J. G. "Hypersonic Flight Vehicles". In: (Jan. 2023). Book Title: Introduction to Aerospace Flight Vehicles Publisher: Embry-Riddle Aeronautical University.

[12] Jorgensen, L. H. and Brownson, J. J. *Effects of Reynolds number and body corner radius on aerodynamic characteristics of a space shuttle-type vehicle at subsonic Mach numbers*. Tech. rep. NASA-TN-D-6615. NTRS Author Affiliations: NASA Ames Research Center NTRS Document ID: 19720005331 NTRS Research Center: Legacy CDMS (CDMS). Jan. 1972.

[13] Xu, J.-H. et al. "Effect of mach number on high-subsonic and low-Reynolds-number flows around airfoils". In: *International Journal of Modern Physics B* 34.14n16 (June 2020). Publisher: World Scientific Publishing Co., p. 2040112. ISSN: 0217-9792.

[14] Charles E. Rogers and David Cooper. *Rogers Aeroscience RASAero II Aerodynamics Analysis and Flight Simulation Program Users Manual*. 2019.

[15] Cole D. Kazemba et al. "Survey of Blunt Body Dynamic Stability in Supersonic Flow". In: *AIAA Atmospheric Flight Mechanics Conference* AIAA 2012-4509 (Aug. 2012).

[16] Heybey, W. H. "Newtonian aerodynamics for general body shapes with several applications". In: *NASA Technical Memorandum* (Feb. 1996).

[17] Maughmer, D. "PREDICTION OF FORCES AND MOMENTS FOR HYPERSONIC FLIGHT VEHICLE CONTROL EFFECTORS". In: ().

[18] F.D. Steketee. *Dynamic Stability of Space Vehicles*. Tech. rep. NSA CR-945. San Diego, California: National Aeronautics and Space Administration, Nov. 1967.

[19] Gerald L. Winchenbach. "Dynamic Stability of Blunt Atmospheric Entry Configurations". In: *Journal of Spacecraft and Rockets* ().

[20] Schoenenberger, M. "Limit Cycle Analysis Applied to the Oscillations of Decelerating Blunt-Body Entry Vehicles". In: ().

[21] Schoenenberger, M., Queen, E., and Litton, D. “Oscillation Amplitude Growth for a Decelerating Object with Constant Pitch Damping”. In: *AIAA Atmospheric Flight Mechanics Conference and Exhibit*. Guidance, Navigation, and Control and Co-located Conferences. American Institute of Aeronautics and Astronautics, Aug. 2006.

[22] Hirschel, E. H. and Weiland, C. *Selected Aerothermodynamic Design Problems of Hypersonic Flight Vehicles*. Berlin, Heidelberg: Springer Berlin Heidelberg, 2009. ISBN: 978-3-540-89973-0 978-3-540-89974-7.

[23] Mehta, R. C. “Effect of geometrical parameters of reentry capsule over flowfield at high speed flow”. In: *Advances in Aircraft and Spacecraft Science* 4.4 (July 2017). Number: 4, pp. 487–501. ISSN: 2287-528X.

[24] Arora, R. and Kumar, P. “Aerodynamic Shape Optimization of a Re-entry Capsule”. In: *AIAA Atmospheric Flight Mechanics Conference and Exhibit*. Austin, Texas: American Institute of Aeronautics and Astronautics, Aug. 2003. ISBN: 978-1-62410-089-5.

[25] Kim, M.-S. et al. “Tensile and Fracture Characteristics of 304L Stainless Steel at Cryogenic Temperatures for Liquid Hydrogen Service”. In: *Metals* 13.10 (2023), p. 1774.

[26] Baptiste, P. “Order Regulating the Operation of Installations of the Guyana Space Center”. In: (2024).

[27] Wertz, J. R., Everett, D. F., and Puschell, J. J. *Space Mission Engineering: the New SMAD*. Space technology library 28. Torrance: Microcosm Press, 2011. ISBN: 978-1-881883-15-9.

[28] Young, W. C., Budynas, R. G., and Roark, R. J. *Roark’s formulas for stress and strain*. 7. ed., reprint. McGraw-Hill international edition, General engineering series. New York: McGraw-Hill, 2011. ISBN: 978-0-07-072542-3.

[29] NASA. *Buckling of thin-walled truncated cones*. 1988.

[30] Prescott, A. “New Glenn Payload User’s Guide”. In: (Oct. 2018).

[31] Singh, Y. P. et al. “Common Bulkhead Tank Design for Cryogenic Stage of an Indian Launch Vehicle”. In: *Defence Science Journal* 72.1 (Jan. 2022), pp. 3–9. ISSN: 0976-464X, 0011-748X.

[32] Cody, K. *The Impact of Multiple Loading Conditions on the Structural Integrity of a Reusable Rocket Fuel Tank*. T452 Project Report. Undergraduate engineering project analyzing fracture, fatigue, and thermal effects on LOX tank structure. 2023.

[33] Choi, H. et al. “Fatigue crack growth characteristics of austenitic stainless steel for cold-stretched pressure vessels at cryogenic temperatures: Ermüdungsrisswachstumseigenschaften von austenitischem rostfreiem Stahl für kaltgestreckte Druckbehälter bei Tiefsttemperaturen”. In: *Materialwissenschaft und Werkstofftechnik* 47.5-6 (2016), pp. 444–451.

[34] Huzni, S. et al. “S-N Curve Estimation of AISI 304 in Air and Corrosive Environment Using Finite Element Method”. In: *Proceedings of the Seminar Nasional Tahunan Teknik Mesin (SNTTM XII)*. Bandar Lampung, Indonesia: Syiah Kuala University, 2013, pp. 1197–1200. ISBN: 978-979-8510-61-8.

[35] Maximov, J. and Duncheva, G. “Effects of Cryogenic- and Cool-Assisted Burnishing on the Surface Integrity and Operating Behavior of Metal Components: A Review and Perspectives”. In: *Machines* 12.5 (May 2024), p. 312. ISSN: 2075-1702.

[36] Ronald Humble. *Space Propulsion Analysis and Design*. McGraw-Hill, 1995. ISBN: 0-07-031320-2.

[37] Vinitha, T., Senthilkumar, S., and Manikandan, K. *Thermal Design and Analysis of Regeneratively Cooled Thrust Chamber of Cryogenic Rocket Engine*. Tech. rep. Department of Aeronautical Engineering, Nehru Institute of Engineering and Technology, June 2013.

[38] P. Van Hooster, K. and Bradley, D. P. *Space Shuttle Main Engine - The Relentless Pursuit of Improvement*. Tech. rep. American Institute of Aeronautics and Astronautics.

[39] Michael, L. M. *Hydrogen Applications for Space Transportation*. July 2019.

[40] Subeom, H., Juhwan, J., and Youngbin, Y. *Spray characteristics of a multi-slit type throttleable pintle injector with different slit heights*. Tech. rep. Feb. 2024.

[41] Tinker, D. C. et al. “Compact Augmented Spark Igniters for Liquid Rocket Engines”. PhD thesis. 2021.

[42] Sippel, M. et al. “Studies on expander bleed cycle engines for launchers”. In: *39th AIAA/ASME/SAE/ASEE Joint Propulsion Conference and Exhibit*. 2003, p. 4597.

[43] Paniagua, G. et al. “Aerodesign of a Transonic Contra-rotating turbine to drive the LOX and LH2 turbopumps in an expander cycle”. In: *International Journal of Numerical Methods for Heat and Fluid Flow* 23 (May 2013), pp. 575–587.

[44] Bell, I. H. et al. “Pure and Pseudo-pure Fluid Thermophysical Property Evaluation and the Open-Source Thermophysical Property Library CoolProp”. In: *Industrial & Engineering Chemistry Research* 53.6 (Feb. 2014), pp. 2498–2508. ISSN: 0888-5885, 1520-5045.

[45] Gordon, S. *Computer program for calculation of complex chemical equilibrium compositions and applications. Part 1: Analysis*. Oct. 1994.

[46] Ponomarenko, A. *RPA: Tool for Rocket Propulsion Analysis*. 2014.

[47] Thies, C. “Investigation of the landing dynamics of a reusable launch vehicle and derivation of dimension loading for the landing leg”. In: *CEAS Space Journal* 14.3 (2022), pp. 565–576.

[48] Purcell, M. V., Wicklund, A. M., and Vadecha, N. *Reusable Launch Vehicles: Designing Legs for Propulsive Rocket Landing*.

[49] Larson, W. J. and Wertz, J. R., eds. *Space Mission Analysis and Design*. 2nd ed. Space technology library. Torrance, Calif. : Dordrecht ; Boston: Microcosm ; Kluwer, 1992. ISBN: 978-0-7923-1998-6 978-1-881883-01-2.

[50] Megson, T. H. G. *Aircraft Structures for engineering students*. 2022.

[51] NASA. *NASA-STD-5001B - Structural Design and Test Factors of Safety for Spaceflight Hardware*. 2014.

[52] ECSS. *ECSS-E-ST-32-10C Rev.2 – Structural factors of safety for spaceflight hardware*. 2019.

[53] NASA. *Calculating Factors of Safety and Margins of Safety From Interaction Equations*. 2019.

[54] Greco, P. et al. “Beyond Gravity’s approach to the multidisciplinary design, analysis and optimization of reusable payload fairings”. In: (2022).

[55] Bergman, T. L. et al. *Incropera’s principles of heat and mass transfer*. 8th edition, global edition. Hoboken, NJ: Wiley, 2017. ISBN: 9781119382911.

[56] Zoelly, R. *Ueber ein Knickungsproblem an der Kugelschale*. Buchdr. Zürcher & Furrer, 1915.

[57] Evkin, A. Y. and Lykhachova, O. V. “Design buckling pressure for thin spherical shells: Development and validation”. In: *International Journal of Solids and Structures* 156-157 (Jan. 2019), pp. 61–72. ISSN: 00207683.

[58] Mohammadi-pour, M. et al. “Microstructure and mechanical properties of joints welded by friction-stir welding in aluminum alloy 7075-T6 plates for aerospace application”. In: *Rare Metals* 44.3 (2025), pp. 2085–2093.

[59] Mooij, E. *Re-entry Systems*. 1st ed. 2024. Springer Aerospace Technology. Cham: Springer Nature Switzerland, 2024. ISBN: 978-3-031-62174-1.

[60] Locke, J. M. and Landrum, D. B. “Study of Heat Transfer Correlations for Supercritical Hydrogen in Regenerative Cooling Channels”. In: *Journal of Propulsion and Power* 24.1 (Jan. 2008), pp. 94–103. ISSN: 0748-4658, 1533-3876.

[61] Mills, A. F. and Coimbra, Carlos F.M. *Basic heat and mass transfer*. Third edition. OCLC: 954592884. San Diego, California: Prentice Hall, 2015. ISBN: 9780996305303.

[62] Sutton, G. P. and Biblarz, O. *Rocket propulsion elements*. Ninth edition. Hoboken, New Jersey: John Wiley & Sons Inc, 2017. ISBN: 978-1-118-75365-1.

[63] Song, H. *Engineering Fluid Mechanics*. 1st ed. 2018. Singapore: Springer Singapore : Imprint: Springer, 2018. ISBN: 978-981-13-0173-5.

[64] Asadi, M., Xie, G., and Sunden, B. “A review of heat transfer and pressure drop characteristics of single and two-phase microchannels”. In: *International Journal of Heat and Mass Transfer* 79 (Dec. 2014), pp. 34–53. ISSN: 00179310.

[65] NASA. *Fuel Cell Power Plants*. Space Shuttle Reference. Sept. 2020.

[66] Burke, K. “Fuel Cells for Space Science Applications”. In: *1st International Energy Conversion Engineering Conference (IECEC)*. Portsmouth, Virginia: American Institute of Aeronautics and Astronautics, Aug. 2003. ISBN: 978-1-62410-088-8.

[67] United Space Alliance. *Shuttle Crew Operations Manual*. Rev. A. Space Program Operations Contract NNJ06VA01C. Dec. 2008.

[68] Pipher, M. D. *Electrical Power System Database for Consumables Analysis Volume I: Electrical Equipment List, Activity Blocks, and Time Lines*. Tech. rep. NASA-CF-144459). Consumables Analysis Section, EPS Task Support Group, McDonnel Douglas, May 1975.

[69] Shin, D. K. *Frequency and Channel Assignments*. Tech. rep. NASA JPL Deep Space Network, Oct. 2014.

[70] Launer, R. et al. "Launcher Tracking Support from ESTRACK". In: *SpaceOps 2010 Conference*. Huntsville, Alabama: American Institute of Aeronautics and Astronautics, Apr. 2010. ISBN: 978-1-62410-164-9.

[71] Gill, E. K. A. et al. "Overview of Space-Capable Global Navigation Satellite Systems Receivers: Heritage, Status and the Trend towards Miniaturization". In: (2023).

[72] Terzibaschian, T. et al. *High Torque Wheels for agile Satellite Maneuvers - in Orbit Experiences and future Steps with Recuperation of Energy*. Oct. 2020.

[73] NASA. *International Docking System Standard (IDSS) Interface Definition Document (IDD) Revision F*. 2022.

[74] NASA. *NASA Technical Memorandum 83688: On-Orbit Cryogenic Fluid Transfer*. 1984.

[75] NASA. *NASA DOCKING SYSTEM (NDS) USERS GUIDE*. 2010.

[76] Al Ghafri, S. Z. S. et al. "Modelling of Liquid Hydrogen Boil-Off". In: *Energies* 15.3 (Jan. 2022). Number: 3 Publisher: Multidisciplinary Digital Publishing Institute, p. 1149. ISSN: 1996-1073.

[77] Rebis, J. and Stroom, C. *ESATAN, A Review After Four Years in Use*. Tech. rep. SAE Technical Paper, 1989.

[78] Henninger, J. H. *Solar absorptance and thermal emittance of some common spacecraft thermal-control coatings*. Vol. 1121. National Aeronautics, Space Administration, Scientific, and Technical …, 1984.

[79] Klein, M. J. "The historical origins of the van der Waals equation". In: *Physica* 73.1 (1974), pp. 28–47.

[80] *U.S. Standard Atmosphere, 1976*. Tech. rep. NOAA-S/T-76-1562. NTRS Document ID: 19770009539 NTRS Research Center: Legacy CDMS (CDMS). Oct. 1976.

[81] Loh, W. H. T. *Re-entry and Planetary Entry Physics and Technology: I / Dynamics, Physics, Radiation, Heat Transfer and Ablation*. Ed. by Loh, W. H. T. Vol. 2. Applied Physics and Engineering. Berlin, Heidelberg: Springer Berlin Heidelberg, 1968. ISBN: 978-3-642-48929-7 978-3-642-48927-3.

[82] Zandbergen, B. *Launch Vehicle Design and Sizing Reader*. TU Delft, Feb. 2010.

[83] Malec, A. and Packard, H. "Reliability and Maintainability (RAM) Training". In: *Glenn Research Center* (July 2000).

[84] Carlier, S. et al. "Evaluation of reliability, availability, maintainability and safety requirements for manned space vehicles with extended on-orbit stay time". In: *Acta Astronautica* 38.2 (Jan. 1996), pp. 115–123. ISSN: 0094-5765.

[85] Gillespie, A. M. "Reliability, Maintainability, and Availability". In: *NASA* (Dec. 2012).

[86] Federal Aviation Administration. *Guide to Reusable Launch and Reentry Vehicle Reliability Analysis*. Tech. rep. Washington, D.C., May 2005.

[87] Lehner, M. M. (.-D. "APR 8715.1 Chapter 15 – Cryogenic Safety". In: (July 2023).

[88] *ECSS-Q-ST-40C-Rev.1(15February2017)*. Feb. 2017.

[89] "Space Debris Mitigation Guidelines of the Committee on the Peaceful Uses of Outer Space". In: (Jan. 2010).

[90] Drenthe, N. T. "Small Orbital Launch Systems, a Tentative Initial Cost Estimate". MA thesis. TU Delft, Dec. 2016.

[91] Koelle, D. E. *The Transcost-Model for Launch Vehicle Cost Estimation and its Application to Future System Analysis*. Tech. rep. Munich, Germany: Messerschmitt-Boelkow-Blohm GmbH, Mar. 1984.

[92] McAfee, J., Culver, G., and Naderi, M. *NASA Air Force Cost Model (NAFCOM) Capabilities and Results*. Huntsville, United States, 2011.

[93] Reinbold, G. *Successful Cost Estimation with T1 Equivalents*. Tech. rep. Bristol, United Kingdom: ESA, Oct. 2016.

[94] Brundtland, G. H. and Khalid, M. *Report of the World Commission on Environment and Development : "Our common future" Our common future*. Aug. 1987.

[95] Zhang, T. C. et al. *Sustainability: Fundamentals and Applications*. Newark: John Wiley & Sons, Incorporated, 2020. ISBN: 978-1-119-43389-7.

[96] Shokouhi, M. and Senisel Bachari, M. "An overview of the aspects of sustainability in project management". In: *Progress in Engineering Science* 2.1 (Mar. 2025), p. 100048. ISSN: 2950-4252.

[97] Fischer, J.-S. et al. *Recommendations for the development of space systems life cycle assessment methodology for space transportation systems*. Apr. 2024.

[98] European Space Agency Life Cycle Assessment Working Group. "Space system Life Cycle Assessment (LCA) guidelines". In: *ESA internal* 1 (2016).

[99] Vogtlander, J. *LCA-based assessment of sustainability: the Eco-costs/Value Ratio EVR*. Jan. 2010. ISBN: 978-90-6562-233-4.

[100] Dowling, N. E. *Stress-Life (S-N) Fatigue Analysis – Constant Amplitude Loading*. Accessed: 2025-06-18. 2024.

[101] *NASA's Exploration Systems Architecture Study*. Tech. rep. NASA, Nov. 2005.